INVERSE STRATEGIES FOR CHARACTERIZATION OF MATERIAL PROPERTIES

A Dissertation

Presented to the Faculty of the Graduate School

of Cornell University

in Partial Fulfillment of the Requirements for the Degree of

Doctor of Philosophy

by

Miguel Alejandro Aguiló

January 2011

INVERSE STRATEGIES FOR CHARACTERIZATION OF MATERIAL PROPERTIES

Miguel Alejandro Aguiló, Ph.D.

Cornell University 2011

The imaging of constitutive parameters is of interest in many science and engineering fields. Indeed, non-invasive and nondestructive techniques are used to characterize key properties of a system given its response due to an external excitation. Then, assuming a priori a given model of the system, the measured response and an inverse approach are used to identify material properties. This work was undertaken in the context of identification of spatially-varying elastic and viscoelastic parameters of solids using vibroacoustics based techniques.

Two optimization approaches, nongradient and gradient-based optimization, were investigated in this work. Initially, nongradient-based algorithms were preferred over gradient-based algorithms because of there ability to find global minima irrespective of initial guesses. For instance, Gaussian radial basis functions were used to construct a finite-dimensional representation of the elastic moduli. Then, an inverse approach was used to approximate the spatially-varying elastic moduli through the system response induced by the radiation force of ultrasound. The inverse problem was cast as an optimization problem in which a least-square error functional that quantified the misfit between the experimental and finite element representation system response is minimized by searching over a space of admissible vectors that best describe the spatial distribution of the elastic moduli. Subsequently, gradient-based optimization was preferred over nongradient-based optimization as the number of design

variables increased due to the increment in computational cost.

Two inverse approaches, L2-adjoint and concept of error in constitutive equation, were investigated in the context of gradient-based optimization. First, the L2-adjoint inverse approach was used to characterize spatially-varying viscoelastic properties because of its advantage to efficiently calculate the gradient of the error functional with respect to the design variables by solving the corresponding adjoint equations. The inverse problem was cast as an optimization problem in which a least-square error functional that quantified the misfit between the experimental and the finite element representation system response is minimized by searching over a space of admissible functions that best describe the spatially-varying viscoelastic properties.

Given that the least-square error functional is non-convex, an inverse approach based on the concept of error in constitutive equation was investigated. The convexity property of the error in constitutive equation functionals, shown extensively for elliptic boundary value problems, reduce the sensitivity of the inverse solution to parameter initialization. The inverse problem was cast as an optimization problem in which an error in constitutive equation functional that quantified the misfit between the kinematically and dynamically admissible stress fields is minimized by searching over a space of admissible functions that best describe the spatially-varying viscoelastic properties. Contrary to the L2-adjoint inverse approach, the gradient equation is easily derived by taking the direct derivative of the error in constitutive equation functional with respect to the design variables.

The feasibility of the proposed inverse approaches is demonstrated through a series of numerical and physical experiments. Results show that the proposed inverse approaches have the potential to characterize spatially-varying elastic

and viscoelastic properties of solids in realistic settings. Furthermore, it will be shown that the inverse approach based on the concept of error in constitutive equation outperformed the L2-adjoint inverse approach.

BIOGRAPHICAL SKETCH

Miguel Alejandro Aguiló was born on July 8, 1982 in Río Piedras, Puerto Rico. He is the youngest member of a family of four brothers. Both of his parents graduated from the university and placed a high value in education as a means for their children to become responsible members of society. During his childhood, Miguel Alejandro Aguiló had the opportunity to live in Santiago, Dominican Republic for four years. Then, as promise by his father, he moved back to Puerto Rico and obtained his high school diploma at the high school he attended as a child. During this time his parents lived in Venezuela and Mexico, which allow him to visit them regularly for extensive periods of time. The exposure to various cultures and societies allowed him to realize the need for good engineering work throughout the world. These experiences served as primary motivation for him to pursue a career in engineering.

Miguel Alejandro Aguiló received a Bachelor's degree in Civil and Environmental Engineering from the University of Puerto Rico Mayagüez in 2005. After graduation, he continued his graduate studies at Cornell University, where he obtained his Master of Science in Structural Engineering in 2009. Currently he is PhD candidate in the Department of Civil and Environmental Engineering at Cornell University under the supervision of Professor Wilkins Aquino. He is expected to defend his dissertation work on September 7, 2010 and afterward join the Sandia National Laboratories as a postdoctoral fellow in the Department of Optimization and Uncertainty Quantification.

Seamos realistas, soñemos con lo imposible

Ernesto Guevara

ACKNOWLEDGEMENTS

I would like to acknowledge the people that made this work possible:

Professor Wilkins Aquino, for his guidance during my studies at Cornell University and the ideas that made this work possible. I am the researcher that I am today because of his guidance and advices, for this I am grateful.

Professor Anthony R. Ingraffea, Professor Subrata Mukherjee, and Professor Lawrence J. Bonassar for serving as members of my graduate committee, and for their careful reading of this dissertation and ideas.

Professor Christopher J. Earls for his technical support with the computer cluster, specially during my time away from Cornell University. The example problems shown in this work will have never been done without his technical support.

Professor Peter J. Diamessis and Professor Kenneth C. Hover, for giving me their friendship and support during my time at Cornell University. Their advices about graduate school and life helped me endured tough moments during my time at Cornell University.

To my great friends Jacob D. Hochhalter and Steve Rodriguez, without them my experience at Cornell University would have been completely different. They were always there, and continue to be, every time I needed a sincere advise. Their examples helped me eliminate prejudice I had created because of past personal experiences and made the assimilation of a different culture possible. Without their friendship, I would be a different person today.

To all my friends at Cornell University, specially Gabriel De Frías, Brett Richard, Coalton Bennett, Jean-Pierre Laurenceau, Daniel Rosario, and Jeff Bozek. They made my time at Cornell University an unforgettable experience.

Above all, I would like to thank my parents, Miguel G. Aguiló and Vivian Valentín for their never ending love and support. I have been blessed with parents who taught me that through hard work, responsibility, and commitment anything is attainable. These values allow me to become a responsible member of society and served as the primary foundations for the person I have become. I will always be in great debt to them for their support and never ending love, but as a small payment to that debt, I dedicate this work to them. I love you both!

This research was supported by Cornell University, The Coleman Foundation, and The National Institute of Biomedical Imaging and Bioengineering under grant 5R01EB002167-19s. The support of the university, foundation. and agency is gratefully acknowledged.

TABLE OF CONTENTS

LIST OF TABLES

LIST OF FIGURES

CHAPTER 1

INTRODUCTION

Direct characterization of material properties is not always possible, and in some cases not desirable. This has led researchers in many science and engineering fields to develop noninvasive and nondestructive techniques for damage identification or characterization of material properties [2, 5, 6, 7, 8, 10, 77, 86, 94]. As an example in aeronautics, the airline industry and the military are driving the need for more capable, cost-effective maintenance techniques for damage identification. For instance, Bloomberg News recently reported that US airlines replaced aircraft devices in almost 1500 aircraft at a cost of $12.5 millions due to undetected damages during routinely maintenance services [60]. Much cost saving would be attained from more efficient maintenance programs, which will result from a symptom-based approach that combines noninvasive and nondestructive techniques with robust inverse methods. In the medical field, material properties provide valuable information about the onset and progression of diseases. Furthermore, the fact that these properties can be used as a metric to differentiate between healthy an unhealthy tissue has led researchers to combine noninvasive and nondestructive techniques with inverse method for characterization of material properties [12, 31, 32, 38, 62, 80, 84, 92, 97, 98, 101, 104, 112, 118].

Different methodologies have been employed for imaging spatially-varying material properties in soft tissue [11, 14, 15]. The basic premise is that current medical imaging techniques such as ultrasound (US) and magnetic resonance (MR) imaging can provide information about complex deformation processes that can in turn be used to image the spatial distribution of material proper-

ties. For instance, Skovoroda *et al.* [110] presented a method for elastic modulus imaging of soft tissue based on ultrasonic displacement and strain images for incompressible and compressible media. Bishop *et al.* [15] proposed a methodology for imposing plane strain conditions in MR elastography for incompressible linear elastic material. The present work uses vibroacoustic based techniques to characterize the elastic and viscoelastic properties of solids.

In Vibroacoustography (VA), the radiation force of US is used to produce a localized oscillatory force to vibrate tissue at low kilohertz frequencies at the focal point of the US beam [36, 37]. The resulting mechanical vibrations produce an acoustic field emanating from the structure that is detected at a surrounding accessible point by a sensitive microphone (or hydrophone). Changes in tissue properties normally produce significant variations in the acoustic field. Thus, this method can provide detailed information on tissue mechanics at high resolution that is not available from conventional methods.

Brigham *et al.* [18] and Rosario *et al.* [102] show that vibroacoustic based techniques can be used to characterize the elastic and viscoelastic properties of solids. However, it was assumed that the geometry and location of the different material regions were known a priori. The present work extends the work done in [18] and [102] by using the radiation force of ultrasound to characterized spatially-varying elastic and viscoelastic properties of solids, without a priori knowledge of the different material boundaries.

Overview

In Chapter 2 the problem of estimating the spatial distribution of elastic modu-

lus using the steady-state dynamic response of solids immersed in fluids is presented. Gaussian radial basis functions (GRBF) are used to represent the spatial variation of the elastic modulus. GRBF are shown to possess the advantage of representing smooth functions with quasi-compact support and can efficiently represent elastic modulus distributions such as those that occur in soft biological tissue in the presence of unhealthy tissue. The inverse problem is cast as an optimization problem and nongradient-based optimization algorithms are used to solve the resulting optimization problem. A disadvantage of this technique is that depending on the basis that is selected, a large number of parameters may be needed, increasing the computational cost associated with the inverse problem. This led to the exploration of other inverse approaches based on the adjoint method and the concept of error in constitutive equation (ECE) for the identification of spatially-varying constitutive parameters.

In Chapter 3 the problem of reconstructing the spatially-varying complex tensor from the steady-state system response is presented. The inverse problem is cast as an optimization problem and a gradient-based optimization algorithm is used to solve the problem. The gradient with respect to the design variables is efficiently calculated by solving the resulting adjoint system of equations, minimizing the computational expense associated with the inverse problem. A disadvantage of this methodology is that the least-square error functional is nonconvex, which makes the inverse solution sensitive to parameter initialization. An alternative is to define an error functional based on the concept of ECE.

In Chapter 4 and Chapter 5 the concept of ECE is presented. Contrary to least-square error functionals, the ECE functionals have been shown to be convex for elliptic boundary value problems, see [50, 51, 52]. In Chapter 4 an in-

verse approach for the identification of spatially-varying complex tensor from the steady-state system response using the concept of ECE is presented. The inverse problem was cast as an optimization problem in which an ECE functional is minimized using gradient-based optimization. The gradient is easily calculated by taking direct derivatives of the ECE functional with respect to the design variables. Similar to the inverse approach using the adjoint method, two finite element problems are solved in each of the iteration of the minimization process. In Chapter 5, the feasibility of the ECE inverse approach for in-vivo characterization of material properties is tested. Finally, concluding remarks and areas of future research are discussed at the end.

CHAPTER 2

AN INVERSE PROBLEM APPROACH FOR ELASTICITY IMAGING THROUGH VIBROACOUSTICS

2.1 Introduction

In this chapter an inverse approach for estimating the spatial distribution of elastic modulus of solids immersed in fluids using the steady-state dynamic response and vibroacoustics based techniques is considered. Brigham et al. [18] showed that the radiation force of ultrasound and the ensuing acoustic emissions can be used for the characterization of viscoelastic parameters of solids. However, in [18], it was assumed that the boundaries of different material regions were known a priori. The present work extends the work in [18] by applying the vibroacoustic testing method to estimate spatially-varying elastic properties.

The inverse estimation of spatially-varying mechanical properties is cast as an optimization problem in which a least-square error functional that measures the misfit between experimental and approximate responses is minimized by searching over a space of admissible functions that describe the distribution of elastic modulus. Multiple techniques have been proposed in the literature for solving inverse problems in which the unknown is a function. For instance, the adjoint method was used by Oberai et al. [92] for solving elasticity imaging problems. This method has the advantage that only two evaluations of the forward problem are required in each of the iteration of the minimization process. The disadvantage of the adjoint method is that it is a gradient based method, and only local minima are guaranteed to be found. An alternate ap-

proach is to approximate the unknown function using a finite dimensional basis and search for the unknown coefficients using non-gradient-based optimization methods [18, 96]. The advantage of this approach is that global minima can then be found irrespective of initial guesses, but with the disadvantage that, depending on the basis that is selected, a large number of parameters may be needed, increasing the computational cost significantly. Despite this, non-gradient based optimization methods are favored in this work for their robustness and lack of sensitivity to initial guesses.

Since a finite dimensional representation will be used to approximate spatially varying elastic modulus and the computation expense of the inverse problem increases with the dimension of the basis, it is very important that an adequate basis be selected. The quality of a basis for the problem at hand can be judged based on the dimensionality of the subspace needed to satisfactorily approximate the desired distribution of elastic modulus. Intuitively speaking, a basis should intrinsically capture the nature of the possible solutions. One application of the present work is the detection and characterization of tumors in breast tissue. Tumors are expected to be localized regions with differing properties with respect to the surrounding material. This work proposes the use of Gaussian radial basis functions (GRBF) to represent this property distribution in a region of interest. It is important to point out that the notion of representing tissue stiffness distribution by using quasi-compactly supported functions has also been suggested by Skovoroda et al. [110]. However, in their work GRBF were not used as a finite-dimensional basis for inverse elasticity imaging as proposed herein.

The inverse approach presented in this chapter employs vibroacoustic based

techniques in combination with GRBF and non-gradient based optimization algorithms to inversely characterize the elastic modulus field of solids immersed in fluids. In Section II, the finite element formulation for the coupled fluid-structure problem is presented. In Section III, the inverse problem formulation is described, as well as the optimization solution strategy. In Section IV, the results obtained for the series of simulations and an experiment are shown. Conclusions and future directions are given at the end.

2.2 Formulation

The vibroacoustic system considered here can be described by a coupled system of partial differential equations (PDEs) derived from the conservation of linear momentum. The surrounding fluid was taken to be a semi-infinite medium, and the only excitation in the fluid was assumed to be due to the motion of the solid. The equations describing the boundary value problems used in this work are well known. The reader can consult [18] for further details. Each dot on top of a variable denotes a time derivative, vector valued functions will be represented with bold letters or within curly brackets, second order tensors will be represented with lowercase bold greek letters, and matrices will be enclosed within square brackets.

2.2.1 Forward Problem

Boundary Value Problem

The boundary value problem for the solid domain is defined as

$$\nabla \cdot \boldsymbol{\sigma}(\vec{x}, t) + \boldsymbol{b}(\boldsymbol{x}, t) = \rho_s \ddot{\boldsymbol{u}}(\boldsymbol{x}, t) + \alpha \rho_s \dot{\boldsymbol{u}}(\boldsymbol{x}, t) \text{ in } \Omega \subset \mathbb{R}^n \tag{2.1}$$

$$\boldsymbol{u}(\boldsymbol{x}, 0) = \boldsymbol{u}_o(\boldsymbol{x}, t) \text{ on } \Gamma_u \tag{2.2}$$

$$\boldsymbol{\sigma}(\boldsymbol{x}, t)\, \boldsymbol{n}_s(\boldsymbol{x}) = -p(\boldsymbol{x}, t)\, \boldsymbol{n}_s(\boldsymbol{x}) \text{ on } \Gamma_{fs} \setminus \Gamma_u. \tag{2.3}$$

The stress-strain relationship is defined as

$$\boldsymbol{\sigma}(\boldsymbol{x}, t) = \mathbb{C}(\boldsymbol{x})\, \boldsymbol{\epsilon}(\boldsymbol{x}, t) + \mu \mathbb{C}(\boldsymbol{x})\, \dot{\boldsymbol{\epsilon}}(\boldsymbol{x}, t) \tag{2.4}$$

where

$$\boldsymbol{\epsilon}(\boldsymbol{x}, t) = \frac{1}{2} \left(\nabla \boldsymbol{u}(\boldsymbol{x}, t) + \nabla \boldsymbol{u}(\boldsymbol{x}, t)^{\mathrm{T}} \right). \tag{2.5}$$

Here t denotes time, $\boldsymbol{x}$ is the position vector, ρ_s is the solid mass density (assumed constant in this work), μ and α are Rayleigh damping factors, $\mathbb{C}(\boldsymbol{x})$ is the fourth order elasticity tensor, $\boldsymbol{\sigma}(\boldsymbol{x}, t)$ is the stress tensor, $\boldsymbol{b}(\boldsymbol{x}, t)$ is a body force vector, $\boldsymbol{\epsilon}(\boldsymbol{x}, t)$ is the Cauchy infinitesimal strain tensor, $\boldsymbol{u}(\boldsymbol{x}, t)$ is the displacement vector, $\ddot{\boldsymbol{u}}(\boldsymbol{x}, t)$ is the acceleration vector, $\boldsymbol{n}_s(\boldsymbol{x})$ is the unit outward normal vector to the solid surface, Ω is the solid domain, Γ_u is the part of the boundary surface where the displacements are specified (i.e., Dirichlet boundary conditions), and Γ_{fs} is the fluid-structure interface.

The boundary value problem for the fluid domain is defined as

$$\nabla p(\boldsymbol{x},t) = \rho_f \ddot{\boldsymbol{u}}(\boldsymbol{x},t) \text{ in } \Phi \subset \mathbb{R}^n \tag{2.6}$$

$$p(\boldsymbol{x},t) = -B_f \nabla \cdot \boldsymbol{u}(\boldsymbol{x},t) \text{ in } \Phi \tag{2.7}$$

$$\nabla p(\boldsymbol{x},t) \cdot \boldsymbol{n}_f(\boldsymbol{x}) = -\rho_f \ddot{\boldsymbol{u}}_n(\boldsymbol{x},t) \text{ on } \Gamma_{fs} \tag{2.8}$$

and

$$\nabla p(\boldsymbol{x},t) \cdot \boldsymbol{n}_f(\boldsymbol{x}) = -f\left(\sqrt{\frac{\rho_f}{B_f}}\dot{p}(\boldsymbol{x},t) + \beta p(\boldsymbol{x},t)\right) \text{ on } \Psi_R \tag{2.9}$$

$$\boldsymbol{u}_n^s(\boldsymbol{x}) = \boldsymbol{u}_n^f(\boldsymbol{x}) \text{ on } \Gamma_{fs} \tag{2.10}$$

For the acoustic fluid formulation, ρ_f is the fluid mass density, B_f is the bulk modulus of the fluid, f and β are geometry -specific parameters for improved non-reflecting radiation condition, $p(\boldsymbol{x},t)$ is the scalar acoustic fluid pressure in excess of hydrostatic pressure, $\boldsymbol{u}^f(\boldsymbol{x},t)$ is the fluid particle displacement vector, $\boldsymbol{u}_n^f(\boldsymbol{x},t)$ is the displacement of the fluid boundary in the direction of the normal, $\boldsymbol{u}_n^s(\boldsymbol{x},t)$ is the displacement of the solid boundary in the direction of the normal, $\boldsymbol{n}_f(\boldsymbol{x})$ is the unit normal vector to the fluid surface, Φ is the fluid domain, $\mathbb{R}^n$ is the n-dimension real Euclidean space, and Ψ_R is the portion of the boundary where the radiation condition is specified.

Finite Element Formulation

The variational statements for the solid and fluids problems are defined as

$$\int_{\Omega} (\nabla \boldsymbol{v} : \boldsymbol{\sigma} + \boldsymbol{v} \cdot (\alpha \rho_s \ddot{\boldsymbol{u}})) \, d\Omega + \int_{\Gamma_{fs} \setminus \Gamma_u} \boldsymbol{v} \cdot (p \boldsymbol{n}_s) \, dS = \int_{\Omega} \boldsymbol{v} \cdot \boldsymbol{b} \, d\Omega \tag{2.11}$$

and

$$\begin{aligned} &\int_{\Phi} w \frac{\rho_f}{B_f} \ddot{p} \, d\Phi + \int_{\Phi} \nabla w \cdot \nabla p \, d\Phi + \int_{\Gamma_{fs}} w \rho_f \ddot{\boldsymbol{u}}_n^f \, d\Gamma_{fs} \\ &\quad + \int_{\Psi_R} w f \sqrt{\frac{\rho_f}{B_f}} \dot{p} \, d\Psi_R + \int_{\Psi_R} w f \beta p \, d\Psi_R = 0 \end{aligned} \tag{2.12}$$

respectively, where $v, w \in H_0^1$. H_0^1 is the Sobolev space of functions that are square integrable up to first derivatives and that satisfy homogeneous essential boundary conditions where Dirichlet conditions are specified for the fields and $\boldsymbol{u}$ and p.

The Galerkin weak-form finite element method (FEM) was applied to solve the coupled system of PDEs. The structural displacements, fluid pressure, and external forces are assumed to vary harmonically; therefore, the resulting coupled system of equations in the frequency domain is defined as

$$\begin{bmatrix} [A] & -\omega [C_s] & [S]^T & 0 \\ \omega [C_s] & [A] & 0 & [S]^T \\ [L] & 0 & [G] & -\omega \left[C_f\right]^T \\ 0 & [L] & \omega \left[C_f\right]^T & [G] \end{bmatrix} \times \begin{Bmatrix} \Re \left(\{\bar{u}(\omega)\}\right) \\ \Im \left(\{\bar{u}(\omega)\}\right) \\ \Re \left(\{\bar{p}(\omega)\}\right) \\ \Im \left(\{\bar{u}(\omega)\}\right) \end{Bmatrix} = \begin{Bmatrix} \Re \left(\{\bar{R}_s^{ext}\}\right) \\ \Im \left(\{\bar{R}_s^{ext}\}\right) \\ \vec{0} \\ \vec{0} \end{Bmatrix} \tag{2.13}$$

where

$$[A] = [K_s] - \omega^2 [M_s] \tag{2.14}$$

$$[G] = \left[K_f\right] - \omega^2 \left[M_f\right] \tag{2.15}$$

$$[L] = -\omega^2 \rho_f [S] \tag{2.16}$$

$$[C_s] = \alpha [M_s] + \mu [K_s] \tag{2.17}$$

$$[M_s] = \sum_{solid\ elements} \int_{\Omega^e} \rho_s [N]^T [N] \, d\Omega^e \tag{2.18}$$

$$[K_s] = \sum_{solid\ elements} \int_{\Omega^e} [B]^T [D] [B] \, d\Omega^e \tag{2.19}$$

$$\{R_s^{ext}\} = \sum_{solid\ elements} \int_{\Omega^e} \rho_s [N]^T \{b\} d\Omega^e \tag{2.20}$$

$$\left[M_f\right] = \frac{\rho_f}{B_f} \sum_{fluid\ elements} \int_{\Phi^e} \rho_s [H]^T [H] d\Phi^e \tag{2.21}$$

$$\left[K_f\right] = \sum_{fluid\ elements} \left(\int_{\Phi^e} \rho_s [F]^T [F] \, d\Phi^e + \int_{\Psi_R^e} f\beta [H]^T [H] \, d\Psi_R^e \right) \tag{2.22}$$

$$\left[C_f\right] = f \sqrt{\frac{\rho_f}{B_f}} \sum_{fluid\ elements} \int_{\Psi_R^e} [H]^T [H] \, d\Psi_R^e \tag{2.23}$$

$$[S] = \sum_{elements} \int_{\Gamma_{fs} \backslash \Gamma_u} [N]^T \vec{n}_s [H] \, dS \tag{2.24}$$

In the preceding formulation $[M_s]$ is the solid mass matrix, $[K_s]$ is the solid stiffness matrix, $\{R_s^{ext}\}$ is the solid external force vector, $[C_s]$ is the solid damping matrix, $[D]$ is the stiffness matrix representation of the elasticity tensor, $\left[M_f\right]$ is the fluid mass matrix, $\left[K_f\right]$ is the fluid stiffness matrix, $\left[C_f\right]$ is the fluid damping matrix, $[S]$ is the interaction matrix, Γ_{fs} is the interaction boundary between the structure and the fluid, is the $[N]$ matrix of interpolation functions for the solid elements, $[H]$ is the matrix of interpolation functions for the acoustic elements, $[B]$ is the matrix of spatial derivatives of the solid interpolation functions, $[F]$ and is the matrix of derivatives of the interpolation functions, ω represents angular frequency, $\Re$ denotes real components, $\Im$ and denotes imaginary component. For more details on the derivations of (2.13) the reader is referred to [18]

2.3 Inverse Problem

2.3.1 Elasticity Representation

Tumors are presumed to be localized regions of abnormal cells with differing properties to the surrounding healthy tissue [83]. Therefore, the presence of tumors will cause localized changes in elastic properties. For this reason, GRBF were used in this work since they can represent gradual or sharp changes in localized regions [20]

The spatial distribution of elastic modulus is represented as an expansion of n-radially symmetric basis functions augmented by a constant term as

$$E(\boldsymbol{x}) = E_o + \sum_{i=1}^{n} \lambda_i \phi\left(\|\boldsymbol{x} - \boldsymbol{\xi}_i\|_2\right) \tag{2.25}$$

where E_o is theYoung's modulus of the background material, λ_i are real-valued coefficients, $\boldsymbol{\xi}_i$ are the coordinates of the GRBF centers, and ϕ is the GRBF, which is defined herein as

$$\phi\left(\|\boldsymbol{x} - \boldsymbol{\xi}_i\|_2\right) = \exp\left(-\frac{(\|\boldsymbol{x} - \boldsymbol{\xi}_i\|_2)}{c_i^2}\right). \tag{2.26}$$

In the above formulation $\|\cdot\|$ is the $\ell^2 - norm$ and c_i are the locality parameters that control the size of the GRBF region of influence.

To compute the λ_i parameters, the interpolation scheme shown in [21] and [43] was used. The values of the Young's modulus at the centers of the GRBF are denoted as $\hat{E}(\boldsymbol{\xi}_i)$. These values were taken as the main unknown

variables in the inverse problem and were computed using the parameters by requiring that the following interpolation condition was satisfied

$$E\left(\boldsymbol{\xi}_i\right) = \hat{E}\left(\boldsymbol{\xi}_i\right). \tag{2.27}$$

This approach attaches a physical meaning to the solution of the inverse problem as opposed to the nonphysical parameters λ_i. In addition, setting constraints on $\hat{E}\left(\boldsymbol{\xi}_i\right)$ (e.g., strictly positive) is easier than setting constraints on λ_i (e.g., could be negative or positive).

2.3.2 Inverse Problem Formulation

An optimization approach was used to inversely characterize the spatial distribution of elastic modulus through the acoustic emissions induced by the radiation force of ultrasound. First, an error functional was defined to measure the misfit between the experimental and approximate responses and it is given by

$$J\left(E\left(\boldsymbol{x}\right)\right) = \int_{\Omega}\int_{\omega_1}^{\omega_2} \left|r^{Exp}\left(\boldsymbol{x},\omega\right) - r^{FEA}\left(\boldsymbol{x},\omega,E\left(\boldsymbol{x}\right)\right)\right|^2 d\omega\, d\Omega. \tag{2.28}$$

The quantities $r^{Exp}\left(\boldsymbol{x},\omega\right)$ and $r^{FEA}\left(\boldsymbol{x},\omega,E\left(\boldsymbol{x}\right)\right)$ represent the experimental and approximate responses, respectively. After parameterization of (2.28), the error functional can be expressed as

$$J\left(\{c\},\{\hat{E}\},\{\zeta\},E_o\right) = \sqrt{\sum_{j=1}^{t}\sum_{k=1}^{m}\left(r_{jk}^{Exp}\left(\boldsymbol{x}_j,\omega_k\right) - r_{jk}^{FEA}\left(\boldsymbol{x}_j,\omega_k,\{c\},\{\hat{E}\},\{\zeta\},E_o\right)\right)^2} \tag{2.29}$$

where $\{\zeta\} = \{\zeta_1,\cdots,\zeta_n\}$ is the set of coordinates of the GRBF centers, $\{\hat{E}\} = \{\hat{E}_1,\cdots,\hat{E}_n\}$ is the set of Young's modulus at the center of the GRBF, and $\{c\} = \{c_1,\cdots,c_n\}$ is the set of locality parameters.

The inverse problem is then cast as an optimization problem in which the error functional defined in (2.29) is minimized by searching over a space of admissible vectors that describe the spatial distribution of elastic modulus. Therefore, the minimization problem is described as

$$\underset{\substack{\{\hat{E}\},\{c\}\in\mathbb{R}^n\\ \{\zeta\}\in\mathbb{R}^{d\cdot n}\\ E_o\in\mathbb{R}^+}}{\arg\ \min}\ J\left(\{c\},\{\hat{E}\},\{\zeta\},E_o\right) \tag{2.30}$$

2.3.3 Optimization Algorithm

It is well known that gradient based algorithms guarantee convergence only to local minima in non-convex problems. For problems where data sparsity is significant, non-gradient based methods are preferred over gradient based methods since data sparsity can create non-convex error surfaces. Through simulations it was determined that the error surfaces encountered in the problems addressed herein are non-convex. Therefore, global optimization methods were used for the inverse problems presented in this chapter. Since the main focus

of the work is not on optimization, the global search algorithms used herein are briefly described below.

Two global optimization methods were employed to solve the inverse problem studied in this work: a real value genetic algorithm (GA) [85, 53] and the Surrogate-Model Accelerated Random Search (SMARS) algorithm proposed in [17] The GA was used for the less computationally demanding simulations, while SMARS was used for the more computationally demanding experiment. Three common operators were used for the GA: stochastic uniform sampling as the selection operator, single point crossover as the reproduction operator, and a uniform distribution for mutation.

The SMARS algorithm is a combination between a random search algorithm [19] and a surrogate-model optimization approach [100]. The random search part of SMARS is used to efficiently search vast and complex error surfaces. It has been shown that the random search algorithm is guaranteed to converge to a global solution in a probabilistic sense [82]. However, the number of iterations needed for finding a global solution is high. Therefore, SMARS uses a surrogate-model approach where an artificial neural network is used to map local regions of the search space, producing a computationally inexpensive estimate of the solution. By using the surrogate-model, SMARS reduces the number of objective function evaluations needed to find an optimal solution.

2.4 Results and Discussion

Two simulated experiments were performed to test the potential of the proposed technique to inversely characterize the spatial distribution of elastic mod-

ulus in general solid domains. To validate the methodology in a realistic setting, a physical experiment was performed. For the simulations, the solid body was excited at multiple locations and the acoustic pressure and surface velocity responses were measured at several points. For the experiment, the solid body was excited at one location and the acoustic surface velocity response was measured at several points. These measured responses were used to inversely reconstruct the spatial variation of Young's modulus in the solid. All calculations are performed on a Linux workstation with a $1.86 - GHz$ Intel processor and 16 GB of RAM.

2.4.1 Simulations

The forward problem was modeled using the commercial finite element package ABAQUS/Standard [1] with fully integrated eight-node biquadratic plane strain quadrilateral linear pressure hybrid finite elements. A plane strain condition was used for the simulations in order to reduce computational demand. Figure 2.1 shows a schematic for the simulations. The solid domain had dimensions of $14\ mm \times 14\ mm$. Displacements in the vertical direction were constrained at the bottom edge of the solid and the displacements at the lower left corner were fixed. The density and the Poisson's ratio of the solid were assumed to be 1050 kg/m^3 and 0.49, respectively. The solid was immersed in a circular fluid domain with radius, r_f, of 30 mm. To avoid reflection effects, the Sommerfeld radiation boundary condition was specified in the outer fluid boundary. The Sommerfeld radiation boundary condition parameters f and β were set to 1 and $1/2r_f$, respectively. The properties of the fluid were assumed to be known for the inverse problem, with density of 1000 kg/m^3 and bulk modulus of 2.2 GPa.

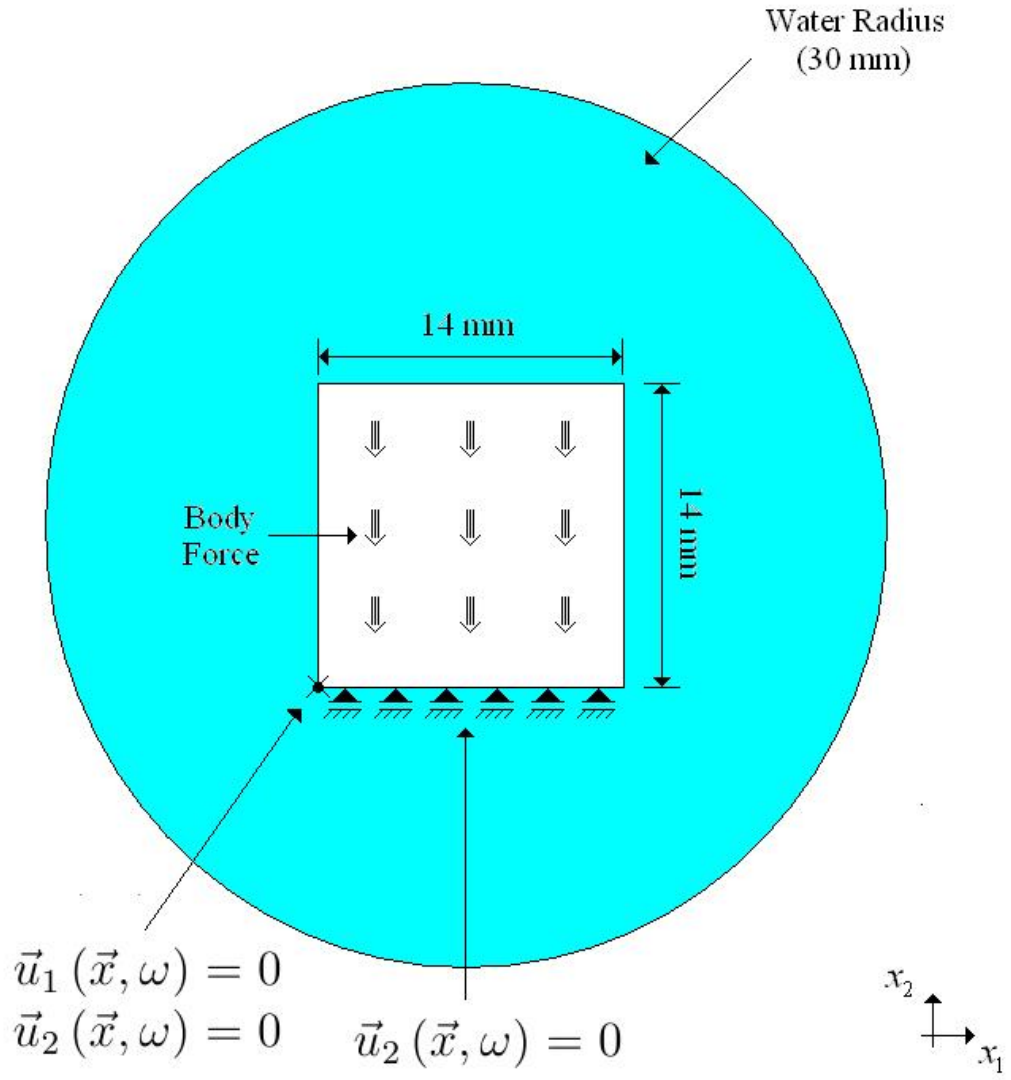

Figure 2.1: Schematic of the finite element model used for the simulations.

The mass proportional damping parameter, α, was set to 5000 and the stiffness proportional damping parameter, μ, was set to 0. These parameters were determined through simulation studies. For more details on the appropriate method and criteria to select these parameters, the reader is referred to [83].

The first simulation consisted of a single stiff inclusion embedded in a soft matrix. The inclusion was represented with a combination of five GRBFs. The

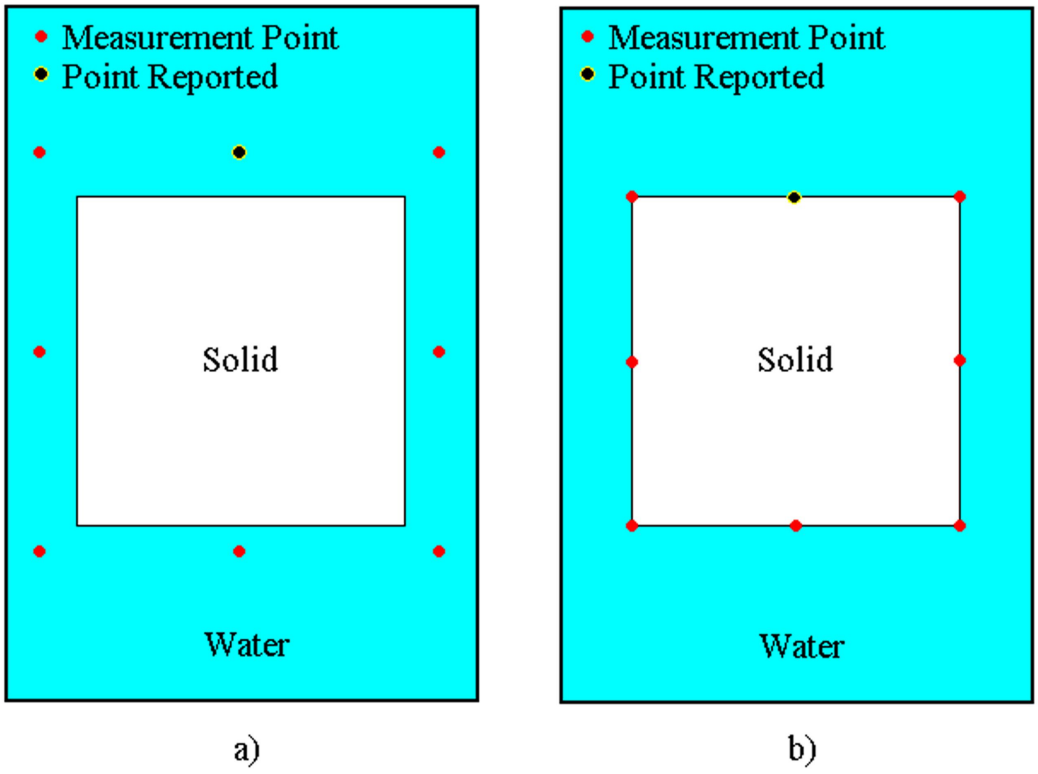

Figure 2.2: Measurement points selected to solve the inverse problem for (a) the acoustic pressure response and (b) the surface velocity response.

Young's modulus at each GRBF center was 4 *GPa*. The second simulation consisted of two inclusions embedded in a soft matrix. Each inclusion was represented with a combination of five GRBFs. The Young's modulus at the GRBF centers for the two inclusions was 4 *GPa* and 2 *GPa*. The matrix Young's modulus was taken as 1 *GPa* for both simulations. The values of the Young's modulus, although unrealistic for soft tissue, were selected so that the wave number in the governing equations remained low and, therefore,the computational cost for performing one finite element analysis was reduced.

The range of frequencies considered for the simulations was $40 - 50$ *kHz*, which resembles frequencies used in VA [37]. Nine body forces were applied

Table 2.1: Simulations Search Range for the Optimization Parameters

Optimization Parameter	Optimization Minimum	Optimization Maximum
E_o	0.8 GPa	20 GPa
E_{inc}	0.5 GPa	5 GPa
c	1.0 mm	3.0 mm
x	-7.0 mm	7.0 mm
y	-7.0 mm	7.0 mm

simultaneously in the x_2-direction at equally spaced points as shown in Figure 2.1. Two response quantities (i.e., acoustic pressure and surface velocity), measured at eight different points, were used separately to solve the inverse problem. As in [17], only the frequencies where extrema and inflection points occurred were used. By reducing the number of frequencies, the computational cost of one forward run was also reduced. For the acoustic pressure response eight frequencies were selected, and for the surface velocity response fourteen frequencies were selected. Figure 2.2 gives a pictorial description of the measurement points and the point used to report its corresponding response.

For simplification, the number of radial basis functions (i.e., terms) used to approximate the spatial distribution of elastic modulus was fixed a priori instead of considering it as an optimization parameter. In all simulations, four radial basis functions were used for the estimation. Therefore, the parameters to be identified were four pairs of coordinates for the GRBF centers, the matrix elastic modulus, four locality parameters, and the four values of the Young's modulus at the centers of the GRBFs for a total of 17 unknowns for the inverse problem. Table 2.1 shows the minimum and maximum parameter values (i.e.,

search range) considered.

Random Gaussian noise was added to both responses to explore the tolerance of the proposed methodology to imperfect data. Random Gaussian noise was added as

$$r_i^n = r_i^o \left(1 + 0.1\eta\right) \tag{2.31}$$

where r_i^n is the response (i.e., velocity or pressure) at the $i - th$ point with noise, r_i^o is the corresponding quantity without noise, and η is a normally distributed variable with zero mean and unit variance.

Due to the stochastic nature of the algorithms used in this work, five optimization runs were performed for each example, while keeping the algorithm parameters constant. The error in the solution of the inverse problem was defined as

$$e = \frac{\|E^{Exp}\left(\boldsymbol{x}\right) - E^{FEA}\left(\boldsymbol{x}\right)\|_2}{\|E^{Exp}\left(\boldsymbol{x}\right)\|_2} \tag{2.32}$$

where $\|u\|_2 = \int_\Omega |u|^2 d\boldsymbol{x}$, E^{Exp} is the target Young's modulus, and E^{FEA} is the solution to the inverse problem using (2.25).

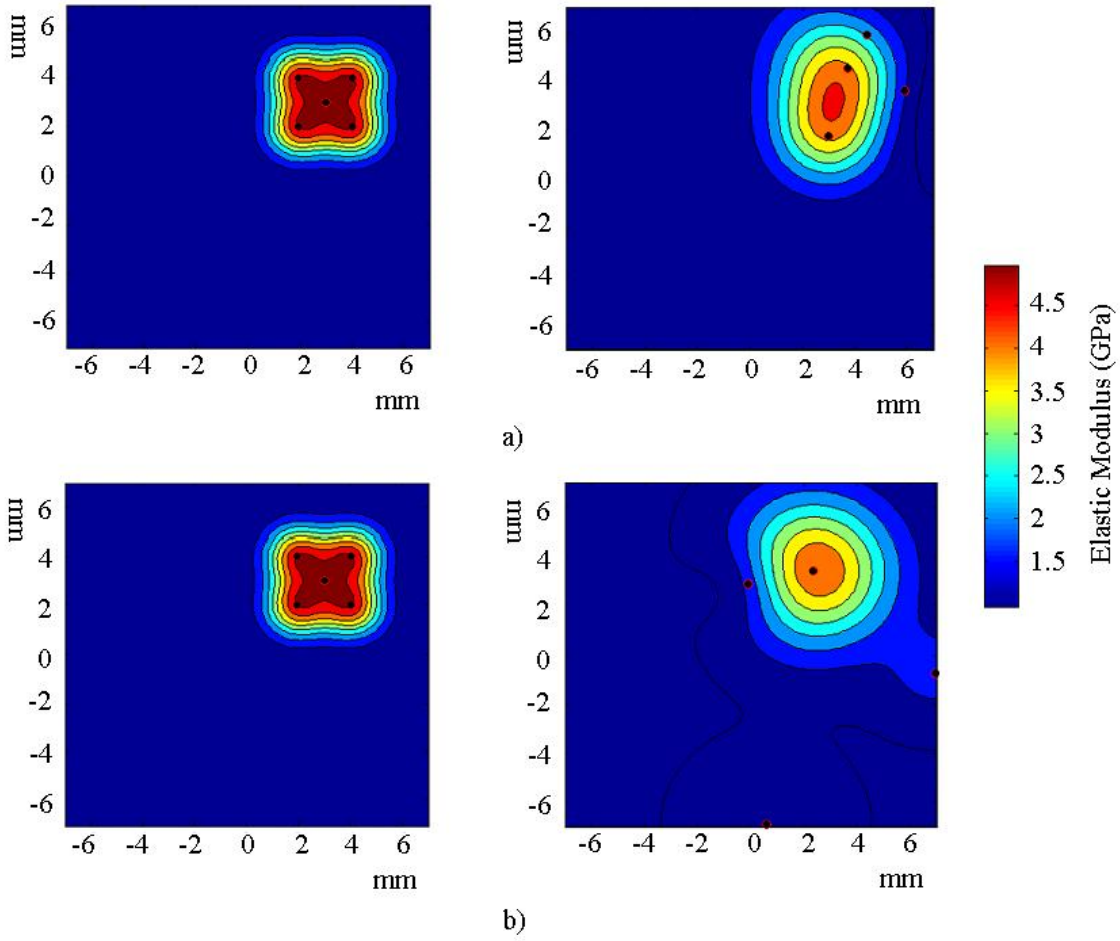

Figure 2.3: Spatial distribution of elastic modulus for the simulation with one inclusion found as solution to the inverse problem using (a) the acoustic pressure response and (b) the surface velocity response.

2.4.2 Simulation with One Inclusion

Results for the Acoustic Pressure Response

In the simulation where the acoustic pressure response was used for identification, the stiff regions and the background material were identified correctly in all optimization runs. Figure 2.3.a shows the spatial distribution of elastic mod-

ulus found for one of the inverse problem runs. The mean and standard deviation of the error in the approximation are shown in Table 2.2. It is important to point out that these values are reported for the sole purpose of contrasting the effectiveness of using acoustic pressure against using surface velocity in the inverse problem. The interpretation of the magnitude of the error is not trivial and may be deceiving. Notice that the quality of the inverse solution may be judged based on two main factors: accuracy in identification of the relative distribution of the elastic modulus (e.g., identification of stiff and soft regions) and the accuracy of the magnitude of the modulus. These criteria cannot be clearly discerned when an L_2-error norm is used. Hence, the quality of the reconstruction is best appreciated from the plots of the solution.

Forward finite element runs were performed using each parameter set found as solution to the inverse problem. The resulting frequency spectra of the acoustic pressure were compared to the target response from the simulated experiment. Figure 2.4.a shows the mean and standard deviation of the acoustic pressure response obtained in the simulation at a selected point. Figure 2.4.a shows that the resulting frequency spectra were estimated with accuracy and low scatter with respect to the target response.

Results for the Surface Velocity Response

In the simulation where the surface velocity response was used for identification, the spatial distribution of elastic modulus was successfully estimated in all runs. Figure 2.3.b shows the distribution found as solutions to the inverse problem for one of these runs. The mean and standard deviation of the error in the approximation are tabulated in Table 2.2. It can be observed that a lower

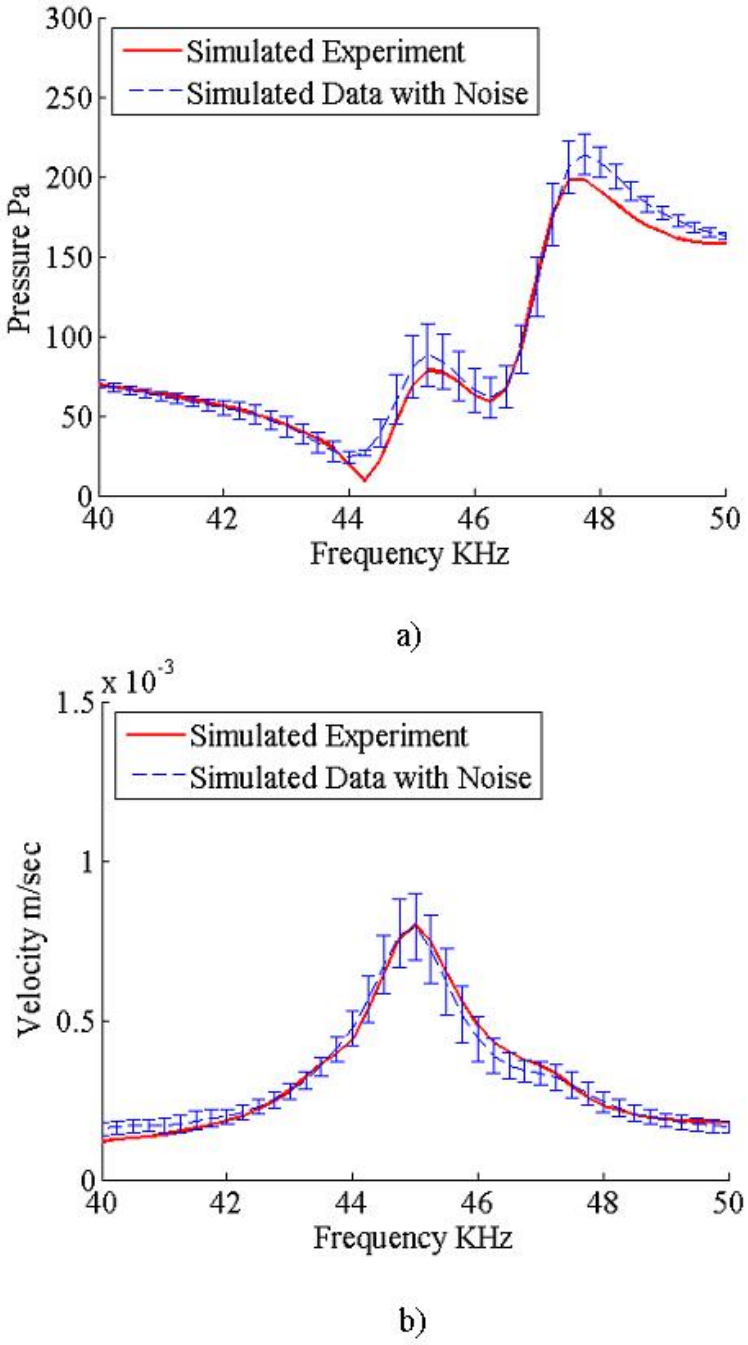

Figure 2.4: Mean and standard deviation obtained from five optimization trials for the simulation with one inclusion using (a) the acoustic pressure response and (b) the surface velocity response.

Table 2.2: Mean and Standard Deviation of e for the Simulation With One Inclusion

Measurements	Mean e	std
Pressure	0.2044	0.036
Surface Velocity	0.1651	0.011

error (on average) in the inverse solution was obtained when surface velocity was used.

Figure 2.4.b shows the velocity frequency spectra corresponding to the point reported. These results show that the surface velocity response was estimated with accuracy and low scatter with respect to the target response.

2.4.3 Simulation with Two Inclusions

Results for the Acoustic Pressure Response

When the acoustic pressure was used as the measured response, the spatial distribution of elastic modulus was identified in four of the five optimization runs performed. In the unsuccessful optimization run, the stiffer region was identified, but the softer region was not identified. A possible explanation for this behavior may be that a higher value of the error functional was attained in this case as compared to the other four cases. Therefore, the algorithm may have been delayed in convergence because of a local minimum in this case. Figure 2.5.a shows the spatial distribution of the elastic modulus found as solution to the inverse problem for one of the four successful optimization runs. The

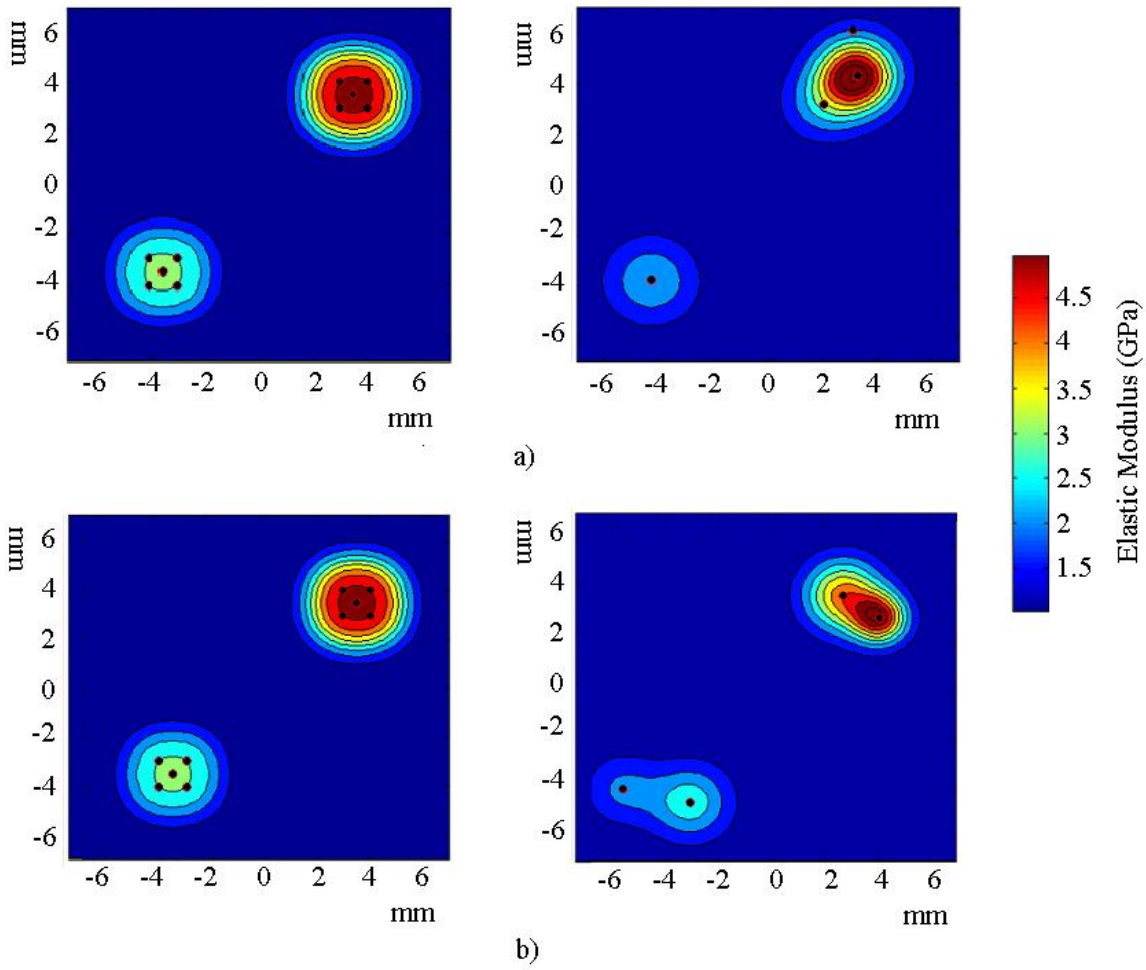

Figure 2.5: Spatial distribution of elastic modulus for the simulation with two inclusions found as solution to the inverse problem using (a) the acoustic pressure response and (b) the surface velocity response.

mean and standard deviation of the error in the approximation of the material properties are shown in Table 2.3. Notice that the mean error is higher for the case of two inclusions as compared to the case for one inclusion. This may be attributed to the fact that the same number of radial basis functions was used in both examples, while the example with two inclusions would require a larger number of basis functions for the representation of its modulus distribution.

Table 2.3: Mean and Standard Deviation of e for the Simulation With Two Inclusions

Measurements	Mean e	std
Pressure	0.2318	0.0254
Surface Velocity	0.1839	0.0565

Similar to the simulation with one inclusion, forward finite element analyses were performed using the solution of each successful optimization run. Figure 2.6.a shows the mean and standard deviation of the acoustic pressure response corresponding to the point reported in the fluid. Again, the results show good accuracy in the mean and low scatter from the target response

Results for the Surface Velocity Response

The elastic modulus distribution was successfully estimated in all the optimization runs in contrast to the case when acoustic pressure was used. This fact reinforces our previous finding that velocity response produced more accurate results than the pressure response. Figure 2.5.b shows the distribution of the elastic modulus found as solution to the inverse problem for one of the five successful optimization runs. The mean and standard deviation of the error in the approximation are tabulated in Table 2.3. It can be observed that, as for the example problems with one inclusion, the average error for the velocity response was lower than that of the pressure response.

Forward finite element analyses were performed using the parameter set found as solution to each optimization run. Figure 2.6.b shows the mean and standard deviation of the surface velocity corresponding to the point chosen on

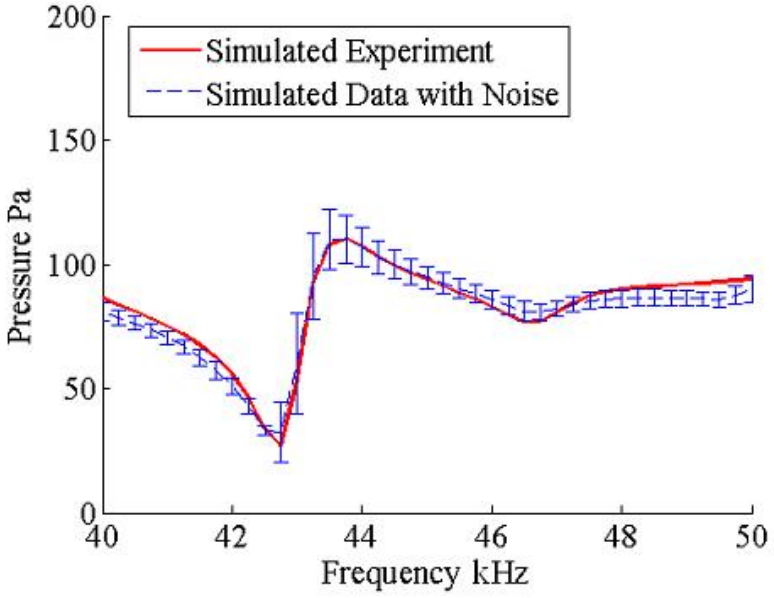

a)

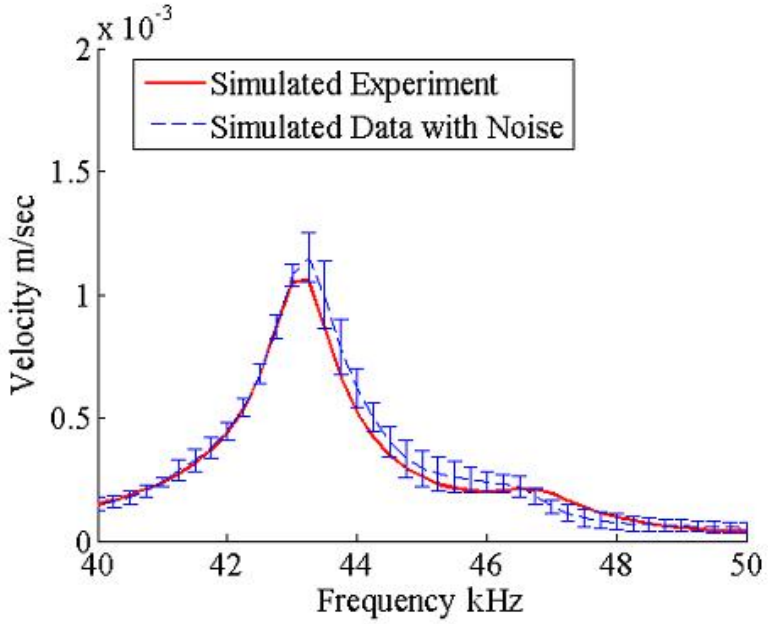

b)

Figure 2.6: Mean and standard deviation obtained from five optimization trials for the simulation with one inclusion using (a) the acoustic pressure response and (b) the surface velocity response.

the solid surface. The resulting frequency spectra show accuracy and low scatter with respect to the target response.

Remarks on Simulations

Results suggest that better estimation of material properties can be obtained when the surface velocity response is used instead of the acoustic pressure response. A possible explanation can be attributed to higher sensitivity of the surface velocity response to changes in material properties for the frequency range considered in the simulations.

It is important to point out that the number of basis functions used to solve the inverse problem in all cases was different from the number of basis functions used to construct the target spatial distribution of elastic modulus. The use of different number of basis functions (i.e., different dimensions of the solution space) for the target and inverse problem solution avoids, at least partially, what is called an inverse crime. Furthermore, it can be noticed that no regularization was called for in the description of the inverse problem. The reason for this is that the use of low-dimensional basis is in itself a form of regularization. However, if the number of basis functions were to be increased significantly, then some form of regularization (e.g., Total Variation) has to be used.

A word is in order about advantages and disadvantages of using acoustic pressure versus velocity response for the inverse problem described herein. Acoustic pressure measurements can be obtained with good precision in the laboratory, but higher frequencies are needed for the response to experience sensitivity to changes in material properties and to avoid boundary reflections.

It is well known that computational cost increases with increasing frequency (i.e., a finer mesh is needed in the numerical model). Contrary to acoustic pressure measurements, surface velocity measurements have shown strong sensitivity to changes in material properties at lower frequencies, allowing the use of a coarser mesh in the numerical model. This translates into a reduction of computational cost, but with the disadvantage that surface velocity measurements obtained in the laboratory are less accurate than acoustic pressure measurements.

2.4.4 Experiment

Description

This experiment was designed to measure the vibration of a cylinder with a spherical inclusion in response to a harmonic radiation force applied to the sphere. A cylinder having a diameter of 45 *mm* and 45 *mm* length was created using a 4% concentration agar (Bacto Agar, Becton- Dickinson, Sparks, MD) solution. The cylinder contained a 16 – *mm*– diameter solid neoprene rubber sphere suspended in its center. The test object and the experimental setup are shown in Figure 2.7.

The cylinder rested on a platform in a water tank. To prevent the cylinder from moving due to its almost neutral buoyancy, a thin 1.4 – *cm*–diameter metal disk weighing 16.4 *g* was placed sitting on its top surface. A vertical narrow stripe was painted on one side of the cylinder using a thin layer of white latex paint to provide optimal reflectivity for the motion measurement by a laser vibrometer. The driving force for the sphere was provided by the radiation force

of a $3 - MHz$ ultrasound transducer having a 44 mm diameter and 7 cm focal length. This transducer was focused at a fixed location on the surface, directed towards the center of the sphere.

The excitation that was used to drive the transducer consisted of a suppressed-carrier amplitude modulated (AM) tone burst with the carrier frequency of 3 MHz and the modulation frequency of $f_m/2$. The resulting ultrasound beam generated a harmonic radiation force at frequency f_m on the sphere. The duration of the tone burst was equal to four cycles of the radiation force, i.e., $4/f_m$. The frequency values used were $f_m = 100, 200, 300, 400$, and 500 Hz.

The laser vibrometer (Polytec GmbH,Waldbronn, Germany) used in this experiment is capable of measuring surface velocity. The laser beam was aimed at several points on the painted portion along the length of the cylinder. Vibration of the cylinder surface resulting from the neoprene sphere vibration was detected along the vertical line indicated in Figure 2.7 at 2 mm intervals over a total length of 22.5 mm. The laser vibrometer velocity output was digitized and stored to computer disk for later analysis.

Finite Element Model

A 3-D finite element model was built using the finite element package ABAQUS/Standard [1] with 20−node quadratic brick linear pressure hybrid finite elements to simulate the experiment. Agar gel and rubber are well known to be nearly incompressible; therefore, Poisson's ratio was taken as $\nu = 0.49$. The density of the agar gel and the inclusion were also assumed known and were taken as 1000 kg/m^3 and 1111 kg/m^3 , respectively. To represent the displacement

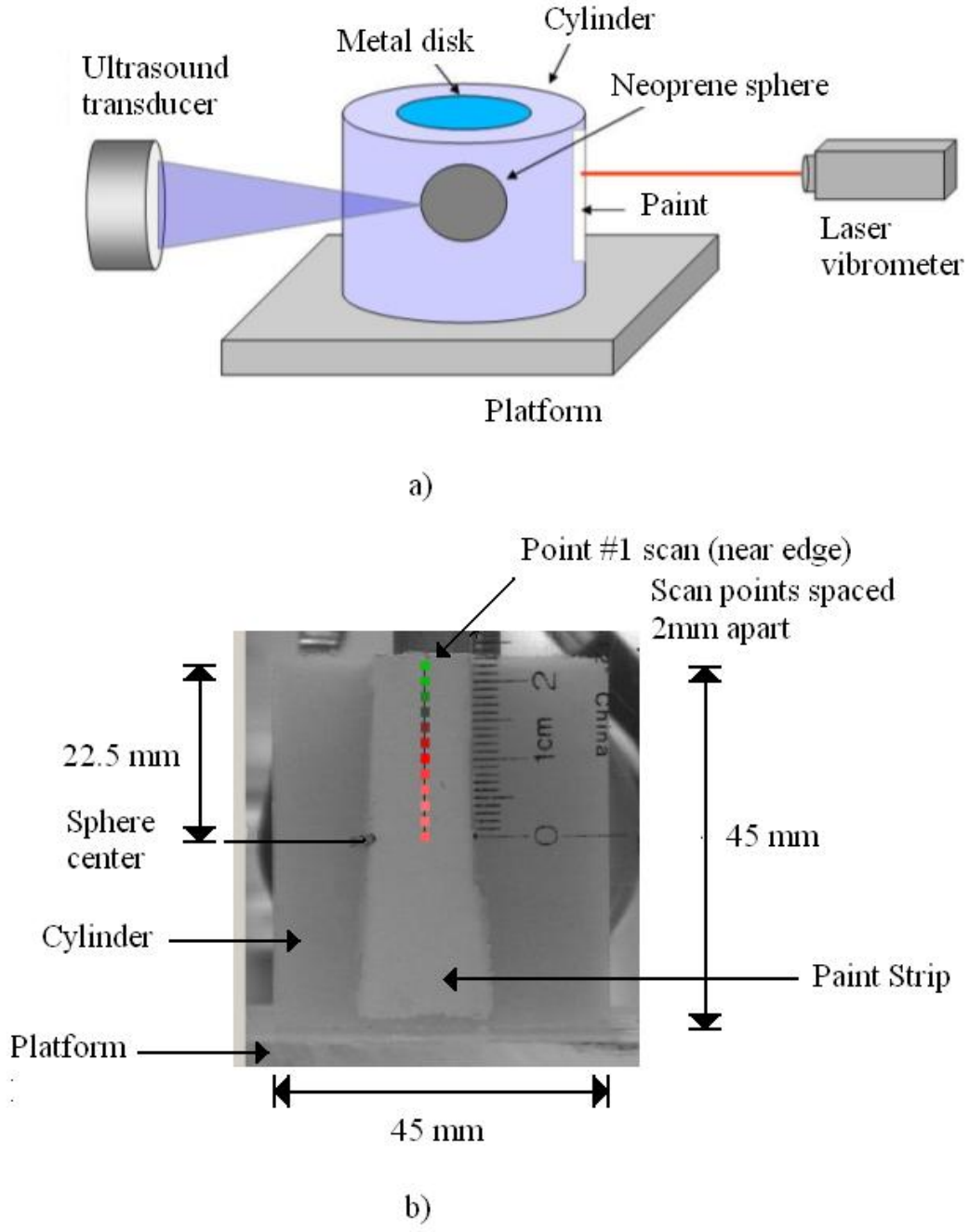

Figure 2.7: (a) Diagram of the experiment. (b) Experimental setup. The photo shows the agar cylinder. The marking on the cylinder are the laser motion measurement points that are 2 *mm* apart. The transducer is behind the cylinder.

Table 2.4: Experiment Search Range for the Optimization Parameters

Optimization Parameter	Optimization Minimum	Optimization Maximum
E_o	10 kPa	50 kPa
E_{inc}	100 kPa	500 kPa
α	5000	15000
c	1.0 mm	3.0 mm
x	0.0 mm	45.0 mm
y	0.0 mm	45.0 mm
z	0.0 mm	70.0 mm

boundary conditions of the experiment, displacements in the vertical direction were constrained at the bottom face and the displacements at the lower left corner of the solid were fixed. The solid was immersed in a spherical fluid domain with radius, r_f, of 50 mm. The properties of the surrounding water were assumed to be known, with density and bulk modulus of 1000 kg/m^3 and 2.2 GPa, respectively. To avoid reflection effects, the Sommerfeld radiation boundary condition was specified in the outer fluid boundary. The Sommerfeld radiation boundary condition parameters f and β were set to 1 and $1/2r_f$, respectively.

The radiation force was modeled as a pressure force confined on a circular region with a 0.7 mm diameter on the inclusion surface [6] Due to the linearity of the fluid-structure equations, the surface velocity response was normalized at each measurement point by their respective maximum amplitude occurring over the frequency range. By normalizing the surface velocity response, any uncertainty in the knowledge of the magnitude of the ultrasound radiation force used in the experiment is eliminated.

It is important to point out that the velocity response was used for the experiment because of the low frequencies involved. These low frequencies have corresponding larger wave lengths in the fluid, which would result in reflections from the tank walls and interfere with the acoustic emission emanating directly from the solid. This problem can be avoided by using higher excitation frequencies (i.e., lower wave lengths), but this leads to a computationally demanding problem to model in 3-D due to the small wavelengths in the soft matrix. For this proof of concept, we opted for using velocity response to keep the computational demand low.

Two GRBF were a priori selected to inversely characterize the spatial distribution of elastic modulus. Consequently, the locality parameters of the GRBF, the coordinates of the GRBF centers, the Young's modulus at the GRBF centers, and the matrix Young's modulus were identified in the inverse problem. The stiffness proportional damping parameter, μ, was set to 0 and the mass proportional damping parameter, α, was identified through the inverse problem. Table 2.4 shows the minimum and maximum values considered for the optimization problem [95, 59].

Results

The Young's modulus of the inclusion was measured through mechanical testing as 350 kPa. For the matrix material, the Young's modulus was not measured though mechanical testing, but the search space for the optimization problem was selected according to data given in [91]. Figure 2.8 shows the spatial distribution of the elastic modulus found as a solution to the inverse problem. It can be observed from this figure that the algorithm identified a stiff region in the do-

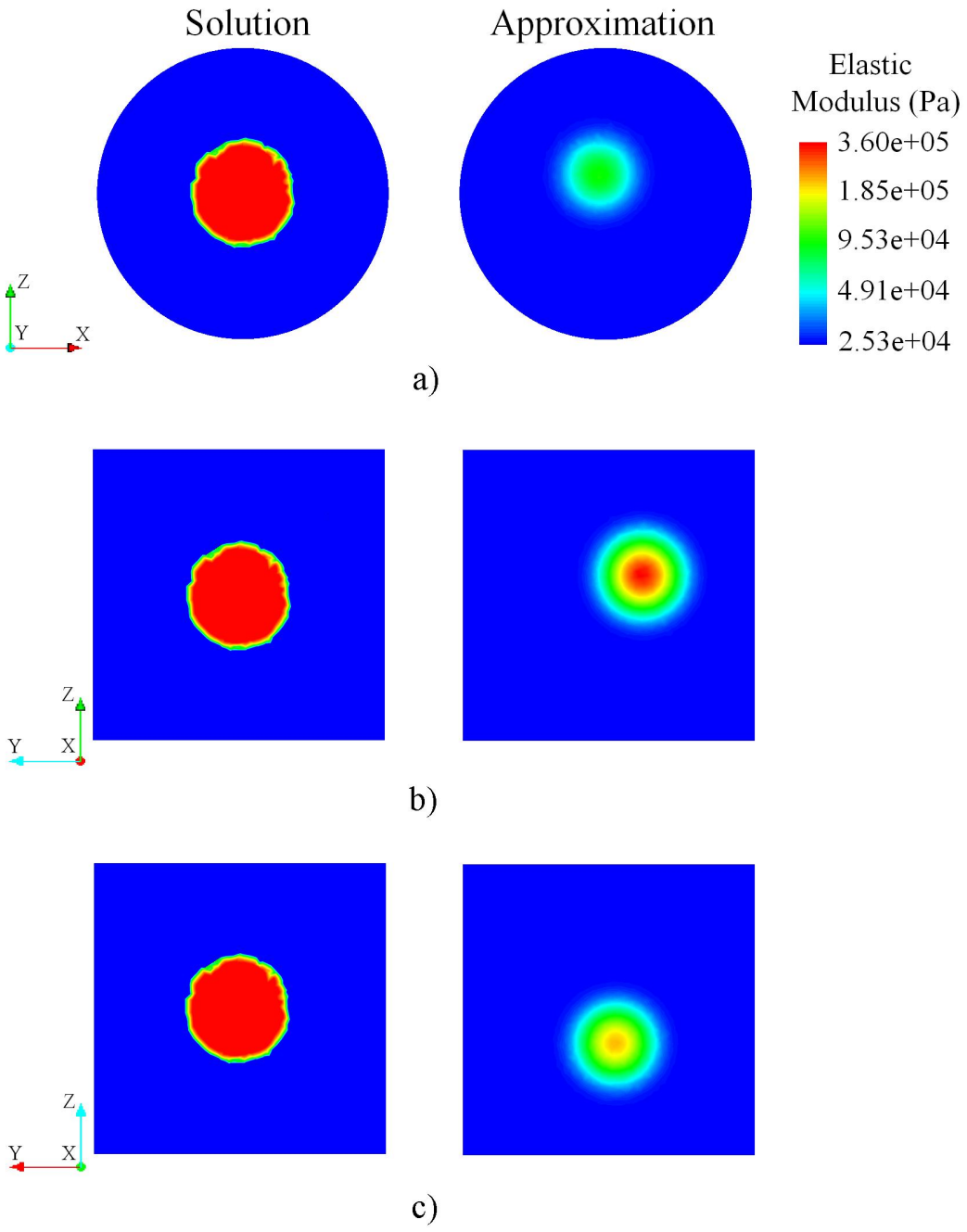

Figure 2.8: Plane views for the spatial distribution of elastic moduli found as solution to the inverse problem for (a) the z-x plane, (b) the z-y plane, (c) and the x-y plane.

main, as expected. However, the estimated modulus distribution is not perfectly aligned with the target solution, but there is reasonable agreement between the two given assumptions involved in the forward and inverse problems. Furthermore, the background material was accurately identified and the magnitude of the modulus at the center of the inclusion is close to that of the target.

Figure 2.9 shows the normalized magnitude of the surface velocity for the 12 measurements points for five excitation frequencies. It is important to point out that the discrepancies observed in these plots and in Figure 2.8 between the estimated response and the observed/experimental measurements can likely be attributed to the simplifications in the rate dependent material behavior in the numerical model (i.e., use of Rayleigh damping) and the low dimensionality of the radial basis function expansion. Future work will incorporate more general viscoelastic behavior into the formulations presented herein and study adaptive techniques to determine the optimal number of radial basis functions for a given problem.

2.5 Summary

A methodology to inversely characterize the spatial distribution of elastic modulus using vibroacoustics based techniques in combination with Gaussian radial basis function representations, non-gradient based optimization methods, and the finite element method was presented. Through simulations and an experiment it was shown that the proposed methodology could be used to estimate the spatial distribution of the elastic modulus of solids immersed in fluids using the acoustic pressure response. It was consistently observed that more ac-

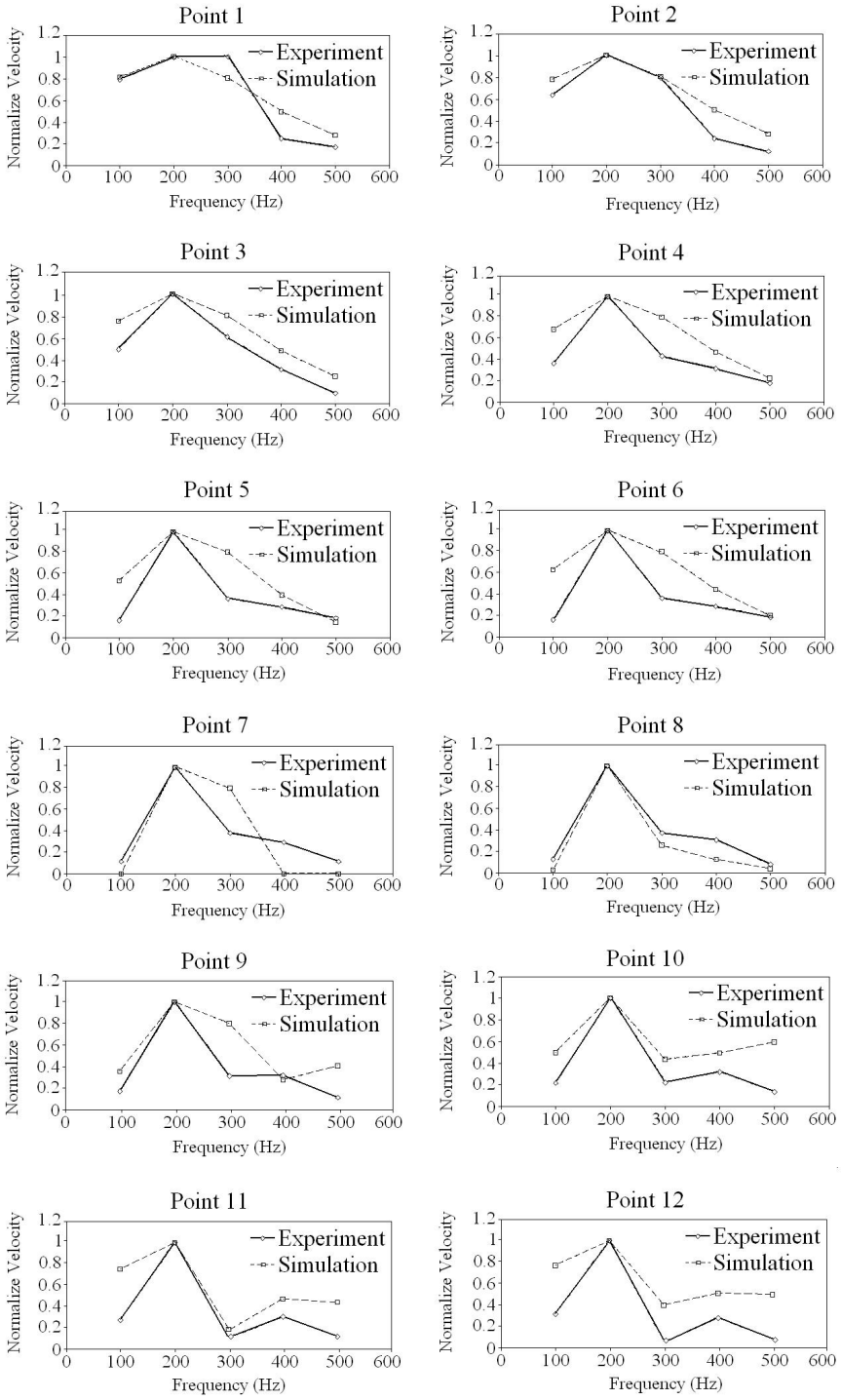

Figure 2.9: Comparison between the normalized magnitudes of the surface velocity response found as solution to the inverse problem (IP) and the target response for $f = 100, 200, 300, 400, 500\ Hz$

curate elastic modulus distributions can be obtained when the surface velocity response is used as opposed to acoustic pressure. However, there is a trade off in terms of signal-to-noise ration in the experimental setting when velocity response is used as opposed to acoustic pressure. Future work will study the optimal number of radial basis needed to improve the approximation as the complexity of material properties increase.

In general, the results reveal that Gaussian radial basis functions have the potential to approximate elastic modulus distribution such as those that occur in soft biological tissue in the presence of unhealthy tissue. The number of measurement points needed to inversely characterize the spatial distributions of elastic modulus is relatively small, making the use of the proposed methodology feasible for realistic applications.

Although the results presented in this paper are promising, it is well known that biological tissues have rate dependent viscoelastic behavior [44]; therefore, future work will consider estimating the spatial distributions of viscoelastic properties (viscoelasticity imaging).

CHAPTER 3

AN INVERSE APPROACH BASED ON THE L2-ADJOINT METHOD FOR CHARACTERIZATION OF SPATIALLY-VARYING VISCOELASTIC PROPERTIES IN STEADY-STATE DYNAMICS

3.1 Introduction

In this chapter, the inverse approach based on the adjoint method is presented. Aguiló *et al.* [3] showed that vibroacoustics based techniques can be used to estimate the spatial distribution of elastic modulus of solids submerged in fluid. The work presented herein extends the work in [3] by using the steady-state system response to characterize the spatially-varying complex tensor using the finite element method, adjoint method, and gradient-based optimization.

The inverse problem is cast as an optimization problem in which a least-square error functional that measures the misfit between experimental and finite element representation system response is minimized by searching over a space of admissible functions that best describe the spatially-varying complex tensor. Multiple techniques have been proposed in the literature for viscoelasticity imaging [61, 111, 115, 117]. For instance, Viola *et al.* [115] used acoustic radiation force to produce localized displacements within the tissue. The returning echoes were processed using ultrasonic tracking and by combining a Voigt material model with signal processing techniques, images of the spatial distribution of the damping ratio, natural frequency, and relaxation time were produced. A disadvantage of the technique proposed in [115] is that it is sensitive to imperfect data. Furthermore, the damping ratio and natural frequency, are less physically intuitive than viscoelastic properties such as the storage and

loss moduli.

An alternate technique is to use an inverse approach based on the adjoint method [39, 40, 78, 80, 93, 105, 106] to characterize the spatially-varying complex tensor. Oberai *et al.* [92] used a similar inverse approach to reconstruct the spatially-varying shear moduli of incompressible linear elastic solids. The advantage of this approach is that regardless of the number of design variables, the gradient of the error functional with respect to the design variables is computed very efficiently solving the corresponding adjoint equations. Consequently, minimizing the computational cost.

The remainder of this chapter is organized as follows. In Section II, the finite element formulation for an isotropic linear viscoelastic solid undergoing small deformations is presented. Furthermore, the inverse problem formulation and discretization of the state and adjoint problems are described, as well as the optimization strategy implemented herein. In Section III, the results obtained for the simulated example problems are shown and discussed. Concluding remarks and future directions are given at the end of this chapter.

3.2 Formulation

In this section we define the equilibrium equations that describe the behavior of an isotropic linear viscoelastic solid undergoing small deformations. In the following formulation, vector-valued functions will be represented with bold letters, second-order tensors are represented with lowercase bold greek letters, vectors will be denoted within curly brackets, and matrices will be enclosed within square brackets.

3.2.1 Preliminaries

The domain under consideration is $\Omega \subseteq \mathbb{R}^n$, n denotes dimensions and $[\omega_1, \omega_2]$ is the frequency interval under interest. We will work with the Hilbert space $L_2(\Omega \times [\omega_1, \omega_2])$. Given $f(\boldsymbol{x})$, $g(\boldsymbol{x}) \in L_2(\Omega)$ and $\boldsymbol{u}(\boldsymbol{x})$, $\boldsymbol{v}(\boldsymbol{x}) \in L_2(\Omega)$, we define in $L_2(\Omega)$ the *L_2-norm* $|f|_2 = \sqrt{\langle f, f \rangle}$, inner product $\langle f, f \rangle = \int_\Omega f f^* \, d\Omega$, and vector-valued functions inner product $\langle \boldsymbol{u}, \boldsymbol{v} \rangle = \int_\Omega \boldsymbol{u}\boldsymbol{v}^* \, d\Omega$, where $\boldsymbol{u}^*\boldsymbol{v} = \sum_{i=1}^{n} u_i v_i^*$. The asterisk denotes the complex conjugate. The Gâteaux derivative in this space is given as $(J'(f), \boldsymbol{h}) = \lim_{\eta \to 0} \frac{1}{\eta} [J(f + \eta \boldsymbol{h}(f)) - J(f)]$. It can be shown that the previous expression is equivalent to $(J'(f), \boldsymbol{h}) = \frac{d}{d\eta} J'(f + \eta \boldsymbol{h}(f)) \Big|_{\eta=0}$ [27, 99]. The following notation will be used $D_f J = (J'(f), \boldsymbol{h})$ to denote the derivative of J in the direction of $\boldsymbol{h}$ evaluated at f.

For brevity we let $H^1 = W^{1,2}$, where $W^{1,2}$ is the Sobolev space of all functions $\boldsymbol{f}(\boldsymbol{x}, \omega) \in L^2(\Omega \times [\omega_1, \omega_2])$ such that $D^1 \boldsymbol{f}(\boldsymbol{x}, \omega) \in L_2(\Omega \times [\omega_1, \omega_2])$, where $D^1 = \partial / \partial \boldsymbol{x}$. Further, $H_0^1 = W_0^{1,2} \subset W^{1,2}$ with compact support (i.e. functions vanishing on the boundaries). $\mathbb{R}$ is the set of reals and $\mathbb{Z}$ is the set of integers.

3.2.2 Forward Problem

Strong Formulation

The steady state dynamics boundary value problem is defined as

$$\nabla \cdot \boldsymbol{\sigma}(\boldsymbol{x}, \omega) = -\rho \omega^2 \boldsymbol{u}(\boldsymbol{x}, \omega) \text{ in } \Omega \tag{3.1}$$

$$\boldsymbol{u}(\boldsymbol{x}, \omega) = \boldsymbol{u}_0(\boldsymbol{x}, \omega) \text{ on } \Gamma_u \tag{3.2}$$

$$\boldsymbol{\sigma}(\boldsymbol{x},\omega)\,\boldsymbol{n}_s(\boldsymbol{x}) = \boldsymbol{t}(\boldsymbol{x},\omega) \text{ on } \Gamma_t \tag{3.3}$$

$$\boldsymbol{u}(\boldsymbol{x},0) = 0 \text{ in } \Omega \tag{3.4}$$

$$\dot{\boldsymbol{u}}(\boldsymbol{x},0) = 0 \text{ in } \Omega \tag{3.5}$$

Here Ω represents the interior of a body whose boundary is $\Gamma = \Gamma_u \cup \Gamma_t$, Γ_t is the portion of the boundary where external tractions are specified, Γ_u is the portion of the boundary where displacements are specified, $\boldsymbol{x}$ is the spatial position vector, ω denotes angular frequency, $\boldsymbol{\sigma}(\boldsymbol{x},\omega)$ is the stress tensor, ρ is the mass density (assumed constant in this work), $\boldsymbol{u}(\boldsymbol{x},\omega)$ is the displacement field, $\boldsymbol{t}(\boldsymbol{x},\omega)$ denote tractions, and $\boldsymbol{n}_s(\boldsymbol{x})$ is the unit normal vector to the solid surface. For the purpose of this chapter, body forces are negligible.

For sinusoidal varying stresses and strains, the stress-strain relationship for a linear viscoelastic material is defined as

$$\boldsymbol{\sigma}(\boldsymbol{x},\omega) = \mathbb{C}(\boldsymbol{x},\omega) : \epsilon(\boldsymbol{x},\omega) \tag{3.6}$$

$$\mathbb{C}(\boldsymbol{x},\omega) = \int_{-\infty}^{\infty} \hat{\mathbb{C}}(\boldsymbol{x},t-s)\exp(-i\omega t)\ dt \tag{3.7}$$

$$\boldsymbol{\epsilon}(\boldsymbol{x},\omega) = \frac{1}{2}\left(\nabla\boldsymbol{u}(\boldsymbol{x},\omega) + \nabla\boldsymbol{u}(\boldsymbol{x},\omega)^T\right) \tag{3.8}$$

where t denotes time, $\mathbb{C}(\boldsymbol{x},\omega)$ is the fourth-order complex tensor, $\hat{\mathbb{C}}(\boldsymbol{x},t-s)$ is the fourth-order relaxation tensor, and $\boldsymbol{\epsilon}(\boldsymbol{x},\omega)$ is the strain tensor.

Viscoelastic Constitutive Model

In this chapter, the stress-strain relationship was considered to be defined by a linear viscoelastic model obeying an exponential series relaxation law (i.e.,

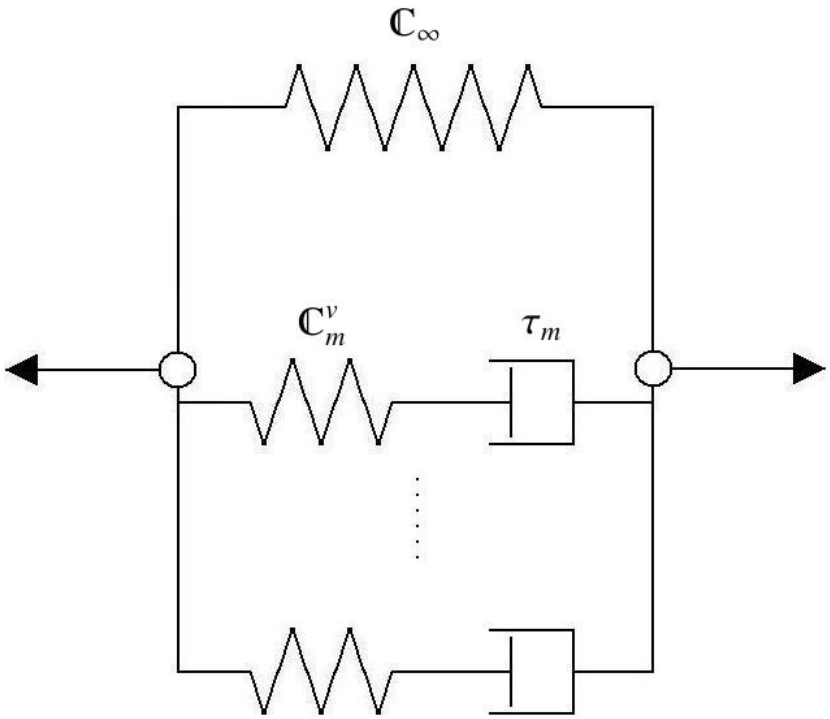

Figure 3.1: One-dimensional generalized Maxwell model for viscoelasticity

Prony series) and is defined as

$$\boldsymbol{\sigma}(\boldsymbol{x},t) = \mathbb{C}_\infty(\boldsymbol{x}) : \boldsymbol{\epsilon}(\boldsymbol{x},\boldsymbol{t}) + \sum_{r=1}^{M}\left[\int_0^t \mathbb{C}_r^v(\boldsymbol{x}) : \frac{\partial \boldsymbol{\epsilon}(\boldsymbol{x},s)}{\partial s}\exp^{-(t-s)/\tau_r}\, ds\right] \tag{3.9}$$

Here, $\mathbb{C}_\infty$ is the long-term fourth-order tensor, $\mathbb{C}_r^v$ is the r-term viscous fourth-order tensor, and τ_r is the r-term relaxation time. This viscoelastic model consists of M Maxwell elements in parallel with an additional spring element to represent purely elastic deformation, see Figure 3.1.

The frequency dependence of equation (3.9) is obtained by using Fourier transforms. This yields the stress-strain relationship defined in equation (3.6), where now $\mathbb{C}$ is defined as follows

$$\mathbb{C}(\boldsymbol{x},\omega) = \mathbb{C}_{\infty}(\boldsymbol{x}) + \sum_{r=1}^{M} \mathbb{C}_r^{v}(\boldsymbol{x}) \left(\frac{\omega^2 \tau_r^2 + i\omega\tau_r}{1 + \omega^2 \tau_r^2} \right) \tag{3.10}$$

For more details on the theory of linear viscoelasticity the reader is referred to [13, 24, 35, 41, 42].

Variational Formulation

Using a weak-form Galerkin approach, an arbitrary virtual displacement field $\boldsymbol{v}(\boldsymbol{x},\omega) \in \Omega$ is defined. Taking the product of the virtual displacement field with Equation (3.1) and applying the divergence theorem, the variational boundary value problem is defined as

$$a(\mathbb{C};\boldsymbol{v},\boldsymbol{u}) = \ell(\boldsymbol{v}) \;\; \forall\, \boldsymbol{v} \in V \tag{3.11}$$

where

$$a(\mathbb{C};\boldsymbol{v},\boldsymbol{u}) = \int_{\Omega} \nabla \boldsymbol{v}^* : \boldsymbol{\sigma} \, d\Omega - \rho\omega^2 \int_{\Omega} \boldsymbol{v}^* \cdot \boldsymbol{u} \, d\Omega \tag{3.12}$$

$$\ell(\boldsymbol{v}) = \int_{\Gamma_t} \boldsymbol{v}^* \cdot \boldsymbol{t} \, d\Gamma_t, \tag{3.13}$$

where the test function space V and the trial solution space U are defined as

$$V = \{\boldsymbol{v} : \boldsymbol{v} \mid v_i \in H_0^1(\Omega), \boldsymbol{v} = 0 \text{ on } \Gamma_u\} \tag{3.14}$$

$$U = \{\boldsymbol{u} : \boldsymbol{u} \mid u_i \in H^1(\Omega), \boldsymbol{u} = \boldsymbol{u}_0 \text{ on } \Gamma_u\}. \tag{3.15}$$

Finite-dimensional subspaces associated with the test function and trial solution spaces were introduced in order to solve Equation (3.11) numerically. These spaces are denoted by $V^h \subset V$ and $U^h \subset U$ respectively. This leads to the Galerkin approximation: find $\boldsymbol{u}^h \in U^h$, such that

$$a\left(\mathbb{C}^h; \boldsymbol{v}^h, \boldsymbol{u}^h\right) - \ell\left(\boldsymbol{v}^h\right) = 0 \;\forall\; \boldsymbol{v}^h \in V^h, \tag{3.16}$$

note that the superscript h is used to denote finite-dimensional approximation.

3.2.3 Inverse Problem

Inverse Problem Formulation

An optimization approach was used to inversely reconstruct the spatially-varying complex tensor $\mathbb{C}$ from the steady-state system response. The objective is to find the complex tensor such that the following error functional

$$J(\mathbb{C}) = \sum_{j=1}^{freq} \left[\frac{1}{2} \int_{\Omega} \left(|\boldsymbol{u} - \boldsymbol{u}^m|_2^2 + \frac{\beta}{\alpha} \left(|\nabla \mathbb{C}|_2^2 + \gamma^2 \right)^{\alpha} \right) d\Omega \right] \tag{3.17}$$

is minimized. In Equation (3.17), β denotes the regularization parameter and γ is a small positive parameter. For $\alpha = 1$ and $\gamma = 0$ Tikhonov regularization is obtained and for $\alpha = 1/2$ and $0 < \gamma \leqslant 1$ Total Variation (TV) regularization is obtained [34].

The inverse problem was cast as an optimization problem in which the error functional defined in (3.17) is minimize by searching over a space of admissi-

ble functions that best describe the spatial distribution of the complex tensor. Therefore, the minimization problem is given by

$$\hat{J}(\mathbb{C}) = \arg \min_{\mathbb{C} \in \Xi} J(\mathbb{C}) \quad \text{subject to } a(\mathbb{C}; \boldsymbol{v}, \boldsymbol{u}) - \ell = 0 \text{ in } \Omega \tag{3.18}$$

where $\Xi = \{\mathbb{C}\colon \mathbb{C} \mid \mathbb{C}_{ijkl} \in L_2(\Omega), \mathbb{C}_{ijkl} \geq 0\}$.

Calculation of the gradient using the adjoint method

In this section we propose an efficient approach to calculate the gradient of the objective function in Equation (3.17) with respect to the complex tensor. The approach is based on the adjoint method. First, a Lagrangian $\mathcal{L}$ is defined as

$$\mathcal{L}(\mathbb{C}; \boldsymbol{v}, \boldsymbol{u}) = \sum_{j=1}^{freq} \Big[J(\mathbb{C}) + \Re\Big[a(\mathbb{C}; \boldsymbol{v}, \boldsymbol{u}) - \ell(\boldsymbol{v})\Big]\Big] \tag{3.19}$$

where $\boldsymbol{v}$ plays the role of a Lagrange multiplier and $\Re$ denotes the real component. Since $\boldsymbol{u}$ satisfies the variational boundary value problem defined in (3.11), the following identity holds

$$J(\mathbb{C}) = \mathcal{L}(\mathbb{C}; \boldsymbol{v}, \boldsymbol{u}) \;\; \forall \, \boldsymbol{v} \;\in\; V \tag{3.20}$$

and subsequently

$$D_{\mathbb{C}} J(\mathbb{C}) \cdot \delta\mathbb{C} = D_{\mathbb{C}} \mathcal{L}(\mathbb{C}; \boldsymbol{v}, \boldsymbol{u}) \cdot \delta\mathbb{C} \;\forall\, \boldsymbol{v} \in V \tag{3.21}$$

Thus, the directional derivative of the Lagrangian $\mathcal{L}(\mathbb{C};\boldsymbol{v},\boldsymbol{u})$ is defined as

$$\begin{aligned} D_{\mathbb{C}}\mathcal{L}(\mathbb{C};\boldsymbol{v},\boldsymbol{u})\cdot\delta\mathbb{C} &= D_{\mathbb{C}}J(\mathbb{C})\cdot\delta\mathbb{C} + D_{u}J(\mathbb{C})\cdot\delta\boldsymbol{u} \\ &+ D_{\mathbb{C}}a(\mathbb{C};\boldsymbol{v},\boldsymbol{u})\cdot\delta\mathbb{C} + D_{u}a(\mathbb{C};\boldsymbol{v},\boldsymbol{u})\cdot\delta\boldsymbol{u} \end{aligned} \tag{3.22}$$

where the term $\delta\boldsymbol{u}$ is defined as

$$\delta\boldsymbol{u} = \frac{d}{d\eta}\boldsymbol{u}(\mathbb{C}+\eta\delta\mathbb{C})\Big|_{\eta=0}. \tag{3.23}$$

The terms $D_{\mathbb{C}}J(\mathbb{C})\cdot\delta\mathbb{C}$, $D_{u}J(\mathbb{C})\cdot\delta\boldsymbol{u}$, $D_{\mathbb{C}}\,a(\mathbb{C};\boldsymbol{v},\boldsymbol{u})\cdot\delta\mathbb{C}$, and $D_{u}\,a(\mathbb{C};\boldsymbol{v},\boldsymbol{u})\cdot\delta\boldsymbol{u}$ in (3.20) are defined as

$$D_{\mathbb{C}}J(\mathbb{C})\cdot\delta\mathbb{C} = \beta\int_{\Omega}\left(|\nabla\mathbb{C}|_2^2+\gamma^2\right)^{\alpha-1}(\nabla\mathbb{C}\cdot\nabla\delta\mathbb{C})^{*}\,d\Omega \tag{3.24}$$

$$D_{u}J(\mathbb{C})\cdot\delta\boldsymbol{u} = \int_{\Omega}(\boldsymbol{u}-\boldsymbol{u}^{exp})\cdot\delta\boldsymbol{u}^{*}\,d\Omega \tag{3.25}$$

$$D_{\mathbb{C}}\,a(\mathbb{C};\boldsymbol{v},\boldsymbol{u})\cdot\delta\mathbb{C} = \int_{\Omega}\nabla\boldsymbol{v}\cdot(\delta\mathbb{C}:\,\epsilon)^{*}\;d\Omega \tag{3.26}$$

$$D_{u}\,a(\mathbb{C};\boldsymbol{v},\boldsymbol{u})\cdot\delta\boldsymbol{u} = \int_{\Omega}\left(\nabla\boldsymbol{v}\cdot(\mathbb{C}:\,\nabla\delta\epsilon)^{*}-\rho\omega(\boldsymbol{v}\cdot\delta\boldsymbol{u}^{*})\right)d\Omega \tag{3.27}$$

The expression for $D_{\mathbb{C}}\mathcal{L}(\mathbb{C};\boldsymbol{v},\boldsymbol{u})\cdot\delta\mathbb{C}$, defined in Equation (3.22), is simplified considerably given that $D_{u}\mathcal{L}(\mathbb{C};\boldsymbol{v},\boldsymbol{u})\cdot\delta\boldsymbol{u}=0\;\forall\;\delta\boldsymbol{u}\in V$. This condition yields the following problem

$$b(\mathbb{C};\boldsymbol{v},\delta\boldsymbol{u}) = -(\delta\boldsymbol{u},\boldsymbol{u}-\boldsymbol{u}^{exp})\;\;\forall\;\delta\boldsymbol{u}\in V \tag{3.28}$$

where

$$b\left(\mathbb{C};\boldsymbol{v},\delta\boldsymbol{u}\right)=D_{\boldsymbol{u}}\,a\left(\mathbb{C};\boldsymbol{v},\boldsymbol{u}\right)\cdot\delta\boldsymbol{u} \tag{3.29}$$

The term $\delta\boldsymbol{u}$ in Equation (3.28) does not need to be calculated if $\boldsymbol{v}$ is chosen such that the adjoint equation is satisfied. Since (3.29) is self-adjoint, that is $\hat{b}\left(\mathbb{C};\delta\boldsymbol{u},\boldsymbol{v}\right)=b\left(\mathbb{C};\boldsymbol{v},\delta\boldsymbol{u}\right)\ \forall\ \delta\boldsymbol{u},\boldsymbol{v}\in V$, Equation (3.28) reduces to

$$\hat{b}\left(\mathbb{C};\delta\boldsymbol{u},\boldsymbol{v}\right)=-\left(\delta\boldsymbol{u},\boldsymbol{u}-\boldsymbol{u}^{exp}\right)\ \forall\ \delta\boldsymbol{u}\subset V \tag{3.30}$$

The variational problem defined in (3.30) is known as the adjoint problem.

Since $\boldsymbol{v}$ is the solution to the adjoint problem for all values of $\delta\boldsymbol{u}$, Equation (3.22) reduces to

$$D_{\mathbb{C}}\mathcal{L}\left(\mathbb{C};\boldsymbol{v},\boldsymbol{u}\right)\cdot\delta\mathbb{C}=\sum_{j=1}^{freq}\Re\Big[D_{\mathbb{C}}J\left(\mathbb{C}\right)+D_{\mathbb{C}}a\left(\mathbb{C};\boldsymbol{v},\boldsymbol{u}\right)\Big]\cdot\delta\mathbb{C} \tag{3.31}$$

and the expression to calculate the gradient is given by

$$D_{\mathbb{C}}\mathcal{L}\left(\mathbb{C};\boldsymbol{v},\boldsymbol{u}\right)=\sum_{j=1}^{freq}\Re\Big[D_{\mathbb{C}}J\left(\mathbb{C}\right)+D_{\mathbb{C}}a\left(\mathbb{C};\boldsymbol{v},\boldsymbol{u}\right)\Big] \tag{3.32}$$

Finite-dimensional subspaces associated with the test functions and trial solution spaces defined in (3.14) and (3.15) are introduced in order to solve (3.30) and (3.32) numerically. This leads to the Galerkin approximation of the adjoint problem: find $\boldsymbol{v}^h\in U^h$, such that

$$\hat{b}\left(\mathbb{C}^h;\delta\boldsymbol{u}^h,\boldsymbol{v}^h\right)=-\left(\delta\boldsymbol{u}^h,\boldsymbol{u}^h-\boldsymbol{u}^{exp}\right)\ \forall\ \delta\boldsymbol{u}^h\in V^h \tag{3.33}$$

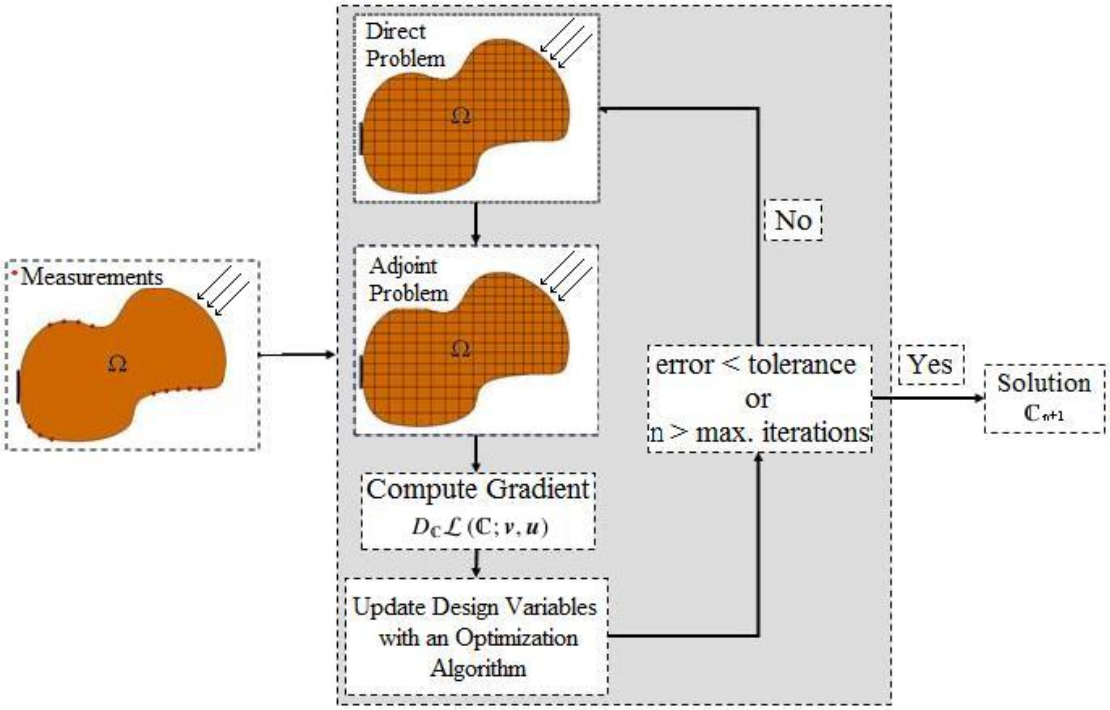

Figure 3.2: L2-Adjoint inverse problem flowchart

Similarly, the Galerkin approximation for $D_{\mathbb{C}}\mathcal{L}(\mathbb{C};\boldsymbol{v},\boldsymbol{u})$ is defined as

$$D_{\mathbb{C}}\mathcal{L}\left(\mathbb{C}^h;\boldsymbol{v}^h,\boldsymbol{u}^h\right) = \sum_{j=1}^{freq} \Re\left[D_{\mathbb{C}}J\left(\mathbb{C}^h\right) + D_{\mathbb{C}}a\left(\mathbb{C}^h;\boldsymbol{v}^h,\boldsymbol{u}^h\right)\right] \tag{3.34}$$

3.2.4 Algorithm

The following algorithm may be used to compute the complex tensor at each iteration of the minimization process

i. Solve Equation (3.16) to evaluate the state variable $\boldsymbol{u}^h$.

ii. Solve Equation (3.33) to evaluate the adjoint variable $\boldsymbol{v}^h$.

iii. Solve Equation (3.34) to compute the gradient.

iv. Update design variables and evaluate cost function.

v. Check stopping criteria, if one of the stopping criteria is satisfied, stop optimization. If none of the stopping criteria are satisfied, repeat Steps i-v until convergence.

Figure 3.2 shows a pictorial description of the algorithm described above. A limited memory BFGS algorithm [120] was used to minimized the least-square error functional defined in Equation 3.15. The computer program for the limited memory BFGS algorithm was downloaded from `http://www-fp.mcs.anl.gov/otc/Tools/LBFGS-B`. All calculations are performed on a Linux workstation with a 1.86-GHz Intel processor and 16 GB of RAM.

3.2.5 Discretization

The discretization of problems (3.16), (3.33), and (3.34) using the finite element method leads to the construction of vectors of nodal values for fields $\boldsymbol{u}^h$ and $\boldsymbol{v}^h$, given by

$$\boldsymbol{u}^h = \{u^h\} = [N(\boldsymbol{x})]\{u^e(\omega)\} \tag{3.35}$$

$$\boldsymbol{v}^h = \{v^h\} = [N(\boldsymbol{x})]\{v^e(\omega)\} \tag{3.36}$$

Here $[N(\boldsymbol{x})]$ denotes the matrix of interpolation functions for the elements. Similarly, the strains are approximated within each element as

$$\boldsymbol{\epsilon}^h = \{\boldsymbol{\epsilon}^h\} = [B(\boldsymbol{x})]\{u^e(\omega)\} \tag{3.37}$$

$$\hat{\boldsymbol{\epsilon}}^h = \{\hat{\boldsymbol{\epsilon}}^h\} = [B(\boldsymbol{x})]\{v^e(\omega)\} \tag{3.38}$$

where $[B(\boldsymbol{x})]$ is the matrix of derivative of interpolation functions.

Complex Moduli

For isotropic linear viscoelastic materials, the complex moduli is defined as

$$\mathbb{C}(\boldsymbol{x},\omega) = G(\boldsymbol{x},\omega)\left(\boldsymbol{I}+\boldsymbol{I}^T\right) + K(\boldsymbol{x},\omega)\,\boldsymbol{I}\otimes\boldsymbol{I} \tag{3.39}$$

where the complex shear and bulk modulus are approximated within each element as

$$G^h = \{G^h\} = [N(\boldsymbol{x})]\{G_S(\omega)\} + i[N(\boldsymbol{x})]\{G_L(\omega)\} \tag{3.40}$$

$$K^h = \{K^h\} = [N(\boldsymbol{x})]\{K_S(\omega)\} + i[N(\boldsymbol{x})]\{K_L(\omega)\} \tag{3.41}$$

,respectively. The absolute value of the dynamic shear and bulk modulus (e.g. equivalent modulus) is defined as

$$G_{eq} = |G| = \sqrt{G_S^2 + G_L^2} \tag{3.42}$$

$$K_{eq} = |K| = \sqrt{K_S^2 + K_L^2} \tag{3.43}$$

Another useful quantity to characterize linear viscoelastic behavior when stresses and strains vary harmonically is the dissipation factor. The dissipation factor measures the energy dissipation in the material and is defined as

$$\tan(\delta_G) = G_L/G_S \tag{3.44}$$

$$\tan(\delta_K) = K_L/K_S \tag{3.45}$$

In the preceding equations, $\boldsymbol{I}$ is the second-order identity tensor, G_S is the storage shear moduli, G_L is the loss shear moduli, K_S is the storage bulk moduli, K_L is the loss bulk moduli, G_{eq} is the equivalent shear modulus, G_{eq} is the equivalent bulk modulus, $\tan(\delta_G)$ is the shear dissipation factor, and $\tan(\delta_K)$ is the bulk dissipation factor.

In this chapter, the material behavior at low frequencies of an isotropic linear viscoelastic soft material subjected to small deformations is studied. For some linear viscoelastic materials, the shear and bulk modulus are similar in magnitude at high frequencies, and the assumption that viscous effects are negligible in the bulk modulus will not be applicable. This situation correspond to values of Poisson's ratio much less than 0.5 [41]. Furthermore, for soft materials subjected to small deformations, the change in volume caused by these deformations is negligible in comparison to the change in shape [81]. Consequently, bulk viscous effects could be considered negligible. For a more detailed discussion on this subject, the reader is referred to [13, 24, 41, 42, 103].

State and Adjoint System of Equations

Substituting Equations (3.35)–(3.38) and the corresponding interpolated quan-

tities into Equations (3.16) and (3.33), the discretized state and adjoint system of equations are defined as

$$[A]\{u(\omega)\} = \{R^{ext}\} \tag{3.46}$$

$$[A]\{v(\omega)\} = -\{R^{adj}\} \tag{3.47}$$

where

$$[A] = [K_G] + [K_K] - \omega^2 [M] \tag{3.48}$$

$$[M] = \sum_{elements} \rho \int_{\Omega^e} [N]^T [N] \, d\Omega^e \tag{3.49}$$

$$[K_G] = \sum_{elements} 2 \int_{\Omega^e} [B]^T G(\boldsymbol{x}, \omega) [D_G] [B] \, d\Omega^e \tag{3.50}$$

$$[K_K] = \sum_{elements} \int_{\Omega^e} [B]^T K(\boldsymbol{x}, \omega) [D_K] [B] \, d\Omega^e \tag{3.51}$$

$$\{R^{ext}\} = \sum_{elements} \int_{\Omega^e} [N]\{t\} \, d\Omega^e \tag{3.52}$$

$$\{R^{adj}\} = \sum_{elements} \int_{\Omega^e} [N]\{u - u^{exp}\} \, d\Omega^e \tag{3.53}$$

Here $[M]$ denotes the mass matrix, $[K_G]$ is the shear stiffness matrix, $[K_K]$ is the volumetric stiffness matrix, $\{R^{ext}\}$ is the forward problem force vector, $\{R^{ext}\}$ is the adjoint problem force vector.

The matrices $[D_G]$ and $[D_K]$ denote the deviatoric and volumetric elasticity matrix, respectively. For instance, in two-dimensional problems these matrices are defined as

$$[D_G] = \begin{bmatrix} 2.0/3.0 & -1.0/3.0 & 0.0 \\ sym. & 2.0/3.0 & 0.0 \\ & & 1.0/2.0 \end{bmatrix} \tag{3.54}$$

$$[D_K] = \begin{bmatrix} 1.0 & 1.0 & 0.0 \\ sym. & 1.0 & 0.0 \\ & & 0.0 \end{bmatrix} \tag{3.55}$$

Discrete Gradient Equations

After discretization of Equation (3.34) using the finite element method, the complex shear and bulk modulus are given by Equations 3.40 and 3.41, respectively. Then, the k-node complex shear and bulk modulus are defined as

$$G_k^h = N_k(\boldsymbol{x})\, G_S^k(\omega) + iN_k(\boldsymbol{x})\, G_L^k(\omega) \tag{3.56}$$

$$K_k^h = N_k(\boldsymbol{x})\, K_S^k(\omega) + iN_k(\boldsymbol{x})\, K_L^k(\omega) \tag{3.57}$$

where

$$G_S^k(\omega) = G_\infty^k + \sum_{r=1}^{M} \frac{\check{G}_r^k \omega^2 \left(\tau_r^k\right)^2}{1 + \omega^2 \left(\tau_r^k\right)^2} \tag{3.58}$$

$$G_L^k(\omega) = \sum_{r=1}^{M} \frac{\check{G}_r^k \omega \tau_r^k}{1 + \omega^2 \left(\tau_r^k\right)^2} \tag{3.59}$$

$$K_S^k(\omega) = K_\infty^k + \sum_{r=1}^{M} \frac{\check{K}_r^k \omega^2 \left(\tau_r^k\right)^2}{1 + \omega^2 \left(\tau_r^k\right)^2} \tag{3.60}$$

$$K_L^k(\omega) = \sum_{r=1}^{M} \frac{\check{K}_r^k \omega \tau_r^k}{1 + \omega^2 \left(\tau_r^k\right)^2} \tag{3.61}$$

Here, G_∞ is the long-term shear moduli, K_∞ is the long-term bulk moduli, $\check{G}_r$ is the r-term viscous shear modulus, $\check{K}_r$ is the r-term viscous bulk modulus, and τ_r is the r-term relaxation time.

The k-th node vector of design variables is defined as follows

$$\{p^k\} = \{G_\infty^k, K_\infty^k, \check{G}_1^k, \cdots, \check{G}_r^k, \check{K}_1^k, \cdots, \check{K}_r^k, \tau_1^k, \cdots, \tau_r^k\} \tag{3.62}$$

Then, the k-node variation of the shear and bulk modulus with respect to the vector of design variables are defined as follows

$$\delta G_k^h = N_k(\boldsymbol{x})\, \delta G_S^k(\omega) + i N_k(\boldsymbol{x})\, \delta G_L^k(\omega) \tag{3.63}$$

$$\delta K_k^h = N_k(\boldsymbol{x})\, \delta K_S^k(\omega) + i N_k(\boldsymbol{x})\, \delta K_L^k(\omega) \tag{3.64}$$

where

$$\delta G_S^k(\omega) = \delta G_\infty^k + \sum_{r=1}^{M} g_r^k \delta \check{G}_r^k + \sum_{r=1}^{M} \dot{g}_r^k \check{G}_r^k \delta \tau_r^k \tag{3.65}$$

$$\delta G_L^k(\omega) = \sum_{r=1}^{M} f_r^k \left(\delta G_r^v\right)^k + \sum_{r=1}^{M} \dot{f}_r^k \left(G_r^v\right)^k \delta \tau_r^k \tag{3.66}$$

$$\delta K_S^k(\omega) = \delta K_\infty^k + \sum_{r=1}^{M} g_r^k \delta \check{K}_r^k + \sum_{r=1}^{N} \dot{g}_r^k \check{K}_r^k \delta \tau_r^k \tag{3.67}$$

$$\delta K_L^k(\omega) = \sum_{r=1}^{M} f_r^k \left(\delta K_r^v\right)^k + \sum_{r=1}^{M} \dot{f}_r^k \left(K_r^v\right)^k \delta \tau_r^k \tag{3.68}$$

In the preceding equations

$$g_r^k = \frac{\omega^2 \left(\tau_r^k\right)^2}{1 + \omega^2 \left(\tau_r^k\right)^2} \tag{3.69}$$

$$\dot{g}_r^k = \frac{\left(2\omega^2 \tau_r^k\right)\left(1 + \omega^2 \left(\tau_r^k\right)^2\right) - \left(\omega^2 \left(\tau_r^k\right)^2\right)\left(2\omega^2 \tau_r^k\right)}{1 + \omega^2 \left(\tau_r^k\right)^2} \tag{3.70}$$

$$f_r^k = \frac{\omega \tau_r^k}{1 + \omega^2 \left(\tau_r^k\right)^2} \tag{3.71}$$

$$\dot{f}_r^k = \frac{\omega\left(1 + \omega^2 \left(\tau_r^k\right)^2\right) - \left(\omega \tau_r^k\right)\left(2\omega^2 \tau_r^k\right)}{1 + \omega^2 \left(\tau_r^k\right)^2} \tag{3.72}$$

The terms δG_S^k, δG_L^k, δK_S^k, and δK_L^k can be expressed in vector form as follow

$$\begin{aligned} \delta G_S^k &= \{C_{G_S}^k\}^T \{\delta p^k\} \\ &= \begin{Bmatrix} 1 \\ 0 \\ g_1^k \\ \vdots \\ g_r^k \\ 0 \\ \vdots \\ 0 \\ \check{G}_1^k \dot{g}_1^k \\ \vdots \\ \check{G}_r^k \dot{g}_r^k \end{Bmatrix}^T \begin{Bmatrix} \delta G_\infty \\ dK_\infty \\ \delta \check{G}_1^k \\ \vdots \\ \delta \check{G}_r^k \\ \delta \check{K}_1^k \\ \vdots \\ \delta \check{K}_r^k \\ \delta \tau_1^k \\ \vdots \\ \delta \tau_r^k \end{Bmatrix} \end{aligned} \tag{3.73}$$

$$
\begin{aligned}
\delta G_L^k &= \{C_{G_L}^k\}^T \{\delta p^k\} \\
&= \begin{Bmatrix} 0 \\ 0 \\ f_1^k \\ \vdots \\ f_r^k \\ 0 \\ \vdots \\ 0 \\ \check{G}_1^k \dot{f}_1^k \\ \vdots \\ \check{G}_r^k \dot{f}_r^k \end{Bmatrix}^T \begin{Bmatrix} \delta G_\infty \\ dK_\infty \\ \delta \check{G}_1^k \\ \vdots \\ \delta \check{G}_r^k \\ \delta \check{K}_1^k \\ \vdots \\ \delta \check{K}_r^k \\ \delta \tau_1^k \\ \vdots \\ \delta \tau_r^k \end{Bmatrix}
\end{aligned} \tag{3.74}
$$

$$
\begin{aligned}
\delta K_S^k &= \{C_{K_S}^k\}^T \{\delta p^k\} \\
&= \begin{Bmatrix} 0 \\ 1 \\ 0 \\ \vdots \\ 0 \\ g_1^k \\ \vdots \\ g_r^k \\ \check{K}_1^k \dot{g}_1^k \\ \vdots \\ \check{K}_r^k \dot{g}_r^k \end{Bmatrix}^T \begin{Bmatrix} \delta G_\infty \\ dK_\infty \\ \delta \check{G}_1^k \\ \vdots \\ \delta \check{G}_r^k \\ \delta \check{K}_1^k \\ \vdots \\ \delta \check{K}_r^k \\ \delta \tau_1^k \\ \vdots \\ \delta \tau_r^k \end{Bmatrix}
\end{aligned} \tag{3.75}
$$

$$
\begin{aligned}
\delta K_L^k &= \{C_{K_L}^k\}^T \{\delta p^k\} \\
&= \begin{Bmatrix} 0 \\ 0 \\ 0 \\ \vdots \\ 0 \\ f_1^k \\ \vdots \\ f_r^k \\ \check{K}_1^k \dot{f}_1^k \\ \vdots \\ \check{K}_r^k \dot{f}_r^k \end{Bmatrix}^T \begin{Bmatrix} \delta G_\infty \\ dK_\infty \\ \delta \check{G}_1^k \\ \vdots \\ \delta \check{G}_r^k \\ \delta \check{K}_1^k \\ \vdots \\ \delta \check{K}_r^k \\ \delta \tau_1^k \\ \vdots \\ \delta \tau_r^k \end{Bmatrix}
\end{aligned} \tag{3.76}
$$

Now, the terms G_S, G_L, K_S, and K_L are approximated within each element as follows

$$
\begin{aligned}
\{G_S^h\} &= \begin{bmatrix} N_1 & \cdots & N_k \end{bmatrix} \begin{Bmatrix} G_S^1 \\ \vdots \\ G_S^k \end{Bmatrix} \\
&= \begin{bmatrix} N \end{bmatrix} \begin{Bmatrix} G_S \end{Bmatrix}
\end{aligned} \tag{3.77}
$$

$$
\begin{aligned}
\{G_L^h\} &= \begin{bmatrix} N_1 & \cdots & N_k \end{bmatrix} \begin{Bmatrix} G_L^1 \\ \vdots \\ G_L^k \end{Bmatrix} \\
&= \begin{bmatrix} N \end{bmatrix} \begin{Bmatrix} G_L \end{Bmatrix}
\end{aligned} \tag{3.78}
$$

$$\{K_S^h\} = \begin{bmatrix} N_1 & \cdots & N_k \end{bmatrix} \begin{Bmatrix} K_S^1 \\ \vdots \\ K_S^k \end{Bmatrix} \tag{3.79}$$
$$= \begin{bmatrix} N \end{bmatrix} \begin{Bmatrix} K_S \end{Bmatrix}$$

$$\{K_L^h\} = \begin{bmatrix} N_1 & \cdots & N_k \end{bmatrix} \begin{Bmatrix} K_L^1 \\ \vdots \\ K_L^k \end{Bmatrix} \tag{3.80}$$
$$= \begin{bmatrix} N \end{bmatrix} \begin{Bmatrix} K_L \end{Bmatrix}$$

where the superscript k denotes the number of nodes in each element. Similarly, the terms δG_S, δG_L, δK_S, and δK_L are approximated within each element as follows

$$\{\delta G_S^h\} = \begin{bmatrix} N_1 & \cdots & N_k \end{bmatrix} \begin{bmatrix} \{C_{G_S}^1\} & 0 & 0 \\ & \ddots & 0 \\ & & \{C_{G_S}^k\} \end{bmatrix} \begin{Bmatrix} \{\delta p^1\} \\ \vdots \\ \{\delta p^k\} \end{Bmatrix} \tag{3.81}$$
$$= \begin{bmatrix} N \end{bmatrix} \begin{bmatrix} C_{G_S} \end{bmatrix} \begin{Bmatrix} \delta p \end{Bmatrix}$$

$$\{\delta G_L^h\} = \begin{bmatrix} N_1 & \cdots & N_k \end{bmatrix} \begin{bmatrix} \{C_{G_L}^1\} & 0 & 0 \\ & \ddots & 0 \\ & & \{C_{G_L}^k\} \end{bmatrix} \begin{Bmatrix} \{\delta p^1\} \\ \vdots \\ \{\delta p^k\} \end{Bmatrix} \tag{3.82}$$
$$= \begin{bmatrix} N \end{bmatrix} \begin{bmatrix} C_{G_L} \end{bmatrix} \begin{Bmatrix} \delta p \end{Bmatrix}$$

$$\{\delta K_S^h\} = \begin{bmatrix} N_1 & \cdots & N_k \end{bmatrix} \begin{bmatrix} \{C_{K_S}^1\} & 0 & 0 \\ & \ddots & 0 \\ & & \{C_{K_S}^k\} \end{bmatrix} \begin{Bmatrix} \{\delta p^1\} \\ \vdots \\ \{\delta p^k\} \end{Bmatrix} \tag{3.83}$$
$$= \begin{bmatrix} N \end{bmatrix} \begin{bmatrix} C_{K_S} \end{bmatrix} \begin{Bmatrix} \delta p \end{Bmatrix}$$

$$\begin{aligned}\{\delta K_L^h\} &= \begin{bmatrix} N_1 & \cdots & N_k \end{bmatrix} \begin{bmatrix} \{C_{K_L}^1\} & 0 & 0 \\ & \ddots & 0 \\ & & \{C_{K_L}^k\} \end{bmatrix} \begin{Bmatrix} \{\delta p^1\} \\ \vdots \\ \{\delta p^k\} \end{Bmatrix} \\ &= \begin{bmatrix} N \end{bmatrix} [C_{K_L}] \{\delta p\}\end{aligned} \tag{3.84}$$

Here, $[C_{G_S}]$ is the element shear storage moduli matrix of coefficient vectors, $[C_{G_L}]$ is the element shear loss moduli matrix of coefficient vectors, $[C_{K_S}]$ is the element bulk storage moduli matrix of coefficient vectors$[C_{K_L}]$ is the element bulk loss moduli matrix of coefficient vectors, and $\{\delta p\}$ is the variation of the vector of design variables.

The discretized gradient of the complex shear and bulk modulus are defined as

$$\nabla G^h = \nabla\{G^h\} = [\hat{B}]\{G_S\} + i[\hat{B}]\{G_L\} \tag{3.85}$$

$$\nabla K^h = \nabla\{K^h\} = [\hat{B}]\{K_S\} + i[\hat{B}]\{K_L\} \tag{3.86}$$

Similarly, the discretized gradient of dG^h and dK^h are defined as

$$\nabla \delta G^h = \nabla\{\delta G^h\} = [\hat{B}]\,[C_G]\,\{\delta p\} \tag{3.87}$$

$$\nabla \delta K^h = \nabla\{\delta K^h\} = [\hat{B}]\,[C_K]\,\{\delta p\} \tag{3.88}$$

In the preceding equations, the matrices $[C_G]$, $[C_K]$, and $[\hat{B}]$ are defined as follows

$$[C_G] = [C_{G_S}] + i\,[C_{G_L}] \tag{3.89}$$

$$[C_K] = [C_{K_S}] + i\,[C_{K_L}] \tag{3.90}$$

$$[\hat{B}] = \begin{bmatrix} B_1^1 & & B_1^k \\ B_2^1 & \cdots & B_2^k \\ B_3^1 & & B_3^k \end{bmatrix} \tag{3.91}$$

Substituting the respective discretized quantities into (3.34) yields

$$\begin{aligned} \nabla\{\hat{J}\}\cdot\{\delta p\} &= \sum_{j=1}^{freq} \Re\left[\sum_{elements}\int_{\Omega^e} \{\hat{\boldsymbol{\epsilon}}^h\}^T\Big(\Big(2[\hat{B}]\,[C_G]\,[D_G] + [\hat{B}]\,[C_K]\,[D_K]\Big)\{\boldsymbol{\epsilon}^h\}\Big)^* d\Omega^e\right]\cdot\{\delta p\} \\ &+ \sum_{j=1}^{freq} \Re\left[\beta\sum_{elements}\int_{\Omega^e}\left(|\nabla\{K^h\}|^2+\gamma^2\right)^{\alpha-1}\left(\nabla\{K^h\}^T[\hat{B}]\,[C_K]\right)^* d\Omega^e\right]\cdot\{\delta p\} \\ &+ \sum_{j=1}^{freq} \Re\left[\beta\sum_{elements}\int_{\Omega^e}\left(|\nabla\{G^h\}|^2+\gamma^2\right)^{\alpha-1}\left(\nabla\{G^h\}^T[\hat{B}]\,[C_G]\right)^* d\Omega^e\right]\cdot\{\delta p\} \end{aligned} \tag{3.92}$$

where the discretized gradient equation is given by

$$\begin{aligned} \nabla\{\hat{J}\} &= \sum_{j=1}^{freq} \Re\left[\sum_{elements}\int_{\Omega^e} \{\hat{\boldsymbol{\epsilon}}^h\}^T\Big(\Big(2[\hat{B}]\,[C_G]\,[D_G] + [\hat{B}]\,[C_K]\,[D_K]\Big)\{\boldsymbol{\epsilon}^h\}\Big)^* d\Omega^e\right] \\ &+ \sum_{j=1}^{freq} \Re\left[\beta\sum_{elements}\int_{\Omega^e}\left(|\nabla\{K^h\}|^2+\gamma^2\right)^{\alpha-1}\left(\nabla\{K^h\}^T[\hat{B}]\,[C_K]\right)^* d\Omega^e\right] \\ &+ \sum_{i=1}^{freq} \Re\left[\beta\sum_{elements}\int_{\Omega^e}\left(|\nabla\{G^h\}|^2+\gamma^2\right)^{\alpha-1}\left(\nabla\{G^h\}^T[\hat{B}]\,[C_G]\right)^* d\Omega^e\right] \end{aligned} \tag{3.93}$$

3.3 Results and Discussion

Two simulated experiments were performed to test the potential of the proposed methodology for the inverse characterization of spatially-varying vis-

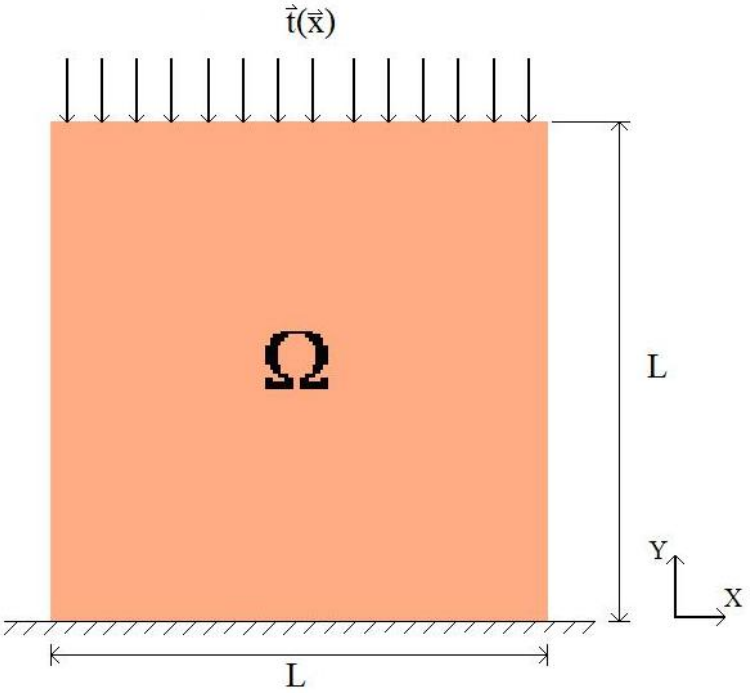

Figure 3.3: Schematic of the example problem used for the simulations

coelastic properties. Each example problems was solved using the optimization strategy described in Section 3.2.4. In the case ultrasound is used, the resolution in the direction perpendicular to the axis of the transducer is poor, and only one component of the displacement field is measured [37]. Thus, it was assumed that only the x_2- component of the displacement field was known. This is the case when the transducer is aligned along the x_2-direction. The measured displacement field was used to solve the inverse problem.

3.3.1 Problem Description

Figure 3.3 shows a pictorial description of the example problem used for the numerical studies. The domain $\Omega = (0, L) \times (0, L)$, where $L = 1\ cm$. On $x_2 = 1$, $t_1 = 0\ Pa$ and $t_2 = 1 + i0\ MPa$; on the $x_2 = 0$, $u_1 = u_2 = 0$, where u_i and t_i

Table 3.1: Viscoelastic Properties for Example With One Inclusion

Material Properties	Background	Inclusion
G_∞	1.0 MPa	4.0 MPa
K_∞	2.0 MPa	5.0 MPa
$\check{G}$	0.2 MPa	0.4 MPa
τ	6×10^{-3}	3×10^{-3}

Table 3.2: Viscoelastic Properties for Example With Two Inclusions

Material Properties	Background	Inclusion 1	Inclusion 2
G_∞	1.0 MPa	2.0 MPa	4.0 MPa
K_∞	2.0 MPa	3.0 MPa	5.0 MPa
$\check{G}$	0.2 MPa	0.3 MPa	0.4 MPa
τ	6×10^{-3}	4×10^{-3}	2×10^{-3}

are components of the displacement and traction vectors $\boldsymbol{u}$ and $\boldsymbol{t}$, respectively. The density of the solid was assumed to be 1000 kg/m^3 and the frequency range considered for the simulations was 5 – 20 Hz in steps of $\triangle_f$ = 5 Hz.

Two example problems were solved to test the proposed methodology. The first example problem consisted of a single stiff inclusion embedded in a soft matrix; the second, consisted of two stiff inclusions embedded in a soft matrix. The experimental displacement field for each example problem was generated by solving one linear viscoelastic finite element problem using the benchmark properties shown in Table 3.1 and Table 3.2.

Gaussian noise was added to both responses to explore the tolerance to im-

Table 3.3: Choice of the Regularization Parameters

Noise, $\triangle_n$	0%	5%	10%
Regularization parameter, β	1×10^{-9}	5×10^{-9}	1×10^{-8}
Regularization parameter, γ	1×10^{-4}	1×10^{-4}	1×10^{-4}

perfect data. Two levels of Gaussian noise were considered for the example problems, $\triangle_n = 10$ and 5%, and were added as

$$\boldsymbol{u}_j^n = \boldsymbol{u}_j \left(1 + \frac{\triangle_n}{100}\right) \tag{3.94}$$

where $\boldsymbol{u}_j^n$ is the j-th frequency displacement field with noise and $\boldsymbol{u}_j$ is the corresponding displacement field without noise.

The efficiency of the proposed methodology was quantified by calculating the equivalent shear modulus and bulk modulus reconstruction error. This error was defined as

$$e = \frac{|q_{target} - q_{appx.}|_2}{|q_{target}|_2} \tag{3.95}$$

where q_{target} is the target quantity (i.e. equivalent shear modulus or bulk modulus), $q_{appx.}$ is the reconstructed quantity.

3.3.2 Regularization

TV regularization was preferred over Tikhonov regularization because of its ability to produce qualitatively correct reconstruction of functions that are

nearly piecewise constant with jump discontinuities, and the length of the curves on which the discontinuities occur is relatively small [29, 116]. By replacing the smoothing norm $|\cdot|_{L_2}$ with the norm $|\cdot|_{L_1}$, large values of partial derivatives typically found near edges and discontinuities are allowed. Consequently, images with better defined edges can be reconstructed [56]. However, this change in smoothing norm can lead to difficulties due to nondifferentiability of the $|\cdot|_{L_1}$ norm at the origin. To avoid this difficulty, $|\cdot|_{L_1} \approx \sqrt{|\cdot|_2^2 + \gamma}$, where γ is a small positive parameter.

Although various methods have been developed for the optimal selection of the regularization parameters (e.g. Discrepancy principle, L-curve, and Generalized cross validation method); the regularization parameters β and γ were selected through numerical experiments. The values selected for each regularization parameters in this study are posted in Table 3.3. For more details on the theory of regularization and the appropriate methods and criteria to select the optimal regularization parameters, the reader is referred to [56] and [116].

3.3.3 Example Problems

The finite element models used for the inverse problem were built using a 60×60 finite element mesh with fully integrated eight-node biquadratic elements. A plane strain condition was assumed to reduced computational demand. To avoid an inverse crime, the finite element models used to generate the experimental data were built using a 80×80 finite element mesh with fully integrated eight-node biquadratic elements.

For simplification, the number of Maxwell elements was fixed a priori. In all

Table 3.4: Design Variables Upper and Lower Bounds for Example Problems with One Inclusion

Design Variable	Lower Bound	Upper Bound
G_∞	0.9 MPa	10.0 MPa
K_∞	1.0 MPa	10.0 MPa
$\check{G}$	0.1 MPa	1.0 MPa
τ	1×10^{-3} sec	1×10^{-2} sec

the example problems, one Maxwell element was used to construct the benchmark solution and for the inverse problem. Furthermore, the bulk viscous effects were assumed negligible. Therefore, the design variables to be identified per node were the long-term shear moduli (G_∞), the long-term bulk moduli (K_∞), the viscous shear modulus $\left(\check{G}\right)$, and the relaxation time (τ), for a total of 44164 design parameters.

In all the example problems, the maximum number of iterations to solve the minimization problem was set to 3000. In quasi-Newton optimization algorithms, such as BFGS, within each iteration several sub-iterations may be made to the routine to evaluate the cost function and compute the gradient. In each sub-iteration the state and adjoint equations are solved in order to compute the gradient. The number of sub-iterations was set to 5 for all example problems. Table 3.4 shows the upper and lower bounds considered for each design variable.

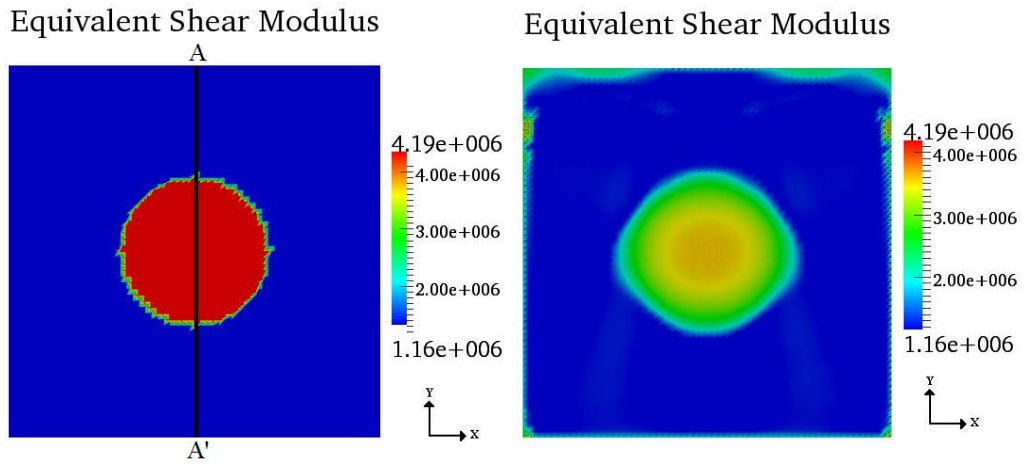

(a) Benchmark Solution (b) 0% Noise

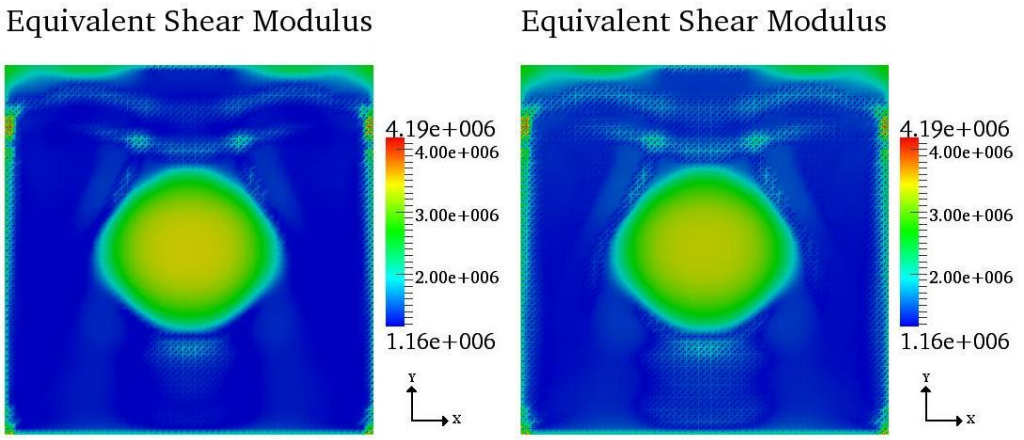

(c) 5% Noise (d) 10% Noise

Figure 3.4: Equivalent shear modulus spatial distribution for example problem with one inclusion and $f = 5\ Hz$

Example Problem with One Inclusion

The initial guess for the example problems with one inclusion was $G_\infty = 2.0\ MPa$, $K_\infty = 3.0\ MPa$, $\check{G} = 0.2\ MPa$, and $\tau = 5.0 \times 10^{-2}\ sec$. Figures 3.4 and 3.5 show the benchmark solution and three inverse solutions for the equivalent shear modulus and the bulk modulus, respectively. These inverse solutions correspond to three perturbation cases, $\triangle_n = 0\%, 5\%$, and 10%. The plots show that the location and geometry of the inclusion was recovered accurately for each

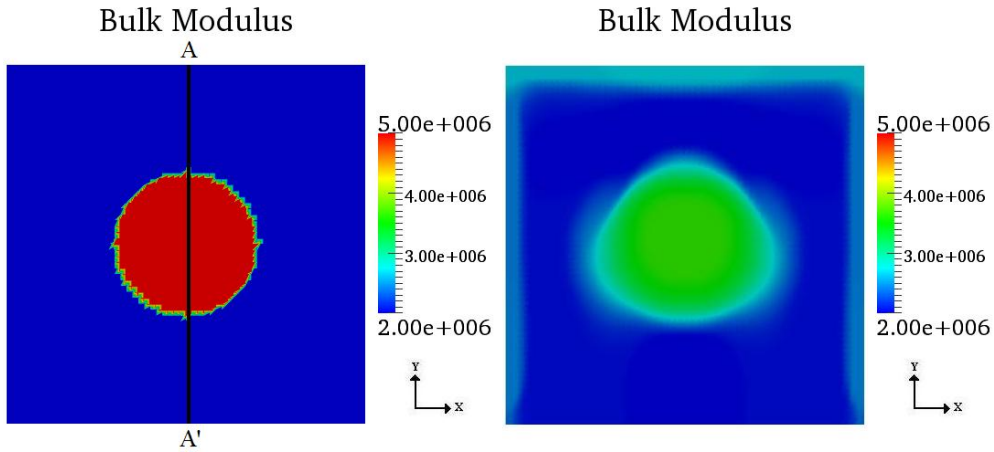

(a) Benchmark Solution

(b) 0% Noise

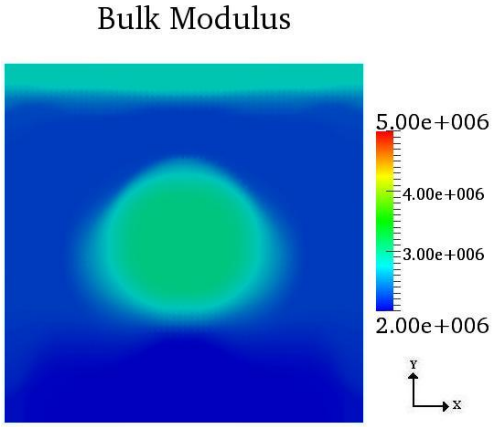

(c) 5% Noise

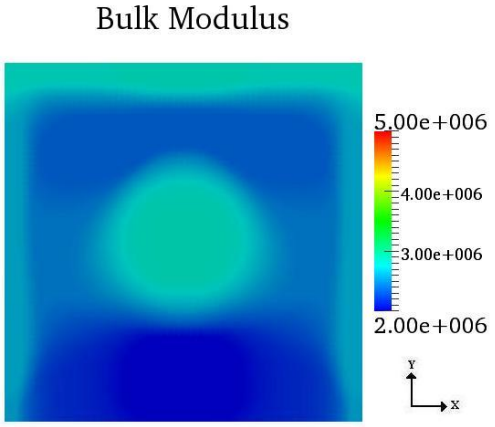

(d) 10% Noise

Figure 3.5: Bulk modulus spatial distribution for example problem with one inclusions

Table 3.5: G_{eq} and K_{∞} Reconstruction Error for Example Problem With One Inclusion for $f = 5Hz$

Noise, $\triangle_n$	G_{eq} (e) (%)	K_{∞} (e) (%)
0%	23.18	25.87
5%	28.08	26.99
10%	30.56	32.70

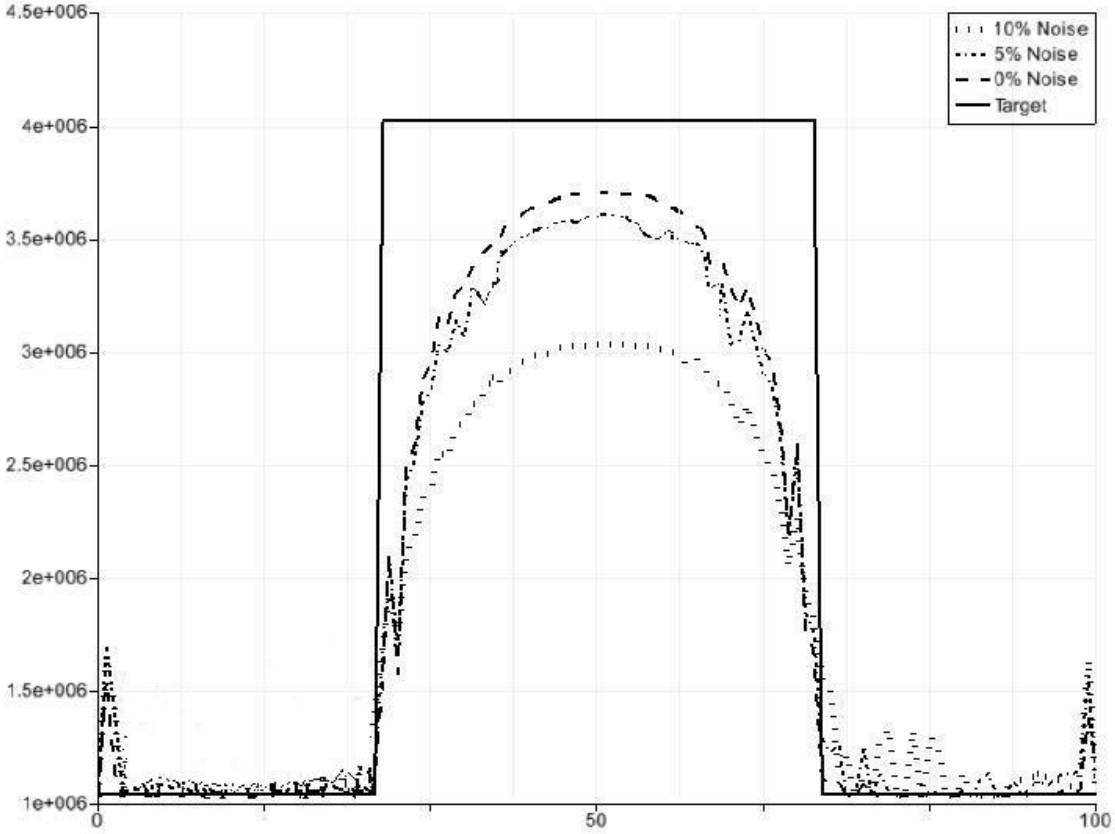

Figure 3.6: Equivalent shear modulus along line A-A′ for $f = 5\ Hz$ and $\triangle_n = 0\%, 5\%$, and 10%

case. However, the accuracy of the magnitude of the equivalent shear modulus and bulk modulus is less accurate. The reconstruction errors reported in Table 3.5 support this remark. However, the interpretation of the reconstruction errors is not trivial and may be deceiving. Notice that the quality of the inverse solution may be judged based on three main factors: accuracy in reconstructing the geometry of the inclusion, accuracy in identifying the location of the inclusion, and the accuracy of the magnitude of the modulus (i.e. equivalent shear modulus and bulk modulus). These criteria cannot be clearly discerned from the reconstruction errors. Hence, the quality of the reconstruction is best appreciated from the plots of the solutions.

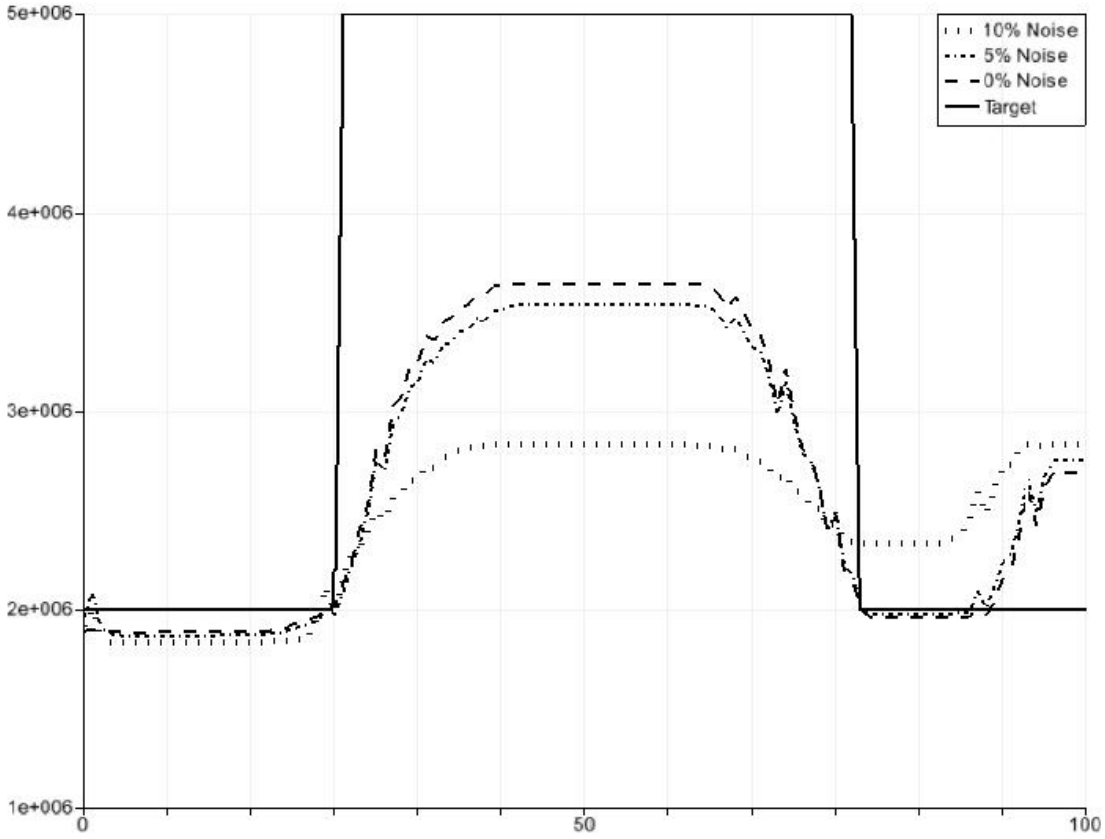

Figure 3.7: Bulk modulus along line A-A′ for $\triangle_n = 0\%, 5\%$, and 10%

Figures 3.6 and 3.7 show the equivalent shear modulus and the bulk modulus along the line A-A′ for $f = 5\ Hz$ and $\triangle_n = 0\%, 5\%$, and 10%. The plots show a decrease in the quality of the reconstruction as the perturbation in the experimental data increased. Notice that the regularization parameters were chosen through numerical experiments; hence, these are not the optimal values and too much emphasis is being put on the regularization term. By doing this, the inverse solution is smoothed, resulting in lower magnitudes for the reconstructed fields (i.e. higher reconstruction errors). Moreover, the reconstruction errors shown in Table 3.5 indicate that the material is less sensitive to volume changes than to shape changes. This reduces the quality of the reconstruction

for the bulk modulus, resulting in higher errors.

Figures 3.8–3.10 show the equivalent shear modulus for different frequencies and $\triangle_n = 0\%, 5\%$, and 10%. The location and geometry of the inclusion was accurately reconstructed for each frequency despite the increase in reconstruction error as the perturbation in the experimental data increased (see Table 3.5). Figure 3.11 and Figure 3.12 show the equivalent shear modulus and the dissipation factor frequency spectrum, respectively. These plots show that the G_{eq} and $\tan(\delta)$ frequency spectrum were closer to the benchmark solution inside the soft matrix than inside the inclusion. This can be attributed to the non-convexity of the least-square error functional, given that the inverse solution becomes sensitive to parameter initialization. The design variables initial guess was closer to the benchmark values of the soft matrix than of the inclusion, which resulted in more accurate results inside the soft matrix. Indeed, when the initial guess was closer to the benchmark solution of the inclusion, the quality of the reconstruction inside the inclusion improved and deteriorated in the soft matrix.

Example Problem with Two Inclusions

The initial guess for the example problems with one inclusion was $G_\infty = 1.5\ MPa$, $K_\infty = 2.5\ MPa$, $\check{G} = 0.25\ MPa$, and $\tau = 5.0 \times 10^{-2}\ sec$. Figures 3.13 and 3.14 show the benchmark solution and three inverse solutions for the equivalent shear modulus and the bulk modulus, respectively. These inverse solutions correspond to three perturbation cases, $\triangle_n = 0\%, 5\%$, and 10%. The plots show that the location and geometry of the inclusions were recovered accurately for each case. However, similar to the example problem with one inclusion, the accuracy of the magnitude of the equivalent shear modulus and bulk modulus

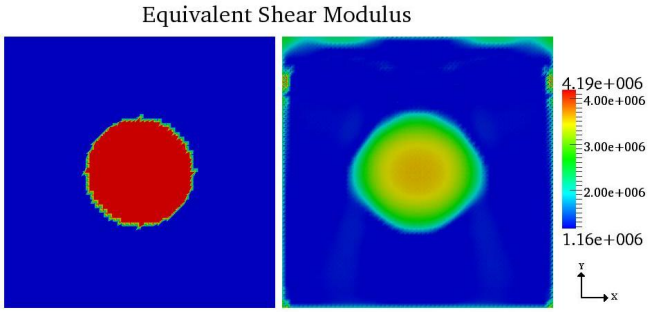

(a) 5 Hz

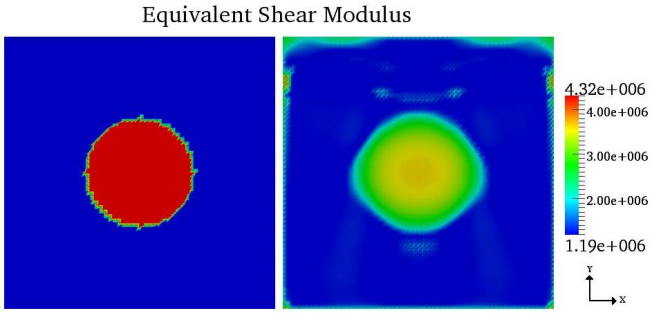

(b) 10 Hz

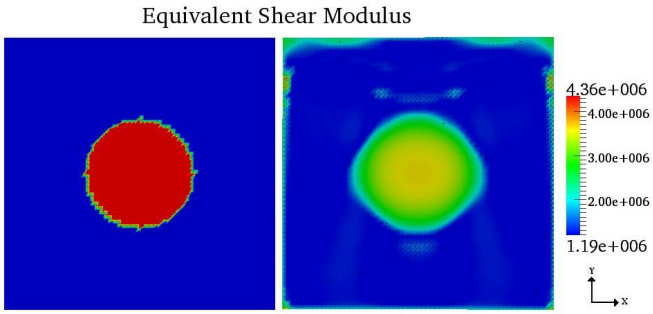

(c) 15 Hz

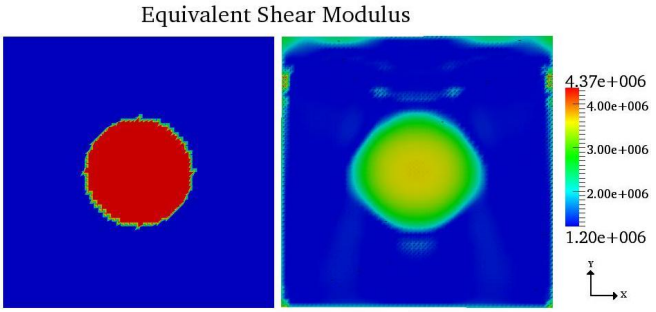

(d) 20 Hz

Figure 3.8: Equivalent shear modulus for example problem with one inclusion and $\triangle_n = 0\%$

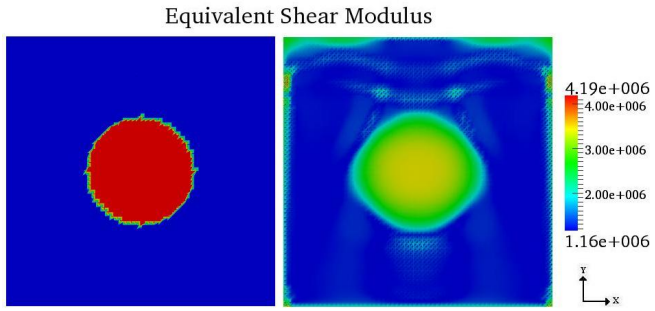

(a) 5 Hz

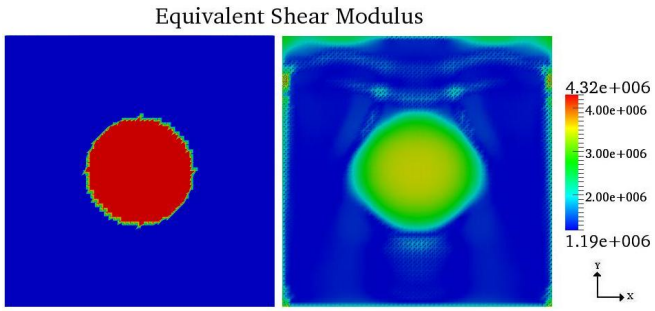

(b) 10 Hz

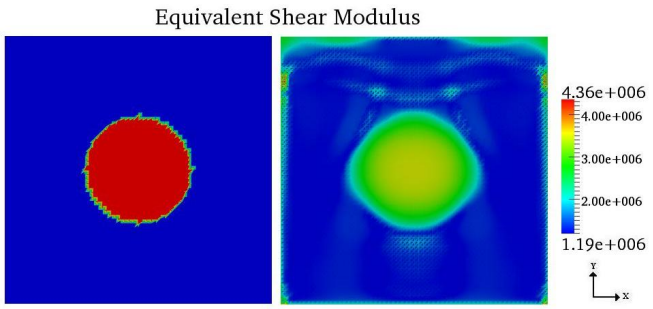

(c) 15 Hz

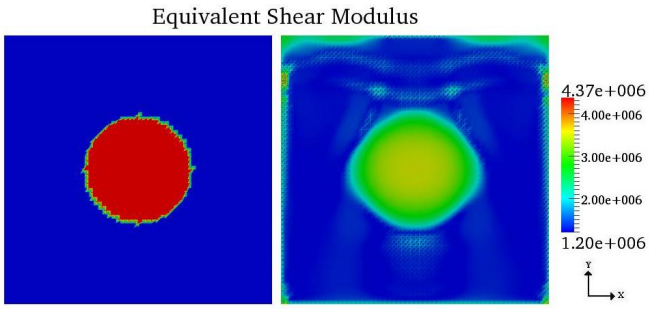

(d) 20 Hz

Figure 3.9: Equivalent shear modulus for example problem with one inclusion and $\triangle_n = 5\%$

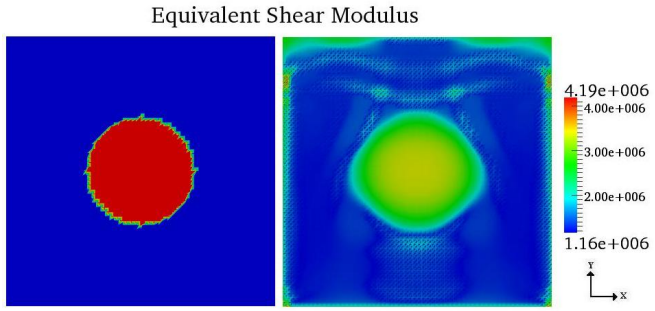

(a) 5 Hz

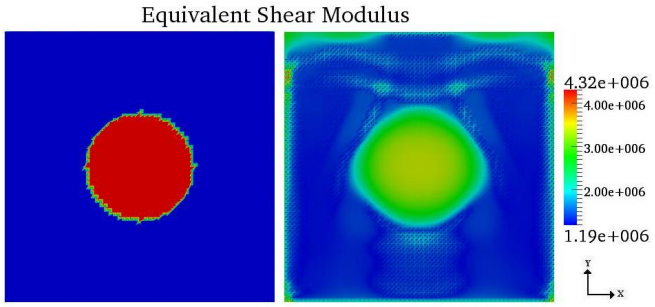

(b) 10 Hz

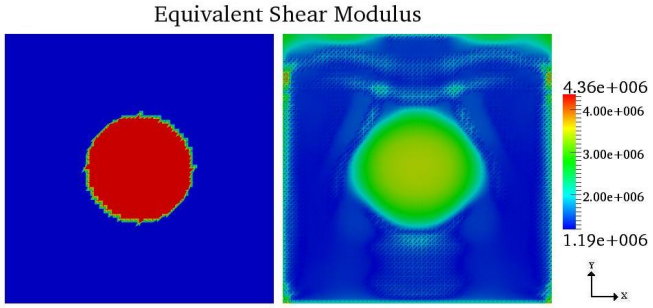

(c) 15 Hz

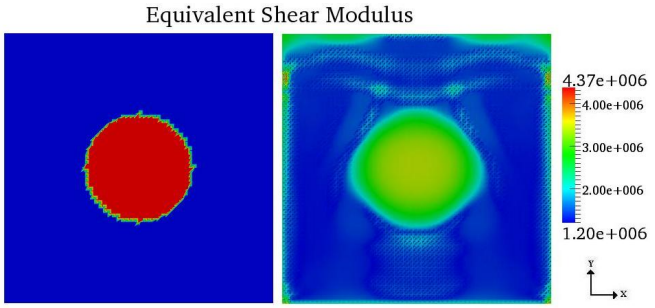

(d) 20 Hz

Figure 3.10: Equivalent shear modulus for example problem with one inclusion and $\triangle_n$ = 10%

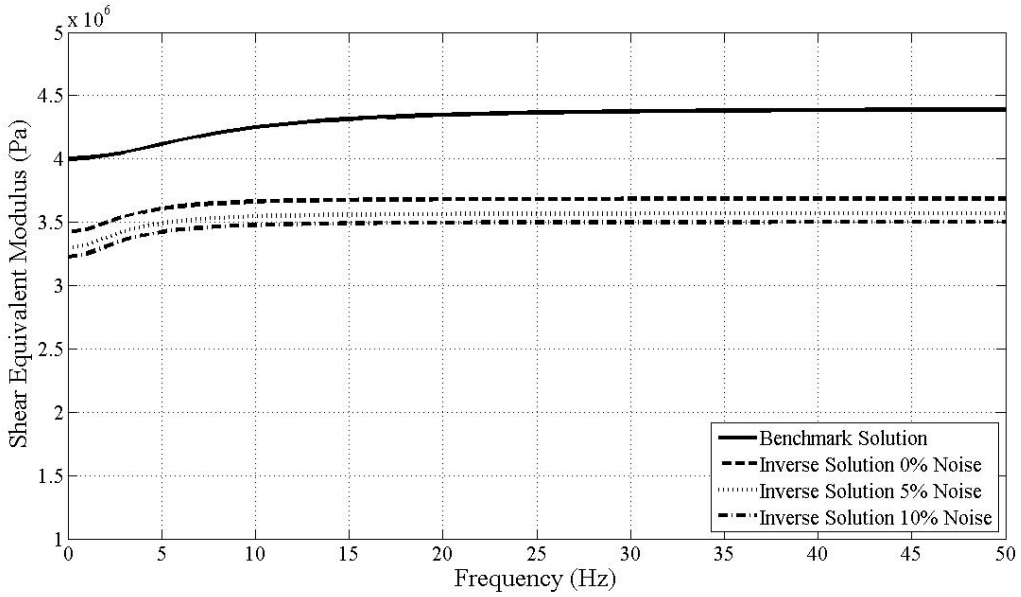

(a) *Position*: $x = 0.5, y = 0.5$

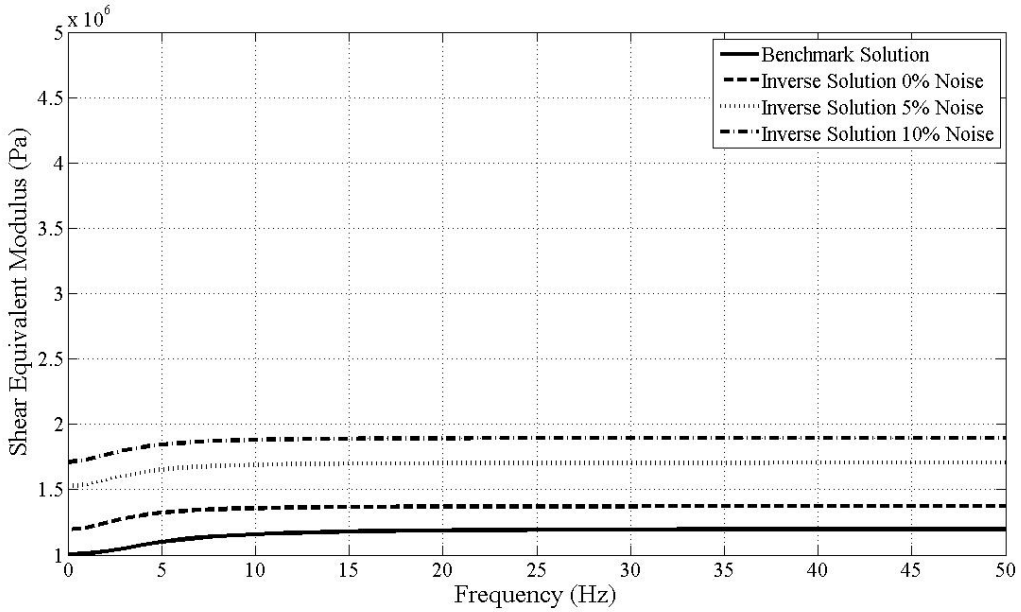

(b) *Position*: $x = 0.5, y = 0.25$

Figure 3.11: Equivalent shear modulus frequency spectrum for example problem with one inclusion at a point inside the: (a) inclusion and (b) background material.

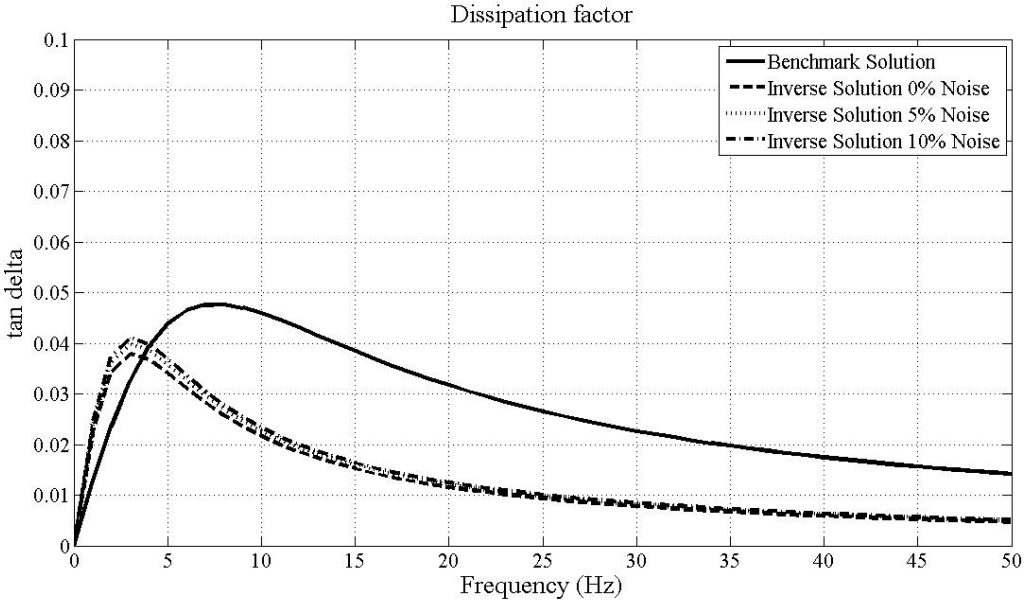

(a) *Position*: $x = 0.5, y = 0.5$

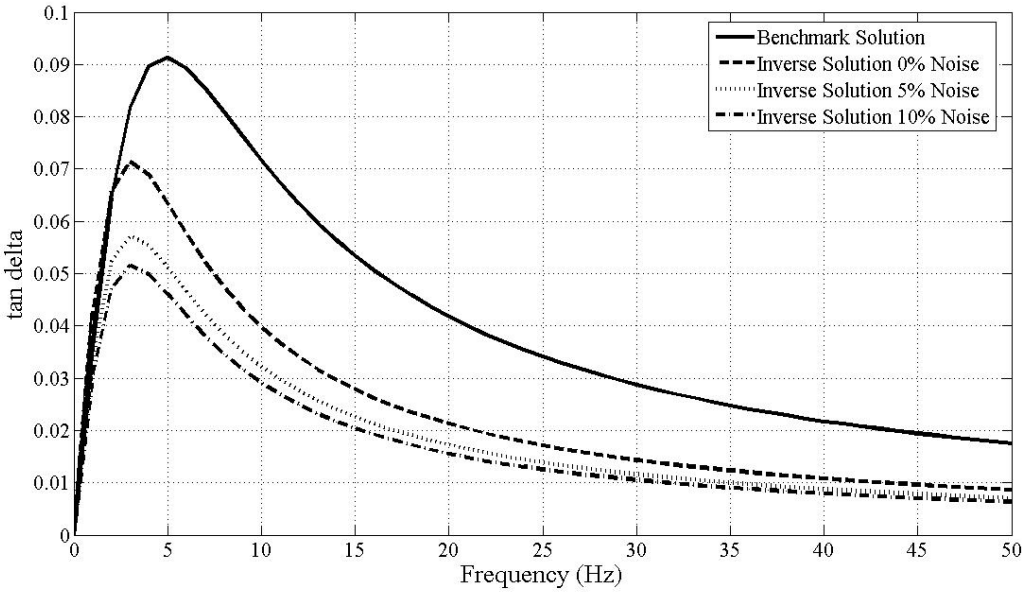

(b) *Position*: $x = 0.5, y = 0.25$

Figure 3.12: Dissipation factor frequency spectrum for example problem with one inclusion at a point inside the: (a) inclusion and (b) background material.

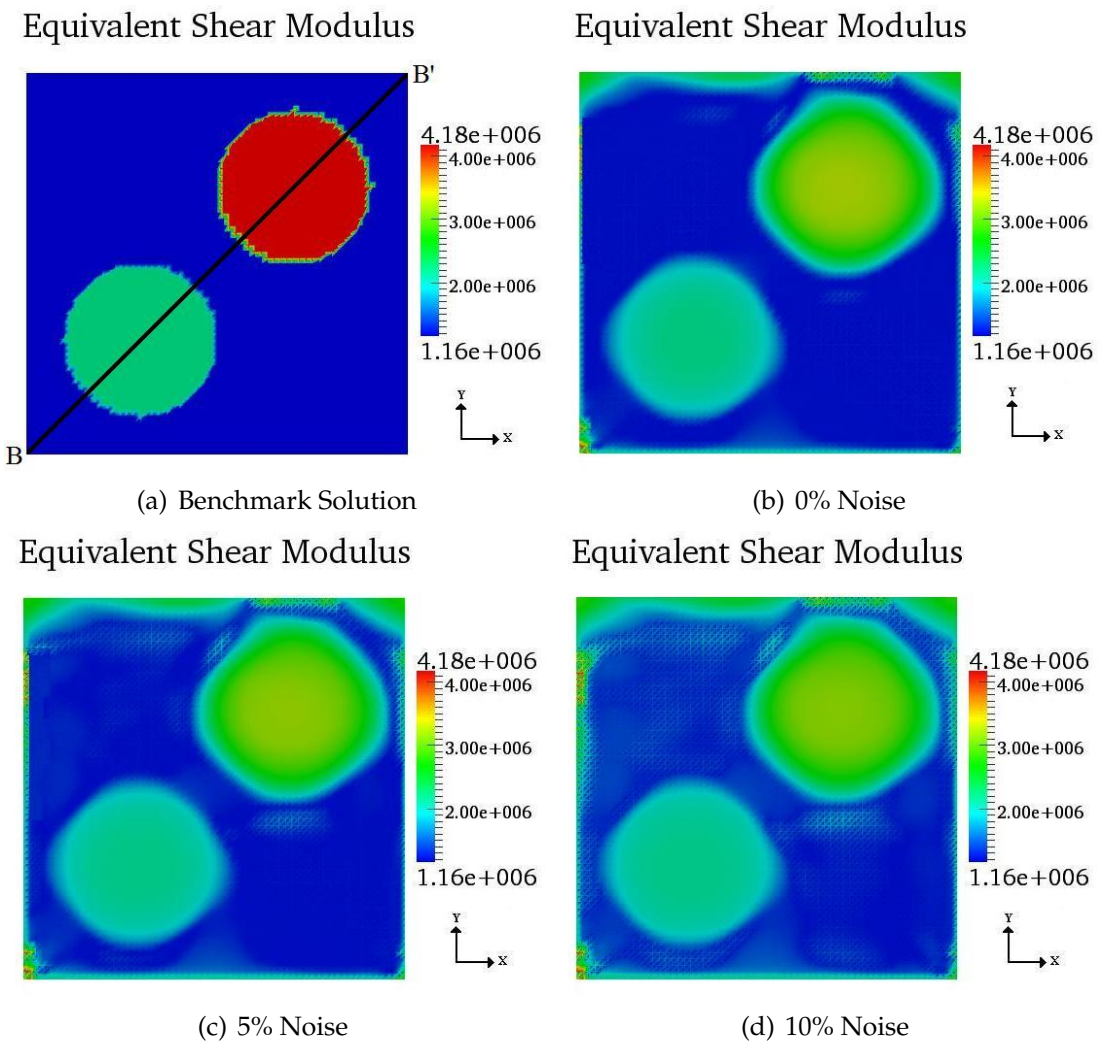

(a) Benchmark Solution

(b) 0% Noise

(c) 5% Noise

(d) 10% Noise

Figure 3.13: Equivalent shear modulus spatial distribution for example problem with two inclusions and $f = 5\ Hz$

is less accurate. The reconstruction errors reported in Table 3.6 support this remark. Furthermore, the reconstruction errors shown in Table 3.6 indicate that the reconstruction for the spatially-varying equivalent shear modulus is better than for the bulk modulus. These results reinforces the previous finding that the material is less sensitive to volume than to shape changes.

Figures 3.16 and 3.15 show the equivalent shear modulus and the bulk modulus along the line B-B′ for $f = 5\ Hz$ and $\triangle_n = 0\%, 5\%$, and 10%. The plots show

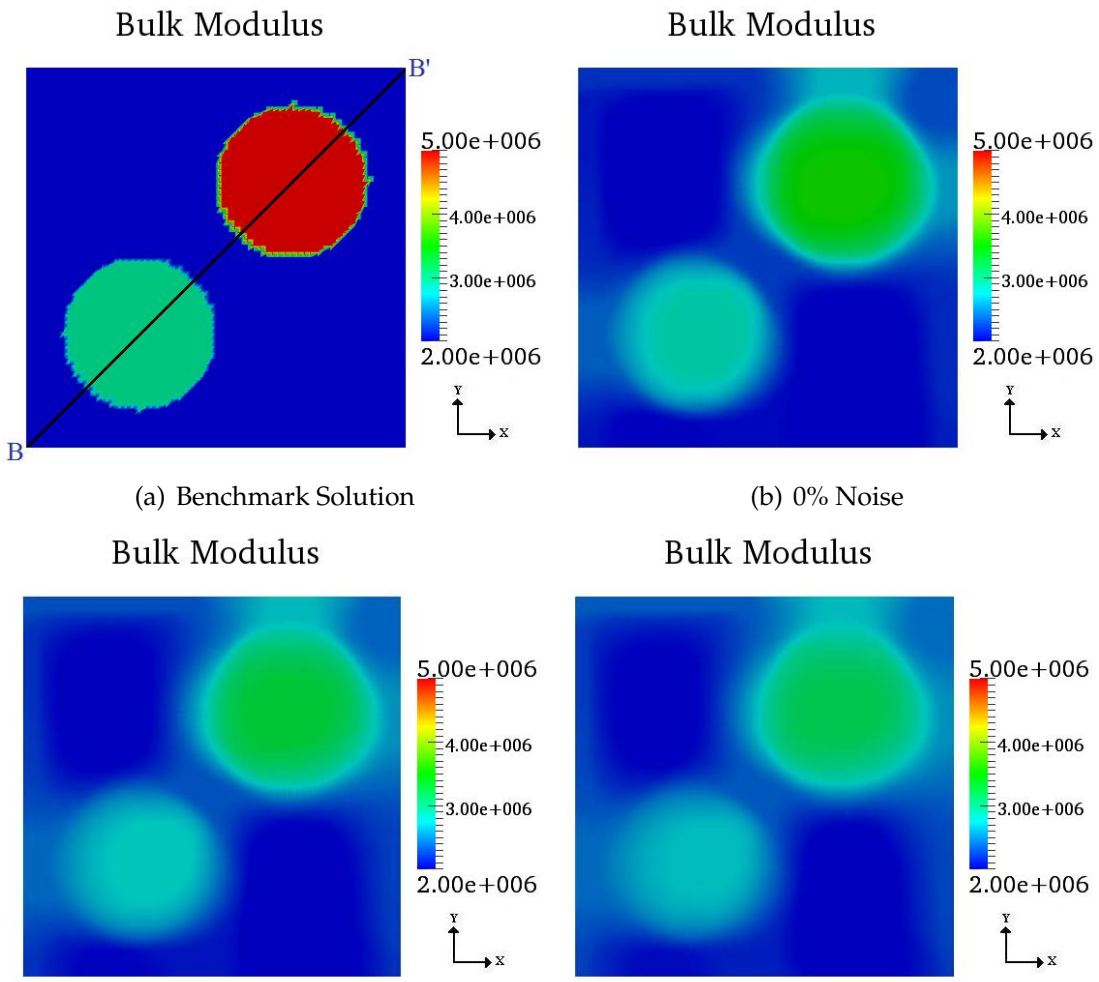

(a) Benchmark Solution (b) 0% Noise

(c) 5% Noise (d) 10% Noise

Figure 3.14: Bulk modulus spatial distribution for example problem with two inclusions

that as the perturbation in the experimental data increased, the quality of the reconstruction decreased (see Table 3.6). Similar to the example problem with one inclusion, this can be attributed to the increase of the regularization parameter to alleviate the perturbation error.

Figures 3.17–3.19 show the equivalent shear modulus for different frequencies and $\triangle_n = 0\%, 5\%$, and 10%. Even with a more complex distribution of the viscoelastic properties, the methodology successfully located both inclusions

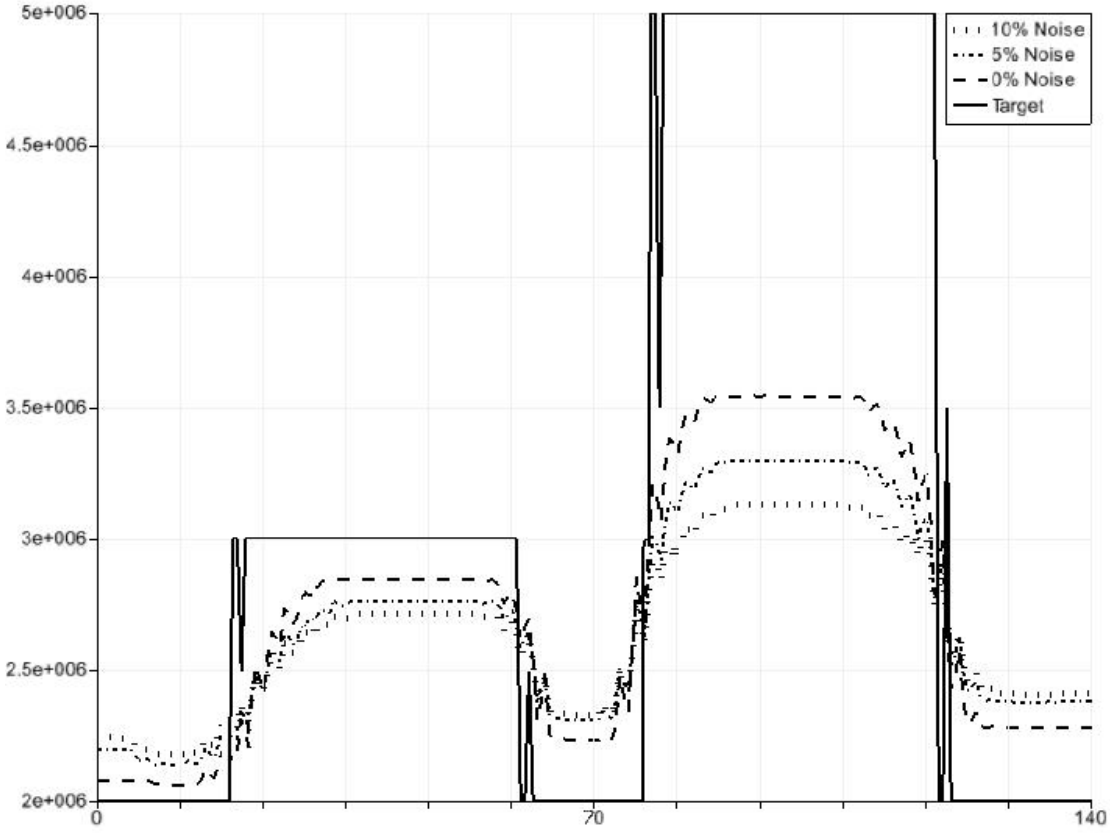

Figure 3.15: Bulk modulus along line B-B′ for $\triangle_n = 0\%, 5\%$, and 10%

and reconstructed each geometry. However, as for the example problem with one inclusion, the magnitude of the equivalent shear modulus and bulk modulus was not recovered with similar accuracy.

Figures 3.20 and 3.21 show the equivalent shear modulus and the dissipation factor, respectively, for a point inside the inclusions and soft matrix. The quality of the reconstruction was superior inside the soft matrix and inclusion than inside the stiff inclusion. Again, the initial guess was closer to the benchmark

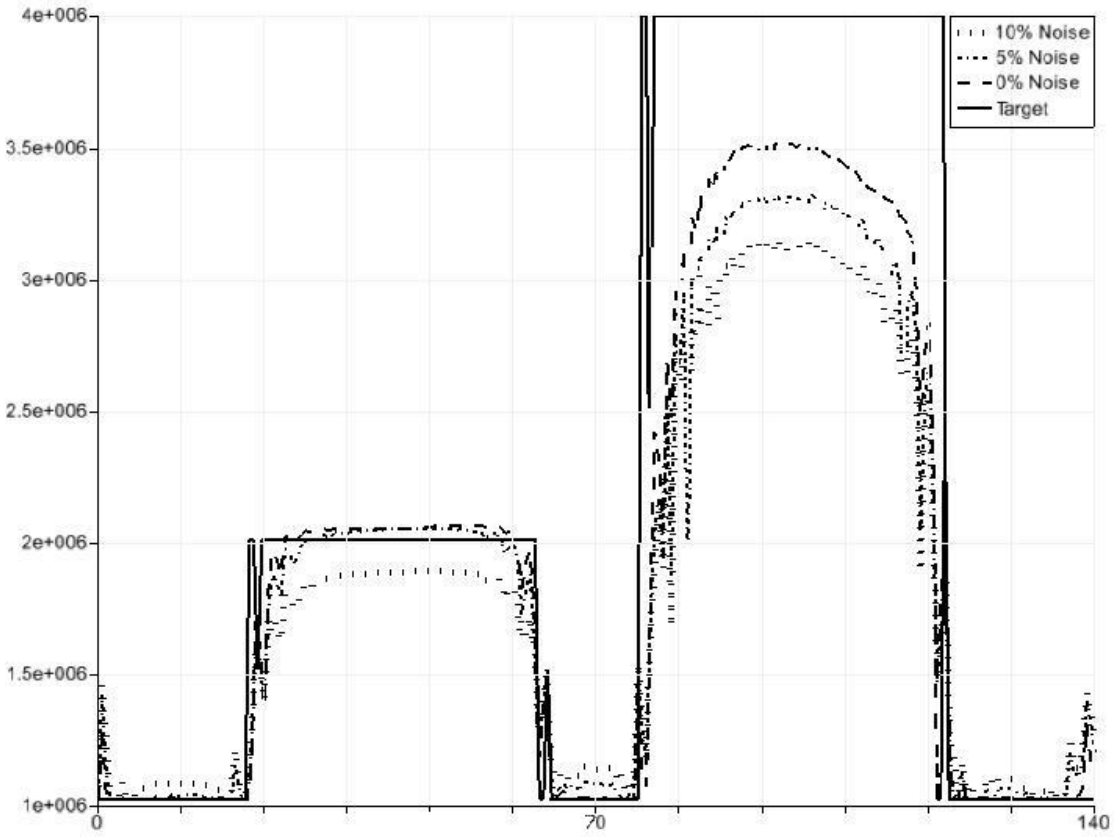

Figure 3.16: Equivalent shear modulus along line B-B′ for $f = 5\ Hz$ and $\triangle_n = 0\%, 5\%$, and 10%

Table 3.6: G_{eq} and K_∞ Reconstruction Error for Example Problem With Two Inclusions for $f = 5Hz$

Noise, $\triangle_n$	G_{eq} (e) $(\%)$	K_∞ (e) $(\%)$
0%	26.72	28.39
5%	28.58	29.74
10%	31.07	32.96

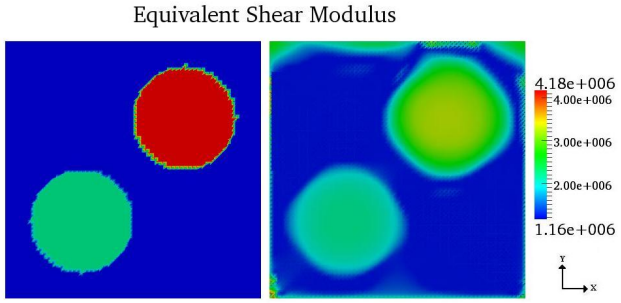

(a) 5 Hz

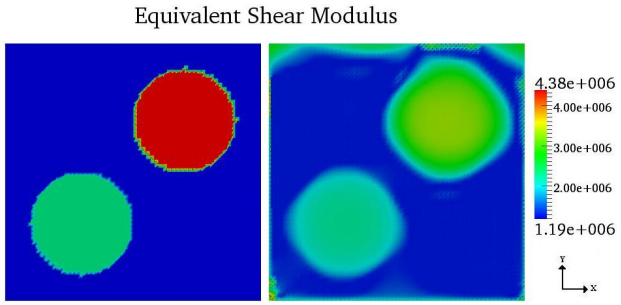

(b) 10 Hz

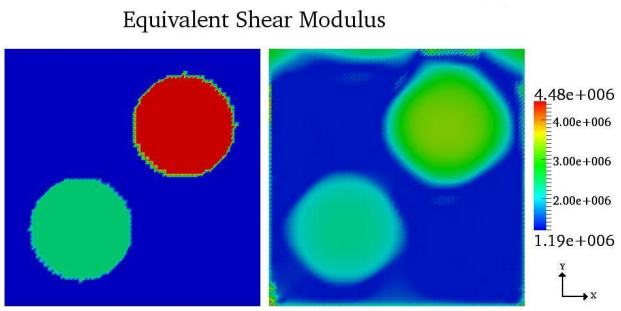

(c) 15 Hz

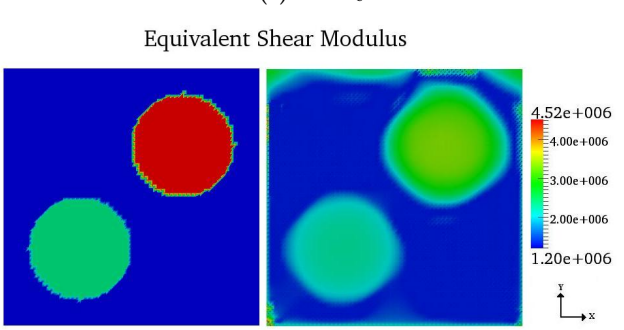

(d) 20 Hz

Figure 3.17: Equivalent shear modulus frequency spectrum for example problem with two inclusions with $\triangle_n = 0\%$

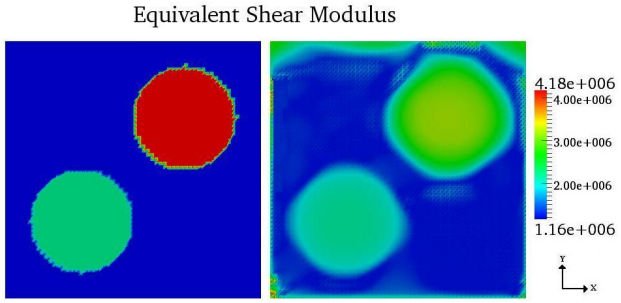

(a) 5 Hz

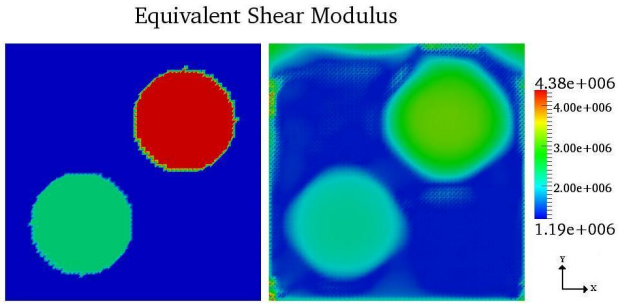

(b) 10 Hz

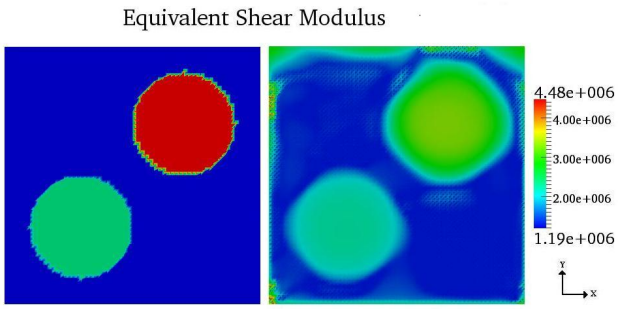

(c) 15 Hz

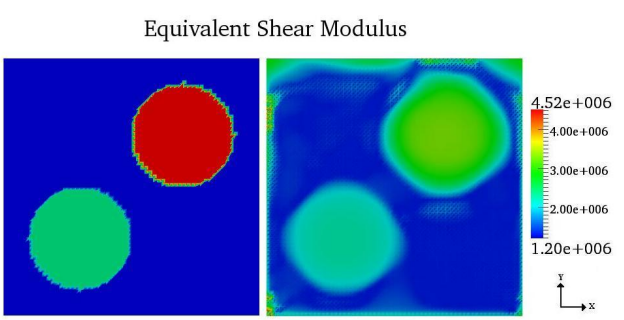

(d) 20 Hz

Figure 3.18: Equivalent shear modulus frequency spectrum for example problem with two inclusions with $\triangle_n = 5\%$

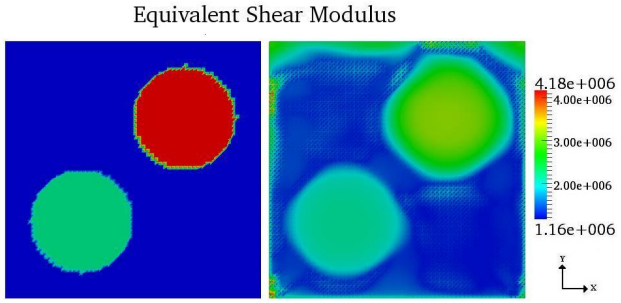

(a) 5 Hz

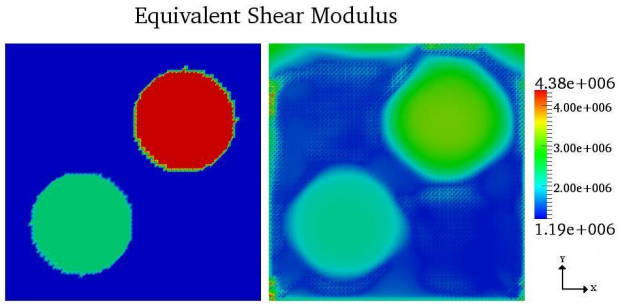

(b) 10 Hz

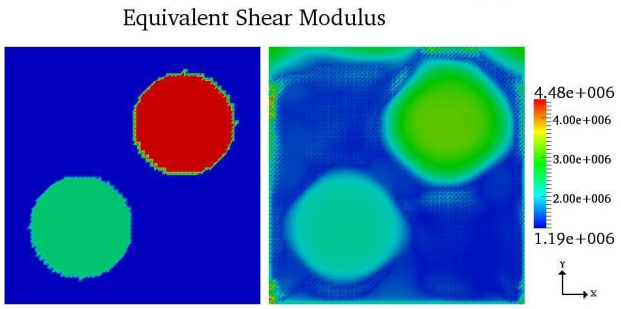

(c) 15 Hz

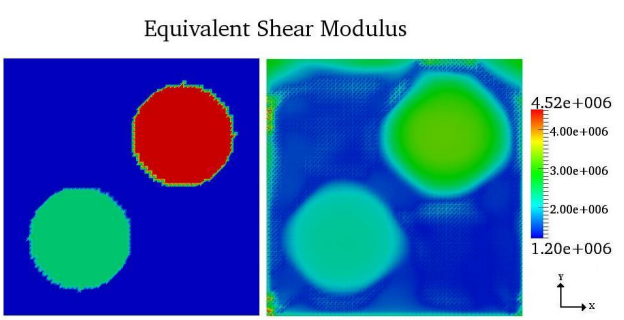

(d) 20 Hz

Figure 3.19: Equivalent shear modulus frequency spectrum for example problem with two inclusions with $\triangle_n = 10\%$

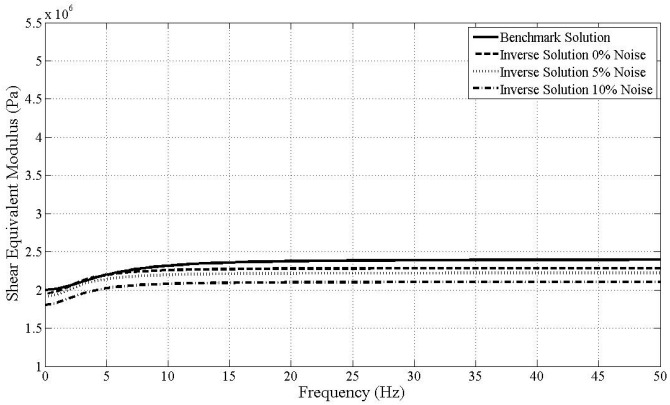

(a) *Position*: $x = 0.3, y = 0.3$

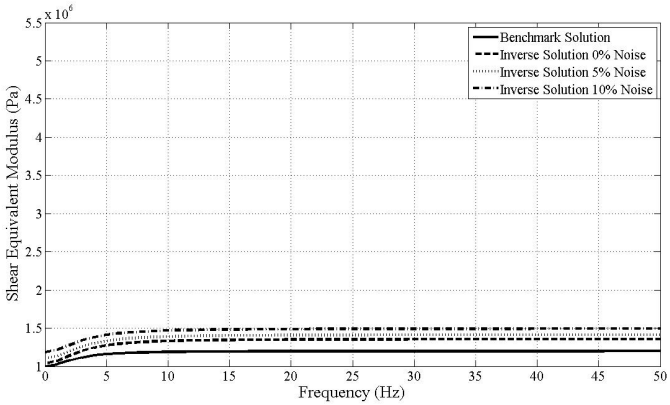

(b) *Position*: $x = 0.5, y = 0.5$

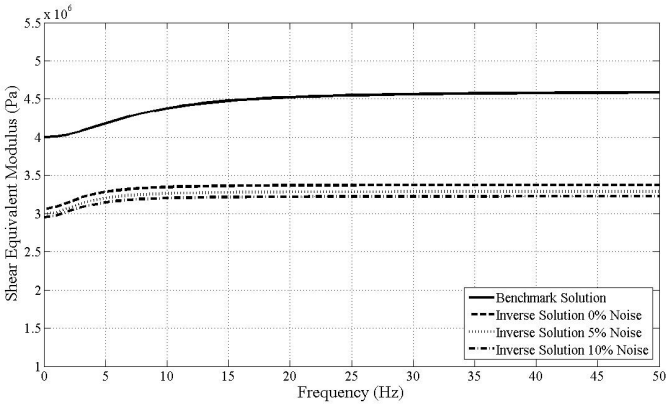

(c) *Position*: $x = 0.7, y = 0.7$

Figure 3.20: Equivalent shear modulus frequency spectrum for example problem with two inclusions at a point inside the: (a) soft inclusion, (b) background material, and (c) hard inclusion.

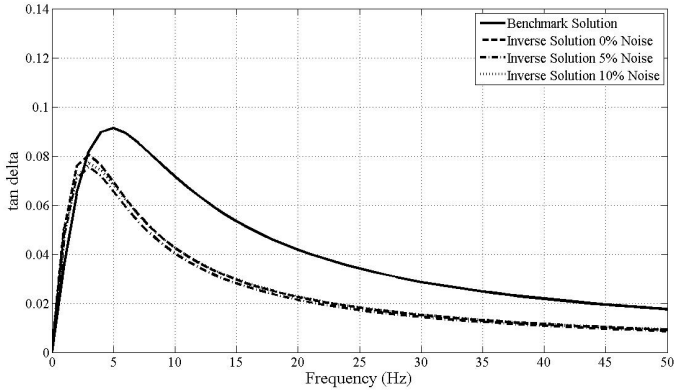

(a) *Position*: $x = 0.3, y = 0.3$

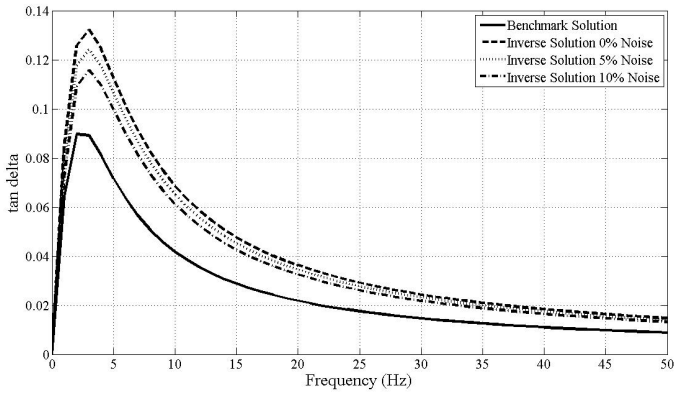

(b) *Position*: $x = 0.5, y = 0.5$

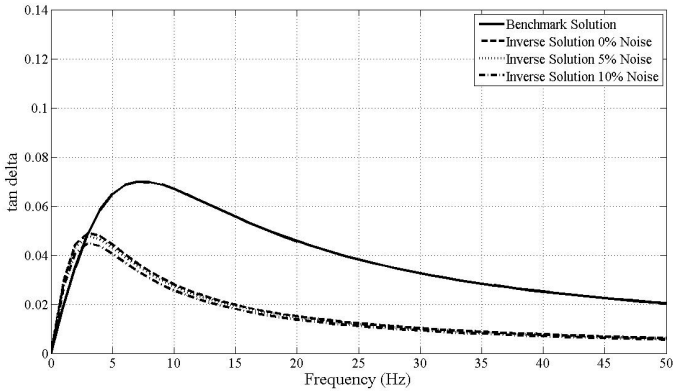

(c) *Position*: $x = 0.7, y = 0.7$

Figure 3.21: Dissipation factor frequency spectrum for example problem with two inclusions at a point inside the: (a) soft inclusion, (b) background material, and (c) hard inclusion.

solution of the softer materials (i.e soft matrix and inclusion) than of the stiff inclusion. Consequently, the quality of the reconstruction is worst inside the stiff inclusion. Moreover, TV regularization tends to penalize larger gradients; thus, the material properties are penalized more inside the stiff inclusion, reducing the quality of the reconstruction. These trends were also observed in other points inside the domain.

Remarks on Results

The quality of the reconstruction could be improved by selecting the optimal regularization parameters. The solution error is the sum of the regularization and the perturbation errors. If the regularization parameter is too small, too much emphasis is put on the experimental data and the solution is influence by the noise in the data. To alleviate the perturbation error, the regularization parameter is increase. If the value of the regularization parameter is too high, too much emphasis is put on the regularization term, thus obtaining a smooth solution with few details [55]. Therefore, in order to reduce the perturbation errors, the regularization parameter was increased. Consequently, the reconstruction quality for the equivalent shear modulus and bulk modulus decreased.

The high reconstruction error for the bulk modulus can be attributed to the loading case and the plane strain assumption. The bulk modulus measures the resistance of an object to hydrostatic pressure and is defined as the pressure increase needed to cause a relative decrease in volume. The example problems used in this chapter are not subjected to hydrostatic pressure. Furthermore, by assuming a plane strain condition, the deformations normal to the plane parallel to the force line of action (e.g. the *x*-*y* plane in the example problems)

are assumed zero, restricting the deformations of the material to two directions (e.g the x and y directions in the example problems). These two factors could reduce the sensitivity of the material to volume changes, resulting in higher reconstruction errors for the bulk modulus.

Other sources of error include the lack of prior information about the original system (i.e. experimental data, geometry, boundary conditions, etc.) and the discretization. For instance, in the present work only one component of the displacement field (i.e. x_2-component) was used for the inverse problem. Therefore, less reliable prior information about the original system was known, which will yield higher reconstruction errors. Furthermore, Dobsony *et al.* [30] observed through numerical studies that the resolution of the reconstruction was affected by the discretization when TV regularization was used. Indeed, it was shown that coarser meshes decreased the resolution of the reconstruction. Therefore, the reconstruction errors in the present chapter could have been higher than expected due to discretization.

Notice that the reconstruction errors for the example problem with two inclusions were higher than for the example problem with one inclusion. A possible explanation is that the equivalent shear modulus and bulk modulus spatial distribution is more complex in the example problem with two inclusions. Therefore, more iterations will be require to minimize the reconstruction error.

3.4 Summary

An inverse approach for the identification of the spatially-varying complex tensor based on the adjoint method was presented. Accurate results were obtained

for perturbation levels up to 10%. However, there was a trade off in accuracy due to the smoothing of the inverse solution, which is correlated to the regularization parameter. Future work will use an effective method to select the optimal regularization parameters. Furthermore, approaches to improve the reconstruction of the bulk modulus will be investigated. For instance, study load cases for which the material is more sensitive to volume changes.

One application of the present work is to use vibroacoustics based techniques for in-vivo characterization of material properties in soft tissue. Then, it is important to test the proposed methodology with data obtained from a physical experiment. Furthermore, the error functional used in this work is non-convex, making the inverse solution sensitive to parameter initialization. In the next chapter, we consider an inverse approach based on the concept of error in the constitutive equation. These error functionals have been shown to be convex for elliptic boundary value problems, which guarantees a solution to the minimization problem.

CHAPTER 4

AN INVERSE APPROACH BASED ON THE CONCEPT OF ERROR IN CONSTITUTIVE EQUATION FOR CHARACTERIZATION OF SPATIALLY-VARYING VISCOELASTIC PROPERTIES IN STEADY-STATE DYNAMICS

4.1 Introduction

In Chapter 3, the L2-adjoint inverse approach for identification of spatially-varying complex moduli was presented. Although the L2-adjoint inverse approach accurately recovered the location and geometry of all the regions with different material properties, the resolution of the reconstruction was poor. In this chapter, an inverse approach based on the concept of error in constitutive equation (ECE) is presented. Through simulated examples it is shown that not only the location and geometry of all the regions with different material properties are accurately recovered; likewise, the quality of the reconstruction is improved.

Multiple methodologies have been proposed in the literature for viscoelasticity imaging; however, these methodologies have disadvantages. For instance, Viola *et al.* [115] developed a methodology for the characterization of spatially-varying viscoelastic properties by using radiation force as a means to produce small, localized displacements within the tissues. Returning echoes are processed using ultrasonic motion tracking so that the response of the tissue to the induced force can be evaluated. By repeating this process at a number of locations, images depicting viscoelastic properties of tissues can be formed. Through the combination of appropriate mechanical modeling and signal pro-

cessing; damping ratio, natural frequency, and relaxation time images are generated. However, this methodology is sensitive to imperfect data and the imaged viscoelastic properties (i.e. damping ratio, natural frequency, and relaxation time) are less intuitive than the storage and loss modulus. Walker *et al.* [117] used a series of focused ultrasonic pulses to generate an acoustic radiation force and process the echoes returned from these pulses to estimate the displacement field as a function of time. This process was repeated at multiple locations to image viscoelastic properties. A one-dimensional Voigt material model was used to characterize the relaxation process at each point in space. The Voigt parameters were characterized by fitting the experimental displacement field and Voigt predicted displacement field. However, this methodology is sensitive to imperfect data and its application for stiffer materials might be limited due to small displacement amplitudes.

An alternate method is to use an inverse approach that combines the finite element method, the concept of error in constitutive equation, and gradient based optimization to identify the spatially-varying viscoelastic properties of solids. The inverse problem is cast as an optimization problem in which an ECE functional, which measures the gap in the constitutive law, is minimized by searching over a space of admissible functions that best describe the spatial distribution of the viscoelastic properties.

The concept of ECE was first introduced in elasticity by Ladevèze *et al.* [73] for error estimation in finite element computations. For instance, Ladevèze *et al.* [75] introduced a posteriori error estimator based on the ECE functional for finite element computations of structures which exhibit plastic/viscoplastic behavior with softening. The concept of ECE has proved to be very fruitful in

solid mechanics, not only in connection with posteriori error estimations for finite element computations [25, 45, 74], but also for parameter identification problems [16, 69, 70, 71]. Ladevèze *et al.* [72] use the concept of ECE to update the mass stiffness and damping properties through an iterative process in which the most erroneous regions were localized first using an ECE functional, and then the material parameters were corrected in these regions.

Gockenbach *et al.* [52, 48] used a coefficient (i.e. constitutive parameter) dependent energy norm, similar to the ECE functional, for the identification of constitutive parameters of elliptic boundary value problems when interior data is available. Furthermore, Gockenbach *et al.* [50, 51] showed that for elliptic boundary value problems the coefficient dependent energy norm is convex. This property guarantees that the minimization problem has a solution; thus, the coefficient dependent energy norm is useful for minimization problems involving the identification of spatially-varying material properties. The ECE functional used in the present work resembles the coefficient dependent energy norm used in [47, 50, 51, 52, 48, 49]. Likewise, the convexity properties of the ECE functionals have been studied extensively in [68, 70, 71].

This chapter is outlined as follows. In Section II, the inverse problem formulation is introduced as well as the concept of error in constitutive equation. In Section III, the example problems used to test the propose methodology are described and the results are discussed. Conclusions and future directions are given at the end of this chapter.

4.2 Formulation

The reader is referred to Chapter 3 for the description of the preliminaries and the strong and weak formulations.

4.2.1 Inverse Problem

An optimization approach based on the concept of error in constitutive equations was used for the identification of the spatially-varying complex tensor through the measured steady-state system response. The minimization strategy consists of two steps; first, the kinematically admissible strain and dynamically admissible stress fields are computed and the error in the constitutive law is quantified. In the second step, the error in the constitutive law is corrected by solving a minimization problem in which the ECE functional is minimized with respect to the spatially-varying complex tensor $\mathbb{C}$.

Error in the Constitutive Equation Inverse Approach

The principle of error in the constitutive equation is meant to define a set of admissible fields $(\boldsymbol{u}_D, \boldsymbol{\sigma}_N)$ which minimize

$$J(\boldsymbol{u}_D, \boldsymbol{\sigma}_N, \mathbb{C}) = \sum_{i=1}^{freq} \frac{1}{2} \int_\Omega \left[|\boldsymbol{\sigma}_N - \mathbb{C} : \boldsymbol{\epsilon}(\boldsymbol{u}_D)|_2^2 + \frac{\beta}{\alpha} \left(|\nabla \mathbb{C}|_2^2 + \gamma^2 \right)^\alpha \right] d\Omega \tag{4.1}$$

such that $\boldsymbol{u}_D \in \hat{U}$ and $\boldsymbol{\sigma}_N \in \hat{S}$, where

$$U = \{\boldsymbol{u} : \boldsymbol{u} \in H^1(\Omega),\ \boldsymbol{u} = \boldsymbol{u}_0 \text{ on } \Gamma_u\} \tag{4.2}$$

$$S = \{\boldsymbol{\sigma} : \boldsymbol{\sigma} \in L_2(\Omega)\} \tag{4.3}$$

$$\hat{U} = \{\boldsymbol{u}_D : \boldsymbol{u}_D \in H^1(\Omega),\ \boldsymbol{u}_D = \boldsymbol{u}_0 \text{ on } \Gamma_u,\ \boldsymbol{u}_D = \bar{\boldsymbol{u}} \in \bar{\Omega} \subset \Omega \cup \Gamma\} \tag{4.4}$$

$$\hat{S} = \{\boldsymbol{\sigma}_N : \boldsymbol{\sigma}_N \in L_2(\Omega),\ \int_\Omega \left(\nabla \boldsymbol{v}^* : \sigma_N - \rho\omega^2 \boldsymbol{v}^* \cdot \boldsymbol{u}_N\right) d\Omega - \int_{\Gamma_t} \boldsymbol{v}^* \cdot (\boldsymbol{\sigma}_N \boldsymbol{n}_s)\, d\Gamma_t = 0 \text{ in } \Omega\} \tag{4.5}$$

Here $\bar{\Omega}$ is the region in which the experimental displacement field $\bar{\boldsymbol{u}}$ is measured, $\hat{U}$ is the space of kinematically admissible fields $\boldsymbol{u}_D$, and $\hat{S}$ is the space of dynamically admissible fields $\boldsymbol{\sigma}_N$. The regularization parameters β, γ, and α were defined in Chapter 3.

A field $\boldsymbol{u}_D$ is said to be kinematically admissible if it satisfies compatibility conditions and Dirichlet boundary conditions but not necessarily Neumann boundary conditions or the equilibrium equations. A field $\boldsymbol{\sigma}_N$ is said to be dynamically admissible if it satisfies equilibrium equations and Neumann boundary conditions but not compatibility or Dirichlet boundary conditions

The set of admissible fields $(\boldsymbol{u}_D, \boldsymbol{\sigma}_N)$ solve the problem defined in Equation (4.1) if and only if $\boldsymbol{u}_D$ and $\boldsymbol{\sigma}_N$ are related through the constitutive equation defined by Equation (3.6). Therefore, $J(\boldsymbol{u}_D, \boldsymbol{\sigma}_N, \mathbb{C}) = 0$ when the complex tensor is compatible with the material complex tensor. These remarks suggest defining an ECE functional for the identification of the spatially-varying viscoelastic properties.

Identification Approach Based on Alternating Directions

An identification approach based on alternating directions [16, 26, 69] was used in the present work for the identification of the spatially-varying viscoelastic properties. From an initial guess for $\mathbb{C}$, the material properties are computed through the following steps:

i. Compute fields $\boldsymbol{u}_D$ and $\boldsymbol{\sigma}_N$ by solving the following problems with $\mathbb{C} = \mathbb{C}_m$

$$a(\mathbb{C}_m; \boldsymbol{v}, \boldsymbol{u}_D) - \ell(\boldsymbol{v}) = 0 \;\forall\; \boldsymbol{v} \in V,\; \boldsymbol{u}_D \in \hat{U} \tag{4.6}$$

and

$$a(\mathbb{C}_m; \boldsymbol{v}, \boldsymbol{u}_N) - \ell(\boldsymbol{v}) = 0 \;\forall\; \boldsymbol{v} \in V,\; \boldsymbol{u}_N \in \hat{S} \tag{4.7}$$

$$\boldsymbol{u}_N = \boldsymbol{u}_0 \text{ on } \Gamma_u \tag{4.8}$$

Here, V denotes the space of test functions and it is defined by Equation (3.14). The subscript m denotes the iteration number.

ii. Compute the new complex moduli tensor $\mathbb{C}_{m+1}$ from

$$\hat{J}(\mathbb{C}) = \arg \min_{\mathbb{C} \in \Xi} J(\boldsymbol{u}_D, \boldsymbol{\sigma}_N, \mathbb{C}) \quad \text{subject to } \sigma_N \in \hat{S},\; \boldsymbol{u}_D \in \hat{U} \tag{4.9}$$

The space Ξ is given by Equation (3.18). Note that $\hat{J}(\mathbb{C})$ depends on $\mathbb{C}$ explicitly and implicitly through $\boldsymbol{u}_D$ and $\boldsymbol{\sigma}_N$.

The variation of $\hat{J}(\mathbb{C})$ with respect to the complex tensor is given by

$$
\begin{aligned}
D_{\mathbb{C}}\hat{J}(\mathbb{C}) \cdot \delta\mathbb{C} &= \sum_{i=1}^{freq} \int_{\Omega} -(\boldsymbol{\sigma}_N - \mathbb{C} : \boldsymbol{\epsilon}(\boldsymbol{u}_D)) \cdot (\delta\mathbb{C} : \boldsymbol{\epsilon}(\boldsymbol{u}_D))^* \, d\Omega \\
&+ \sum_{i=1}^{freq} \beta \int_{\Omega} \left(|\nabla\mathbb{C}|_2^2 + \gamma^2 \right)^{\alpha-1} (\nabla\mathbb{C} \cdot \nabla\delta\mathbb{C})^* \, d\Omega
\end{aligned}
\tag{4.10}
$$

Calculation of the Gradient

As in Chapter 3, finite-dimensional subspaces associated with the space of admissible fields and the test function space were introduced in order to solve Equations (4.6) and (4.7) numerically using the finite-element method. These spaces are denoted by $\hat{U}^h \subset \hat{U}$, $\hat{S}^h \subset \hat{S}$, and $V^h \subset V$. This leads to the Galerkin approximation: find $\boldsymbol{u}_D^h \in \hat{U}^h$ and $\boldsymbol{u}^h{}_N \in \hat{S}^h$ such that:

$$
a\left(\mathbb{C}_t^h; \boldsymbol{v}^h, \boldsymbol{u}_D^h\right) - \ell\left(\boldsymbol{v}^h\right) = 0 \tag{4.11}
$$

$$
a\left(\mathbb{C}_t^h; \boldsymbol{v}^h, \boldsymbol{u}_N^h\right) - \ell\left(\boldsymbol{v}^h\right) = 0 \tag{4.12}
$$

The fields $\boldsymbol{u}_D^h$, $\boldsymbol{u}_N^h$, $\boldsymbol{v}^h$, and $\mathbb{C}^h$ are represented as a linear combination of continuous, piece-wise finite-element shape functions. For example, $\mathbb{C}^h$ is given by

$$
\mathbb{C}^h = \sum_{j=1}^{n} \mathbb{C}_j \phi_j(\boldsymbol{x}) \tag{4.13}
$$

where n denotes the number of finite element nodes and ϕ_j is a finite element shape function. The same shape functions were used to represent $\boldsymbol{u}^h$, $\boldsymbol{v}^h$, and $\mathbb{C}^h$ in order to reduce the programming requirements.

Let $\mathbb{C}^h$ be represented by Equation (4.26). Then, the variation of the complex moduli is given by

$$\delta\mathbb{C}^h = \sum_{j=1}^{n} \delta\mathbb{C}_j \phi_j(\boldsymbol{x}) \tag{4.14}$$

The Galerkin approximation for $D_{\mathbb{C}}\hat{J}(\mathbb{C}) \cdot \delta\mathbb{C}$ is given by

$$\begin{aligned} D_{\mathbb{C}}\hat{J}\left(\mathbb{C}^h\right) \cdot \delta\mathbb{C}^h &= \sum_{i=1}^{freq} \Re\left[\int_{\Omega} -\left(\boldsymbol{\sigma}_N^h - \mathbb{C}^h : \boldsymbol{\epsilon}_D^h\right) \cdot \left(\phi_j \boldsymbol{\epsilon}_D^h\right)^* \, d\Omega\right] \cdot \delta\mathbb{C}_j \\ &+ \sum_{i=1}^{freq} \Re\left[\beta \int_{\Omega} \left(|\nabla\mathbb{C}^h|_2^2 + \gamma^2\right)^{\alpha-1} \left(\nabla\mathbb{C}^h \cdot \nabla\phi_j\right)^* \, d\Omega\right] \cdot \delta\mathbb{C}_j \end{aligned} \tag{4.15}$$

where the expression to calculate the gradient is given by

$$\begin{aligned} D_{\mathbb{C}}\hat{J}\left(\mathbb{C}^h\right) &= \sum_{i=1}^{freq} \Re\left[\int_{\Omega} -\left(\boldsymbol{\sigma}_N^h - \mathbb{C}^h : \boldsymbol{\epsilon}_D^h\right) \cdot \left(\phi_j \boldsymbol{\epsilon}_D^h\right)^* d\Omega\right] \\ &+ \sum_{i=1}^{freq} \Re\left[\beta \int_{\Omega} \left(|\nabla\mathbb{C}^h|_2^2 + \gamma^2\right)^{\alpha-1} \left(\nabla\mathbb{C}^h \cdot \nabla\phi_j\right)^* d\Omega\right] \end{aligned} \tag{4.16}$$

4.2.2 Algorithm

The following algorithm may be used in each iteration of the minimization process to compute the optimal $\mathbb{C}$. The optimization strategy is divided into the following steps described as follows:

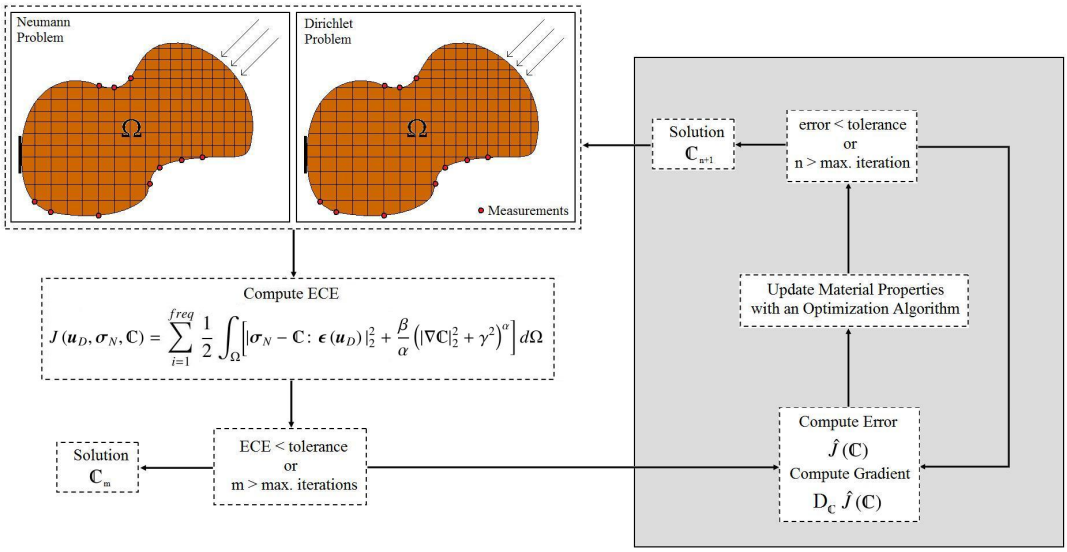

Figure 4.1: Error in constitutive equation inverse problem flowchart

1. Quantify Error in Constitutive Equation

i. Solve Equations (4.11) and (4.12) to evaluate the kinematically and dynamically admissible fields $\boldsymbol{u}_D^h$ and $\boldsymbol{u}_N^h$, respectively.

ii. Evaluate error functional (4.1) and check stopping criteria. If one of the stopping criteria is satisfied, optimal solution has been computed. If none of the stopping criteria are satisfied, go to Step 2 and correct error in constitutive equation.

2. Correct Error in Constitutive Equation

i. Solve Equation (4.16) to compute the gradient and evaluate the cost function defined in Equation (4.1).

ii. Update design variables.

iii. Check stopping criteria, if one of the stopping criteria is satisfied go to Step 1 and compute $\boldsymbol{u}_D^h$ and $\boldsymbol{u}_N^h$. If none of the stopping criteria are satisfied,

continue iterating until one is satisfied.

Figure 4.1 shows a pictorial description of the algorithm described above.

4.2.3 Discretization

In this section the discrete gradient equation is presented. The vectors of nodal values for fields $\boldsymbol{u}_D^h$, $\boldsymbol{u}_N^h$, and $\boldsymbol{v}^h$ are constructed in the same manner as the vectors of nodal values for fields $\boldsymbol{u}^h$ and $\boldsymbol{v}^h$ defined in Equations (3.35) and (3.36). Moreover, the discretized state equations used herein are similar to the state equations of Chapter 3.

Certain equations used for the derivation of the discrete gradient equation were already derived in Chapter 3. However, for the purpose of providing a clear derivation, the equations are presented in this section without providing the details of their derivation. The reader is referred to Section 3.2.5 for the complete derivation of these equations.

Discrete Gradient Equations

After discretization of Equation (4.16) using the finite element method, the k-node complex shear and bulk modulus are defined as

$$G_k^h = N_k(\boldsymbol{x})\, G_S^k(\omega) + iN_k(\boldsymbol{x})\, G_L^k(\omega) \tag{4.17}$$

$$K_k^h = N_k(\boldsymbol{x})\, K_S^k(\omega) + iN_k(\boldsymbol{x})\, K_L^k(\omega) \tag{4.18}$$

, respectively. Let the k-th node vector of design variables be defined as

$$\{p^k\} = \{G_\infty^k, K_\infty^k, \check{G}_1^k, \cdots, \check{G}_r^k, \check{K}_1^k, \cdots, \check{K}_r^k, \tau_1^k, \cdots, \tau_r^k\} \tag{4.19}$$

Then, the k-node variation of the shear and bulk modulus with respect to the vector of design variables are defined as

$$\delta G_k^h = N_k(\boldsymbol{x})\,\delta G_S^k(\omega) + iN_k(\boldsymbol{x})\,\delta G_L^k(\omega) \tag{4.20}$$

$$\delta K_k^h = N_k(\boldsymbol{x})\,\delta K_S^k(\omega) + iN_k(\boldsymbol{x})\,\delta K_L^k(\omega) \tag{4.21}$$

The terms δG_S^k, δG_L^k, δK_S^k, and δK_L^k can be expressed in vector form as follow

$$\delta G_S^k = \{C_{G_S}^k\}^T\{\delta p^k\} \tag{4.22}$$

$$\delta G_L^k = \{C_{G_L}^k\}^T\{\delta p^k\} \tag{4.23}$$

$$\delta K_S^k = \{C_{K_S}^k\}^T\{\delta p^k\} \tag{4.24}$$

$$\delta K_L^k = \{C_{K_L}^k\}^T\{\delta p^k\} \tag{4.25}$$

The terms G_S, G_L, K_S, and K_L are approximated within each element as follows

$$\{G_S^h\} = \Big[N\Big]\Big\{G_S\Big\} \tag{4.26}$$

$$\{G_L^h\} = \Big[N\Big]\Big\{G_L\Big\} \tag{4.27}$$

$$\{K_S^h\} = \Big[N\Big]\Big\{K_S\Big\} \tag{4.28}$$

$$\{K_L^h\} = \Big[N\Big]\Big\{K_L\Big\} \tag{4.29}$$

Similarly, the terms δG_S, δG_L, δK_S, and δK_L are approximated within each element as follows

$$\{G_S^h\} = \Big[N\Big]\,[C_{G_S}]\,\Big\{\delta p\Big\} \tag{4.30}$$

$$\{G_L^h\} = \Big[N\Big]\,[C_{G_L}]\,\Big\{\delta p\Big\} \tag{4.31}$$

$$\{K_S^h\} = \Big[N\Big]\,[C_{K_S}]\,\Big\{\delta p\Big\} \tag{4.32}$$

$$\{K_L^h\} = \Big[N\Big]\,[C_{K_L}]\,\Big\{\delta p\Big\} \tag{4.33}$$

The discretized gradient of G^h and K^h, δG^h, and δK^h are respectively defined as follows

$$\nabla G^h = \nabla\{G^h\} = [\hat{B}]\{G\} \tag{4.34}$$

$$\nabla K^h = \nabla\{K^h\} = [\hat{B}]\{K\} \tag{4.35}$$

$$\nabla \delta G^h = \nabla\{\delta G^h\} = [\hat{B}]\,[C_G]\,\{\delta p\} \tag{4.36}$$

$$\nabla \delta K^h = \nabla\{\delta K^h\} = [\hat{B}]\,[C_K]\,\{\delta p\} \tag{4.37}$$

Substituting the respective discretized quantities into Equation (4.15) yields

$$\begin{aligned}
\nabla\{\hat{J}\}\cdot\{\delta p\} &= \sum_{i=1}^{freq} \Re\left[\sum_{elements}\int_{\Omega^e}\{\triangle\boldsymbol{\sigma}^h\}^T\left(\left(2[\hat{B}]\,[C_G]\,[D_G]+[\hat{B}]\,[C_K]\,[D_K]\right)\{\boldsymbol{\epsilon}_D^h\}\right)^* d\Omega^e\right]\cdot\{\delta p\} \\
&+ \sum_{i=1}^{freq} \Re\left[\beta\sum_{elements}\int_{\Omega^e}\left(|\nabla\{G^h\}|_2^2+\gamma^2\right)^{\alpha-1}\left(\nabla\{G^h\}^T[\hat{B}]\,[C_G]\right)^* d\Omega^e\right]\cdot\{\delta p\} \\
&+ \sum_{i=1}^{freq} \Re\left[\beta\sum_{elements}\int_{\Omega^e}\left(|\nabla\{K^h\}|_2^2+\gamma^2\right)^{\alpha-1}\left(\nabla\{K^h\}^T[\hat{B}]\,[C_K]\right)^* d\Omega^e\right]\cdot\{\delta p\}
\end{aligned} \tag{4.38}$$

where

$$\{\triangle\sigma^h\} = \{\boldsymbol{\sigma}_N^h\} - \{\boldsymbol{\sigma}_D^h\} \tag{4.39}$$

Thus, the discretized gradient equation is given by

$$\begin{aligned}
\nabla\{\hat{J}\} &= \sum_{i=1}^{freq} \Re\left[\sum_{elements}\int_{\Omega^e}\{\triangle\boldsymbol{\sigma}^h\}^T\left(\left(2[\hat{B}]\,[C_G]\,[D_G] + [\hat{B}]\,[C_K]\,[D_K]\right)\{\boldsymbol{\epsilon}_D^h\}\right)^* d\Omega^e\right] \\
&+ \sum_{i=1}^{freq} \Re\left[\beta\sum_{elements}\int_{\Omega^e}\left(|\nabla\{G^h\}|_2^2 + \gamma^2\right)^{\alpha-1}\left(\nabla\{G^h\}^T[\hat{B}]\,[C_G]\right)^* d\Omega^e\right] \\
&+ \sum_{i=1}^{freq} \Re\left[\beta\sum_{elements}\int_{\Omega^e}\left(|\nabla\{K^h\}|_2^2 + \gamma^2\right)^{\alpha-1}\left(\nabla\{K^h\}^T[\hat{B}]\,[C_K]\right)^* d\Omega^e\right]
\end{aligned} \tag{4.40}$$

4.3 Results and Discussion

4.3.1 Problem Description

The same example problems used in Chapter 3 to test the L2-adjoint inverse approach will be used to test the ECE inverse approach. Figure 3.3 shows a pictorial description of the domain of interest. The inverse strategy shown in Figure 4.1 and the vertical component of the displacement field were used to solve the resulting inverse problem. The measured displacement field was generated by solving one linear viscoelastic finite element problem with the benchmark properties shown in Table 3.1 and Table 3.2.

Gaussian noise was added to explore the tolerance of the proposed methodology to imperfect data. Two levels of Gaussian noise, $\triangle_n$ = 5% and 10%, were

considered for the example problems using Equation (3.94). Furthermore, the efficiency of the proposed inverse approach was quantified by calculating the the reconstruction error of the equivalent shear modulus and bulk modulus, see Equation (3.95).

Table 4.1: Choice of the Regularization Parameters

Noise, $\triangle$	0%	5%	10%
Regularization parameter, β	8.5×10^{-3}	1×10^{-2}	1×10^{-2}
Regularization parameter, γ	1×10^{-4}	1×10^{-4}	1×10^{-4}

4.3.2 Regularization

As for the example problems in Chapter 3, TV regularization was preferred over other regularization techniques herein. Table 4.1 shows the values chosen for each regularization parameter. The reader is referred to Section 3.3.2 for further discussion on TV regularization and its advantages.

4.3.3 Example Problems

The example problems used for the inverse problem were built following the same criteria used in Chapter 3. Thus, a 60×60 finite-element mesh with fully integrated eight-node biquadratic elements was built for the finite element models used to solve the inverse problems and a plane strain condition was assumed to reduced the computational demand. To avoid an inverse crime, the experimental displacement field was generated using a 80×80 finite-element mesh

with fully integrated eight-node biquadratic elements.

The number of Maxwell elements was fixed a priori to maintain the similarities between the example problems presented herein and those in Chapter 3; thus, one Maxwell element was used. Furthermore, the bulk viscous effects were ignored. Hence, the design variables at each node were the long-term shear moduli (G_∞), the long-term bulk moduli (K_∞), the viscous shear modulus $\left(\check{G}\right)$, and the relaxation time (τ) for a total of 44164 design variables for the inverse problem.

A limited memory BFGS algorithm was used to minimized the ECE functional defined in Equation (4.1). The maximum number of outer iterations for the inverse problem was set to 500 in all the example problems. One outer iteration correspond to solving steps 1 and 2 (i.e. quantify ECE and correct ECE, respectively) of the optimization strategy shown in Figure 4.1. The maximum number of inner iterations for the minimization problem described in Step 2 (i.e. correct ECE) of Section 4.2.2 was set to 5. A quasi-Newton optimization algorithm was used to solve the resulting minimization problem in Step 2. For this class of optimization algorithms, several sub-iterations may be made to the routine during the minimization process to evaluate the cost function and compute the gradient. The number of sub-iterations was set to 5 for all example problems. The upper and lower bounds considered for the design variables are similar to those used in Chapter 3 (see Table 3.4). All calculations are performed on a Linux workstation with a 1.86-GHz Intel processor and 16 GB of RAM

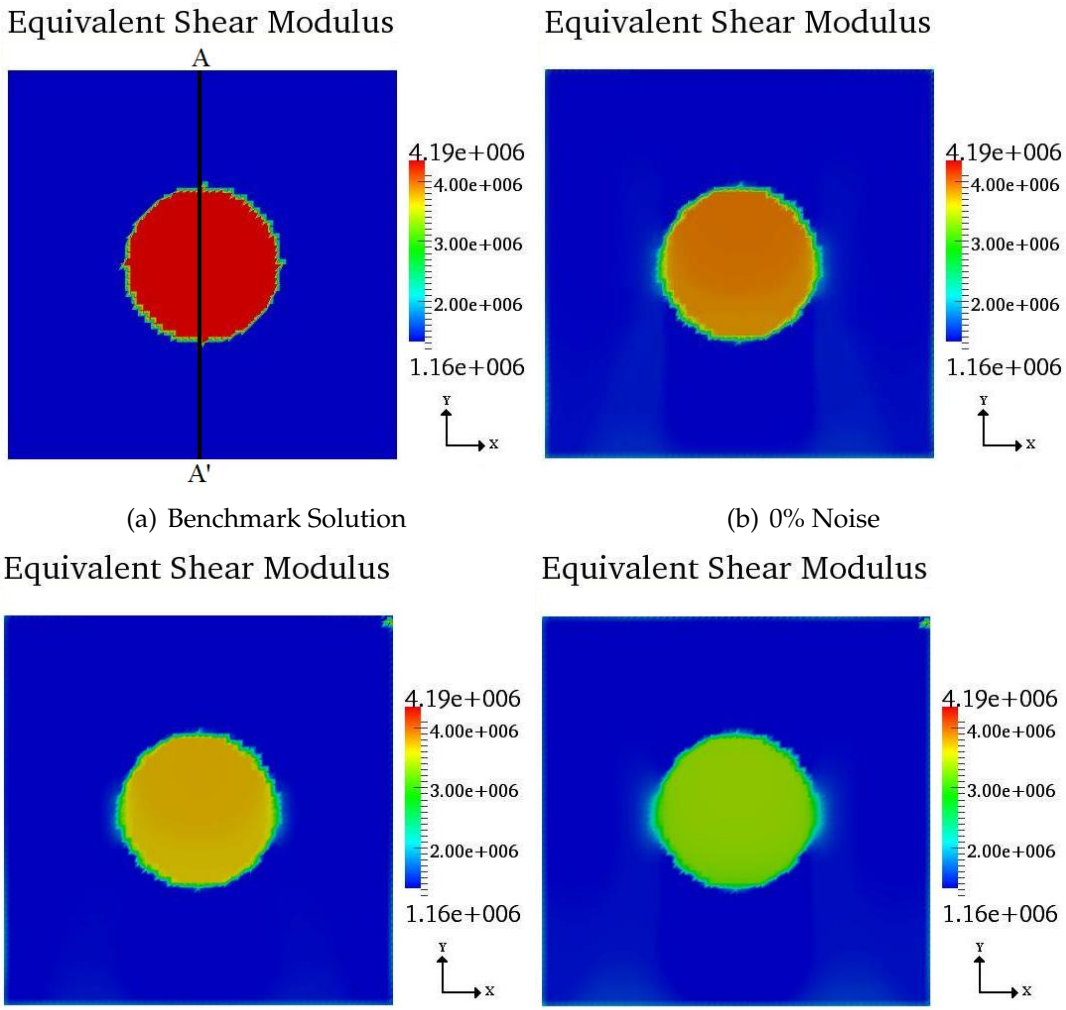

(a) Benchmark Solution

(b) 0% Noise

(c) 5% Noise

(d) 10% Noise

Figure 4.2: Equivalent shear modulus spatial distribution for example problem with one inclusion, $\triangle_n = 0\%, 5\%$, and 10%, and $f = 5\ Hz$

Example Problem with One Inclusion

The initial guess used for the example problem with one inclusion was $G_\infty = 2.0\ MPa$, $K_\infty = 3.0\ MPa$, $\check{G} = 0.2\ MPa$, and $\tau = 5.0 \times 10^{-2}\ sec$. Figures 4.2 and 4.3 show the benchmark solution and the corresponding inverse solution for the equivalent shear modulus and bulk modulus spatial distribution, respec-

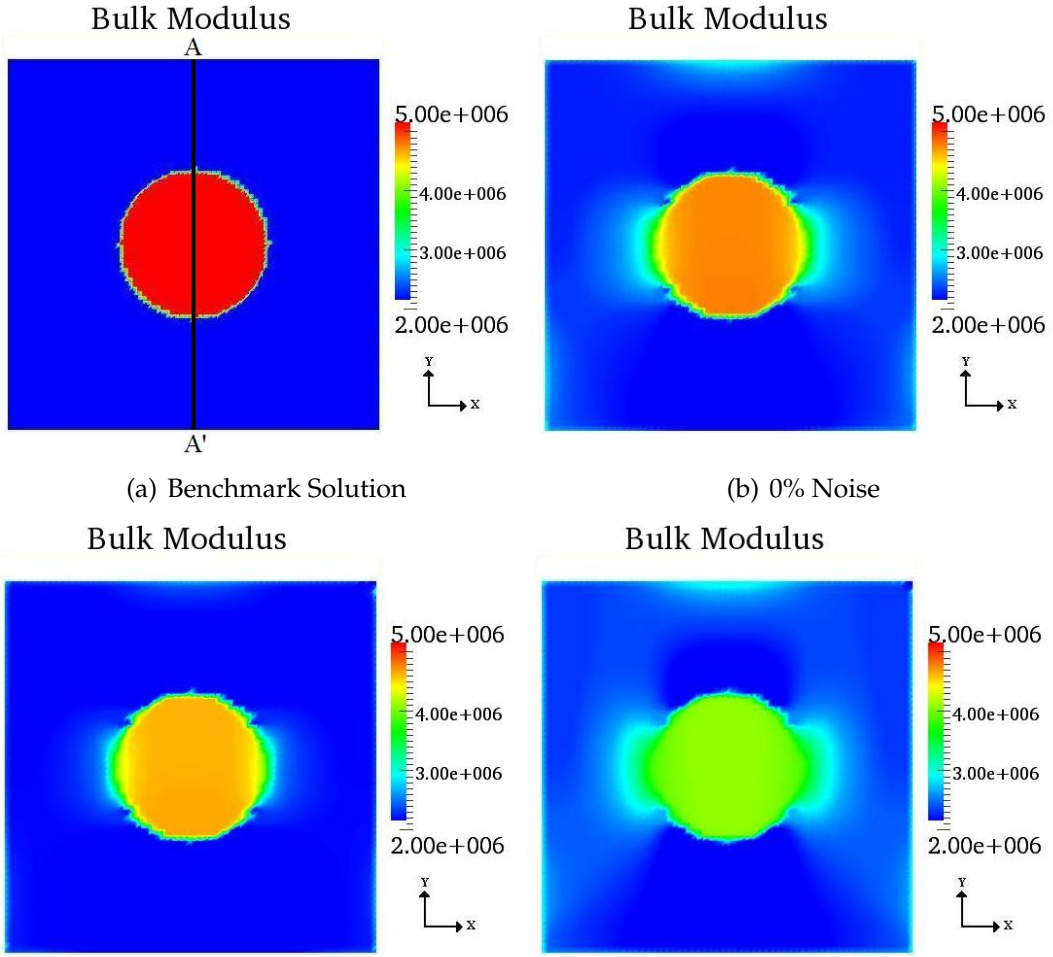

(a) Benchmark Solution

(b) 0% Noise

(c) 5% Noise

(d) 10% Noise

Figure 4.3: Bulk modulus spatial distribution for example problem with one inclusion and $\triangle_n$ = 0%, 5%, and 10%

tively. The plots show that the location and geometry of the inclusion were recovered accurately for all perturbation cases; likewise, the magnitude of these quantities was accurately recovered. As the perturbation in the experimental data increases, the inverse solution becomes highly oscillatory. The regularization parameter is increase in order to reduce these oscillations. However, if the proper technique to select the regularization parameters is not used, most components of the solution are filtered out and the reconstruction errors will

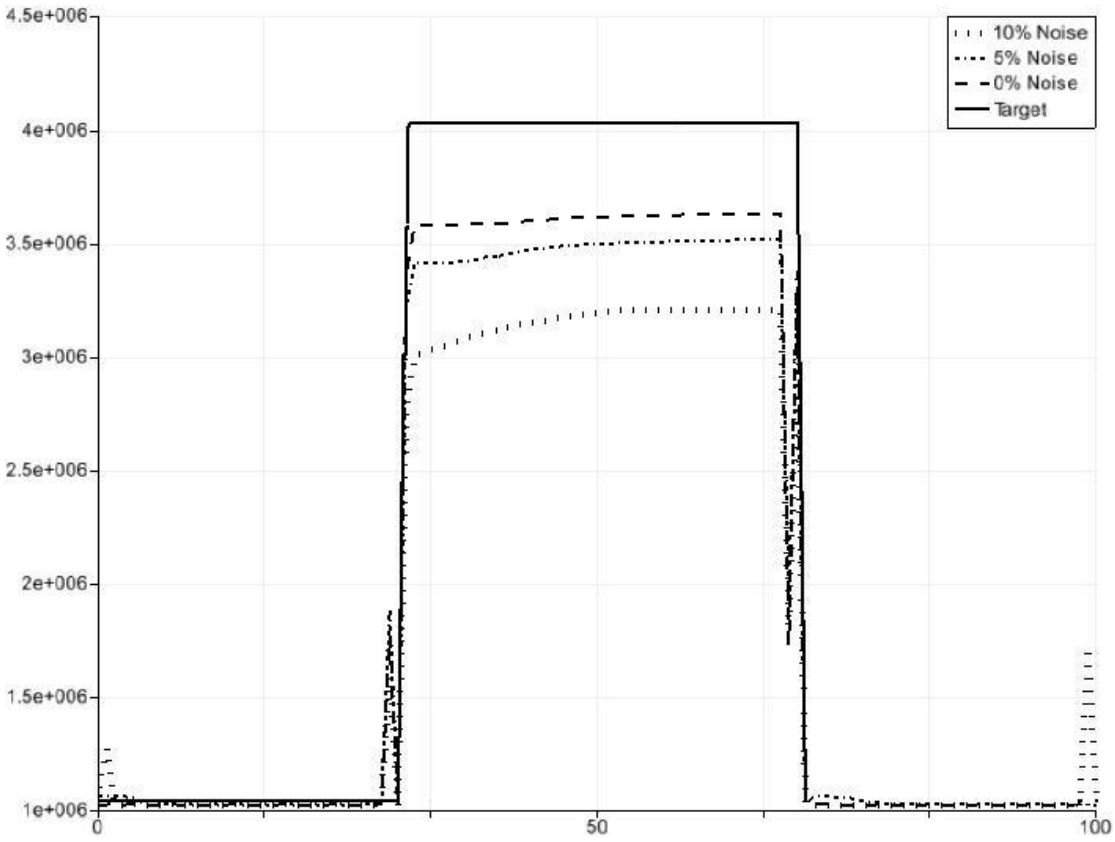

Figure 4.4: Equivalent shear modulus along line A-A′ for $f = 5\ Hz$ and $\triangle_n = 0\%, 5\%$, and 10%

Table 4.2: G_{eq} and K_∞ Reconstruction Error for Example Problem With One Inclusion and $f = 5Hz$

Noise, $\triangle_n$	G_{eq} (e) (%)	K_∞ (e) (%)
0%	10.87	17.32
5%	14.04	19.13
10%	21.58	25.96

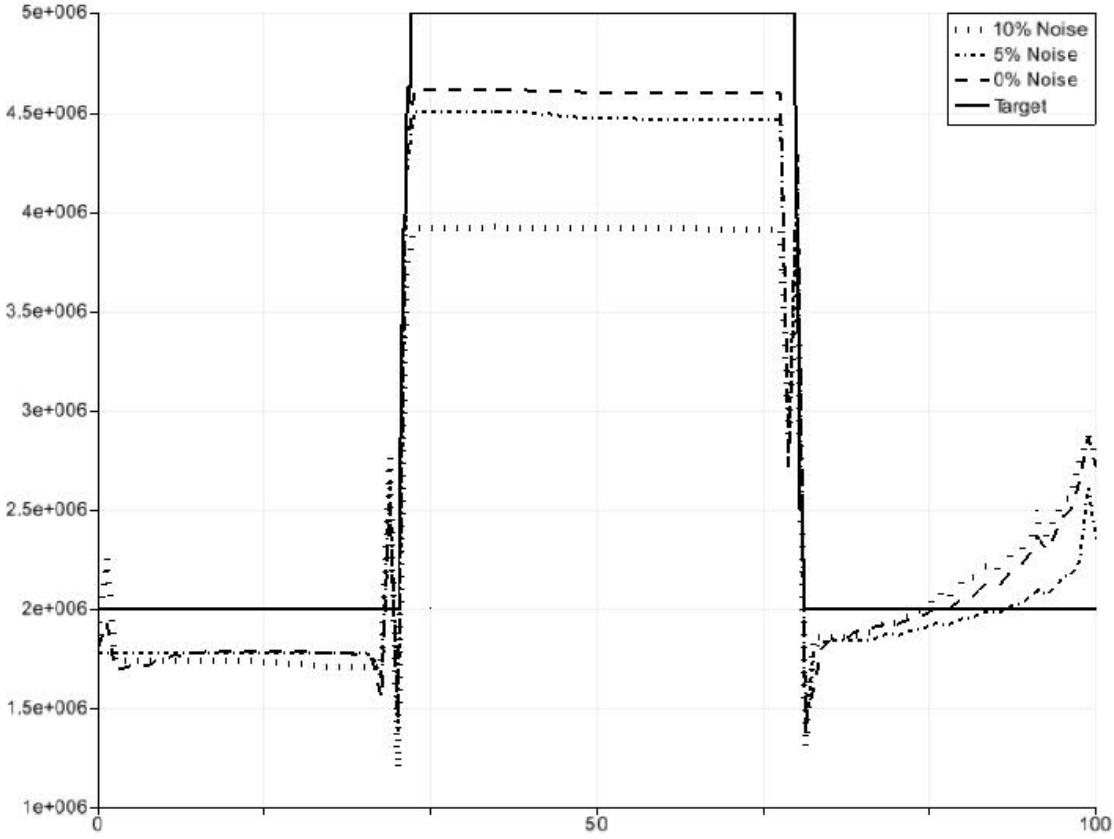

Figure 4.5: Bulk modulus along line A-A′ for $\triangle_n = 0\%, 5\%$, and 10%

increase. Figures 4.4 and 4.5 show the equivalent shear modulus and bulk modulus along line A-A′ for $\triangle_n = 0\%, 5\%$, and 10%. Furthermore, the discretization can affect the resolution of the reconstruction (see [30]).

The reconstruction errors reported in Table 4.2 indicate that the material is less sensitive to volume changes than to shape changes. The lack of sensitivity of the material to volume changes can be attributed to the plane strain condition because the deformations normal to the x-y plane are assumed zero. This could reduce the sensitivity of the material to volume changes.

Figures 4.6–4.8 show the equivalent shear modulus for different frequencies

and $\triangle = 0\%, 5\%, 10\%$. These plots show that the geometry and location of the inclusion were recovered accurately for each frequency. Similar to the results shown in Figures 4.2 and 4.4, the quality of the reconstruction decreased for each frequency as the perturbation in the experimental data increased. However, the magnitude of the equivalent shear modulus was accurately recovered. These trends were also observed for $\triangle = 5\%$ and 10%.

Figures 4.9 and 4.10 show the equivalent shear modulus and dissipation factor frequency spectrum, respectively. The frequency spectrum correspond to one point inside the inclusion and soft matrix. These plots show that the equivalent shear modulus and dissipation factor frequency spectrum were approximated more accurately inside the soft matrix than inside the inclusion, regardless of the perturbation in the experimental data. This could be caused by the TV regularization, given that TV regularization tends to penalize larger gradients [116]. Therefore, larger gradients for the equivalent shear modulus and bulk modulus could have been attained inside the inclusion than inside the soft matrix. Thus, less accurate equivalent shear modulus and dissipation factor spectrum were obtained inside the inclusion. These trends were also observed in other points inside the domain Ω.

Example Problem with Two Inclusions

The initial guess for the example problem with two inclusions was $G_\infty = 1.5\ MPa$, $K_\infty = 2.5\ MPa$, $\check{G} = 0.25\ MPa$, and $\tau = 5.0 \times 10^{-2}\ sec$. Figures 4.11 and 4.12 show the equivalent shear modulus and bulk modulus inverse solutions for $f = 5\ Hz$ and $\triangle_n = 0\%, 5\%$, and 10%. The geometry and location of both inclusions were recovered accurately for all perturbation cases. However, better

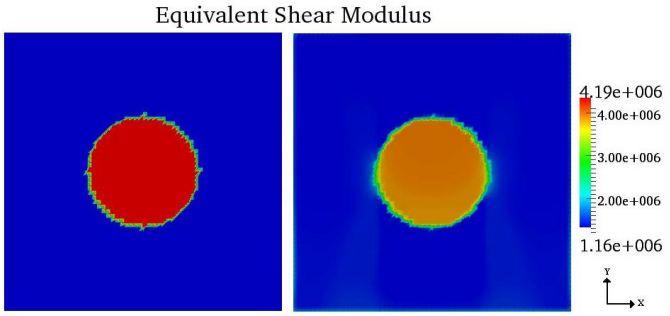

(a) 5 Hz

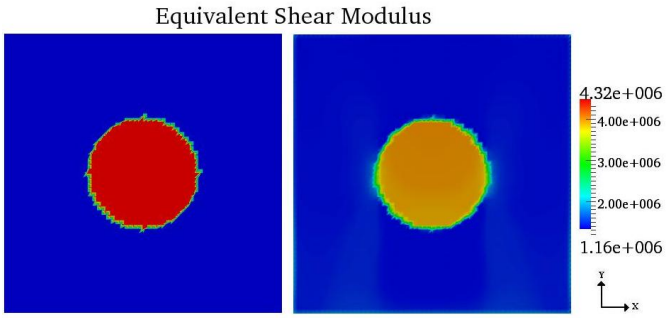

(b) 10 Hz

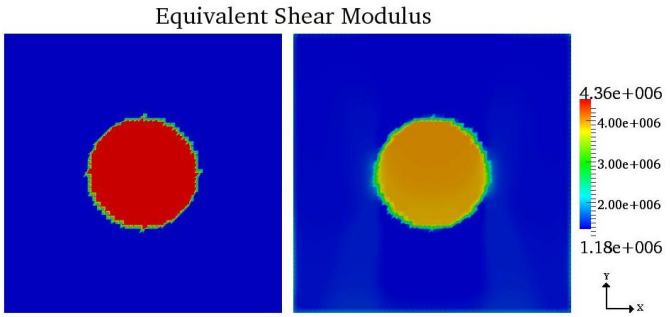

(c) 15 Hz

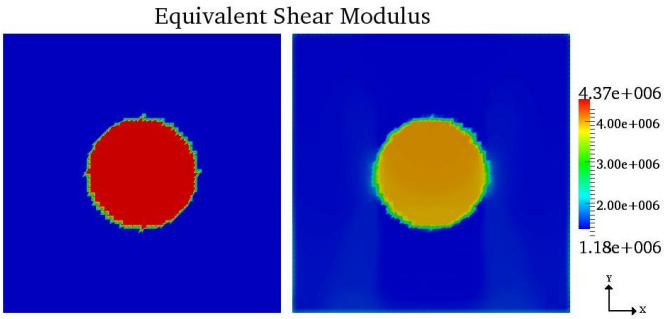

(d) 20 Hz

Figure 4.6: Equivalent shear modulus for example problem with one inclusion, $f = 5, 10, 15, 20\ Hz$, and $\triangle_n = 0\%$

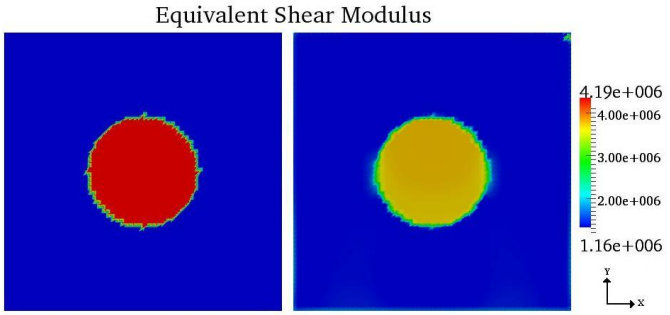

(a) 5 Hz

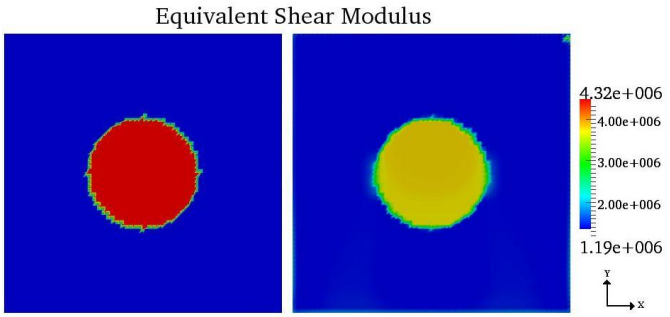

(b) 10 Hz

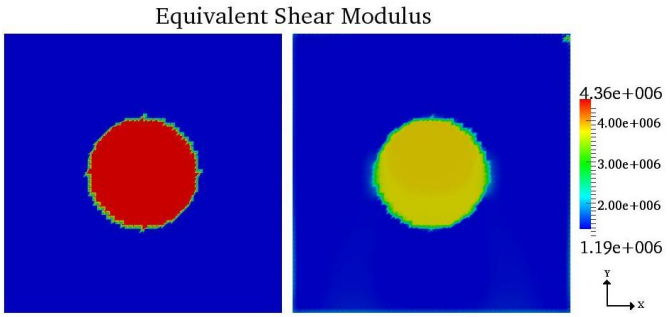

(c) 15 Hz

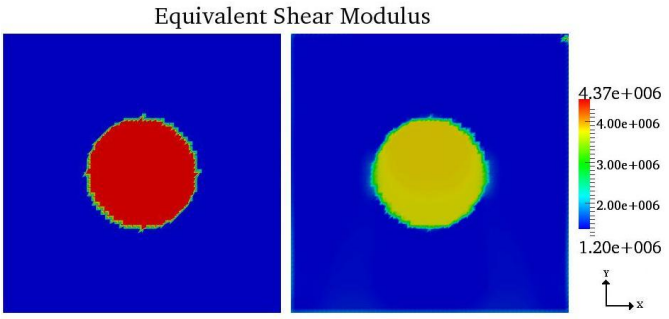

(d) 20 Hz

Figure 4.7: Equivalent shear modulus for example problem with one inclusion, $f = 5, 10, 15, 20\ Hz$, and $\triangle_n = 5\%$

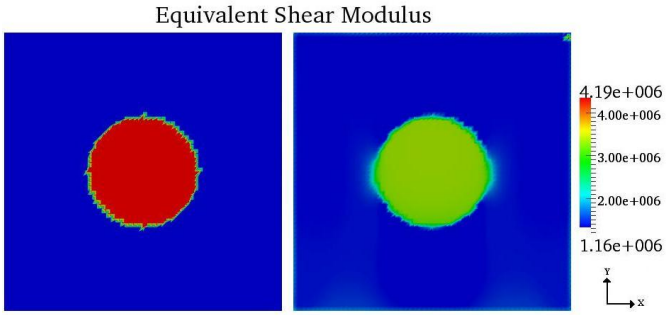

(a) 5 Hz

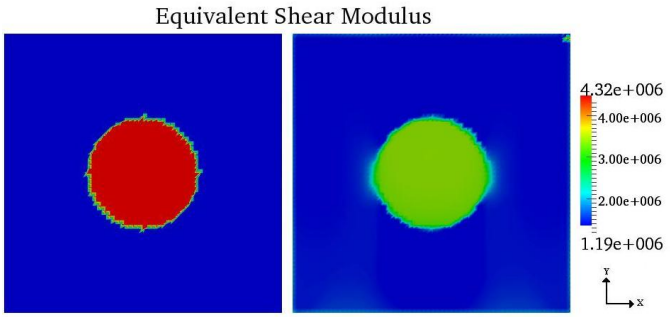

(b) 10 Hz

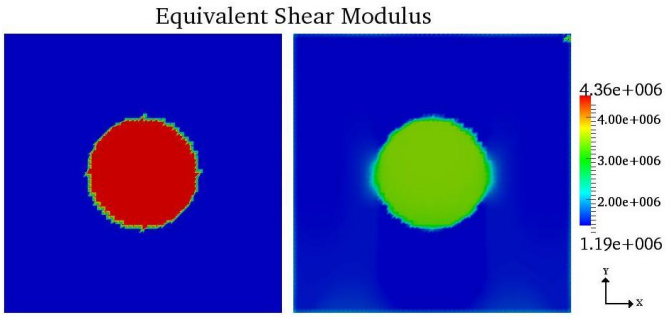

(c) 15 Hz

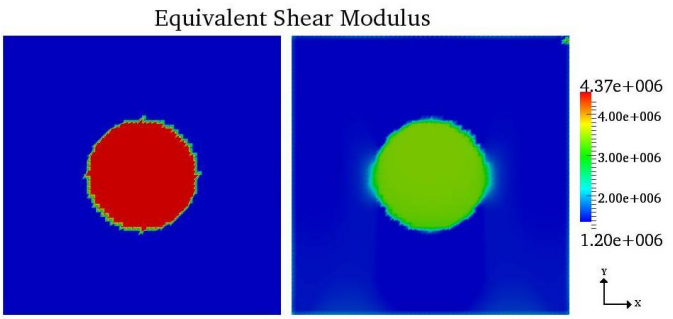

(d) 20 Hz

Figure 4.8: Equivalent shear modulus for example problem with one inclusion, $f = 5, 10, 15, 20\ Hz$, and $\triangle_n = 10\%$

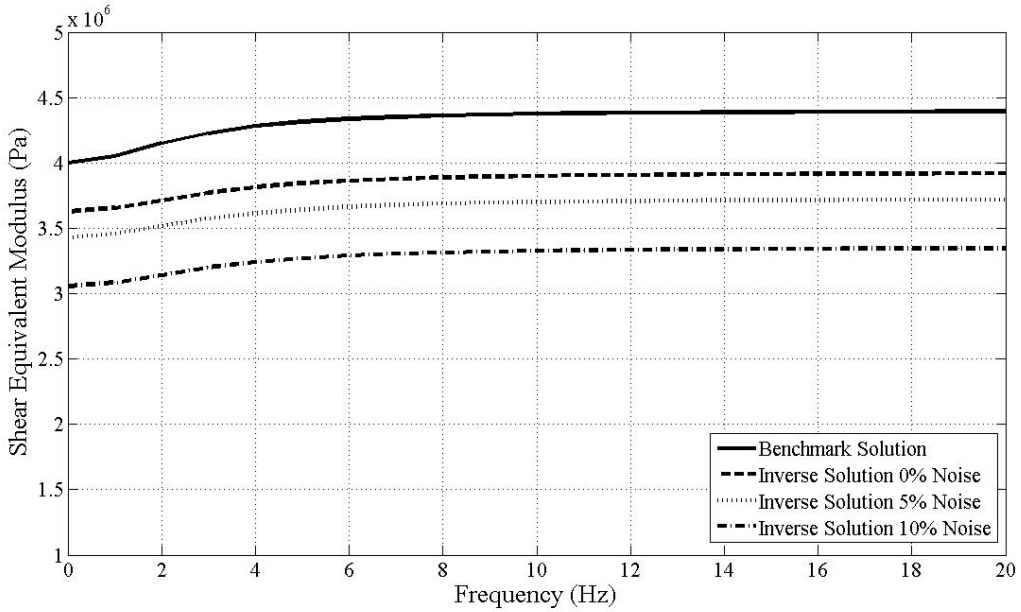

(a) *Position*: $x = 0.5, y = 0.5$

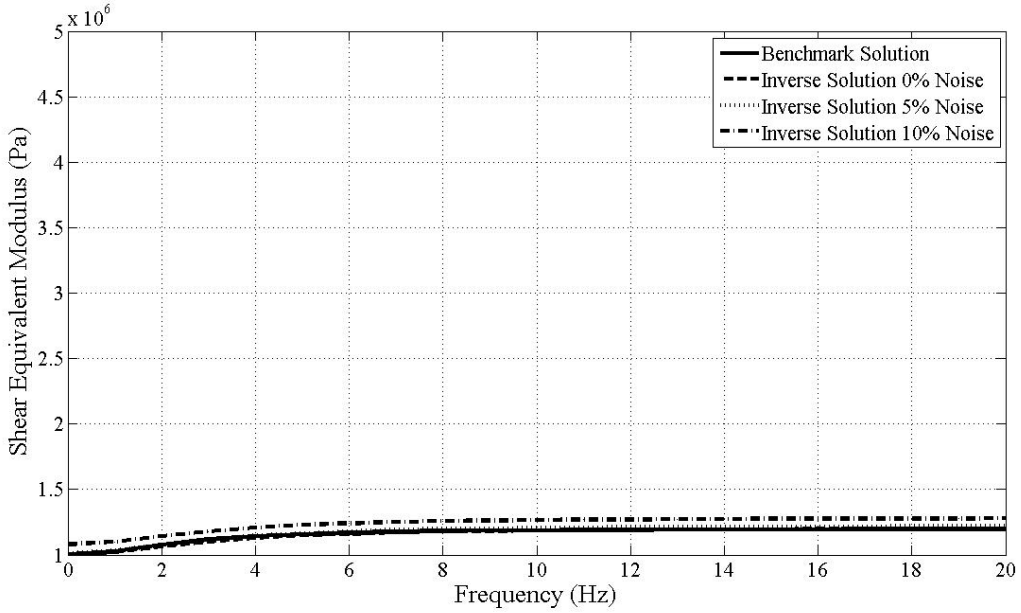

(b) *Position*: $x = 0.5, y = 0.25$

Figure 4.9: Equivalent shear modulus frequency spectrum for example problem with one inclusion at a point inside the: (a) inclusion and (b) background material

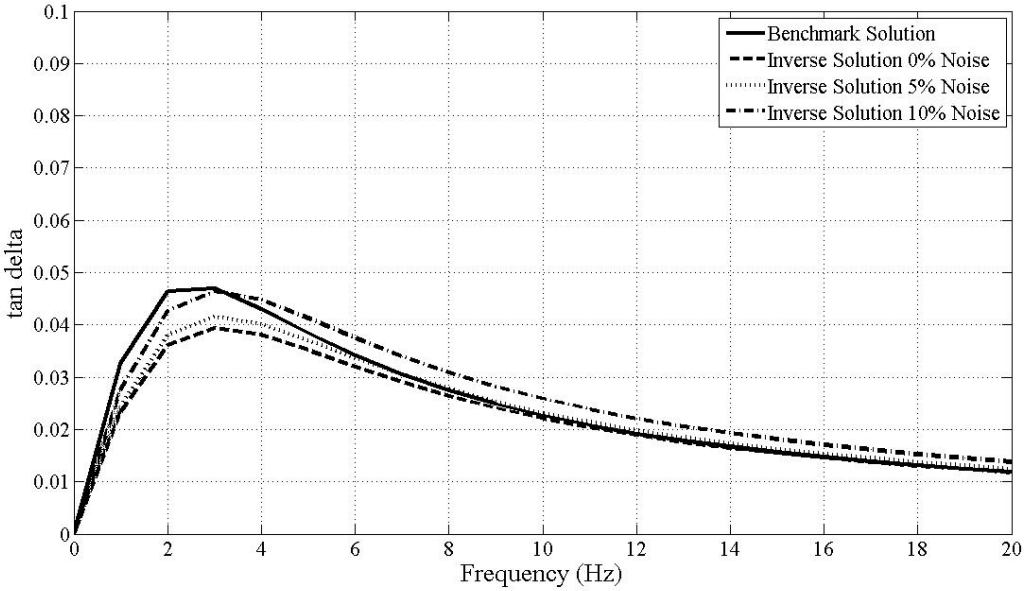

(a) *Position*: $x = 0.5, y = 0.5$

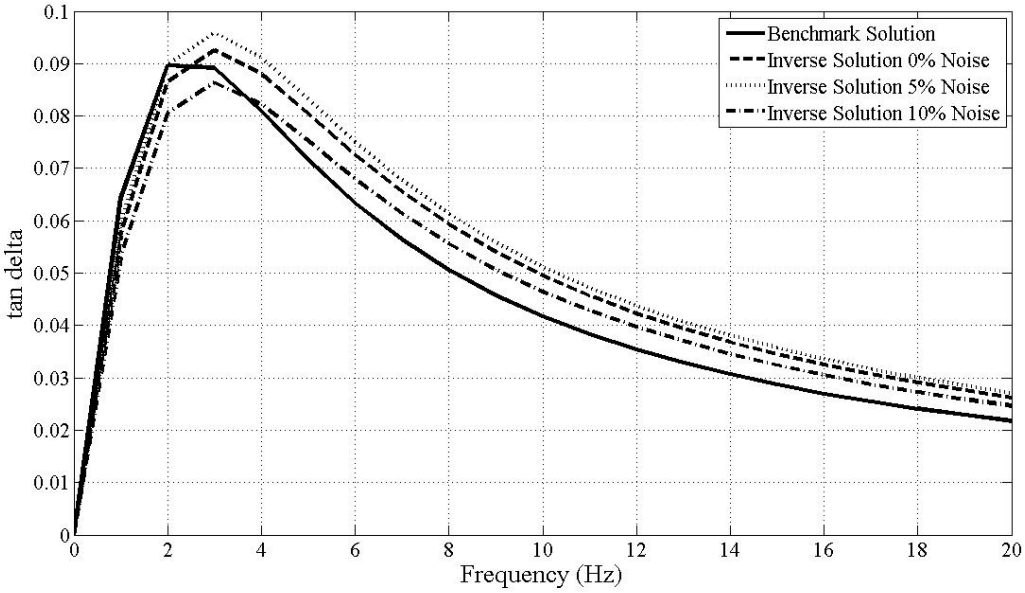

(b) *Position*: $x = 0.5, y = 0.25$

Figure 4.10: Dissipation factor frequency spectrum for example problem with one inclusion at point inside the: (a) inclusion and (b) background material

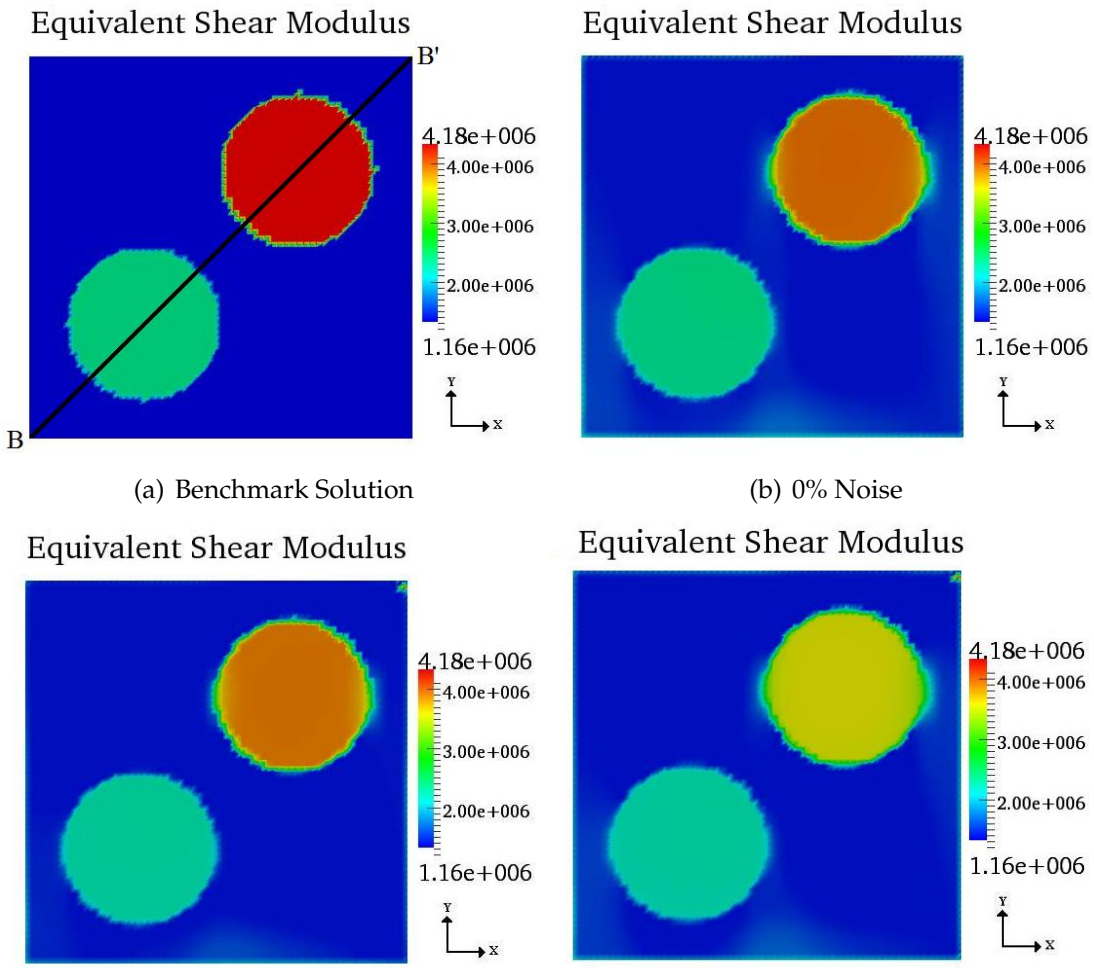

(a) Benchmark Solution

(b) 0% Noise

(c) 5% Noise

(d) 10% Noise

Figure 4.11: Equivalent shear modulus spatial distribution for example problem with two inclusions, $f = 5\ Hz$, and $\triangle_n = 0\%, 5\%$, and 10%

results were attained for the equivalent shear modulus than for the bulk modulus. As for the example problem with one inclusion, this indicate that the material is less sensitive to volume changes than to shape changes. The reconstruction errors reported on Table 4.3 support this remark, since higher errors were consistently obtained for the bulk modulus.

Figures 4.13 and 4.14 show the equivalent shear modulus and the bulk mod-

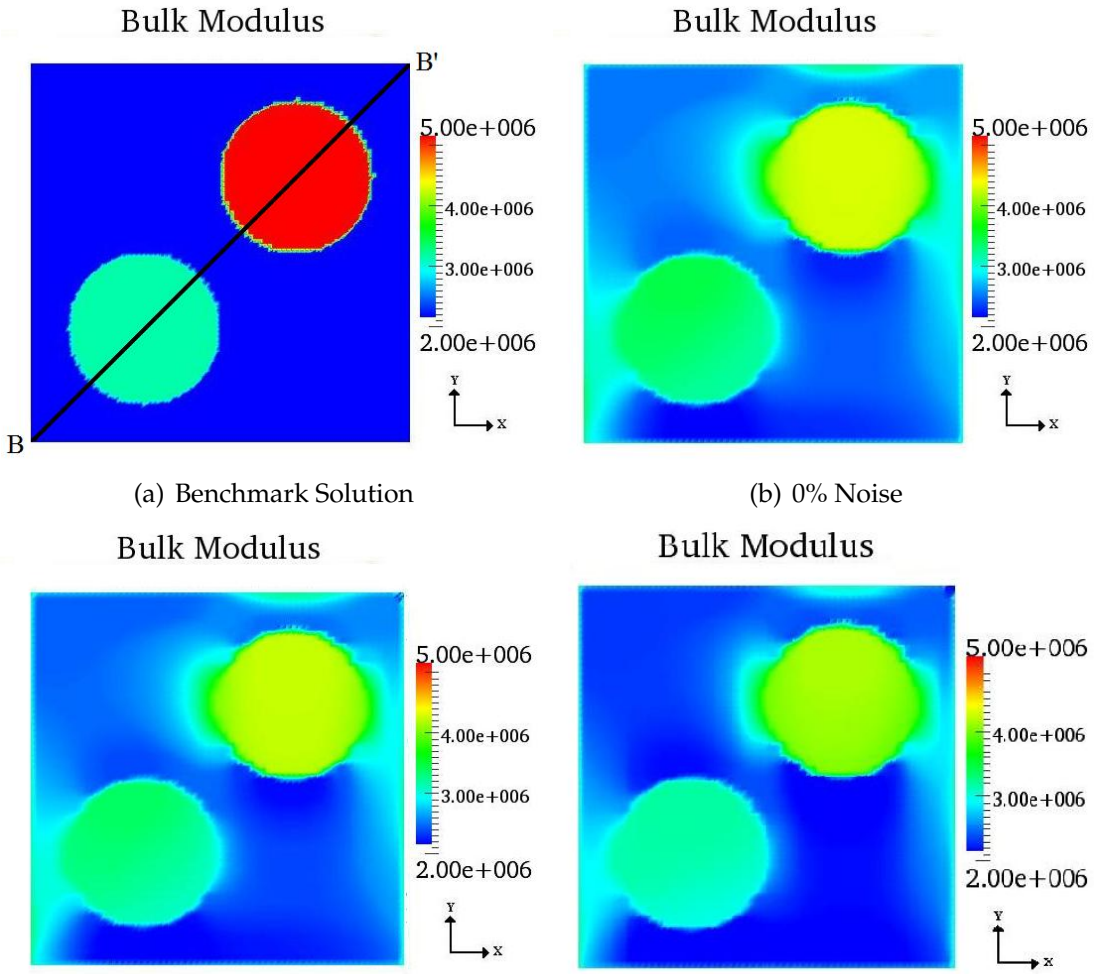

(a) Benchmark Solution

(b) 0% Noise

(c) 5% Noise

(d) 10% Noise

Figure 4.12: Bulk modulus spatial distribution for example problem with two inclusions and $\triangle_n = 0\%, 5\%$, and 10%

Table 4.3: G_{eq} and K_∞ Reconstruction Error for Example Problem With Two Inclusions and $f = 5Hz$

Noise, $\triangle_n$	G_{eq} (e) $(\%)$	K_∞ (e) $(\%)$
0%	11.30	20.61
5%	11.38	21.43
10%	18.04	26.61

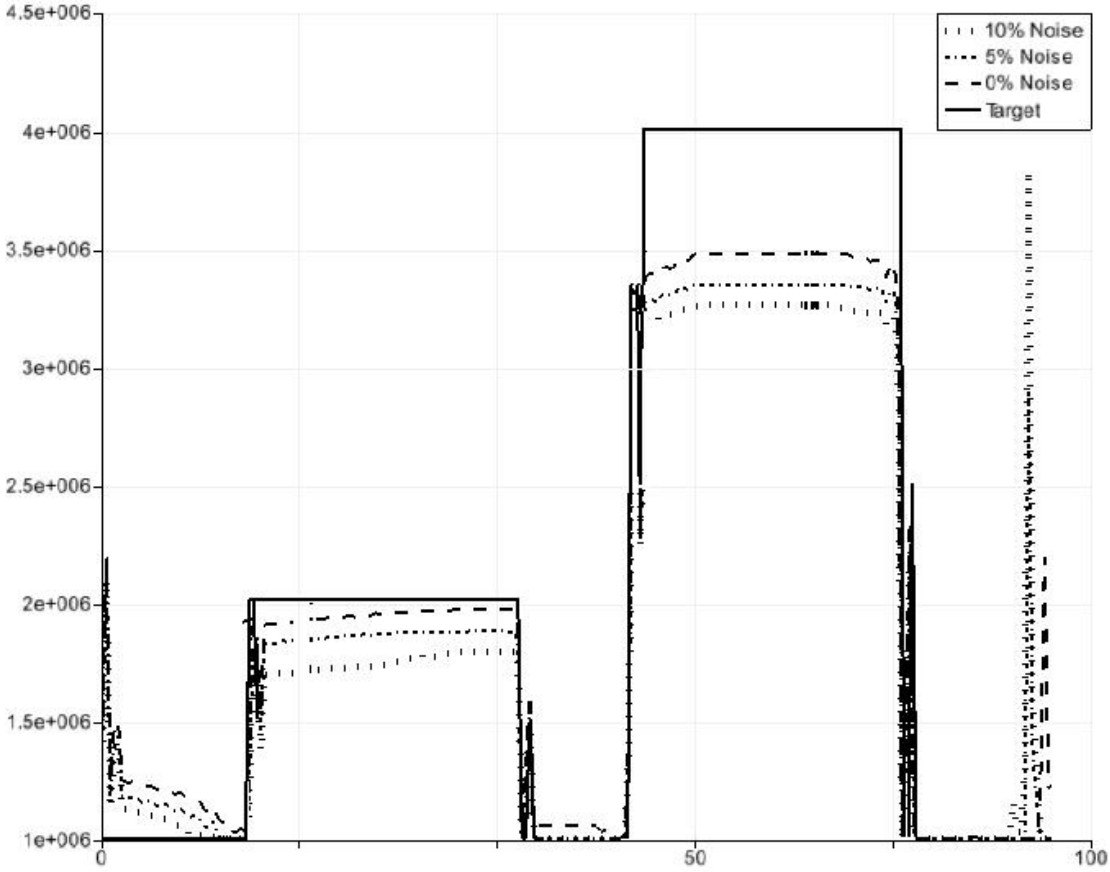

Figure 4.13: Equivalent shear modulus along line B-B′ for $f = 5\ Hz$ and $\triangle_n = 0\%, 5\%$, and 10%

ulus along line B-B′. These plots show that the quality of the reconstruction decrease as the perturbation increase. However, the proposed methodology is less sensitive to imperfect data than the L2-adjoint approach presented in Chapter 3. Similar results were attained for the example problem with one inclusion.

Figures 4.15–4.17 show the equivalent shear modulus for several frequencies and $\triangle = 0\%, 5\%, 10\%$. These plots show that the location and geometry of both inclusions were reconstructed accurately for each frequency, regardless of the perturbation in the experimental data. However, the resolution of the equivalent shear modulus is affected as the perturbation in the experimental data in-

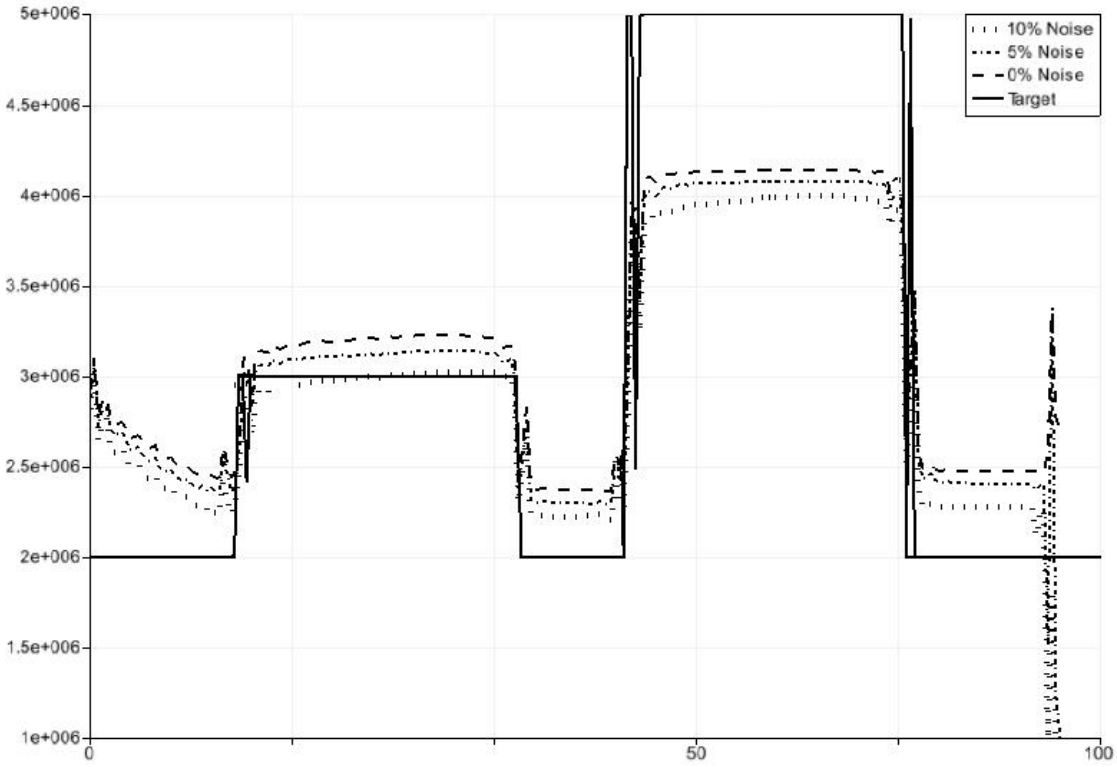

Figure 4.14: Bulk modulus along line B-B′ for $\triangle_n = 0\%, 5\%$, and 10%

creased due to the regularization parameter. As the perturbation increases, the regularization parameter is increase in order to reduce the perturbation error. Consequently, this smoothed the inverse solution; thus, affecting the resolution of the reconstruction.

Figures 4.18 and 4.19 show the frequency spectrum for the equivalent shear modulus and dissipation factor. These plots indicate that the frequency spectrum for both, the equivalent shear modulus and dissipation factor, are more accurate inside the soft inclusion and matrix than inside the stiff inclusion. Similar to the example problem with one inclusion, these results can be attributed

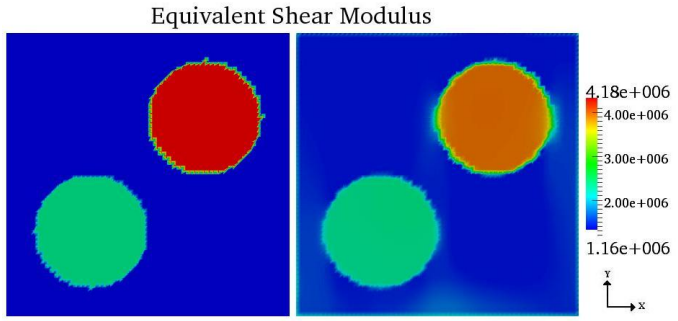

(a) 5 Hz

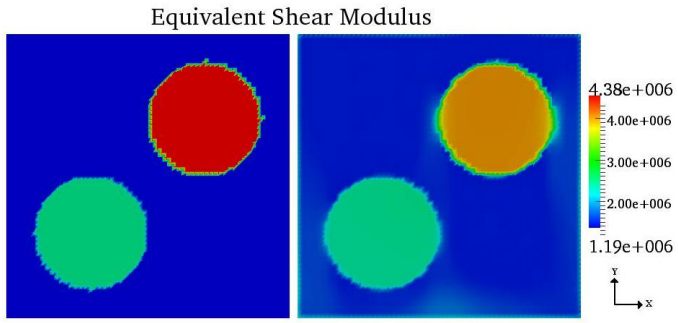

(b) 10 Hz

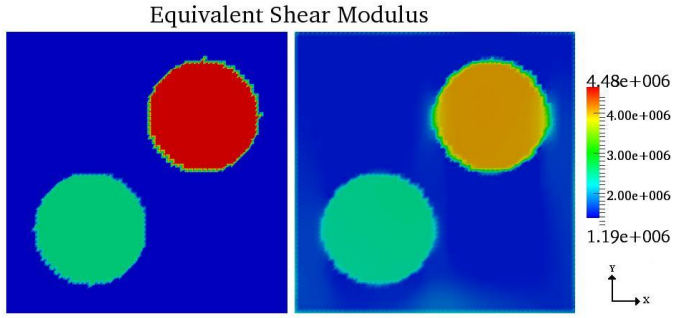

(c) 15 Hz

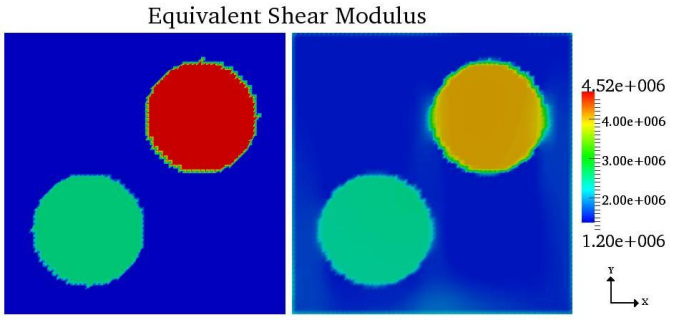

(d) 20 Hz

Figure 4.15: Equivalent shear modulus frequency spectrum for example problem with two inclusions, $f = 5, 10, 15, 20\ Hz$, and $\triangle_n = 0\%$

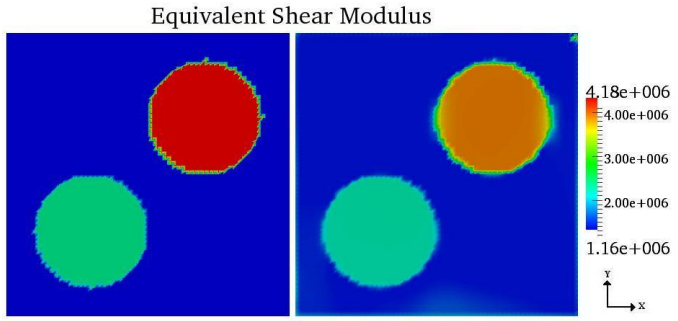

(a) 5 Hz

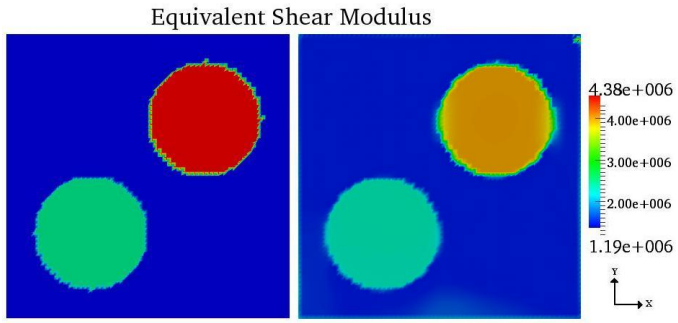

(b) 10 Hz

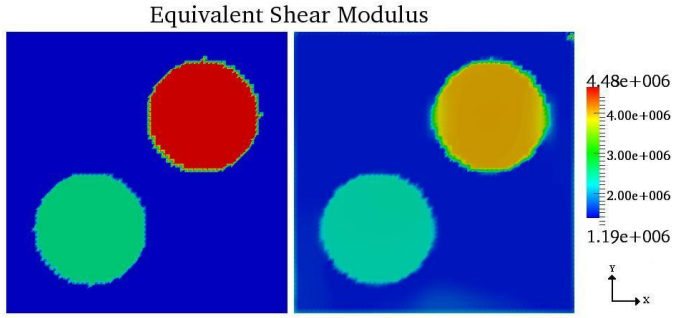

(c) 15 Hz

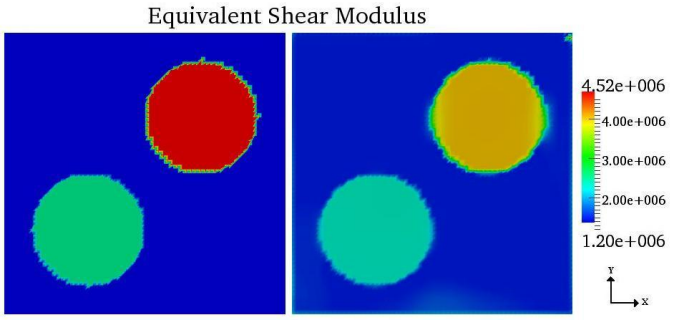

(d) 20 Hz

Figure 4.16: Equivalent shear modulus frequency spectrum for example problem with two inclusions, $f = 5, 10, 15, 20\ Hz$, and $\triangle_n = 5\%$

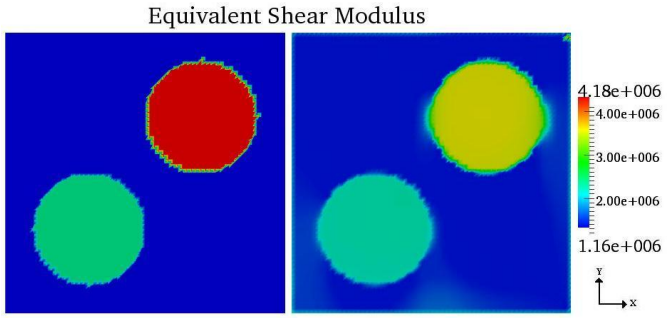

(a) 5 Hz

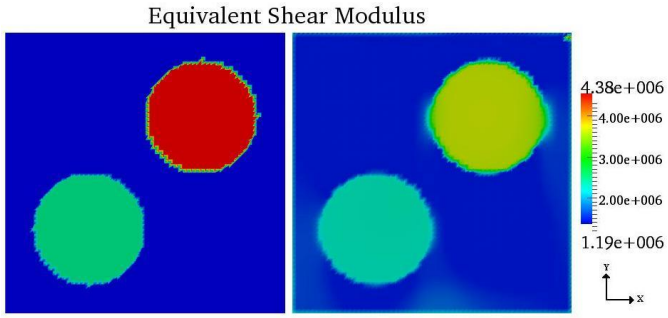

(b) 10 Hz

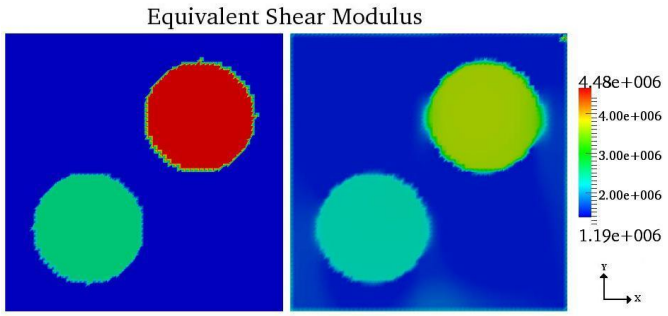

(c) 15 Hz

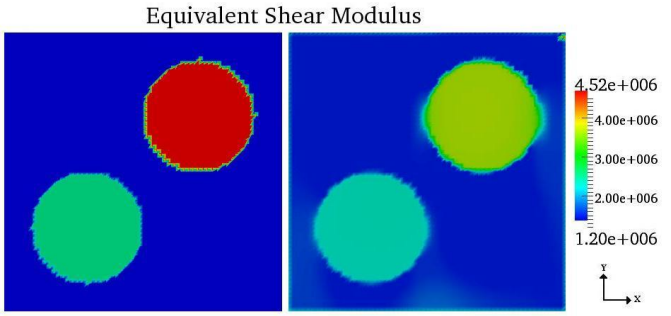

(d) 20 Hz

Figure 4.17: Equivalent shear modulus frequency spectrum for example problem with two inclusions, $f = 5, 10, 15, 20\ Hz$, and $\triangle_n = 10\%$

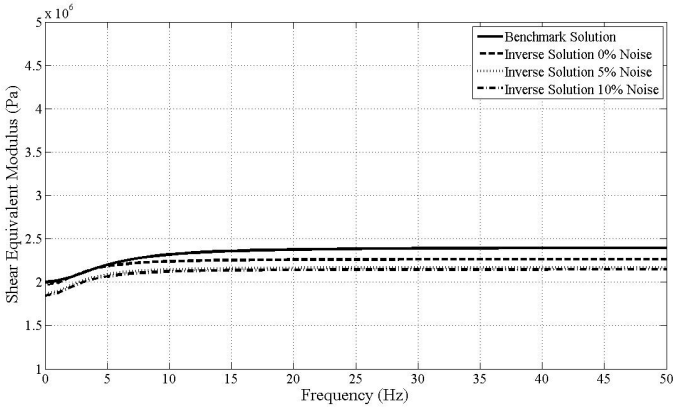

(a) *Position*: $x = 0.3, y = 0.3$

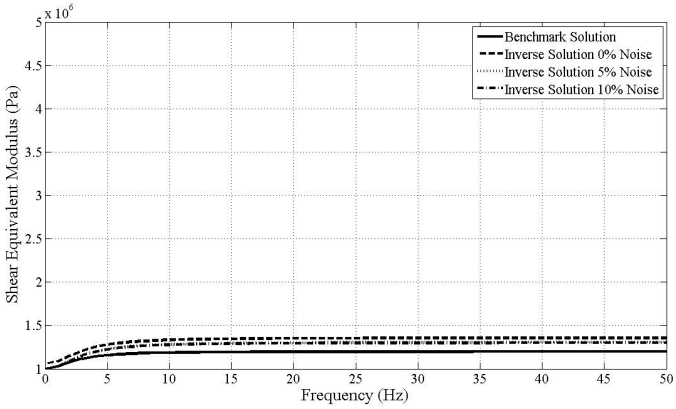

(b) *Position*: $x = 0.5, y = 0.5$

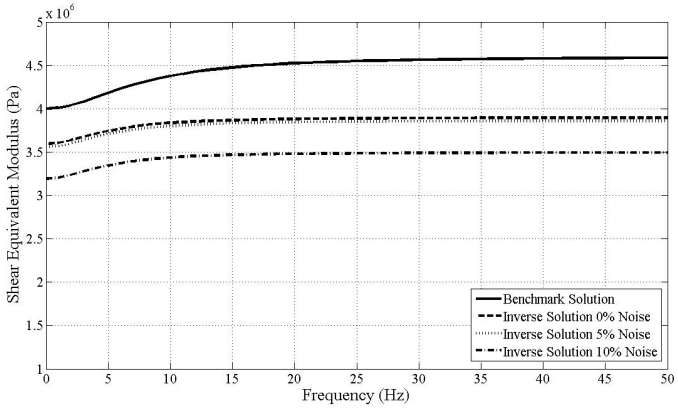

(c) *Position*: $x = 0.7, y = 0.7$

Figure 4.18: Equivalent shear modulus frequency spectrum for example problem with two inclusions at point inside the: (a) soft inclusion, (b) background material, and (c) hard inclusion

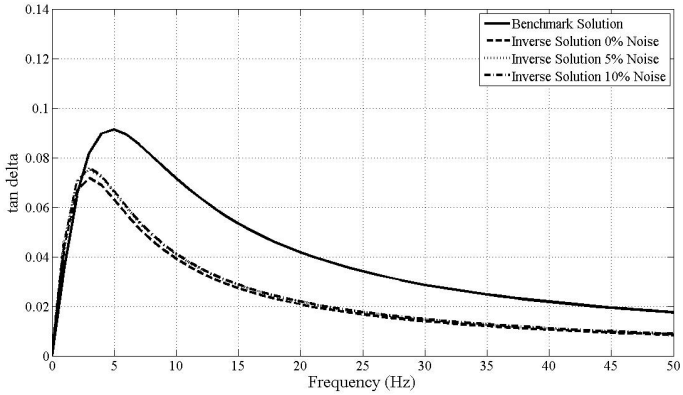

(a) *Position*: $x = 0.3, y = 0.3$

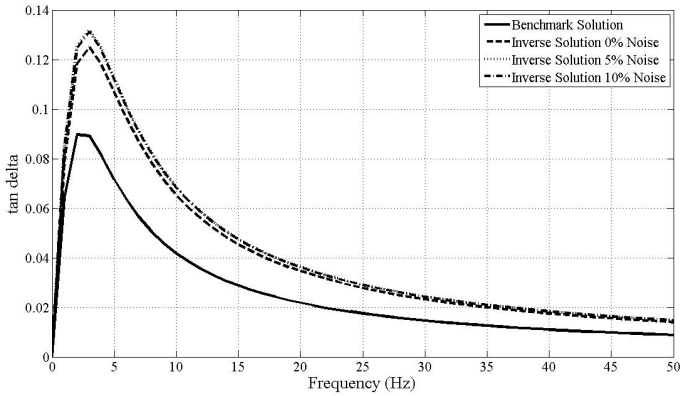

(b) *Position*: $x = 0.5, y = 0.5$

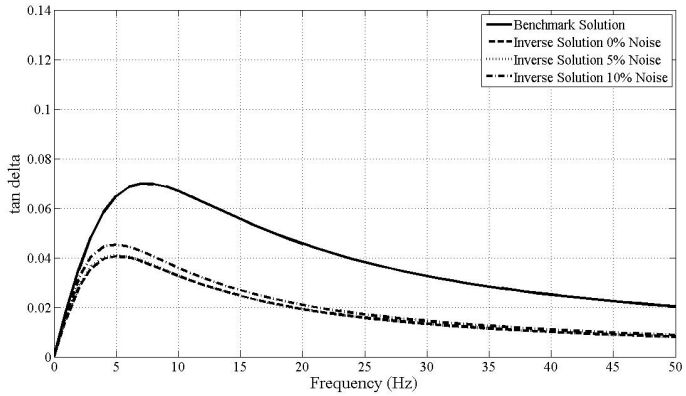

(c) *Position*: $x = 0.7, y = 0.7$

Figure 4.19: Dissipation factor frequency spectrum for example problem with two inclusions at a point inside the: (a) soft inclusion, (b) background material, and (c) hard inclusion

to the regularization. TV regularization tends to penalize larger gradients; thus, smoothing the viscoelastic properties inside the stiff inclusion. These trends were also observed in other points inside the domain Ω.

Overall, the proposed inverse approach was able to locate and reconstruct the boundaries of both inclusions for each frequency. Accurate results were consistently obtained as the perturbation in the experimental data increased, in particular for the equivalent shear modulus. This trend was also observed in each frequency.

Remarks on Results

The solution error is the sum of the regularization and the perturbation errors. If the regularization parameter β is too small, too much emphasis is put on the measured data and the solution is influenced by the noise in the data. Therefore, the regularization parameter is increase to alleviate the perturbation error caused by imperfect experimental data. When the value of the regularization parameter is to high, too much emphasis is put on the regularization term; thus, obtaining a smooth solution with few details [55]. Consequently, the regularization error increases. The optimal solution error is obtained when the proper regularization parameter is use. Techniques, such as the L-curve method, are available in the literature for the proper selection of this parameter. In the present work, such techniques were not used to select the regularization parameter, it was selected through numerical studies. As a result, the reconstruction errors for both example problems were larger than expected. However, it is worth mentioning that larger reconstruction errors will be expected for higher perturbation levels, given that larger values of β will be necessary to reduce the

perturbation error and yield an optimal solution error. As a result, the inverse solution is smoothed; thus, increasing the reconstruction errors.

The results indicate that the material was more sensitive to shape changes than to volume changes. Two factors that could have caused the lack of sensitivity to volume changes are the plane strain assumption and loading case. The bulk modulus measures the resistance of an object to hydrostatic pressure. However, the example problems used in this chapter are not subjected to hydrostatic pressure, which could lead to a reduction of the material sensitivity to volume changes. Furthermore, a plane strain condition was assumed to reduce the computational expense associated with the inverse problem. Thus, the deformations normal to the plane parallel to the force line of action (e.g. the x-y plane in the example problems) are assumed zero. This restricts the change in volume in the material to two directions (e.g the x and y directions in the example problems), reducing the sensitivity of the material to volume changes. These two factors could have led to higher reconstruction errors for the bulk modulus.

The lack of prior information about the original system (i.e. experimental data, geometry, boundary conditions, etc.) will results in higher reconstruction errors. Similar to the example problems in Chapter 3, only the vertical component of the displacement field was used for the inverse problem. Hence, the reconstruction errors increased due to the lack of prior information about the experimental data. Furthermore, in Chapter 3 it was mentioned that discretization affects the resolution of the reconstruction, which could lead to higher reconstruction errors for the equivalent shear modulus and bulk modulus. Therefore, the reconstruction errors reported in this chapter could have been higher than expected due to discretization.

Finally, the errors reported in Tables 4.2 and 4.3 show that there are no great disparities between the reconstruction errors of both examples (i.e. one inclusion and two inclusions). These results indicate that the proposed inverse approach is effective reconstructing spatially-varying viscoelastic properties of solids, regardless of the complexity of the distribution.

4.4 Summary

An inverse approach for the identification of spatially-varying complex tensor from the steady-state response using the concept of error in constitutive equation was presented. Through simulated examples it was shown that the proposed methodology can accurately identify such distributions, regardless of its complexity. Accurate results were consistently observed for perturbation levels up to 10%. However, there was a trade off in accuracy as the perturbation in the experimental data increased due to the smoothing of the regularized solution. In future work, an appropriate technique will be used to select the optimal values for the regularization parameters. Furthermore, an error functional based on the concept of modified error in constitutive equations will be implemented in order to increase the convergence rate as the perturbation in the experimental data augment. These functionals have been shown to provide accurate results for constitutive parameters identification problems in which the perturbation in the experimental data is as high as 40% [90].

One application of this work is to develop an inverse approach that combines vibroacoustics based techniques with computational mechanics for the identification of spatially-varying constitutive parameters in soft tissue in the

presence of unhealthy tissue. Hence, it is important to test the proposed methodology with experimental data obtained from a physical experiment.

CHAPTER 5

AN INVERSE APPROACH BASED ON THE CONCEPT OF ERROR IN CONSTITUTIVE EQUATION FOR CHARACTERIZATION OF VISCOELASTIC PROPERTIES IN TRANSIENT DYNAMICS

5.1 Introduction

In Chapter 4, an inverse approach based on the concept of error in constitutive equation was presented. Results show that this methodology can accurately characterize spatially-varying material properties. Moreover, this methodology outperformed the inverse approach based on the adjoint method presented in Chapter 3. This chapter extends the work done in Chapter 4, the main focus is to test the feasibility of the ECE inverse approach for in-vivo characterization of viscoelastic properties using vibroacoustics based techniques.

Different methodologies have been proposed in the literature for the identification of viscoelastic properties [4, 9, 28, 46, 64, 66, 67, 107, 109]. For instance, Liu *et al.* [79] used an inverse approach to identify viscoelastic properties of polymer gels from experimental data obtained by nanoindentation creep testing. The viscoelastic properties were identified by fitting the finite element system response to the experimental response. The viscoelastic parameters were refine in order to minimize the least-square error between the finite element representation and experimental system response. Moulton *et al.* [87] use an inverse approach to identified passive myocardial material properties from strains measurements obtained by MRI radiofrequency tissue tagging. The inverse problem was cast as an optimization problem in which a least-square error functional that quantified the misfit between the finite element representation and experi-

mental strains is minimized with respect to the unknown viscoelastic properties. Forward difference was used to approximate the entries of the gradient at each iteration of the minimization problem. Thus, as the number of design variables increases the computational cost increases significantly. Furthermore, the least-square error functional used in [79] and [87] is non-convex, causing the inverse solution to become sensitive to parameter initialization. An alternate technique to these approaches is to use an inverse approach based on the concept of error in constitutive equation. The reader is referred to Section 4.1 for a detailed discussion on the concept of error in constitutive equation.

One application of the present work is the characterization of myocardial viscoelastic properties. Though myocardial viscoelastic properties are essential in the evaluation of heart diastolic properties, little work has been done to noninvasive measured these properties in-vivo. Kanai [63] used ultrasonic measurements to compute the phase velocity of the Lamb waves to obtain the myocardial viscoelastic properties in-vivo. By comparing the dispersion of the phase velocity with the theoretical ones predicted by Lamb wave theory, the viscoelastic properties were determined noninvasive. In this chapter, an alternate technique for in-vivo characterization of myocardial viscoelastic properties based on the concept of ECE is presented. The feasibility of the proposed methodology is demonstrated through a numerical and physical experiment.

This chapter is outlined as follows. In Section II, the finite element formulation for an isotropic linear viscoelastic solid subjected to small deformations is presented. In this section, the material model and integration algorithm used to calculate the system response at each time step are described. Furthermore, the inverse problem formulation is presented. In Section III, the simulated and

physical experiments results are discussed. Conclusions and future directions are given at the end of the chapter.

5.2 Formulation

5.2.1 Forward Problem

Boundary Value Problem

The transient dynamics solid boundary value problem is defined as

$$\nabla \cdot \sigma(\boldsymbol{x}, t) + \boldsymbol{b}(\boldsymbol{x}, t) = \rho_s \ddot{\boldsymbol{u}}(\boldsymbol{x}, t) \text{ in } \Omega \subset \mathbb{R}^n \tag{5.1}$$

$$\boldsymbol{u}(\boldsymbol{x}, t) = \boldsymbol{u}_0(\boldsymbol{x}, t) \text{ on } \Gamma_u \tag{5.2}$$

$$\boldsymbol{u}(\boldsymbol{x}, 0) = 0 \text{ in } \Omega \tag{5.3}$$

$$\dot{\boldsymbol{u}}(\boldsymbol{x}, 0) = 0 \text{ in } \Omega \tag{5.4}$$

$$\boldsymbol{\sigma}(\boldsymbol{x}, t)\, \boldsymbol{n}_s(\boldsymbol{x}) = t(\boldsymbol{x}, t) - p(\boldsymbol{x}, t)\, \boldsymbol{n}_s \text{ on } \Gamma_t \tag{5.5}$$

$$\boldsymbol{\sigma}(\boldsymbol{x}, t)\, \boldsymbol{n}_s(\boldsymbol{x}) = -p(\boldsymbol{x}, t)\, \boldsymbol{n}_s \text{ on } \Gamma_{fs} \backslash \Gamma_u \tag{5.6}$$

Here Ω represents the interior of a body whose boundary is $\Gamma = \Gamma_u \cup \Gamma_{fs}$, $\Gamma_{fs} = \Gamma \backslash (\Gamma_u \cup \Gamma_t)$ is the fluid-structure interface, Γ_u is the portion of the boundary where displacements are specified, $\boldsymbol{x}$ is the spatial position vector, t denotes time, $\boldsymbol{\sigma}(\boldsymbol{x}, t)$ is the stress tensor, ρ_s is the mass density (assumed constant in this work), $\boldsymbol{u}(\boldsymbol{x}, t)$ is the displacement field, $\boldsymbol{b}(\boldsymbol{x}, t)$ is the body force vector, $\boldsymbol{t}(\boldsymbol{x}, t)$ is the traction vector, and $\boldsymbol{n_s}(\boldsymbol{x})$ is the unit normal vector to the solid surface.

The stress-strain relationship for a linear viscoelastic material is defined as

$$\boldsymbol{\sigma}(\boldsymbol{x},t) = \int_{-\infty}^{t} \mathbb{C}(t-s) \frac{\partial \boldsymbol{\epsilon}(\boldsymbol{x},s)}{\partial s} ds \tag{5.7}$$

$$\mathbb{C}(t-s) = G(t-s)\left(\boldsymbol{I} + \boldsymbol{I}^T\right) + K(t-s)\,\boldsymbol{I} \otimes \boldsymbol{I} \tag{5.8}$$

$$\boldsymbol{\epsilon}(\boldsymbol{x},t) = \frac{1}{2}\left(\nabla \boldsymbol{u}(\boldsymbol{x},t) + \nabla \boldsymbol{u}(\boldsymbol{x},t)^T\right) \tag{5.9}$$

Here $\mathbb{C}$ is the relaxation fourth-order tensor, G is the shear modulus, K is the bulk modulus, and $\boldsymbol{\epsilon}$ is the strain tensor. For more details on the theory of linear viscoelasticity the reader is referred to [13, 24, 35, 41, 42].

The transient dynamic fluid boundary value problem is defined as

$$\nabla p(\boldsymbol{x},t) = \rho_f \ddot{\boldsymbol{u}}(\boldsymbol{x},t) \text{ in } \Phi \subset \mathbb{R}^n \tag{5.10}$$

$$p(\boldsymbol{x},t) = -B_f \nabla \cdot \boldsymbol{u}^f(\boldsymbol{x},t) \text{ in } \Phi \tag{5.11}$$

$$\nabla p(\boldsymbol{x},t) \cdot \boldsymbol{n}_f(\boldsymbol{x}) = \rho_f \ddot{\boldsymbol{u}}_n^f(\boldsymbol{x},t) \text{ on } \Gamma_{fs} \tag{5.12}$$

$$\boldsymbol{u}_n^s(\boldsymbol{x},t) = \boldsymbol{u}_n^f(\boldsymbol{x},t) \text{ on } \Gamma_{fs} \tag{5.13}$$

For the fluid formulation, ρ_f is the fluid mass density, B_f is the bulk modulus, $p(\boldsymbol{x},t)$ is the scalar acoustic fluid pressure in excess of hydrostatic pressure, $\boldsymbol{u}_n^f(\boldsymbol{x},t)$ is the displacement of the fluid boundary in the direction of the normal, $\boldsymbol{u}_n^s(\boldsymbol{x},t)$ is the displacement of the solid boundary in the direction of the normal, $\boldsymbol{n}_f(\boldsymbol{x})$ is the unit normal vector to the fluid surface, and Φ is the fluid domain.

Rheological Model

The phenomenon at which a constant deformation $\boldsymbol{\epsilon}$ is applied at some time t and a slow decay of stresses is observed in the material is known as relaxation. Multiple material models exist in the literature to describe relaxation process in viscoelastic materials (e.g. Kelvin-Voigt, Maxwell, etc.). In the present work, a Generalized Maxwell material model was used to represent this relaxation process. Hence, the stress-strain relationship defined as

$$\boldsymbol{\sigma}(\boldsymbol{x},t) = 2G_{\infty}\boldsymbol{\epsilon}^{d}(\boldsymbol{x},t) + K_{\infty}(\operatorname{tr}\boldsymbol{\epsilon}(\boldsymbol{x},t))\boldsymbol{I} + \boldsymbol{\theta}(\boldsymbol{x},t) \tag{5.14}$$

$$\boldsymbol{\epsilon}^{d}(\boldsymbol{x},t) = \boldsymbol{\epsilon}(\boldsymbol{x},t) - \frac{1}{3}(\operatorname{tr}\boldsymbol{\epsilon}(\boldsymbol{x},t))\boldsymbol{I} \tag{5.15}$$

where the evolution function for the internal variable is given by

$$\begin{aligned}\boldsymbol{\theta}(\boldsymbol{x},t) = {} & 2\check{G}\int_{-\infty}^{t}\exp\left[-(t-s)/\tau\right]\dot{\boldsymbol{\epsilon}}^{d}(\boldsymbol{x},s)\,ds \\ & +\check{K}\left[\int_{-\infty}^{t}\exp\left[-(t-s)/\tau\right]\operatorname{tr}\dot{\boldsymbol{\epsilon}}(\boldsymbol{x},s)\boldsymbol{I}\,ds\right]\end{aligned} \tag{5.16}$$

If the evolution function is a combination of M symmetric second-order tensor representing the evolution functions, Equation (5.13) is expressed as

$$\begin{aligned}\boldsymbol{\theta}(\boldsymbol{x},t) = {} & \sum_{r=1}^{M}2\check{G}_{r}\left[\int_{-\infty}^{t}\exp\left[-(t-s)\right]/\tau_{r}\right]\dot{\boldsymbol{\epsilon}}^{d}(\boldsymbol{x},s)\,ds\right] \\ & +\sum_{r=1}^{M}\check{K}_{r}\left[\int_{-\infty}^{t}\exp\left[-(t-s)/\tau_{r}\right]\operatorname{tr}\dot{\boldsymbol{\epsilon}}(\boldsymbol{x},s)\boldsymbol{I}\,ds\right]\end{aligned} \tag{5.17}$$

In the preceding equations, G_∞ is the long-term shear moduli, K_∞ is the long-term bulk moduli, $\check{G}_r$ is the viscous shear modulus, $\check{K}_r$ is the viscous bulk modulus, τ_r is the relaxation time, $\boldsymbol{\epsilon}^d$ is the deviatoric strain, $\boldsymbol{I}$ is the second-order identity tensor, $\boldsymbol{\theta}$ is the symmetric second-order tensor representing the evolution function for the internal variables, and the subscript r denotes the number of evolution functions. For more details on the derivation of the rheological model, the reader is referred to [35, 108].

Integration Algorithm for Stress Updating

The second order accurate and unconditionally stable integration algorithm described in this section was first suggested by Taylor *et al*. [113] , and Herrmann *et al*. [58]. The idea is to transform the convolution integral into a two-step recurrence algorithm involving internal variables stored at the integration points of a finite element method. The algorithm is restricted to relaxation functions consisting of linear combination of functions of time and it is described as follows.

Let $[T_0, T] \subset \mathbb{R}^n$, with $T > 0$ and $T > T_0$, be the time interval of interest, where

$$[T_0, T] = \bigcup_{n \in \mathbb{Z}} [t_n, t_{n+1}] \,, \; t_{n+1} = t_n + \triangle t_n \tag{5.18}$$

is a partition of the time interval $[T_0, T]$. Using the following property, $\exp\left[(t + \triangle t)/\tau\right] = \exp\left(\triangle t/\tau\right) \exp\left(t/\tau\right)$, and the additivity property of the integral with respect to the integration interval $[t_n, t_{n+1}]$, a recurrence formula for the evolution function for the internal variables is defined as

$$\boldsymbol{\theta}_r(\boldsymbol{x}, t_{n+1}) = \sum_{r=1}^{M}\left[\exp\left[-\triangle t_n/\tau_r\right]\boldsymbol{\theta}_r(\boldsymbol{x}, t_n) + 2\check{G}_r\int_{t_n}^{t_{n+1}}\exp\left[-\left(t_{n+1}-s\right)/\tau_r\right]\frac{d}{ds}\boldsymbol{\epsilon}^d(\boldsymbol{x}, s)\right]$$
$$+\sum_{r=1}^{M}\left[\exp\left[-\triangle t_n/\tau_r\right]\boldsymbol{\theta}_r(\boldsymbol{x}, t_n) + \check{K}_r\int_{t_n}^{t_{n+1}}\exp\left[-\left(t_{n+1}-s\right)/\tau_r\right]\frac{d}{ds}\,\mathrm{tr}\,\boldsymbol{\epsilon}(\boldsymbol{x}, s)\,\boldsymbol{I}\right] \quad (5.19)$$

The integrals in Equation (5.19) over the time step $[t_n, t_{n+1}]$ is approximated using the midpoint rule as follows

$$2\check{G}_r\int_{t_n}^{t_{n+1}}\exp\left[-\left(t_{n+1}-s\right)/\tau_r\right]\frac{d}{ds}\boldsymbol{\epsilon}^d(\boldsymbol{x}, s)\;ds \quad (5.20)$$
$$\approx 2\check{G}_r\exp\left[-\left(t_n+\triangle t_n-s\right)/\tau_r\right]\frac{d}{ds}\boldsymbol{\epsilon}^d(\boldsymbol{x}, s)\Big|_{s=\frac{t_n+t_{n+1}}{2}}\triangle t_n$$
$$\approx 2\check{G}_r\exp\left[-\triangle t_n/2\tau_r\right]\frac{d}{ds}\boldsymbol{\epsilon}^d\left[(\boldsymbol{x}, t_n+t_{n+1})/2\right]\triangle t_n$$
$$\approx 2\check{G}_r\exp\left[-\triangle t_n/2\tau_r\right]\left[\boldsymbol{\epsilon}^d(\boldsymbol{x}, t_{n+1}) - \boldsymbol{\epsilon}^d(\boldsymbol{x}, t_n)\right]$$

Similarly, the integral for the volumetric part is approximated as

$$2\check{K}_r\int_{t_n}^{t_{n+1}}\exp\left[-\left(t_{n+1}-s\right)/\tau_r\right]\frac{d}{ds}\,\mathrm{tr}\,\boldsymbol{\epsilon}(\boldsymbol{x}s)\,\boldsymbol{I}\,ds \quad (5.21)$$
$$\approx \check{K}_r\exp\left[-\triangle t_n/2\tau_r\right]\left[\mathrm{tr}\,\boldsymbol{\epsilon}(\boldsymbol{x}, t_{n+1}) - \mathrm{tr}\,\boldsymbol{\epsilon}(t_n)\right]\boldsymbol{I}$$

Combining Equations (5.19)–(5.21), the update stress-strain relationships are define as follows

$$\boldsymbol{\sigma}(\boldsymbol{x}, t_{n+1}) = 2G_\infty\boldsymbol{\epsilon}^d(\boldsymbol{x}, t_{n+1}) + K_\infty\left(\mathrm{tr}\,\boldsymbol{\epsilon}(\boldsymbol{x}, t_{n+1})\right)\boldsymbol{I} + \sum_{r=1}^{M}\boldsymbol{\theta}_r(\boldsymbol{x}, t_{n+1}) \quad (5.22)$$

$$\boldsymbol{\epsilon}^d(\boldsymbol{x}, t_{n+1}) = \boldsymbol{\epsilon}(\boldsymbol{x}, t_{n+1}) - \frac{1}{3}\left(\mathrm{tr}\,\boldsymbol{\epsilon}(\boldsymbol{x}, t_{n+1})\right)\boldsymbol{I} \quad (5.23)$$

where the update formula for the evolution function is given by

$$\boldsymbol{\theta}_r(\boldsymbol{x}, t_{n+1}) = \exp[-\triangle t_n/\tau_r]\,\boldsymbol{\theta}_r(\boldsymbol{x}, t_n) + 2\check{G}_r \exp[-\triangle t_n/2\tau_r]\Big[\boldsymbol{\epsilon}^d(\boldsymbol{x}, t_{n+1}) - \boldsymbol{\epsilon}^d(\boldsymbol{x}, t_n)\Big]$$
$$+\exp[-\triangle t_n/\tau_r]\,\boldsymbol{\theta}_r(\boldsymbol{x}, t_n) + \check{K}_r \exp[-\triangle t_n/2\tau_r]\Big[\text{tr}\,\boldsymbol{\epsilon}(\boldsymbol{x}, t_{n+1}) - \text{tr}\,\boldsymbol{\epsilon}(\boldsymbol{x}, t_n)\Big]\boldsymbol{I}. \quad (5.24)$$

For a detailed description on the derivation of this integration algorithm, the reader is referred to [58, 108, 113].

Variational Formulation

Using a weak-form Galerkin approach, an arbitrary virtual displacement field $\boldsymbol{v}(\boldsymbol{x}, t) \in \Omega$ is defined. Taking the product of the virtual displacement field with Equation (5.1) and applying the divergence theorem, the solid variational boundary value problem is defined as

$$\int_\Omega \nabla\boldsymbol{v} : \boldsymbol{\sigma}\, d\Omega + \rho_s \int_\Omega \boldsymbol{v} \cdot \ddot{\boldsymbol{u}}\, d\Omega - \int_\Omega \boldsymbol{v} \cdot \boldsymbol{b}\, d\Omega + \int_{\Gamma_{fs}} \boldsymbol{v} \cdot (p\boldsymbol{n}_s)\, d\Gamma_{fs} = 0,\ \forall\, v \in V \quad (5.25)$$

where the quantities above belong to these function spaces

$$U = \{\boldsymbol{u} : \boldsymbol{u} \in H^1(\Omega), \boldsymbol{u} = \boldsymbol{u}_0 \text{ on } \Gamma_u\} \quad (5.26)$$

$$V = \{\boldsymbol{v} : \boldsymbol{v} \in H_0^1(\Omega), \boldsymbol{v} = 0 \text{ on } \Gamma_u\} \quad (5.27)$$

$$S = \{\boldsymbol{\sigma} : \boldsymbol{\sigma} \in L_2(\Omega)\} \quad (5.28)$$

Similarly, an arbitrary virtual acoustic scalar pressure field $w(\boldsymbol{x}, t) \in \Phi$ is defined. Taking the product of the virtual acoustic scalar pressure field with Equation (5.10) and applying the divergence theorem, the fluid variational boundary value problem is defined as

$$\int_{\Phi} \nabla w \cdot \nabla p \, d\Phi + \frac{\rho_f}{B_f} \int_{\Phi} w \ddot{p} \, d\Phi + \int_{\Gamma_{fs}} w \rho_f \ddot{\boldsymbol{u}}_n^f \, d\Gamma_{fs} = 0, \ \forall \ w \in W \tag{5.29}$$

where the following function spaces are used

$$P = \{p : \ p \in H^1(\Phi), p = p_0 \text{ on } \Gamma_p\} \tag{5.30}$$

$$W = \{p : \ p \in H^1(\Phi), p = 0 \text{ on } \Gamma_p\} \tag{5.31}$$

Discretization

The structural and fluid equations are coupled through their respective external force vectors. The semi-discretized finite element equations for the coupled fluid-structure system can be expressed as

$$[M]\{\ddot{u}(t)\} + \{I(t)\} = \{R(t)\} + [S]\{p(t)\} \tag{5.32}$$

$$\left[M_f\right]\{\ddot{p}(t)\} + \left[K_f\right]\{p(t)\} = -\rho_f [S]^T \{\ddot{u}(t)\} \tag{5.33}$$

where

$$[M] = \sum_{elements} \int_{\Omega} \rho_s [N(\boldsymbol{x})]^T [N(\boldsymbol{x})] \ d\Omega \tag{5.34}$$

$$\{I(t)\} = \sum_{elements} \int_{\Omega} [B(\boldsymbol{x})]^T \{\boldsymbol{\sigma}(\boldsymbol{x}, t)\}\, d\Omega \tag{5.35}$$

$$\{R(t)\} = \sum_{elements} \int_{\Omega} [N(\boldsymbol{x})]^T \{\boldsymbol{b}\}\, d\Omega + \int \Gamma_t [N(\boldsymbol{x})] \{\boldsymbol{t}\}\, d\Gamma_t \tag{5.36}$$

$$\left[M_f\right] = \sum_{elements} \frac{\rho_f}{B_f} \int_{\Phi} [H(\boldsymbol{x})]^T [H(\boldsymbol{x})]\ d\Phi \tag{5.37}$$

$$\left[K_f\right] = \sum_{elements} \int_{\Phi} [F(\boldsymbol{x})]^T [F(\boldsymbol{x})]\ d\Phi \tag{5.38}$$

$$[S] = \sum_{elements} \int_{\Gamma^{fs}} [N(\boldsymbol{x})]^T \boldsymbol{n}_f(\boldsymbol{x}) [H(\boldsymbol{x})]\ d\Gamma_{fs} \tag{5.39}$$

Here, $[M]$ is the solid mass matrix, $\{I(t)\}$ is the internal force vector, $\{R(t)\}$ is the external force vector, $\left[M_f\right]$ is the fluid mass matrix, $\left[K_f\right]$ is the fluid stiffness matrix, $[S]$ is the interaction matrix. The matrices $[N(\boldsymbol{x})]$, $[B(\boldsymbol{x})]$, $[H(\boldsymbol{x})]$, and $[F(\boldsymbol{x})]$ were defined in Chapter 2.

5.2.2 Inverse Problem

Error in the Constitutive Equation

Define a set of admissible fields $(\boldsymbol{u}_D, \boldsymbol{\sigma}_N)$ which minimize

$$J(\boldsymbol{u}_D, \boldsymbol{\sigma}_N, \mathbb{C}) = \frac{1}{2} \sum_{p=1}^{T} \sum_{q=1}^{N} \left(\sigma_N^{pq} - \mathbb{C} : \boldsymbol{\epsilon}\left(\boldsymbol{u}_D^{pq}\right)\right)^2 \tag{5.40}$$

such that $\boldsymbol{u}_N \in \hat{U}$ and $\boldsymbol{\sigma}_N \in \hat{S}$, where

$$\hat{U} = \{\boldsymbol{u}_D : \boldsymbol{u}_D \in H^1(\Omega),\ \boldsymbol{u}_D = \boldsymbol{u}_0 \text{ on } \Gamma_u,\ \boldsymbol{u}_D = \bar{\boldsymbol{u}} \in \bar{\Omega}\ \subset\ \Omega \cup \Gamma\} \tag{5.41}$$

$$\hat{S} = \{\boldsymbol{\sigma}_N : \boldsymbol{\sigma}_N \in L_2(\Omega), \int_\Omega (\nabla v : \boldsymbol{\sigma}_N + \rho_s \boldsymbol{v} \cdot \ddot{\boldsymbol{u}}_N - \boldsymbol{v} \cdot \boldsymbol{b})\, d\Omega + \int_{\Gamma_{fs}} \boldsymbol{v} \cdot (p\boldsymbol{n}_s)\, d\Gamma_{fs} = 0 \text{ in } \Omega\} \tag{5.42}$$

Here $\bar{\Omega}$ is the region in which the experimental displacement field $\bar{\boldsymbol{u}}$ is measured, $\hat{U}$ is the space of kinematic admissible fields, and $\hat{S}$ is the space of dynamic admissible fields.

The set of admissible fields $(\boldsymbol{u}_D, \boldsymbol{\sigma}_N)$ solve the problem defined in Equation (5.22) if and only if $\boldsymbol{u}_D$ and $\boldsymbol{\sigma}_N$ are related through the constitutive Equation (5.4). Hence, $J(\boldsymbol{u}_D, \boldsymbol{\sigma}_N, \mathbb{C}) = 0$ when the relaxation tensor is compatible with the material relaxation tensor.

Identification Approach Based on Alternating Directions

The identification approach based on alternating directions was used for the identification of viscoelastic parameters. The reader is referred to Section 4.2.1 for a detailed description of this identification approach.

Gradient Equation

Let the vector of design variables be defined as

$$\{p\} = \{G_\infty, K_\infty, \check{G}_r, \cdots, \check{G}_r, \check{K}_1, \cdots, \check{K}_r, \tau_1, \cdots, \tau_r\} \tag{5.43}$$

Then, the gradient of the error functional with respect to the vector of design variables is given by

$$\frac{\partial \hat{J}}{\partial G_\infty} = -2 \sum_{p=1}^{T} \sum_{q=1}^{N} \left(\boldsymbol{\sigma}_N^{pq} - \mathbb{C} : \boldsymbol{\epsilon}_D^{pq} \right) : \left(\boldsymbol{\epsilon}^d \right)^{pq} \tag{5.44}$$

$$\frac{\partial \hat{J}}{\partial K_\infty} = - \sum_{p=1}^{T} \sum_{q=1}^{N} \left(\boldsymbol{\sigma}_N^{pq} - \mathbb{C} : \boldsymbol{\epsilon}_D^{pq} \right) : \left(\mathrm{tr} \left(\boldsymbol{\epsilon}_D^{pq} \right) \boldsymbol{I} \right) \tag{5.45}$$

$$\frac{\partial \hat{J}}{\partial G_r^v} = -2 \sum_{p=1}^{T} \sum_{q=1}^{N} \sum_{r=1}^{M} \left(\boldsymbol{\sigma}_N^{pq} - \mathbb{C} : \boldsymbol{\epsilon}_D^{pq} \right) : \left(\beta_r \left(\triangle \boldsymbol{\epsilon}_D^d \right)^{pq} \right) \tag{5.46}$$

$$\frac{\partial \hat{J}}{\partial K_r^v} = - \sum_{p=1}^{T} \sum_{q=1}^{N} \sum_{r=1}^{M} \left(\boldsymbol{\sigma}_N^{pq} - \mathbb{C} : \boldsymbol{\epsilon}_D^{pq} \right) : \left(\beta_r \left(\triangle \boldsymbol{\epsilon}_D^v \right)^{pq} \right) \tag{5.47}$$

$$\begin{aligned} \frac{\partial \hat{J}}{\partial \tau_r} &= -2 \sum_{p=1}^{T} \sum_{q=1}^{N} \sum_{r=1}^{M} \left(\boldsymbol{\sigma}_N^{pq} - \mathbb{C} : \boldsymbol{\epsilon}_D^{pq} \right) : \left(\frac{\partial \boldsymbol{\theta}_r^d \left(t_{n+1} \right)}{\partial \tau_r} \left(\triangle \boldsymbol{\epsilon}_D^d \right)^{pq} \right) \\ &- \sum_{p=1}^{O} \sum_{q=1}^{N} \sum_{r=1}^{M} \left(\boldsymbol{\sigma}_N^{pq} - \mathbb{C} : \boldsymbol{\epsilon}_D^{pq} \right) : \left(\frac{\partial \boldsymbol{\theta}_r^v \left(t_{n+1} \right)}{\partial \tau_r} \left(\triangle \boldsymbol{\epsilon}_D^v \right)^{pq} \right) \end{aligned} \tag{5.48}$$

where

$$\triangle \boldsymbol{\epsilon}_D^d = \left[\boldsymbol{\epsilon}_D^d \left(t_{n+1} \right) - \boldsymbol{\epsilon}_D^d \left(t_n \right) \right] \tag{5.49}$$

$$\triangle \boldsymbol{\epsilon}_D^v = \left[\mathrm{tr}\ \boldsymbol{\epsilon} \left(\boldsymbol{x}, t_{n+1} \right) - \mathrm{tr}\ \boldsymbol{\epsilon} \left(\boldsymbol{x}, t_n \right) \right] \boldsymbol{I} \tag{5.50}$$

$$\beta_r = \exp \left[- \triangle t_n / 2 \tau_r \right] \tag{5.51}$$

$$\frac{\partial \boldsymbol{\theta}_r^d \left(t_{n+1} \right)}{\partial \tau_r} = \frac{\boldsymbol{\theta} \left(t_n \right) \triangle t_n}{\tau_r^2} \exp \left(- \frac{\triangle t_n}{\tau_r} \right) + \frac{\check{G}_r \triangle t_n}{2 \tau_r^2} \exp \left(- \frac{\triangle t_n}{2 \tau_r} \right) \tag{5.52}$$

$$\frac{\partial \boldsymbol{\theta}_r^v \left(t_{n+1} \right)}{\partial \tau_r} = \frac{\boldsymbol{\theta} \left(t_n \right) \triangle t_n}{\tau_r^2} \exp \left(- \frac{\triangle t_n}{\tau_r} \right) + \frac{\check{K}_r \triangle t_n}{2 \tau_r^2} \exp \left(- \frac{\triangle t_n}{2 \tau_r} \right) \tag{5.53}$$

In the preceding equations N is the total number of integration points and T is the total number of time intervals.

5.2.3 Algorithm

The following algorithm may be used in each iteration of the minimization process to compute the optimal viscoelastic properties. The optimization strategy is divided into the following steps described as follows:

1. Quantify Error in Constitutive Equation

i. For $\mathbb{C} = \mathbb{C}_m$, solve Equations (5.25) and (5.29) to evaluate $\boldsymbol{u}_D$ and $\boldsymbol{u}_N$. The subscript m denotes the current outer iteration number.

ii. Evaluate the error in constitutive equation defined in Equation (5.40) and check stopping criteria. If one of the stopping criteria is satisfied, optimal solution computed. If none of the stopping criteria are satisfied, go to Step 2 and correct error in constitutive equation.

2. Correct Error in Constitutive Equation

iv. Solve Equations (5.44) - (5.48) to compute the gradient and evaluate the error in constitutive equation defined in Equation (5.40).

v. Update design variables.

vi. Check stopping criteria, if one of the stopping criteria is satisfied go to Step 1 and compute $\boldsymbol{u}_D^h$ and $\boldsymbol{u}_N^h$. If none of the stopping criteria is satisfied, continue iterating until one is satisfied.

Figure 4.1 shows a pictorial description of the algorithm described above.

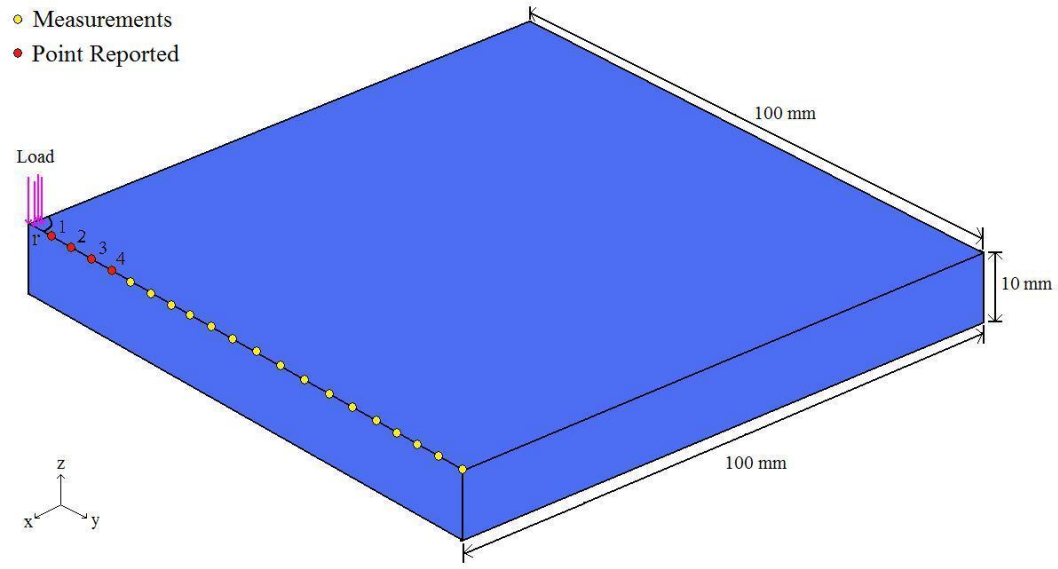

(a) Three Dimensional Model

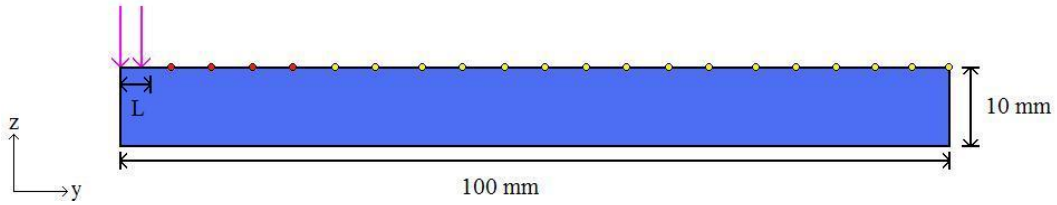

(b) Axisymmetric Model

Figure 5.1: Schematic of the finite element model used for the simulated example problems.

5.3 Results and Discussion

A simulated experiment was solved to test the potential of the proposed inverse approach to inversely characterize viscoelastic parameters of solids. To validate the methodology in a realistic setting, in-vivo displacement measurements from a pig myocardium were used to characterize the viscoelastic properties. A limited memory BFGS algorithm was used to solve minimization problem in Step 2. For the physical and simulated experiments, the maximum number of outer iterations was set to 25 and the maximum number of inner iterations was set

to 10. Within each iteration of the minimization problem several sub-iterations may be made to the routine to evaluate the cost function and compute the gradient. The number of sub-iterations was set to 5 for the physical and simulated experiments. All calculations were performed on a Linux workstation with a 1.86-GHz Intel processor and 16 GB of RAM. The reader is referred to Section 4.3.3 for the description of outer and inner iterations.

5.3.1 Simulated Experiment

A 3-D finite element model was built using the finite element package ABAQUS/Standard [1] with twenty-node quadratic brick finite elements to generate the experimental data for the inverse problem. The domain had dimensions $\Omega = 100\ mm \times 100\ mm \times 10\ mm$. The solid was excited with a pressure force of magnitude $p_z = 1 \times 10^6\ Pa$. The pressure was applied on a quarter-circle with radius $r = 3.5 \times 10^{-4}$ along the z-direction. The density of the material was taken as 1000 kg/m^3. The material properties were taken to simulate those found in soft tissue [33, 54, 63, 76, 88, 114]. The long-term shear and bulk moduli were taken as $1.071 \times 10^5\ Pa$ and $5.0 \times 10^5\ Pa$, respectively. Two evolution functions were used to account for the viscous effects in the shear modulus. The viscous shear modulus and the relaxation time were taken as $\left[G_1^v = 1.191 \times 10^5\ Pa,\ G_2^v = 1.191 \times 10^4\right]$ and $\left[\tau_1 = 1.0 \times 10^{-2}\ sec.,\ \tau_2 = 1.0 \times 10^{-1}\ sec.\right]$, respectively. The total simulation time considered was $2.0 \times 10^{-3}\ sec.$ in steps of $\triangle t = 6.7 \times 10^{-5}\ sec$. Displacements were measured in twenty points; then, used to solve the inverse problem. Figure 5.1.a shows a pictorial description of the simulated experiment used to generate the experimental data.

Table 5.1: Design Variables Upper and Lower Bounds

Design Variable	Lower Bound	Upper Bound
G_∞	$5.0 \times 10^4\ Pa$	$5.0 \times 10^5\ Pa$
K_∞	$1.0 \times 10^5\ Pa$	$1.0 \times 10^6\ Pa$
G_1^v	$5.0 \times 10^4\ Pa$	$5.0 \times 10^5\ Pa$
G_2^v	$5.0 \times 10^3\ Pa$	$5.0 \times 10^4\ Pa$
τ_1	$5.0 \times^{-3}\ sec$	$5.0 \times 10^{-2}\ sec$
τ_2	$5.0 \times^{-2}\ sec$	$5.0 \times 10^{-1}\ sec$

If the system response does not reflect from the boundaries, the three-dimensional finite element model could be approximated with an axisymmetric model, given that the load and material properties are axially symmetric. As a result, the computational cost of one forward run is minimize. For these reasons, an axisymmetric finite element model was built using the finite element package ABAQUS/Standard [1] with eight-node biquadratic axisymmetric quadrilateral finite elements to solve the inverse problem. The domain had dimensions $\Omega = 100\ mm \times 10\ mm$. The solid body was excited with a pressure force applied on $z = 10\ mm$ with $L = 3.5{\times}10^{-4}\ mm$. The magnitude of the pressure force and the material density were similar to those used to generate the experimental data. Displacements were measured at exactly the same location as the points used to generate the experimental data. Figure 5.1.b shows a pictorial description of the 2-D axisymmetric finite element model. For simplification, the number of evolution functions for the internal variables was fixed a priori to two for the inverse problem. Moreover, the bulk viscous effects were assumed negligible for this example problem. As a result, the design variables to be identified were

the long-term shear moduli, long-term bulk moduli, two shear viscous modulus, and two relaxation time for a total of six design variables for the inverse problem. Table 5.1 shows the upper and lower bounds considered for the design variables.

The efficiency of the proposed inverse approach was quantified by calculating the discrete ℓ_2-error of the displacement time response, equivalent shear modulus frequency spectrum, and dissipation factor frequency spectrum. The discrete ℓ_2-error is defined as

$$\ell_2 = \frac{\|q_{bm} - q_{appx}\|_{\ell_2}}{\|q_{bm}\|_{\ell_2}} \times 100 \tag{5.54}$$

were $\|q\|_{\ell_2} = \sqrt{\sum_{i=1}^{T}\sum_{j=1}^{U} |\boldsymbol{q}^{ij}|^2}$, $|\cdot|$ denotes absolute value, $\boldsymbol{q}^{bm}$ is the benchmark quantity of interest (e.g. displacements response, dissipation factor frequency spectrum, etc.), $\boldsymbol{q}^{appx}$ is the inverse quantity of interest, T is the total number of time intervals, and U is the total number of measurement points.

Results

The initial guess was $G_\infty = 4 \times 10^5\ Pa$, $K_\infty = 9 \times 10^5\ Pa$, $\check{G}_1 = 4 \times 10^5\ Pa$, $\check{G}_2 = 4 \times 10^4\ Pa$, $\tau_1 = 4.0 \times 10^{-2}\ sec$, and $\tau_2 = 4.0 \times 10^{-1}\ sec$. The quality of the proposed inverse approach can be judged based on two factors; first, accuracy of the equivalent shear modulus and dissipation factor frequency spectrum. Second, accuracy of the displacement time response. Hence, the quality of the solution is best appreciated from the displacement time response and the frequency spectra, rather than computing the percentage error for each design

variable.

The dissipation factor and equivalent shear modulus are complete measures of the viscoelastic properties of the material, these quantities are defined as

$$\tan(\delta) = \sum_{r=1}^{M} \check{G}_r \frac{\omega^2 \tau_r^2}{1+\omega^2\tau_r^2} \Bigg/ \sum_{r=1}^{M} \check{G}_r \frac{\omega\tau_r}{1+\omega^2\tau_r^2} \tag{5.55}$$

$$G_{eq} = \sqrt{\left[\sum_{r=1}^{M} \check{G}_r \frac{\omega^2 \tau_r^2}{1+\omega^2\tau_r^2}\right]^2 + \left[\sum_{r=1}^{M} \check{G}_r \frac{\omega\tau_r}{1+\omega^2\tau_r^2}\right]^2} \tag{5.56}$$

, respectively. Here G_{eq} is the equivalent shear modulus, $\tan(\delta)$ is the dissipation factor, and ω is the angular frequency. Figure 5.2 shows the equivalent shear modulus and dissipation factor frequency spectrum. The plots reveal that the frequency spectra obtained with the inverse solution are close to the benchmark frequency spectrum. Moreover, the discrete ℓ_2-errors for G_{eq} and $\tan(\delta)$ were 4.12% and 8.02%, respectively. These results indicate that the proposed methodology accurately characterize the viscoelastic properties.

A forward finite element problem was solved using the inverse solution and the displacement response was measured at each measurement point (see Figure 5.1). Figure 5.3 shows the displacement time response for four of the twenty measurements points used for the inverse problem. The plots show that each component of the displacement time responses was accurately recovered. The discrete ℓ_2-error was 5.75%, which indicate that the displacement time response was accurately recovered for each measurement point.

Overall, results show that the proposed ECE approach can effectively char-

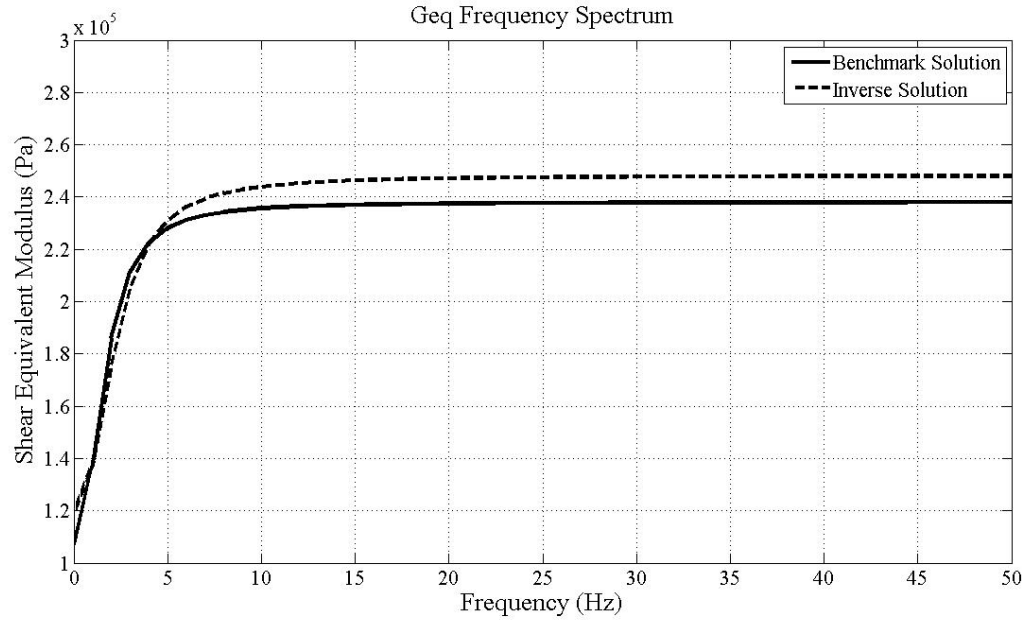

(a) Equivalent shear modulus

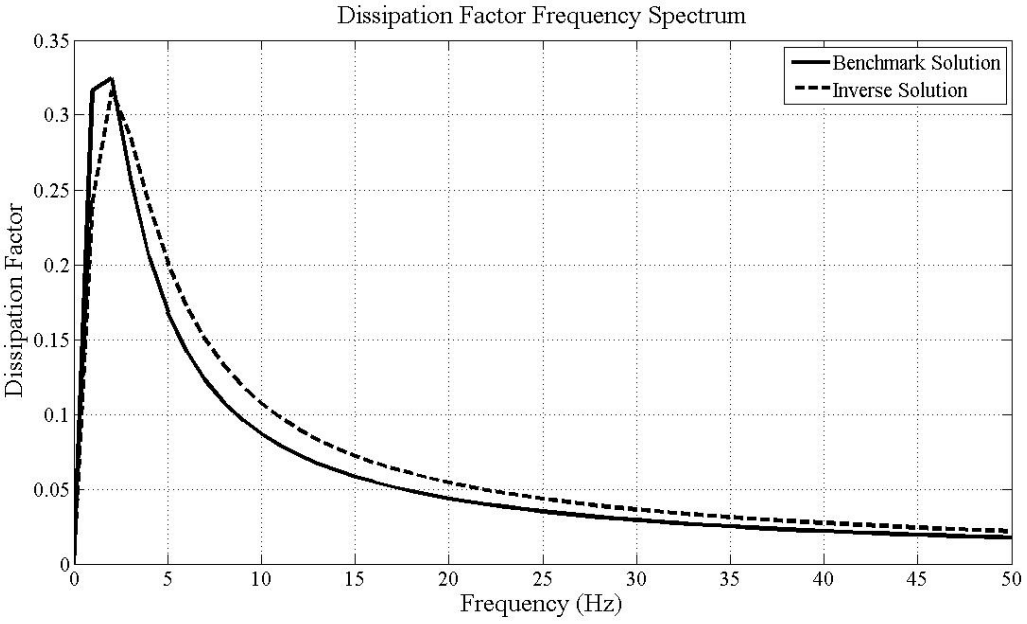

(b) Dissipation factor

Figure 5.2: Material frequency response of the (a) equivalent shear modulus and (b) dissipation factor

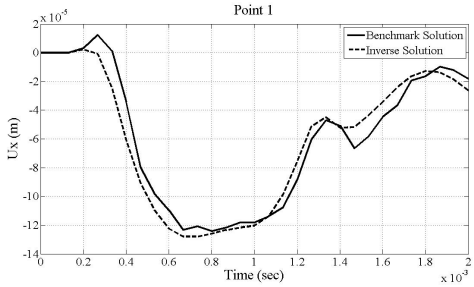

(a) Point 1 *x-dir* displacement

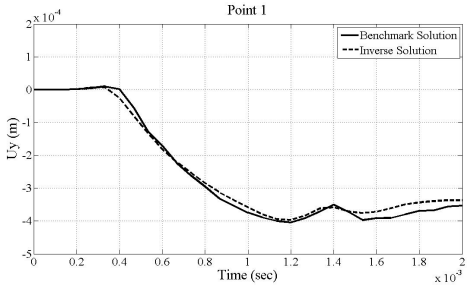

(b) Point 1 *y-dir* displacement

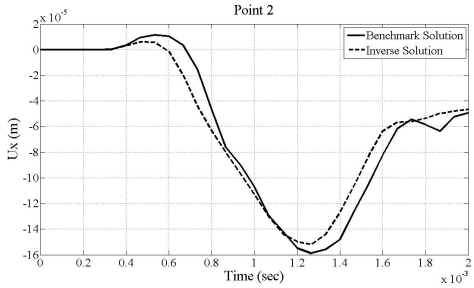

(c) Point 2 *x-dir* displacement

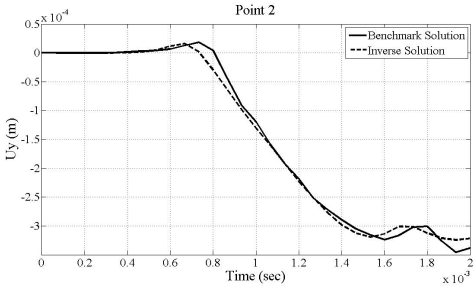

(d) Point 2 *y-dir* displacement

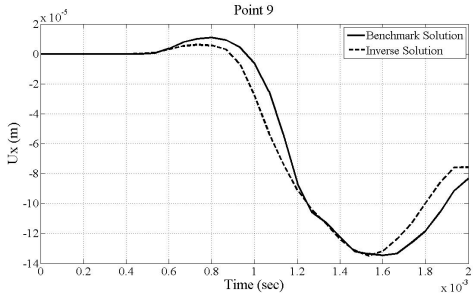

(e) Point 3 *x-dir* displacement

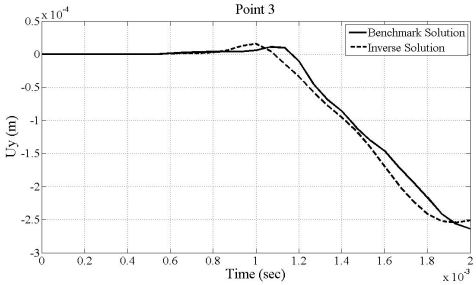

(f) Point 3 *y-dir* displacement

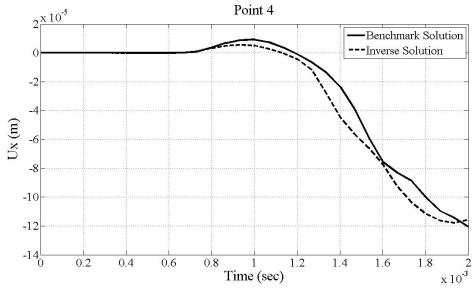

(g) Point 4 *x-dir* displacement

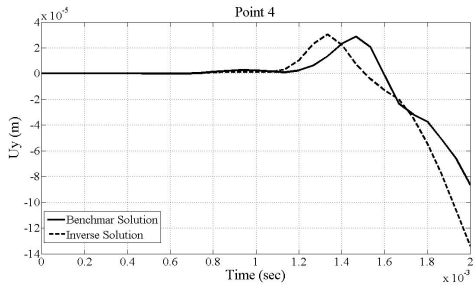

(h) Point 4 *y-dir* displacement

Figure 5.3: Inverse solution versus benchmark solution displacement response for the four measurement points reported.

acterize viscoelastic parameters of solids. Furthermore, when the response is radially symmetric, accurate results are attained with an axisymmetric finite element model. This assumption reduces the computational cost of each finite element forward run. However, this assumption holds as long as the measured response does not reflect back into the region of interest (ROI). In the next section, in-vivo experimental data from a pig myocardium is used to test the potential of the proposed methodology in a realistic setting.

5.3.2 Physical Experiment

Description

An open-chest protocol was used as approved by our Institutional Animal Care and Use Committee. Using the principles of Shearwave Dispersion Ultrasound Vibrometry [22, 23], which measures the change in shear wave velocity with frequency, our collaborators at the Department of Physiology and Biomedical Engineering at the Mayo Clinic College of Medicine designed an experiment that used a mechanical shaker with a 6 mm diameter ball bearing attached to a rod to induce motion into the heart wall. The shaker (V203, Ling Dynamic Systems Limited, Hertfordshire, UK) was driven with a signal generator (33120A, Agilent, Santa Clara, CA) and an amplifier (XLS 202, Crown Audio, Inc., Elkhart, IN). The motion was measured using a high frame rate acquisition sequence using an Ultrasonix Sonix RP system (Sonix RP, Ultrasonix Medical Corporation, Richmond, BC, Canada). The motion was captured using an M-mode type scheme with multiple lines, separated by 0.9 mm. Frame rates were on the order of 2500 Hz. The linear array transducer was first wrapped in a latex cover filled

with ultrasound gel, then another cover filled with water to provide a stand-off. The rod attached to the shaker was centered in the B-mode imaging plane and the sequence was defined to measure waves propagating along the length of the array. The rod was positioned on the mid-anterior left ventricular wall. Care was taken to avoid obstructing the main coronary arteries and branches. Figure 5.4 shows a pictorial description of the experimental setup.

Radiofrequency (RF) data were acquired for one heart cycle. The initiation of the vibration and data acquisition was gated on the electrocardiographic (ECG) R-wave. The data were saved and processed offline using cross-spectral analysis and Kalman filtering to obtain motion and phase of the vibration for discrete segments in space and time [57, 119].

Finite Element Model

In the physical experiment, the load was applied such that the system response was asymmetrical, and measurements were taken before the system response reflected back into the ROI. Furthermore, given that the measurements were taken in a small localized region, it was assumed that the material properties were homogeneous inside the ROI. Therefore, a 2-D finite element model was built using the finite element package ABAQUS/Standard [1] with eight-node biquadratic axisymmetric quadrilateral linear pressure hybrid finite elements for the solid and four-node axisymmetric linear finite elements for the water. Five-node quadratic axisymmetric solid continuum infinite elements and two-node linear axisymmetric acoustic infinite elements were used along the solid and water boundaries, respectively. The body was excited by applying the in-vivo displacement obtained through vibroacoustics based techniques at point

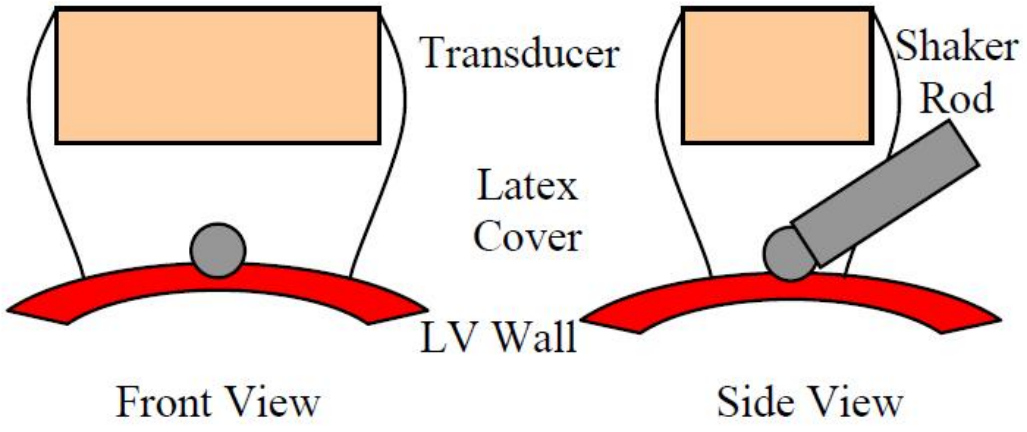

(a) Experimental Setup

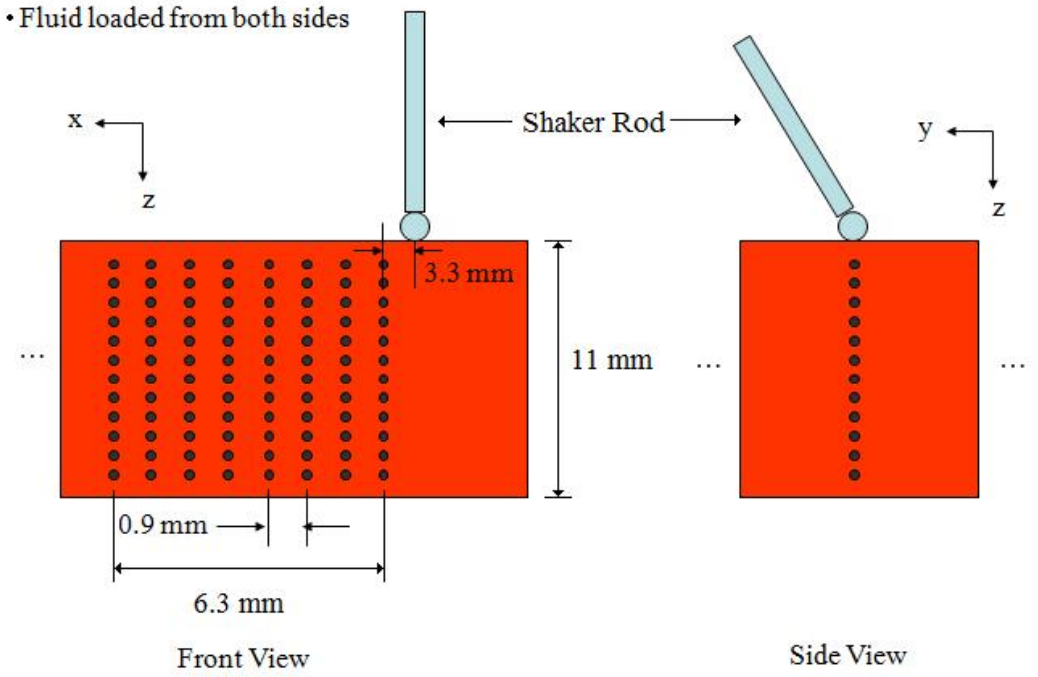

(b) Heart Geometry

Figure 5.4: (a) Experimental setup and (b) heart geometry. A rod with a ball bearing was attached to the mechanical shaker. The ball bearing was placed onto the surface of the myocardial wall. A linear array transducer was suspended above the heart wall and coupled with a water-filled latex cover

(0 mm, 11 mm) in the finite element model. The displacement time response for seven points were measured along $y = 11$ mm and used to inversely characterized the viscoelastic properties. Only the y–component of the displacement time response was measured and used for the inverse problem. Figure 5.5 shows a pictorial description of the finite element model used to represent the physical experiment.

Table 5.2: Design Variables Upper and Lower Bounds for the Physical Experiment

Design Variable	Lower Bound	Upper Bound
G_∞	1.0×10^4 Pa	4.0×10^4 Pa
K_∞	1.0×10^6 Pa	1.0×10^8 Pa
$\check{G}_1$	1.0×10^4 Pa	1.0×10^5 Pa
$\check{G}_2$	1.0×10^3 Pa	1.0×10^4 Pa
τ_1	1.0×10^{-5} sec	1.0×10^{-1} sec
τ_2	1.0×10^{-5} sec	1.0×10^{-1} sec

The ROI had dimensions $H = 11$ mm and $L = 6.3$ mm. The density of the solid was assumed known and taken as 1000 kg/m^3. The properties of the surrounding water were assumed to be known, with density and bulk modulus of 1000 kg/m^3 and 2.2 GPa, respectively. The total time considered was 9.976×10^{-2} sec. in steps of $\triangle t = 3.959 \times 10^{-4}$ sec. Convergence studies were done using the lower bound for each design variable until the displacement time response ℓ_2-error reached 5%.

In the present study, the bulk modulus is assumed purely elastic and the bulk viscous effects are considered negligible. For simplification, the number of

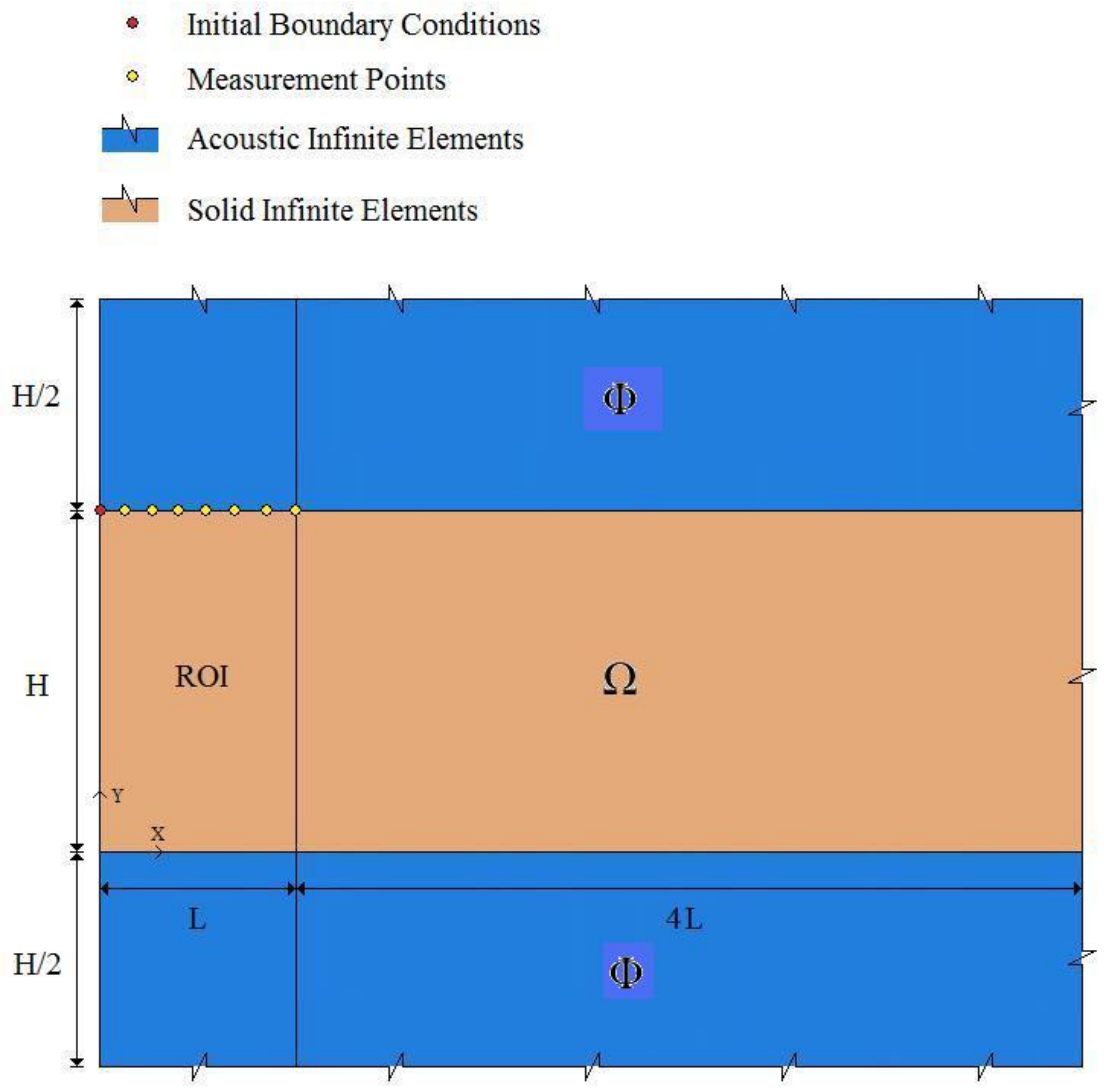

Figure 5.5: Schematic the numerical model geometry for the physical experiment.

evolution functions for the internal variables was fixed a priori to two for the inverse problem. Through mechanical testings of materials commonly used to represent soft tissue, we have observed that the viscoelastic behavior of such materials can be represented with two to three evolution functions. Therefore, taking into consideration that the bulk modulus was assumed purely elastic, the

Table 5.3: Inverse Solution for the Physical Experiment and $f = 200, 250, 300, 350, 400, 450$ and $500\ Hz$

	$K_\infty\ (Pa)$	$G_S\ (Pa)$	$G_L\ (Pa)$	$G_{eq}\ (Pa)$	$\tan(\delta)$
$200\ Hz$	1.045×10^6	18.96×10^3	11.59×10^3	22.22×10^3	3.114×10^{-1}
$250\ Hz$	1.012×10^6	21.67×10^3	8.625×10^3	23.32×10^3	3.980×10^{-1}
$300\ Hz$	1.084×10^6	31.25×10^3	38.23×10^3	38.23×10^3	7.043×10^{-1}
$350\ Hz$	1.072×10^6	33.82×10^3	25.68×10^3	33.82×10^3	8.568×10^{-1}
$400\ Hz$	1.059×10^6	36.46×10^3	26.42×10^3	45.03×10^3	7.246×10^{-1}
$450\ Hz$	1.072×10^6	41.87×10^3	27.40×10^3	50.04×10^3	6.545×10^{-1}
$500\ Hz$	1.299×10^6	69.15×10^3	17.56×10^3	67.40×10^3	4.372×10^{-1}

design variables to be identified were the long-term shear moduli, long-term bulk moduli, two shear viscous modulus, and two relaxation time, for a total of six design variables for the inverse problem. Tables 5.2 show the upper and lower bounds considered for the design variables. The optimization strategy shown in Figure 5.1 was used to solve the resulting inverse problem.

Results

A batch or inline approach can be use for the characterization of viscoelastic properties. In the batch approach, all the signals are used at once to characterize the material properties; thus, identifying the optimal set of viscoelastic properties that best describe the relaxation process in the material. However, more evolution functions are needed to describe the relaxation process in the material, increasing the complexity of the inverse problem. In an inline approach, one set of viscoelastic properties is characterize for each frequency. By dividing

the inverse problem into smaller problem, the complexity of the inverse problem is minimize. The disadvantage is that one set of viscoelastic properties can not be inversely characterize. However, this set could be obtained by fitting the viscoelastic parameters for the Generalized Maxwell model to the experimental results (i.e. shear equivalent modulus and dissipation factor spectrum). In the present work, the inline approach was chosen over the batch approach.

The initial guess was $G_\infty = 2.5 \times 10^4\ Pa$, $K_\infty = 50.5 \times 10^6\ Pa$, $\check{G}_1 = 5.5 \times 10^4\ Pa$, $\check{G}_2 = 5.5{\times}10^3\ Pa$, $\tau_1 = 5.0{\times}10^{-2}\ sec.$, and $\tau_1 = 5.0{\times}10^{-2}\ sec.$ for each frequency. Table 5.3 show the inverse solution obtain for each frequency. The material properties obtained in the present work are comparable with those reported for the myocardium and soft tissues in the literature. For instance, Kanai [63] reported values of 30 kPa, for the shear elasticity of human myocardium for a frequency range of $20 - 90\ Hz$. However, a Voigt material model was used to represent the relaxation process in [63]. Furthermore, the in-vivo experimental data in the present work was for swine myocardium. Therefore, these factors will cause discrepancies between the results reported herein and the results reported by Kanai.

Figure 5.6 shows the resulting equivalent shear modulus and dissipation factor frequency spectrum. The plots capture the material rate dependent behavior. Indeed, the equivalent shear modulus increases with frequency and should reach a steady state value, although the results do not show this. Figures 5.7-5.13 show the displacement time response for each frequency . Notice that the experimental and approximated time responses have similar wavenumber; thus, the material properties found through the inverse problem should be close to

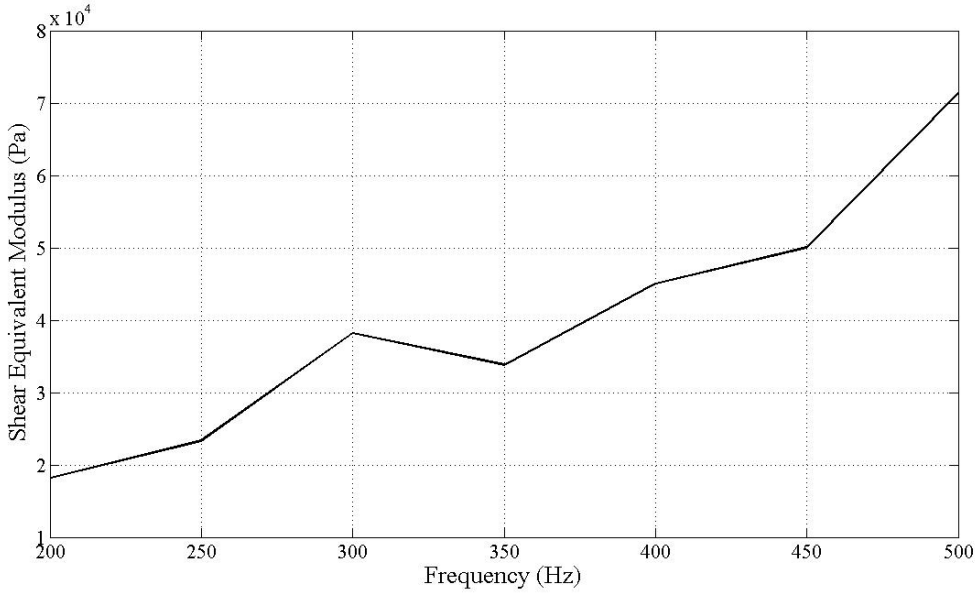

(a) Equivalent shear modulus

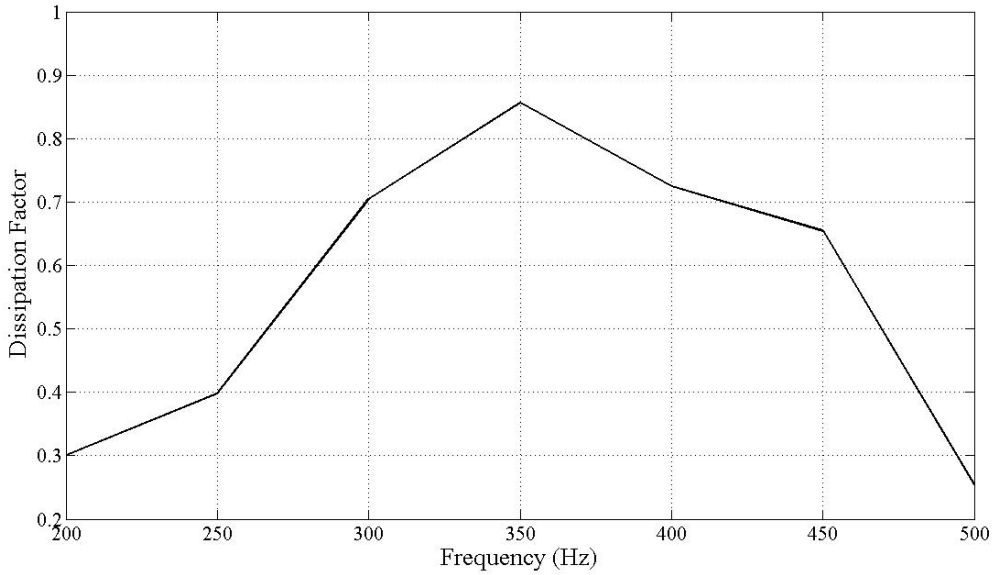

(b) Dissipation factor

Figure 5.6: (a) Equivalent shear modulus and (b) dissipation factor frequency response

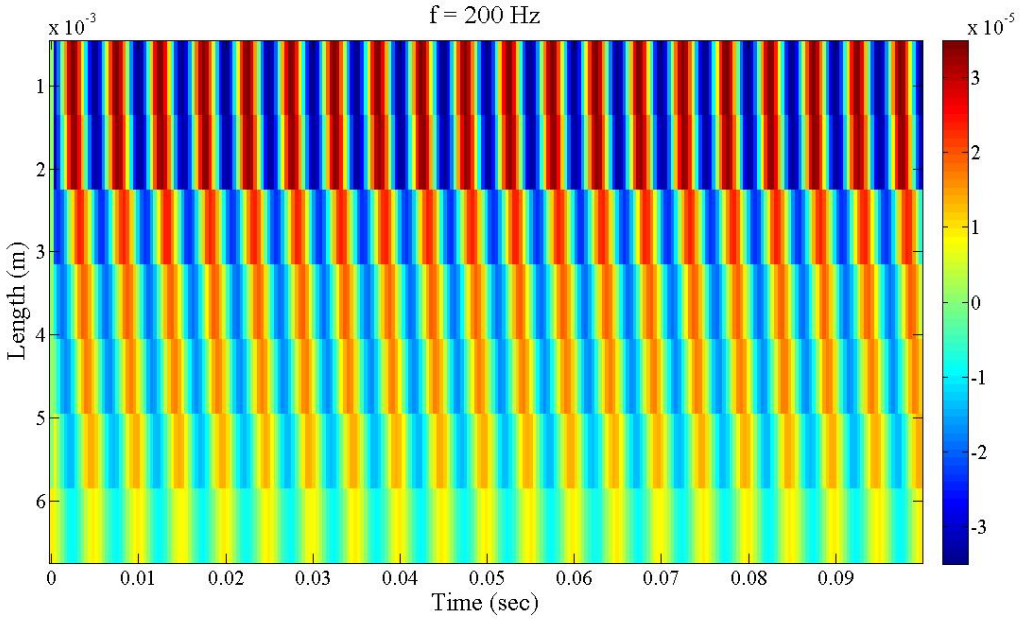

(a) Experiment

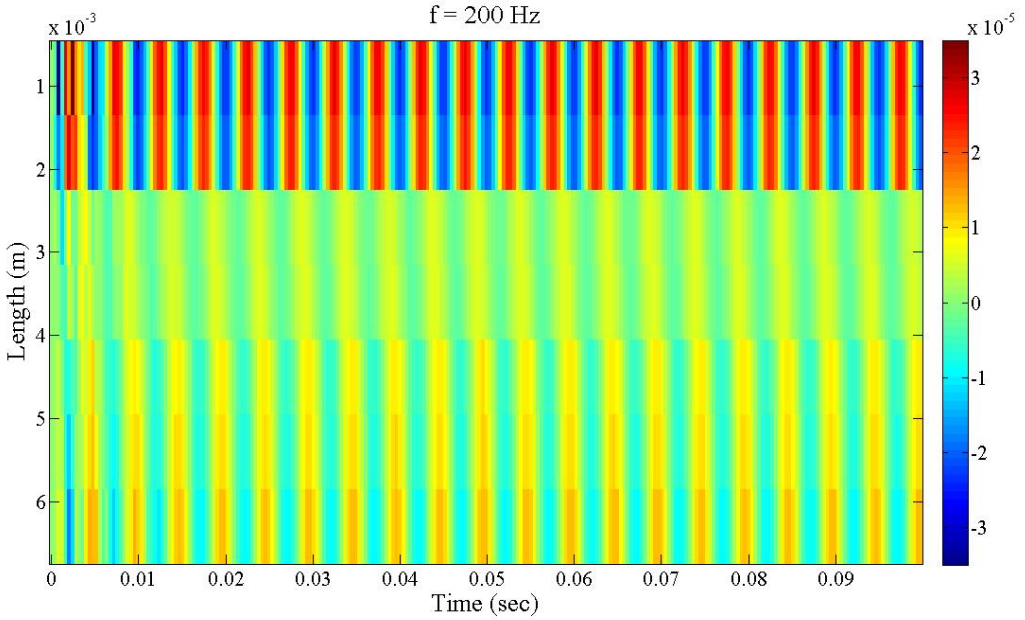

(b) Simulation

Figure 5.7: Displacement time response for $f = 200\ Hz$.

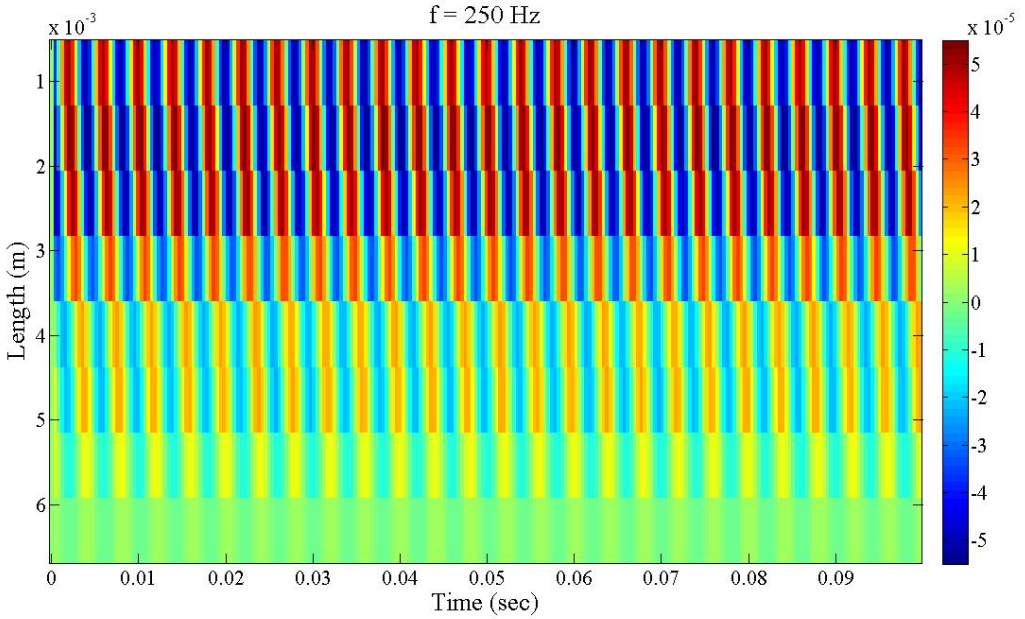

(a) Experiment

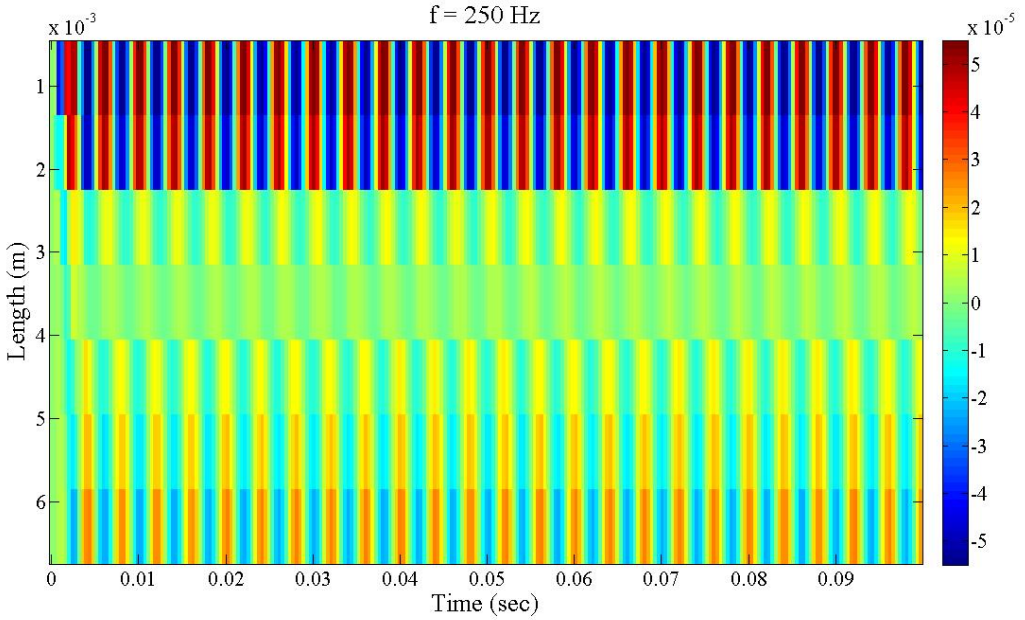

(b) Simulation

Figure 5.8: Displacement time response for $f = 250\ Hz$.

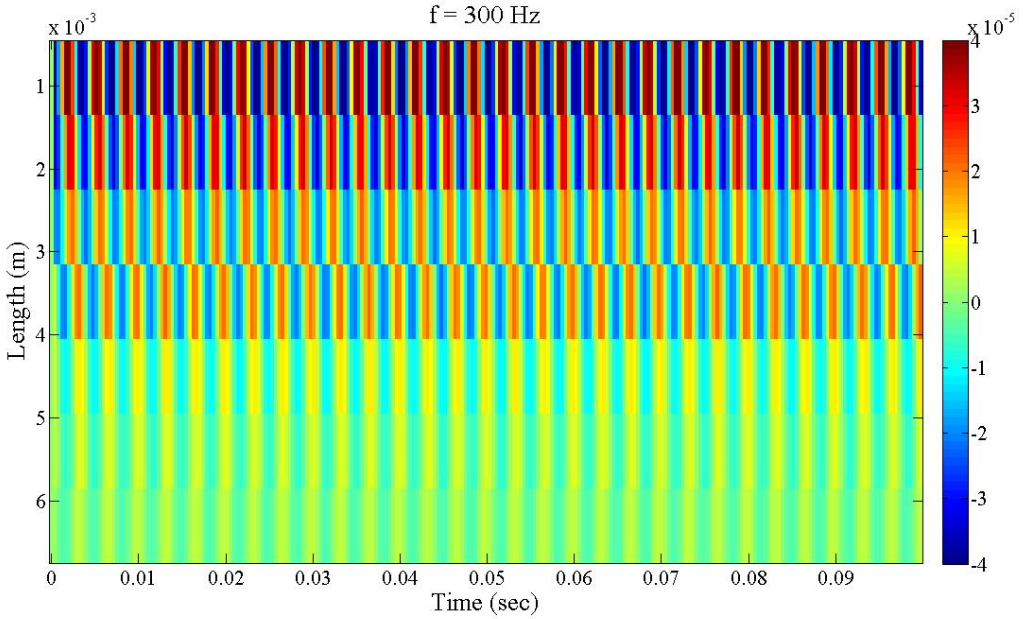

(a) Experiment

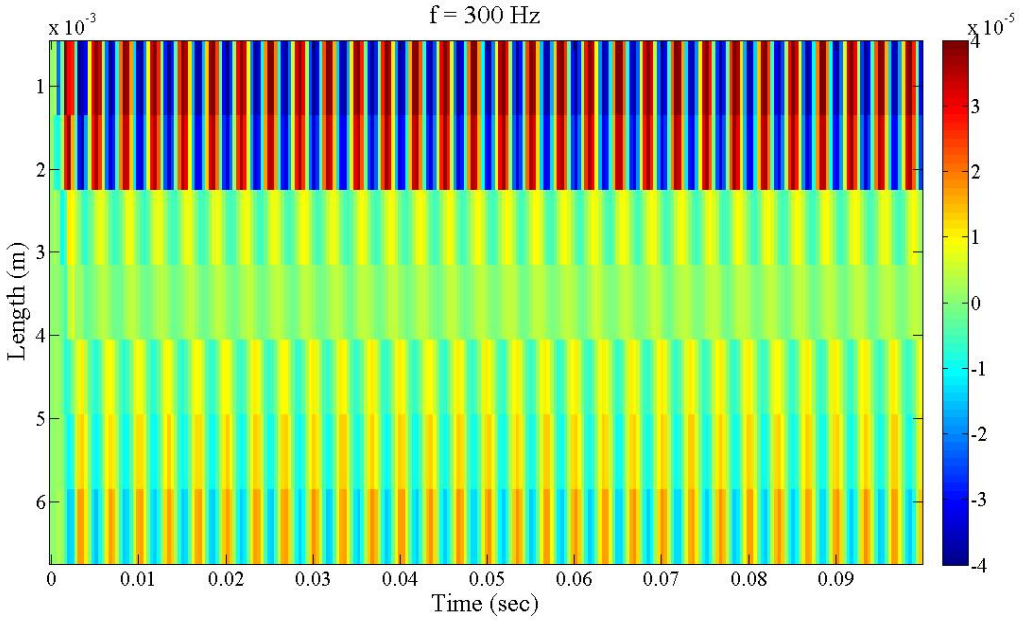

(b) Simulation

Figure 5.9: Displacement time response for $f = 300\ Hz$.

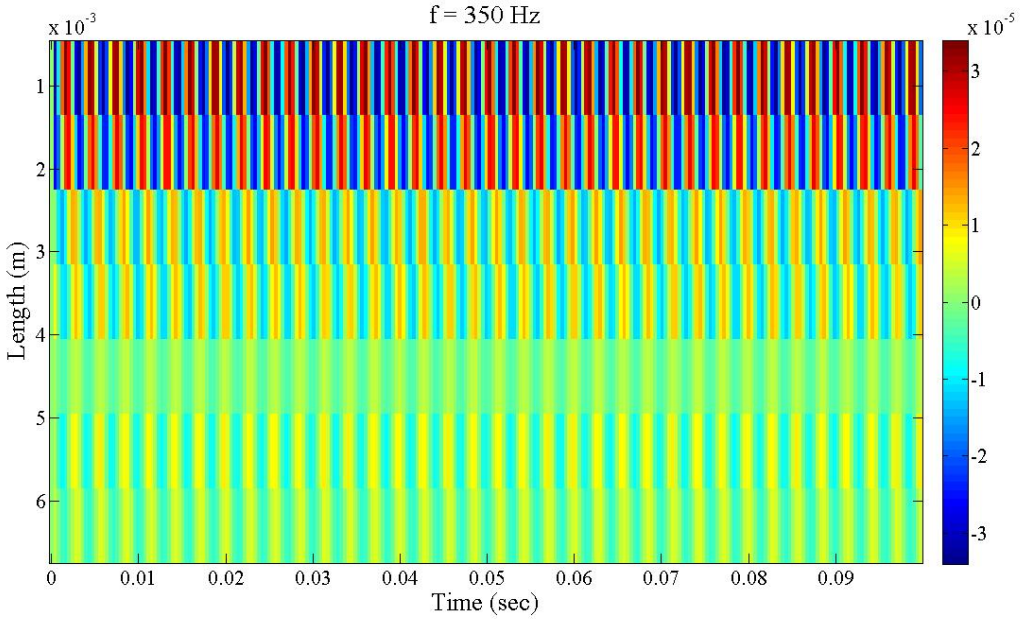

(a) Experiment

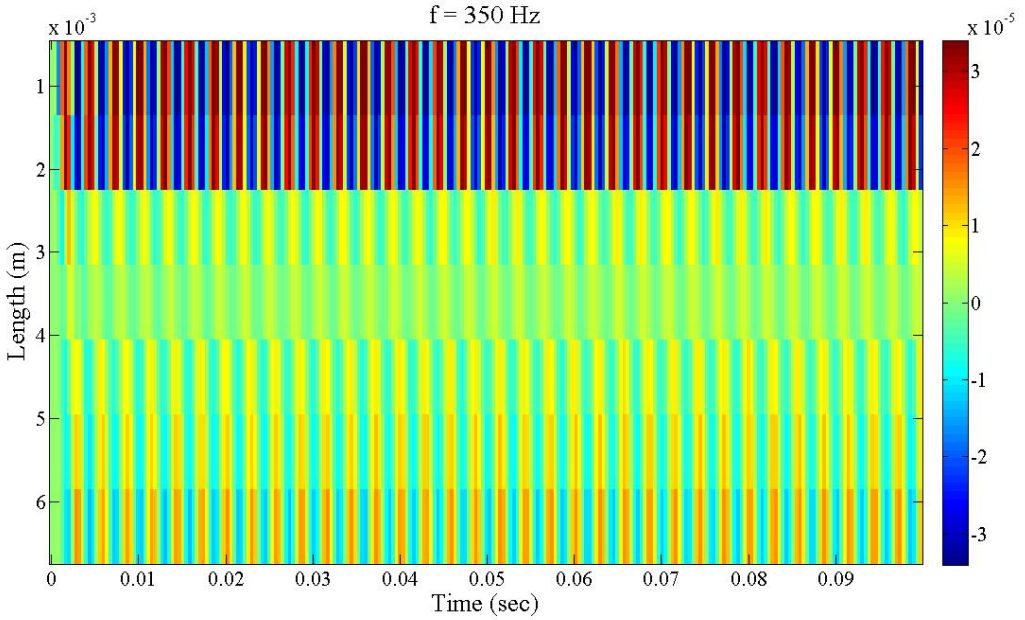

(b) Simulation

Figure 5.10: Displacement time response for $f = 350\ Hz$.

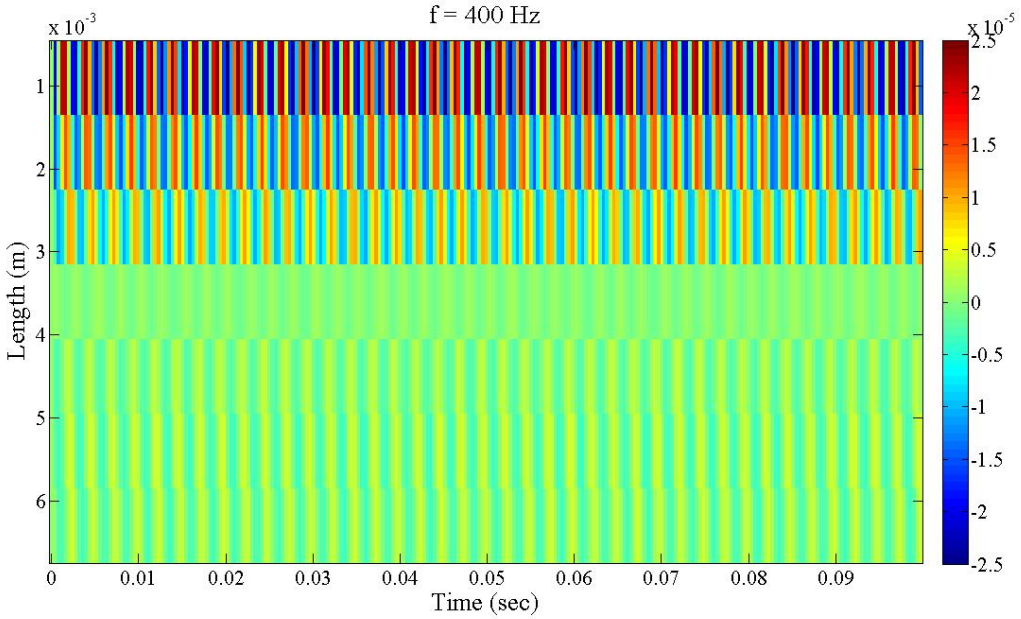

(a) Experiment

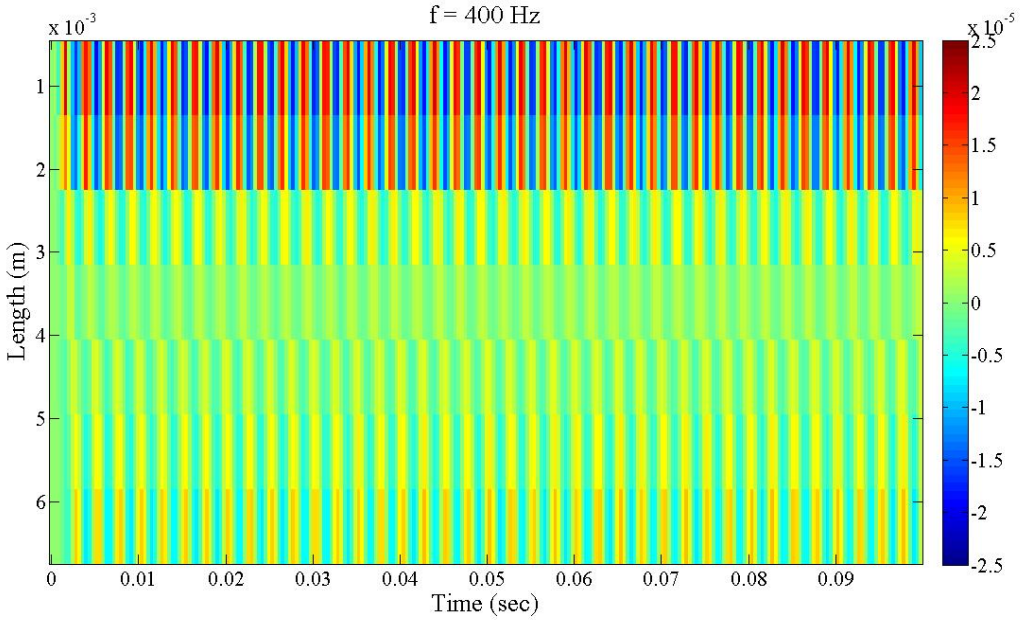

(b) Simulation

Figure 5.11: Displacement time response for $f = 400\ Hz$.

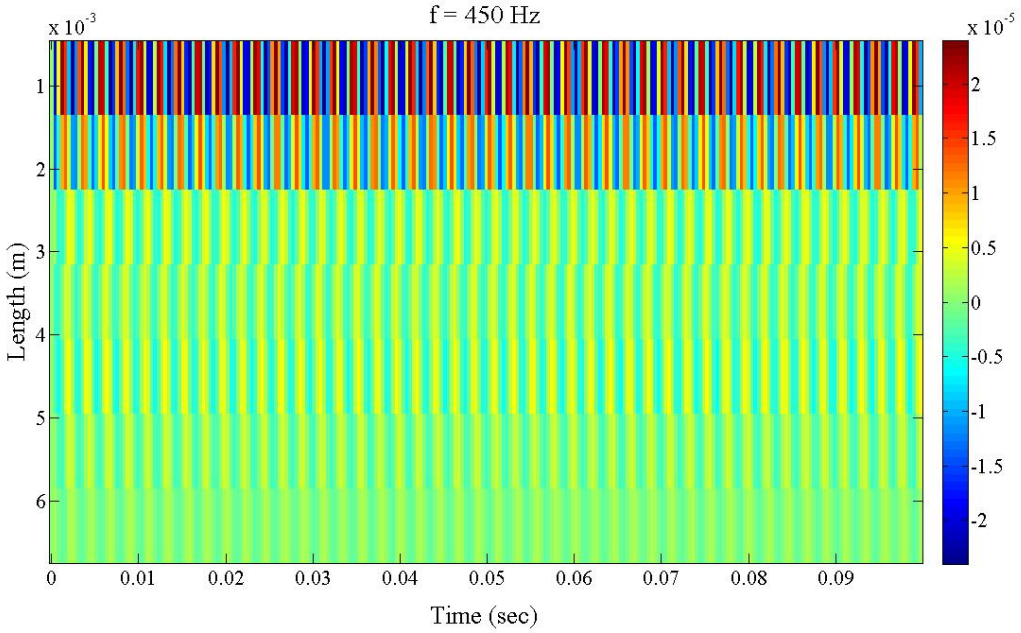

(a) Experiment

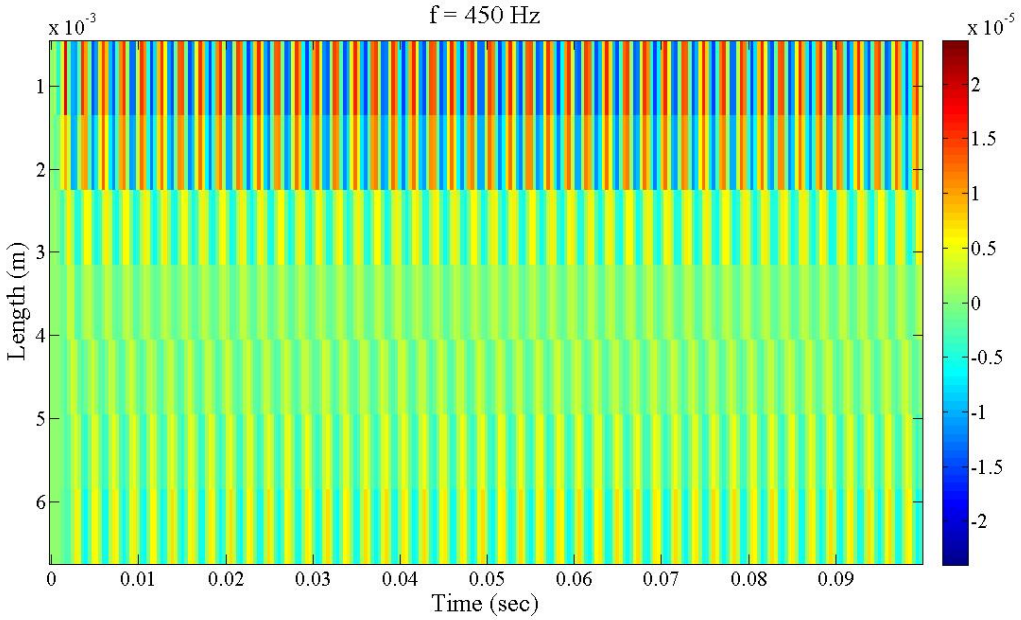

(b) Simulation

Figure 5.12: Displacement time response for $f = 450\ Hz$.

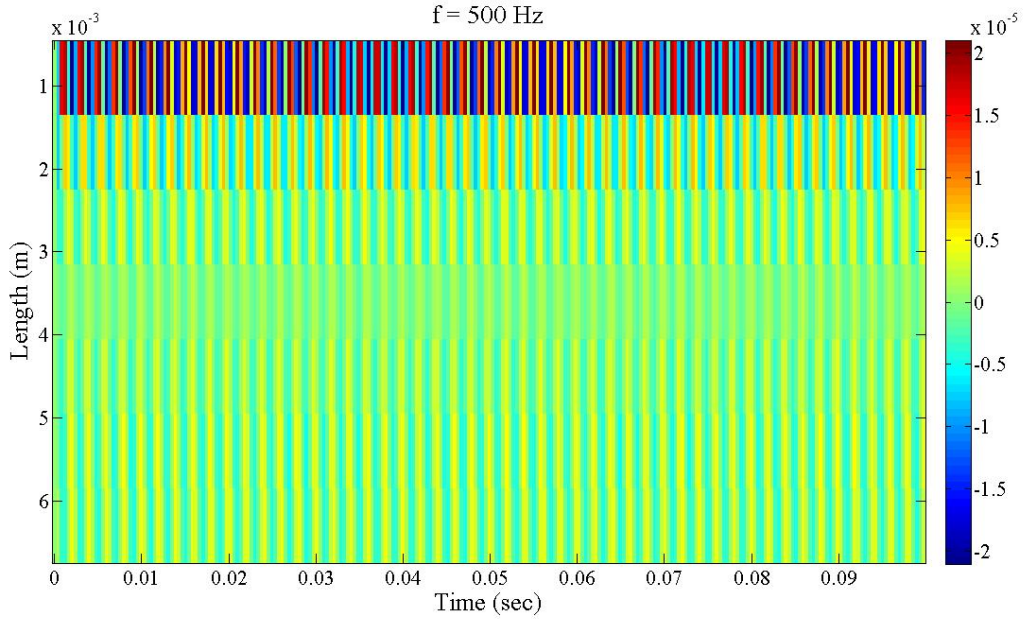

(a) Experiment

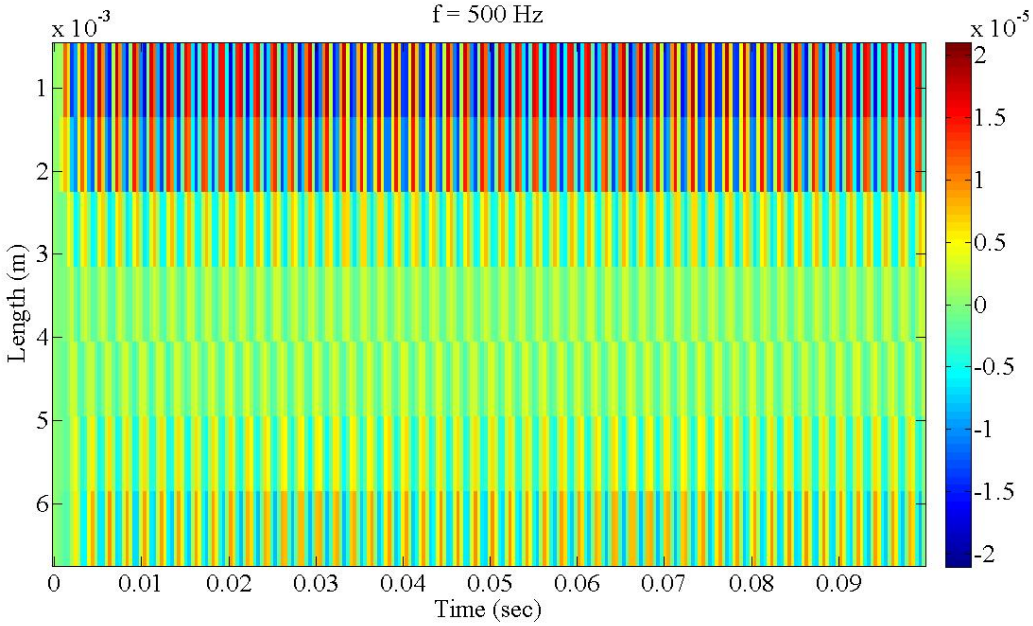

(b) Simulation

Figure 5.13: Displacement time response for $f = 500\ Hz$.

Table 5.4: Displacement Time Response ℓ_2 Error

Frequency (Hz)	ℓ_2 (%)
200	27.06
250	25.58
300	23.77
350	26.96
400	22.97
450	28.71
500	26.65

the true material properties of the pig myocardium. Table 5.4 shows the displacement time response ℓ_2-error for each frequency. The high errors and discrepancies observed between the experimental and simulated time responses can be attributed to the simplification of the the finite element model. In the present work an axisymmetric model was used to reduce the computational for one finite element forward run. Moreover, in the actual heart wall, parallel alignment of muscle cells becomes irregular (myocardial disarray) [63]. However, such anisotropy and change in fibrous orientation are not considered at all in this study. Future work has to take into consideration building a finite element model that best describe the physics of the problem. Furthermore, additional studies should be done to validate the material model used to represent the relaxation process in the material.

5.4 Summary

A methodology for the inverse characterization of viscoelastic properties using vibroacoustics and the concept of error in constitutive equation was presented. Through a simulated and physical experiment it was shown that the proposed methodology could be used for the characterization of viscoelastic properties of soft tissues. The proposed methodology is easy to implement and minimize the sensitivity of the inverse solution to initial guesses. From in-vivo displacement time responses, the viscoelastic properties for a pig myocardium were determined noninvasively. This method offers potential for in-vivo characterization of viscoelastic properties of the myocardium. However, the proposed inverse approach can be easily implemented to characterize viscoelastic properties of other soft tissues (e.g. breast, liver, kidney, etc.).

Overall, the results showed that the proposed methodology has the the potential for in-vivo characterization of viscoelastic properties of soft biological tissue. However, future work will use a finite element model that can better describe the physics of the problem (i.e. geometry, boundary conditions, anisotropy). Furthermore, an inverse approach based on the concept of modified error in constitutive equations will be considered. These error functionals have been shown to provide accurate results for constitutive parameters identification problems in which the perturbation in the experimental data was as high as 40% [90].

CHAPTER 6

CONCLUSIONS

The problem of inverse characterization of spatially-varying material properties was investigated in this work. In Chapter 2 the problem of estimating the spatial distribution of the elastic moduli using Gaussian radial basis functions, nongradient-based optimization, and the finite element method was presented. Through simulations and an experiment in elastography, it was shown that the proposed methodology has the potential to approximate elastic moduli distribution such as those that occur in soft biological tissue in the presence of unhealthy tissue. However, the main objective of the present work is the characterization of spatially-varying viscoelastic properties, and the inverse approach presented in Chapter 2 has limitations. For instance, a non-convex least-square error functional was use for the minimization problem, which increases the sensitivity of the inverse solution to parameter initialization. To minimize the sensitivity of the inverse solution to parameter initialization, nongradient-based optimization algorithms were use in Chapter 2. The advantage of these algorithms is that global minima can be found irrespective of initial guesses. However, depending on the basis that is selected to represent the spatially-varying viscoelastic properties, a large number of design variables are needed to represent complex spatial distribution. Consequently, there is an increase in computational cost.

To minimize the computational cost as the number of design variables increase, additional inverse approaches were investigated. For instance, in Chapter 3 an inverse approach for the reconstruction of spatially-varying viscoelastic properties based on the adjoint method was presented. The main advantage

of this methodology is that regardless of the number of design variables, the gradient of the error functional with respect to the design variables is calculated very efficiently by solving the corresponding adjoint equations. Through simulations, it was shown that the proposed inverse approach could accurately identified the location of the inclusion and reconstruct its geometry. However, the magnitude of the viscoelastic properties was not recovered as accurate as the location and geometry of the inclusion, resulting in high reconstruction errors. Although factors such as the appropriate selection of the regularization parameter and discretization could lead to higher reconstruction errors, the non-convex least-square error functional has the biggest effect in the outcome of the results due to the sensitivity of the inverse solution to parameter initialization. Consequently, the results shown in Chapter 3 are not necessarily optimal. Overall, the proposed inverse approach based on the adjoint method accurately recover the geometry and location of the inclusion, but the inverse solution is sensitive to parameter initialization.

As a mean to minimize the sensitivity of the inverse solution to parameter initialization, an inverse approach based on the concept of error in constitutive equation was investigated in Chapter 4. The error in constitutive equation functional is convex; hence, the sensitivity of the inverse solution to parameter initialization is minimize. Through simulations, it was shown that the proposed methodology can accurately reconstruct the geometry of the inclusion and recover the magnitude of the viscoelastic properties. Furthermore, the inverse approach based on the concept of error in constitutive equation converged faster to an optimal solution than the inverse approach based on the adjoint method (see Appendix A). Consequently, considerable computational savings were attained.

In Chapter 5, the inverse approach based on the concept of error in constitutive equation was tested for in-vivo characterization of viscoelastic properties. From in-vivo displacement measurements, the viscoelastic properties for a pig myocardium were determined noninvasive. Future work will built a finite element model that best describe the physics of the problem, which includes additional tests to validate the material model used to represent the relaxation process. In general, the results reveal that the proposed inverse methodology has the potential to characterize viscoelastic properties of soft biological tissues in-vivo.

Future Work

The work done in this dissertation provides a pathway to the following areas of future research:

1. For the inverse approach developed in Chapter 2, an error functional based on the concept of error in constitutive equation can be defined instead of a least-squared error functional. This change will minimize the sensitivity of the inverse solution to parameter initialization Furthermore, the convexity property of the error functional could allow the use of more design variables without increasing the computational cost. Hence, rate-dependent viscoelastic behavior can be consider in future work.
2. Imperfect data will increase the sensitivity of the inverse solution to parameter initialization. Implementing an inverse approach based on the concept of modified error in constitutive equation will reduce the sensitivity of the inverse solution to parameter initialization. These error functionals have been shown to preserved the convexity properties and pro-

vide accurate results in constitutive parameter identification problems for perturbation level as high as 40% [90]. Furthermore, the inverse problem computational cost will be reduced. This inverse approach can be easily implemented in the work developed in Chapters 2, 4, and 5.

3. In inverse problems, a reliable initial guess should reduced the computational cost to yield an optimal solution through the minimization process. The concept of topological derivative provides a rational principle for selecting a reliable initial guess in terms of its topology, approximate size and location. An extension to the work developed herein is to use the concept of topological derivatives to select a reliable initial guess and reduced the computational cost and sensitivity to parameter initialization due to imperfect data.

4. Mechanical properties can vary somewhat due to its uncertainty in loading, boundary conditions, geometry, and experimental data. Hence, it will be useful to reformulate the work in Chapters 2-5 as problems of statistical inference by means of Bayesian statistics. Allowing the quantification of uncertainty in the material model, design variables, and inverse solution.

5. The concept presented herein, as well as the proposed future work, can be used to solve other types of inverse problems. In particular, these ideas can be extended to inverse problems in fracture mechanics (e.g. crack identification). For example, when the exact values of the constitutive parameters for a material model are unknown, the inverse approaches presented herein could be used to identified this constitutive parameters. This will allow the researcher to understand the behavior of the material model, and from this understanding, improve the material model.

APPENDIX A

COMPARISON BETWEEN THE CONCEPT OF ERROR IN CONSTITUTIVE EQUATION AND THE L2-ADJOINT INVERSE APPROACHES

A.1 Convexity

The performance of the error in constitutive equation (ECE) and the L2-adjoint inverse approaches are discussed herein. The main difference between these inverse approaches is the error functional. For the L2-adjoint inverse approach, a non-convex least-square error functional was used. The non-convexity of the least-square error functional will cause the inverse solution to become sensitive to parameter initialization; thus, affecting the quality of the reconstruction. Contrarily, for the ECE inverse approach, the error functional is convex. By having this property, the sensitivity of the inverse solution to parameter initialization is minimize.

A function $f(\boldsymbol{x}) : \hat{V} \rightarrow \mathbb{R}$, where $\hat{V}$ is a vector space, is called convex if

$$f(tx_1 + (1-t)x_2) \leq tf(x_1) + (1-t)f(x_2) \;\; \forall \; x_1, x_2 \in \hat{V}, \; and \; t \in (0,1), \tag{A.1}$$

Figure A.1 shows a pictorial description.

Gockenback *et al.* [51] show that for elliptic boundary value problem, the coefficient dependent energy norm is convex. For instance, lets define the following linear elastic variational boundary value problem

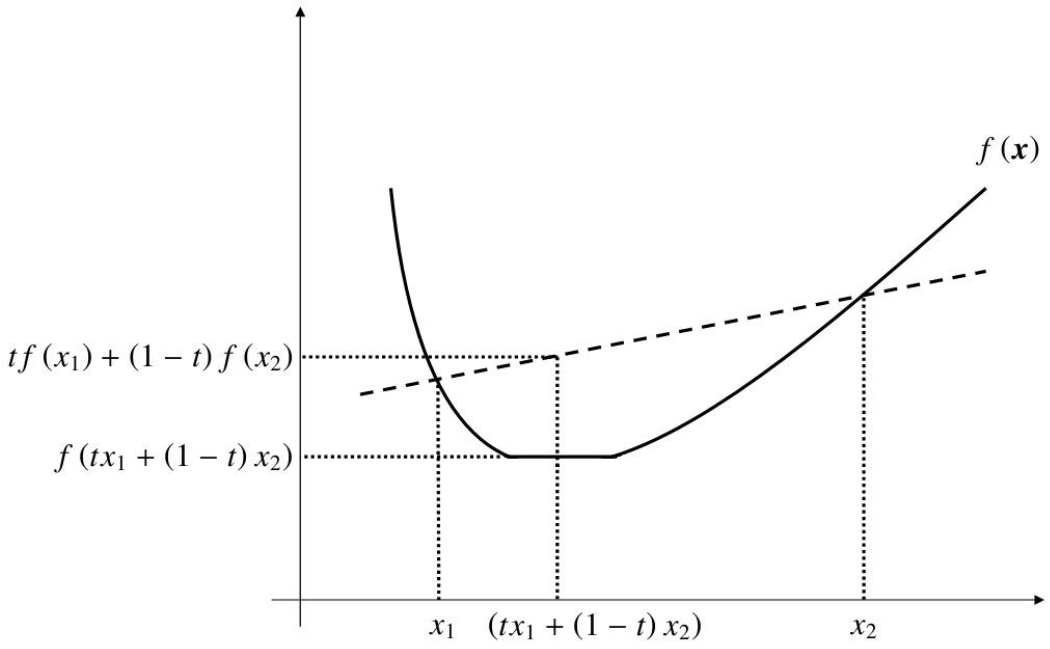

Figure A.1: Pictorial description of a convex function.

$$a(\mathbb{C}; \boldsymbol{v}, \boldsymbol{u}) = \ell(\boldsymbol{v}) \;\; \forall \, \boldsymbol{v} \in V \tag{A.2}$$

where

$$a(\mathbb{C}; \boldsymbol{v}, \boldsymbol{u}) = \int_{\Omega} \nabla \boldsymbol{v} : \boldsymbol{\sigma} \, d\Omega \tag{A.3}$$

$$\ell(\boldsymbol{v}) = \int_{\Gamma_t} \boldsymbol{v} \cdot \boldsymbol{t} \, d\Gamma_t, \tag{A.4}$$

where the test function space V and the trial solution space U are defined as

$$V = \{\boldsymbol{v} : \boldsymbol{v} \mid v_i \in H^1(\Omega), \boldsymbol{v} = 0 \text{ on } \Gamma_u\} \tag{A.5}$$

$$U = \{\boldsymbol{u} : \boldsymbol{u} \mid u_i \in H^1(\Omega), \boldsymbol{u} = \boldsymbol{u}_0 \text{ on } \Gamma_u\}. \tag{A.6}$$

The bilinear form a satisfies the condition

$$a(\mathbb{C}; \boldsymbol{u}, \boldsymbol{u}) \geq \alpha \|\boldsymbol{u}\|_U \ \forall\ u \in U,\ \mathbb{C} \in L^{\infty}(\Omega) \tag{A.7}$$

where $\alpha > 0$ comes from Korn's inequality. A proof of Korn's inequality can be found in [65] or [89].

Now, let the error functional $J(\mathbb{C})$ be defined as

$$J(\mathbb{C}) = \frac{1}{2} a(\mathbb{C}; \boldsymbol{u}(\mathbb{C}) - \hat{\boldsymbol{u}}, \boldsymbol{u}(\mathbb{C}) - \hat{\boldsymbol{u}}) \tag{A.8}$$

This functional is infinitely differentiable and its directional derivative with respect to the fourth-order elasticity tensor $\mathbb{C}$ is given by

$$DJ(\mathbb{C}) \cdot \delta\mathbb{C} = \frac{1}{2} a(\delta\mathbb{C}; \boldsymbol{u}(\mathbb{C}) - \hat{\boldsymbol{u}}, \boldsymbol{u}(\mathbb{C}) - \hat{\boldsymbol{u}}) + a(\mathbb{C}; D\boldsymbol{u}(\mathbb{C})\,\delta\mathbb{C}, \boldsymbol{u}(\mathbb{C}) - \hat{\boldsymbol{u}}). \tag{A.9}$$

Using the following identity

$$a(\mathbb{C}; D\boldsymbol{u}(\mathbb{C})\,\delta\mathbb{C}, \boldsymbol{u}(\mathbb{C}) - \hat{\boldsymbol{u}}) = -a(\delta\mathbb{C}; \boldsymbol{u}(\mathbb{C}) - \hat{\boldsymbol{u}}, \boldsymbol{u}(\mathbb{C}) - \hat{\boldsymbol{u}}) \tag{A.10}$$

and some simplification, the second directional derivative of Equation (A.9) with respect to the fourth-order elasticity tensor is given by

$$D^2 J(\mathbb{C})(\delta\mathbb{C}, \delta\mathbb{C}) = -\frac{1}{2} a(\delta\mathbb{C}; D\boldsymbol{u}(\mathbb{C})\,\delta\mathbb{C}, \boldsymbol{u}(\mathbb{C}) - \hat{\boldsymbol{u}}) \tag{A.11}$$

$$
\begin{aligned}
- \quad & \frac{1}{2} a\left(\delta\mathbb{C}; \boldsymbol{u}\left(\mathbb{C}\right) + \hat{\boldsymbol{u}}, \boldsymbol{u}\left(\mathbb{C}\right) \delta\mathbb{C}\right) \\
= \quad & -a\left(\delta\mathbb{C}; \boldsymbol{u}\left(\mathbb{C}\right), D\boldsymbol{u}\left(\mathbb{C}\right) \delta\mathbb{C}\right) \\
= \quad & a\left(\mathbb{C}; D\boldsymbol{u}\left(\mathbb{C}\right) \delta\mathbb{C}, D\boldsymbol{u}\left(\mathbb{C}\right) \delta\mathbb{C}\right) \\
\geq \quad & \alpha \| D\boldsymbol{u}\left(\mathbb{C}\right) \delta\mathbb{C} \|_V^2
\end{aligned}
$$

Thus, $J\left(\mathbb{C}\right)$ is a smooth and convex functional. Furthermore, Gockenback *et al.* [51] show that the convexity of the error functional $J\left(\mathbb{C}\right)$ is preserved when total variation regularization is used. For more details on this remark and the proofs that led to A.11, the reader is referred to [51, 52].

A.2 Results

Figures A.2−A.4 show the reconstruction error for each iteration of the minimization process using the L2-adjoint and ECE inverse approach for the example problems with one inclusion and $\triangle_n = 0\%, 5\%, 10\%$. These plots show that the error in constitutive equation functional outperformed the least-square error functional for each perturbation case. Indeed, after 10 iterations, the reconstruction errors obtained with the ECE inverse approach are lower than those obtained with the L2-adjoint inverse approach after 3000 iterations. Moreover, for more complex spatial distribution (i.e. two inclusions), the error in constitutive equation functional still outperformed the least-square error functional for each perturbation case. Figures A.5−A.7 show the reconstruction error for each iteration of the minimization process using the L2-adjoint and ECE inverse approach for the example problems with two inclusions and $\triangle_n = 0\%, 5\%, 10\%$.

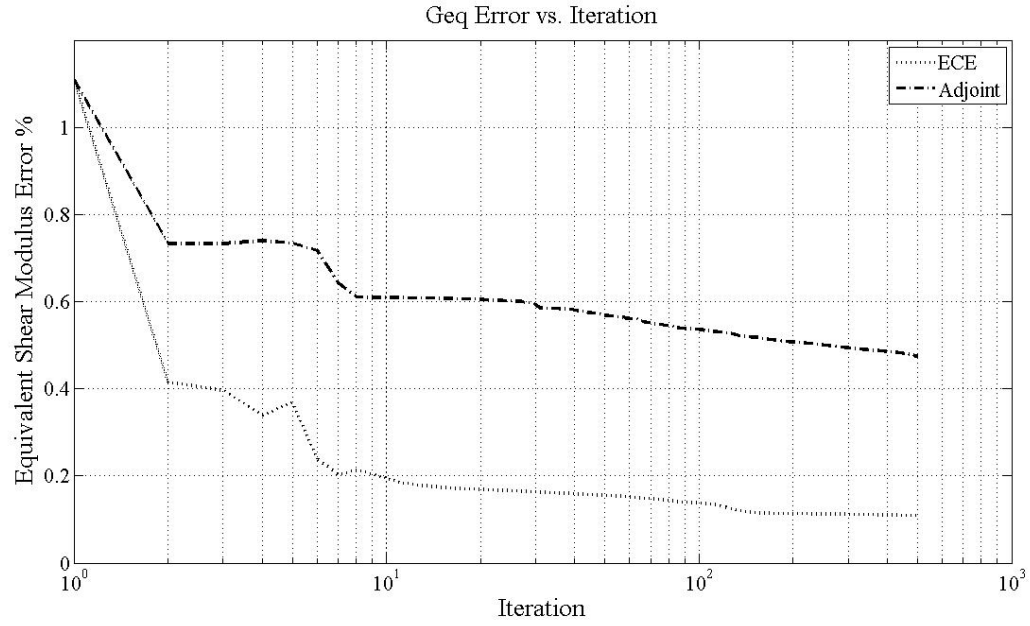

(a) G_{eq} error plot

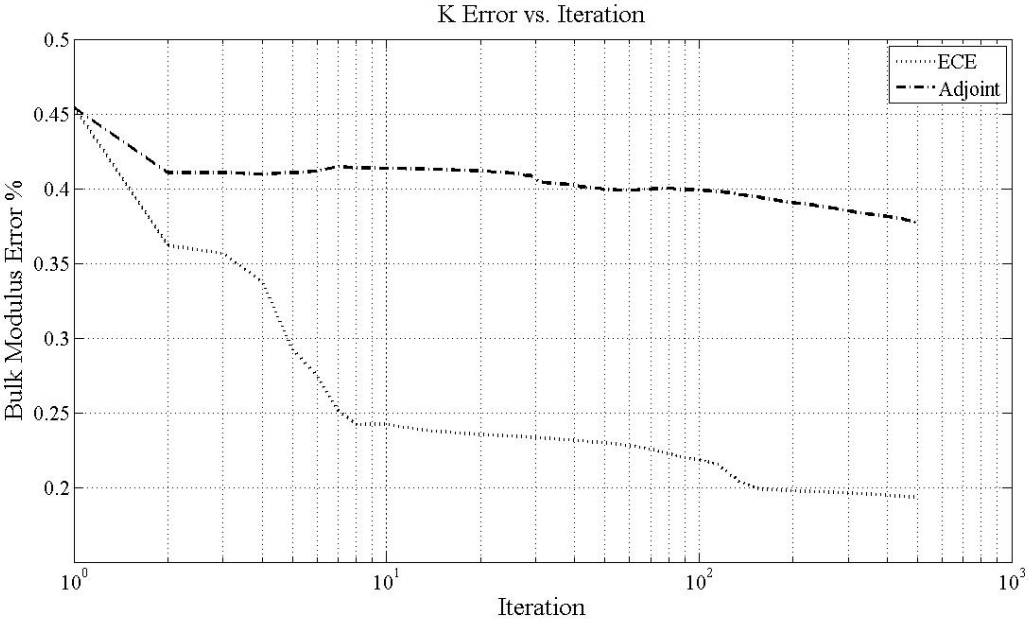

(b) K error plot

Figure A.2: Error plots comparing the performance of the L2-adjoint and ECE inverse approaches reconstructing the spatially-varying (a) equivalent shear modulus and (b) bulk modulus for the numerical example with one inclusion and $\triangle_n = 0\%$

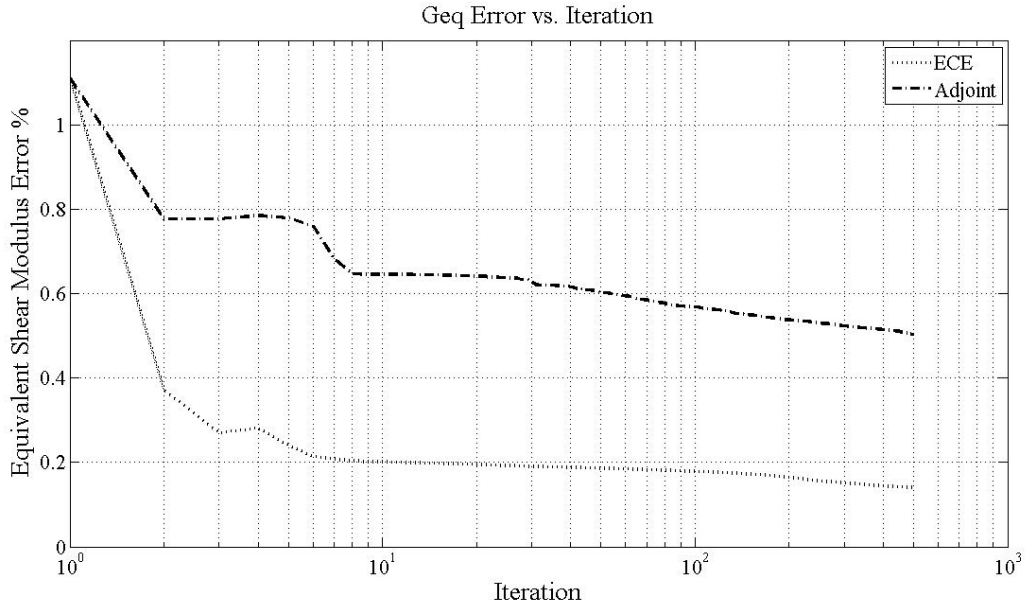

(a) G_{eq} error plot

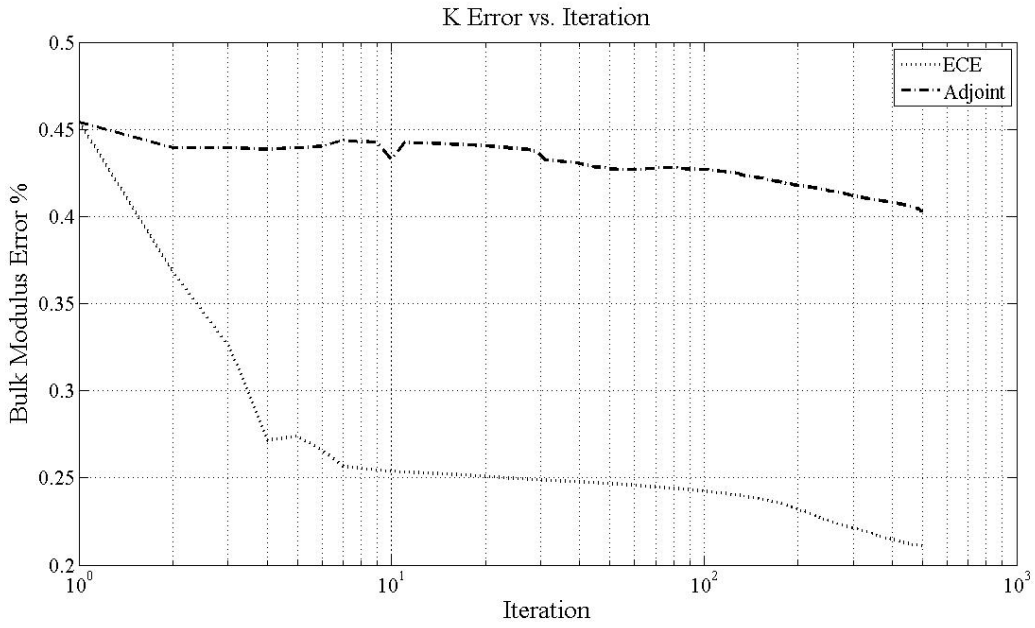

(b) K error plot

Figure A.3: Error plots comparing the performance of the L2-adjoint and ECE inverse approaches reconstructing the spatially-varying (a) equivalent shear modulus and (b) bulk modulus for the numerical example with one inclusion and $\triangle_n = 5\%$

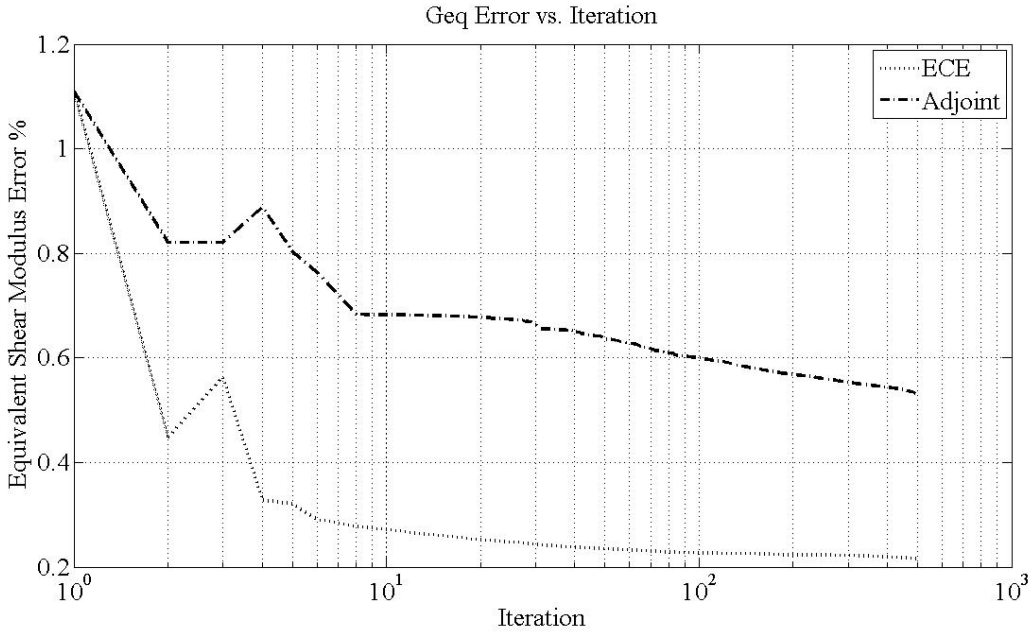

(a) G_{eq} error plot

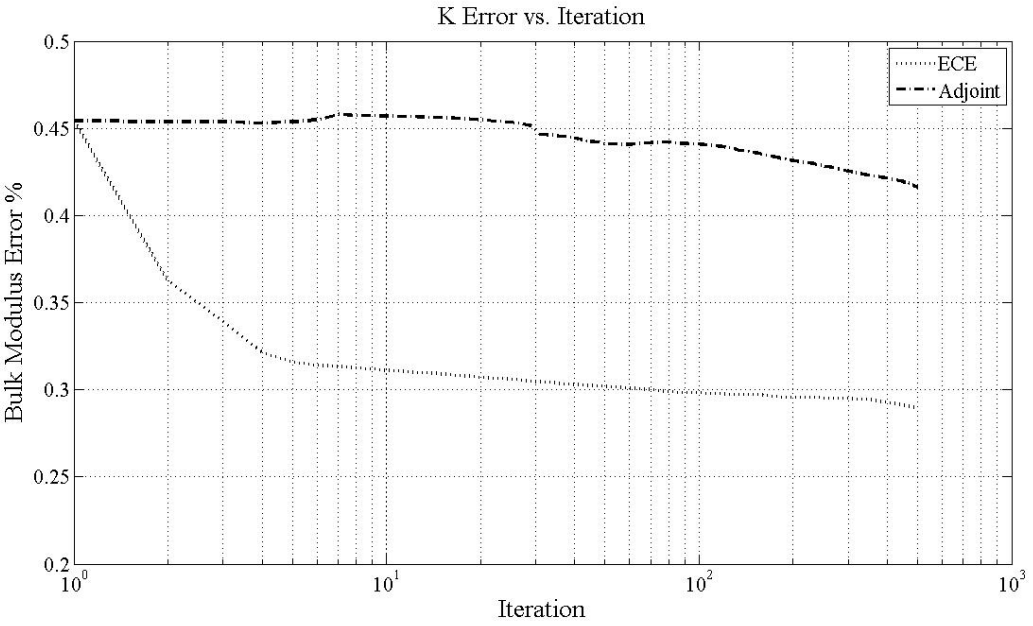

(b) K error plot

Figure A.4: Error plots comparing the performance of the L2-adjoint and ECE inverse approaches reconstructing the spatially-varying (a) equivalent shear modulus and (b) bulk modulus for the numerical example with one inclusion and $\triangle_n$ = 10%

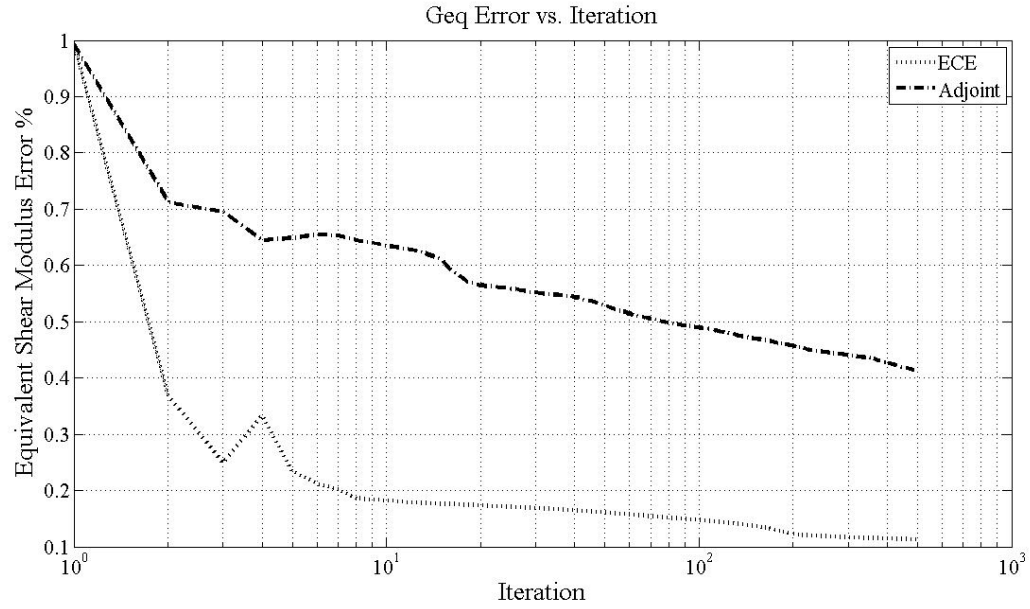

(a) G_{eq} error plot

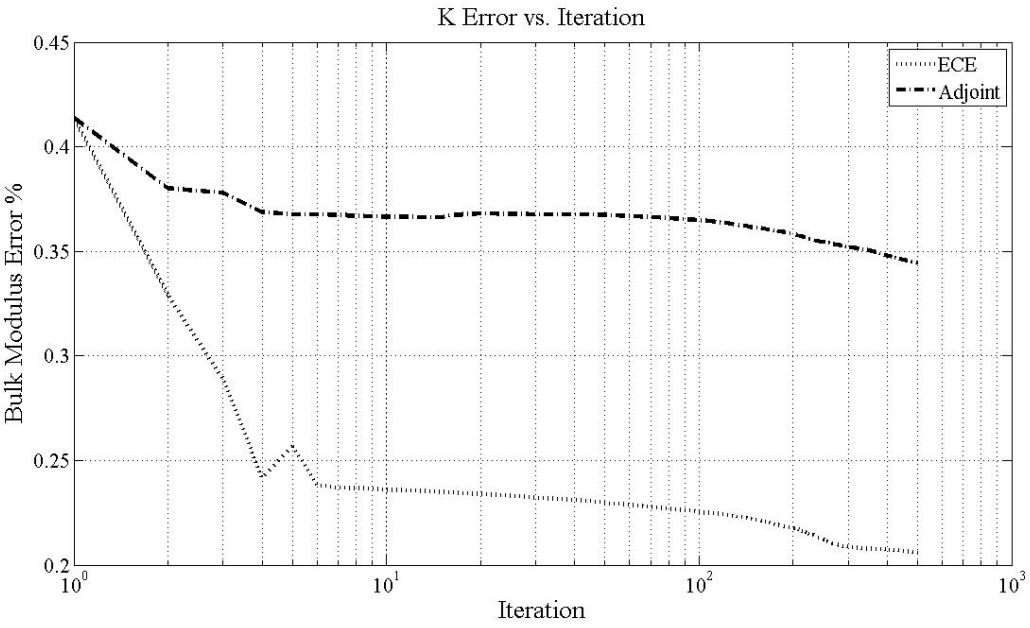

(b) K error plot

Figure A.5: Error plots comparing the performance of the L2-adjoint and ECE inverse approaches reconstructing the spatially-varying (a) equivalent shear modulus and (b) bulk modulus for the numerical example with two inclusions and $\triangle_n = 0\%$

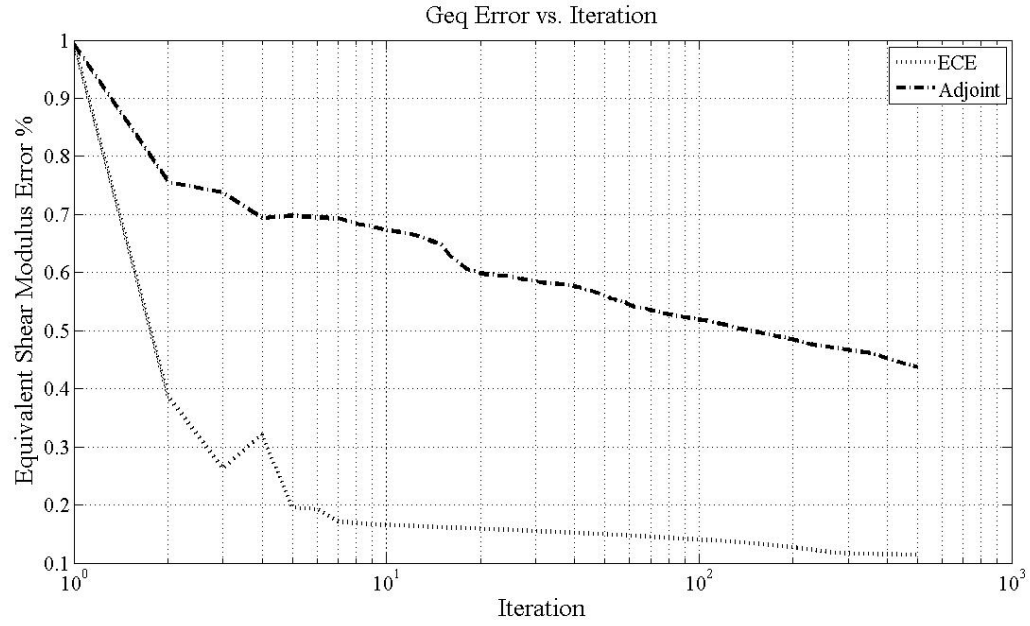

(a) G_{eq} error plot

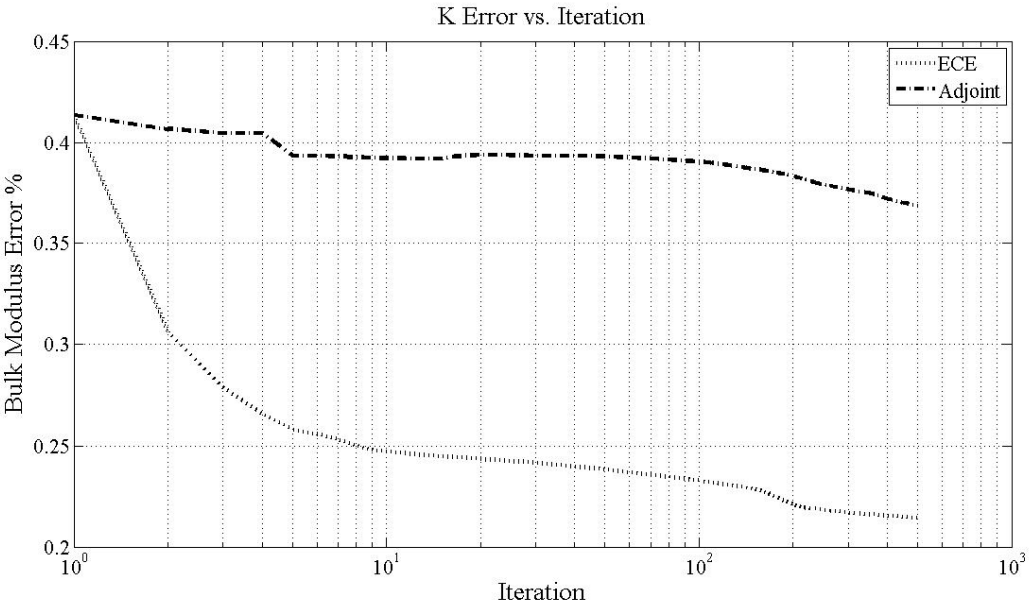

(b) K error plot

Figure A.6: Error plots comparing the performance of the L2-adjoint and ECE inverse approaches reconstructing the spatially-varying (a) equivalent shear modulus and (b) bulk modulus for the numerical example with two inclusions and $\triangle_n = 5\%$

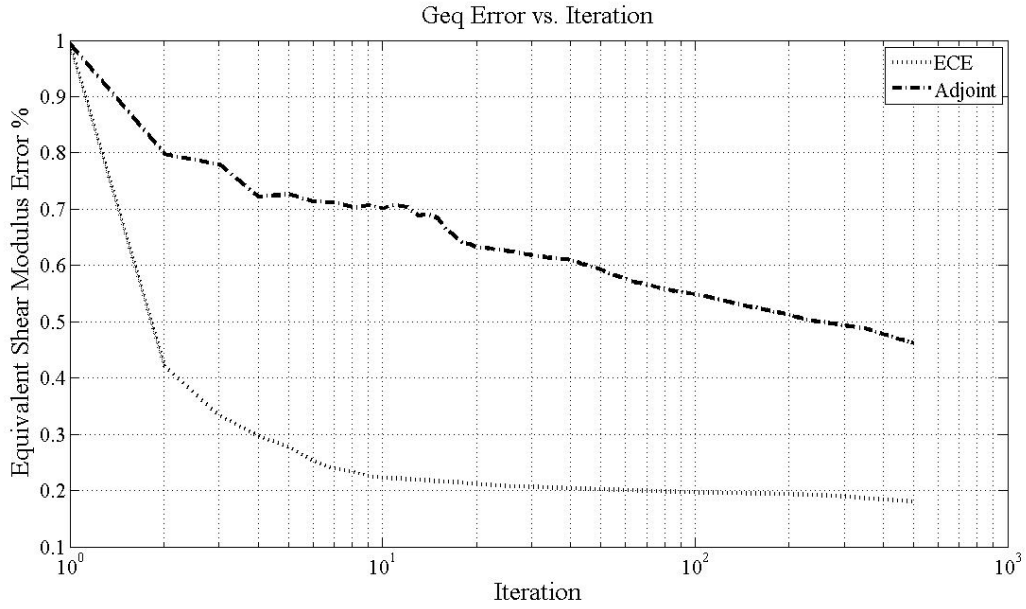

(a) G_{eq} error plot

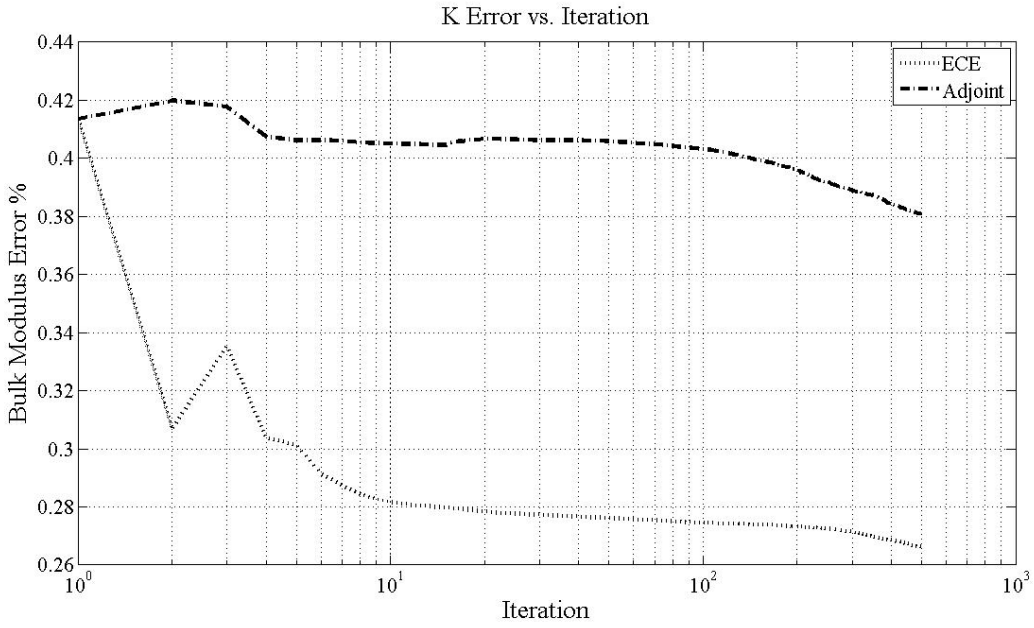

(b) K error plot

Figure A.7: Error plots comparing the performance of the L2-adjoint and ECE inverse approaches reconstructing the spatially-varying (a) equivalent shear modulus and (b) bulk modulus for the numerical example with two inclusions and $\triangle_n$ = 10%

BIBLIOGRAPHY

[1] Abaqus Inc. *Abaqus Theory Manual V6.6*, 2006.

[2] A. B. Abda, H. B. Ameur, and M. Jaoua. Identification of 2D cracks by elastic boundary measurements. *Inverse Problems*, 15:67–77, February 1999.

[3] M.A. Aguilo, W. Aquino, J.C. Brigham, and M. Fatemi. An inverse problem approach for elasticity imaging through vibroacoustics. *IEEE Transactions on Medical Imaging*, 29:1012–1021, April 2010.

[4] R. Al-Khoury, A. Scarpas, C. Kasbergen, and J. Blaauwendraad. Spectral element technique for efficient parameter identification of layered media. Part III: viscoelastic aspects. *International Journal of Solids and Structures*, 39:2189–2201, April 2002.

[5] R. A. Albanese, H. T. Banks, and J. K. Raye. Nondestructive evaluation of materials using pulsed microwave interrogating signals and acoustic wave induced reflections. *Inverse Problems*, 18:1935–1958, December 2002.

[6] A. Alizad, M. Fatemi, L. E. Wold, and J. F. Greenleaf. Performance of vibro-acoustography in detecting microcalcifications in excised human breast tissue: A study of 74 tissue samples. *IEEE Transactions on Medical Imaging*, 23:307–312, March 2004.

[7] S. Andrieux, A. B. Abda, and H. D. Bui. Reciprocity principle and crack identification. *Inverse Problems*, 15:59–65, February 1999.

[8] W. Aquino and J. C. Brigham. Self-learning finite elements for inverse estimation of thermal constitutive models. *International Journal of Heat and Mass Transfer*, 49:2466–2478, March 2006.

[9] A.L. Araújo, C.M. Mota Soares, J. Herskovits, and P. Pedersen. Estimation of piezoelastic and viscoelastic properties in laminated structures. *Composite Structures*, 87:168–174, January 2009.

[10] B. Audoin. Non-destructive evaluation of composite materials with ultrasonic waves generated and detected by lasers. *Ultrasonics*, 40:735–740, May 2002.

[11] P. E. Barbone and J. C. Bamber. Quantitative elasticity imaging: what can

and cannot be inferred from strain images. *Physics in Medicine and Biology*, 47:2147–2164, June 2002.

[12] P.E. Barbone and N.H. Gokhale. Elastic modulus imaging: on the uniqueness and nonuniqueness of the elastography inverse problem in two dimensions. *Inverse Problems*, 20:283–296, 2004.

[13] H.A. Barnes, J.F. Hutton, and K. Walters. *An Introduction to Rheology*. Elsevier, Amsterdam, The Netherlands, 1989.

[14] J. Bercoff, S. Chaffai, M. Tanter, L. Sandrin, S. Catheline, M. Fink, J.L. Gennisson, and M. Meunier. In vivo breast tumor detection using transient elastography. *Ultrasound in Medicine and Biology*, 29:1387–1396, October 2003.

[15] J. Bishop, A. Samani, J. Sciarretta, and D. B. Plewes. Two-dimensional MR elastography with linear inversion reconstruction: methodology and noise analysis. *Physics in Medicine and Biology*, 45:2081–2091, March 2000.

[16] M. Bonnet and A. Constantinescu. Inverse problems in elasticity. *Inverse Problems*, 21:R1–R50, April 2005.

[17] J. C. Brigham and W. Aquino. Surrugate-Model Accelerated Random Search algorithm for global optimization with applications to inverse material identification. *Computer Methods in Applied Mechanics and Engineering*, 196:4561–4576, June 2007.

[18] J. C. Brigham, W. Aquino, F. G. Mitri, J. F. Greenleaf, and M. Fatemi. Inverse estimation of viscoelastic material properties for solids immersed in fluids using vibroacoustic techniques. *Journal of Applied Physics*, 101:23509–023509–14, January 2007.

[19] S. H. Brooks. A discussion of random methods for seeking maxima. *Operations Research*, 6:244–251, September 1958.

[20] M. D. Buhmann. *Radial Basis Functions: Theory and Implementation*. Cambridge University Press, Cambridge, 2003.

[21] J. C. Carr, W. R. Fright, , and R. K. Beatson. Surface interpolation with radial basis functions for medical imaging. *IEEE Transactions on Medical Imaging*, 16:96–107, February 1997.

[22] S. Chen, M. Fatemi, and J. F. Greenleaf. Quantifying elasticity and viscosity from measurement of shear wave speed dispersion. *Journal of the Acoustical Society of America*, June 2004.

[23] S. Chen, M. W. Urban, R. Kinnick C. Pislaru, Y. Zheng, A. Yao, and J. F. Greenleaf. Shearwave dispersion ultrasound vibrometry (SDUV) for measuring tissue elasticity and viscosity. *IEEE Transactions on Ultrasonics, Ferroelectrics and Frequency Control*, January 2009.

[24] Richard M. Christensen. *Theory of viscoelasticity*. Academic Press, New York, 1982.

[25] J.P. Combe, P. Ladevèze, and J.P. Pelle. Constitutive relation error estimator for transient finite element analysis. *Computer Methods in Applied Mechanics and Engineering*, 176:165–185, 1999.

[26] A. Constantinescu. On the identification of elastic moduli from displacement-force boundary measurements. *Inverse Problems in Science and Engineering*, August 1995.

[27] L. Debnath and P. Mikusiński. *Hilbert Spaces with Applications*. Elsevier, Oxford, UK, 2005.

[28] R. Deng, P. Davies, and A.K. Bajaj. Flexible polyurethane foam modeling and identification of viscoelastic parameters for automotive seating applications. *Journal of Sound and Vibration*, 262:391–417, May 2003.

[29] D.C. Dobson and F. Santosa. Recovery of blocky images from noisy and blurred data. *SIAM Journal on Applied Mathematics*, 56:1181–1198, August 1996.

[30] D. Dobsony and O. Scherzer. Analysis of regularized total variation penalty methods for denoising. *Inverse Problems*, October 1996.

[31] M. M. Doyley, P. M. Meaney, and J. C. Bamber. Evaluation of an iterative reconstruction method for quantitative elastography. *Physics in Medicine and Biology*, 45:1521–1540, June 2000.

[32] M.M. Doyley, J.C. Bamber, T. Shiina, and M.O. Leach. Reconstruction of elasticity modulus distribution from envelope detected B-mode data. *IEEE International Ultrasonics Symposium (San Antonio, TX, USA)*, 2:1611–1614, 1996.

[33] E. Ackerman E. R. Fitzgerald and J. W. Fitzgerald. Preliminary measurement of the viscoelastic properties of animal tissues at audio-frequencies. *Journal of the Acoustical Society of America*, January 1957.

[34] I. Epanomeritakis, V. Akcelik, O. Ghattas, and J. Bielak. A Newton-CG method for large-scale three-dimensional elastic full-waveform seismic inversion. *Inverse Problems*, 24, May 2008.

[35] M. Fabrizio and A. Morro. *Mathematical Problems in Linear Viscoelasticity*. SIAM Studies in Applied Mathematics, Philadelphia, PA, USA, 1992.

[36] M. Fatemi and J. F. Greenleaf. Ultrasound-stimulated vibro-acoustic spectrography. *Science*, 280:8285, April 1998.

[37] M. Fatemi and J. F. Greenleaf. Vibro-acoustography: An imaging modality based on ultrasound-stimulated acoustic emission. *Proc. Natl. Acad. Sci. USA*, 96:6603–6608, June 1999.

[38] M. Fatemi, A. Manduca, and J.F. Greenleaf. Imaging elastic properties of biological tissues by low-frequency harmonic vibration. *Proceedings of the IEEE*, 91:1503–1519, October 2003.

[39] G. Feijoo. A new method in inverse scattering based on the topological derivative. *Inverse Problems*, 20:1819–1840, September 2004.

[40] G.R. Feijóo. *On Shape Sensitivity*. PhD thesis, Stanford University, January 2003.

[41] J.D. Ferry. *Viscoelastic properties of polymers*. John Wiley & Sons, New York, NY, USA, 1980.

[42] William N. Findley, James S. Lai, and Kasif Onaran. *Creep and relaxation of nonlinear viscoelastic materials: with an introduction to linear viscoelasticity*. North-Holland Publishing Company, Amsterdam, 1976.

[43] M. Fornefett, K. Rohr, and H. S. Stiehl. Radial basis functions with compact support for elastic registration of medical images. *Image and Vision Computing*, 19:87–96, January 2001.

[44] Y.C. Fung. Elasticity of soft tissues in simple elongation. *American Journal of Physiology*, December 1967.

[45] L. Gallimard, P. Ladevèze, and J.P. Pelle. Error estimation and adaptivity in elastoplasticity. *International Journal for Numerical Methods in Engineering*, 39:189–217, 1996.

[46] A. Gavrus, E. Massoni, and J.L. Chenot. An inverse analysis using a finite element model for identification of rheological parameters. *Journal of Materials Processing Technology*, 60:447–454, June 1996.

[47] M.S. Gockenbach. Numerical analysis of elliptic inverse problems with interior data. *Journal of Physics: Conference Series*, 124:1–12, 2008.

[48] M.S. Gockenbach, B. Jadamba, and A.A. Khan. Numerical estimation of discontinuous coefficients by the method of equation error. *Mathematics and Mechanics of Solids*, 1:343–359, 2006.

[49] M.S. Gockenbach, B. Jadamba, and A.A. Khan. Equation error approach for elliptic inverse problems with an application to the identification of Lamé parameters. *Inverse Problems in Science and Engineering*, 16:349–367, 2008.

[50] M.S. Gockenbach and A.A. Khan. *Mathematical Models and Methods for Real World Systems*, chapter A convex objective functional for elliptic inverse problems. Chapman & Hall/CRC Taylor & Francis Group, 2006.

[51] M.S. Gockenbach and A.A. Khan. An abstract framework for elliptic inverse problems: Part 1. An output least-squares approach. *Mathematics and Mechanics of Solids*, 12:259–276, June 2007.

[52] M.S. Gockenbach and A.A. Khan. An abstract framework for elliptic inverse problems: Part 2. An augmented Lagrangian approach. *Mathematics and Mechanics of Solids*, 14:517–539, August 2009.

[53] D. E. Goldberg. *Genetic algorithms in search, optimization, and machine learning*. Addison-Wesley, Massachusetts, 1989.

[54] B. S. Gow and M. G. Taylor. Measurement of viscoelastic properties of arteries in the living dog. *Circulation Research*, 1968.

[55] Per C. Hansen. *P. Johnston, Computational Inverse Problems in Electrocardiology (Advances in Computational Bioengineering)*, volume 4, chapter The L-curve and its use in the numerical treatment of inverse problems, pages 119–142. WIT Press / Computational Mechanics, Southampton, 2000.

[56] Per C. Hansen, James G. Nagy, and Dianne P. O'Leary. *Deblurring Images: Matrices, Spectra, and Filtering*. Society for Industrial and Applied Mathematics, Philadelphia, PA, USA, 2006.

[57] H. Hasegawa and H. Kanai. Improving accuracy in estimation of artery-wall displacement by referring to center frequency of rf echo. *IEEE Transactions on Ultrasonics, Ferroelectrics and Frequency Control*, January 2006.

[58] L.R. Herrmann and F.E. Peterson. A numerical procedure for viscoelastic stress analysis. In *7th Meeting of ICRPG Mechanical Behavior Working Group*, 1968.

[59] E. E. W. Van Houten, M. M. Doyley, F. E. Kennedy, J. B. Weaver, and K. D. Paulsen. Initial in vivo experience with steady-state subzonebased MR elastography of the human breast. *Journal of Magnetic Resonance Imaging*, 17:72–85, December 2002.

[60] J. Hughes. U. S. airlines may have to inspect, replace parts on boeing jets. `http://www.bloomberg.com/apps/news?pid=newsarchive\&sid=aVh5QlwvK_xg`, October 2009.

[61] M.F. Insana, C. Pellot-Barakat, M. Sridhar, and K.K. Lindfors. Viscoelastic imaging of breast tumor microenvironment with ultrasound. *Journal of Mammary Gland Biology and Neoplasia*, 9:393–404, October 2004.

[62] F. Kallel and M. Bertrand. Tissue elasticity reconstruction using linear perturbation method. *IEEE Transactions on Medical Imaging*, 15:299–313, October 1996.

[63] H. Kanai. Propagation of spontaneously actuated pulsive vibration in human heart wall and in vivo viscoelasticity estimation. *IEEE transactions on ultrasonics, ferroelectrics, and frequency control*, November 2005.

[64] M. Kauer, V. Vuskovicb, J. Duala, G. Szekelyc, and M. Bajkad. Inverse finite element characterization of soft tissues. *Medical Image Analysis*, 6:275–287, September 2002.

[65] N. Kikuchi and J. T. Oden. *Contact Problems in Elasticity: A Study of Variational Inequalities and Finite Element Methods*. SIAM Studies in Applied Mathematics, Philadelphia, PA, USA, 1992.

[66] S.Y. Kim and D.H. Lee. Identification of fractional-derivative-model pa-

rameters of viscoelastic materials from measured frfs. *Journal of Sound and Vibration*, 324:570–586, July 2009.

[67] B. Kleuter, A. Menzel, and P. Steinmann. Generalized parameter identification for finite viscoelasticity. *Computer Methods in Applied Mechanics and Engineering*, 196:3315–3334, July 2007.

[68] R.V. Kohn and B. D. Lowe. A variational method for parameter identification. *Mathematical Modeling and Numerical Analysis*, 22:119–158, 1988.

[69] R.V. Kohn and A. McKenney. Numerical implementation of a variational method for electrical impedance tomography. *Inverse Problems*, 6:389–414, June 1990.

[70] R.V. Kohn and M. Vogelius. Determining conductivity by boundary measurements. *Communications on Pure and Applied Mathematics*, 37:289–298, May 1984.

[71] R.V. Kohn and M. Vogelius. Determining conductivity by boundary measurements II. interior results. *Communications on Pure and Applied Mathematics*, 38:643–667, September 1985.

[72] P. Ladevèze and A. Chouaki. A modeling error estimator for dynamic model updating of damped structures. In *Inverse Problems in Engineering Mechanics*, pages 187–196, London, UK, 1998. Elsevier.

[73] P. Ladevèze and D. Leguillon. Error estimates procedures in the finite element method and applications. *SIAM Journal on Numerical Analysis*, 20:485–509, June 1983.

[74] P. Ladevèze, N. Moës, and B. Douchin. A new posteriori error estimation for nonlinear time-dependent finite element analysis. *Computer Methods in Applied Mechanics and Engineering*, 157:45–68, April 1998.

[75] P. Ladevèze, N. Moës, and B. Douchin. Constitutive relation error estimators for (visco)plastic finite element analysis with softening. *Computer Methods in Applied Mechanics and Engineering*, 176:247–264, July 1999.

[76] B. M. Learoyd and M. G. Taylor. Alterations with age in the viscoelastic properties of human arterial walls. *Circulation Research*, 1966.

[77] N. Leymarie, C. Aristegui, B. Audoin, and S. Baste. Identification of complex stiffness tensor from waveform, reconstruction. *Journal of the Acoustical Society of America*, 111:1232–1244, March 2002.

[78] H.L. Liew and P.M. Pinsky. Recovery of shear modulus in elastography using an adjoint method with B-spline representation. *Finite Elements in Analysis and Design*, 41:778–799, April 2005.

[79] K. Liu, M.R. VanLandingham, and T.C. Ovaert. Mechanical characterization of soft viscoelastic gels via indentation and optimization-based inverse finite element analysis. *Journal of the Mechanical Behavior of Biomedical Materials*, 2:355–362, August 2009.

[80] Y. Liu, G. Wang, and L.Z. Sun. Anisotropic elastography for local passive properties and active contractility of myocardium from dynamic heart. *International Journal of Biomedical Imaging*, 20:1–15, 2006.

[81] A. Y. Malkin. *Rheology Fundamentals*. ChemTec Publishing, Toronto, Ontario, Canada, 1998.

[82] S. F. Masri, A. W. Smyth, A. G. Chassiakos, M. Nakamura, and T. K. Caughey. Training neural networks by adaptive random search techniques. *Journal of Engineering Mechanics-ASCE*, 125:123–132, February 1999.

[83] M. D. J. McGarry and E. E. W. Van Houten. Use of rayleigh damping model in elastography. *Medical and Biological Engineering and Computing*, 46:759–766, June 2008.

[84] M. I. Miga. A new approach to elastography using mutual information and finite elements. *Physics in Medicine and Biology*, 48:467–480, June 2003.

[85] M. Mitchell. *An introduction to genetic algorithm*. MIT Press, Massachusetts, 1998.

[86] F.G. Mitri and M. Fatemi. Improved vibroacoustography imaging for nondestructive inspection of materials. *Journal of Applied Physics*, 98:114901–114908, December 2005.

[87] M.J. Moulton, L.L. Creswell, R.L. Actis, K.W. Myers, M.W. Vannier, B.A. Szabo, and M.K. Pasque. An inverse approach to determining myocardial material properties. *Journal of Biomechanics*, 28:935–948, August 1995.

[88] S. Nasseri, L. E. Bilston, and N. Phan-Thien. Viscoelastic properties of pig kidney in shear, experimental results and modelling. *Rheologica Acta*, 2002.

[89] J. Nečas and I. Hlavaček. *Mathematical Theory of Elastic and Elastoplastic Bodies: An Introduction*. Elsevier, Amsterdam, 1981.

[90] H. M. Nguyen, O. Allix, and P. Feissel. A robust identification strategy for rate-dependent models in dynamics. *Inverse Problems*, 24, October 2008.

[91] V. Normand, D. L. Lootens, E. Amici, K. P. Plucknett, and P. Aymard. New insight into agarose gel mechanical properties. *Biomacromolecules*, 1:730–738, August 2000.

[92] A. A. Oberai, N. H. Gokhale, and G. R. Feijoo. Solution of inverse problems in elasticity imaging using the adjoint method. *Inverse Problems*, 19:297–313, April 2003.

[93] A.A. Oberai, N.H. Gokhale, M.M. Doyley, and J.C. Bamber. Evaluation of the adjoint equation based algorithm for elasticity imaging. *Physics in Medicine and Biology*, 49:2955–2974, June 2004.

[94] H. Ogi, K. Sato, T. Asada, and M. Hirao. Complete mode identification for resonance ultrasound spectroscopy. *Journal of the Acoustical Society of America*, 112:2553–2557, December 2002.

[95] A. Peters, S. Wortmann, R. Elliott, M. Staiger, J. G. Chase, and E. Van Houten. Digital image-based elasto-tomography: First experiments in surface based mechanical property estimation of gelatine phantoms. *JSME International Journal Series C-Mechanical Systems Machine Elements and Manufacturing*, 48:562–569, December 2005.

[96] S. W. Phillips, W. Aquino, and W. Chirdon. Simultaneous inverse identification of transient thermal properties and heat sources using sparse sensor information. *Journal of Engineering Mechanics*, 133:1341–1351, December 2007.

[97] D. B. Plewes, J. Bishop, A. Samani, and J. Sciarretta. Visualization and quantification of breast cancer biomechanical properties with magnetic resonance elastography. *Physics in Medicine and Biology*, 45:1591–1610, June 2000.

[98] K. R. Raghavan and A. E. Yagle. Forward and inverse problems in elasticity imaging of soft-tissues. *IEEE Transactions on Nuclear Science*, 41:1639–1648, August 1994.

[99] B. Daya Reddy. *Introductory Functional Analysis : With Applications to Boundary Value Problems and Finite Elements*. Springer-Verlag, New York, NY, USA, 1998.

[100] R. G. Regis and C. A. Shoemaker. Constrained global optimization of expensive black box functions using radial basis functions. *Journal of Global Optimization*, 31:153–171, January 2005.

[101] A.J. Romano, J.J. Shirron, and J.A. Bucaro. On the noninvasive determination of material parameters from a knowledge of elastic displacements: theory and numerical simulation. *IEEE Transactions on Ultrasonics, Ferroelectrics, and Frequency Control*, 45:751–759, May 1998.

[102] D. E. Rosario, J. C. Brigham, and W. Aquino. Identification of material properties of orthotropic elastic cylinders immersed in fluid using vibroacoustic techniques. *Ultrasonics*, 48:547–552, November 2008.

[103] R. Roscoe. Mechanical models for the representation of visco-elastic properties. *British Journal of Applied Physics*, 1:171–173, April 1950.

[104] A. Samani, J. Bishop, C. Luginbuhl, and D. B. Plewes. Measuring the elastic modulus of ex vivo small tissue samples. *Physics in Medicine and Biology*, 48:2183–2198, July 2003.

[105] R. Sampath and N. Zabaras. An object-oriented framework for the implementation of adjoint techniques in the design and control of complex continuum systems. *International Journal for Numerical Methods in Engineering*, 48:239–266, 2000.

[106] R. Schneider. *Applications of the discrete adjoint method in computational fluid dynamics*. PhD thesis, The University of Leeds School of Computing, April 2006.

[107] Y. Shia, H. Sola, and H. Hua. Material parameter identification of sandwich beams by an inverse method. *Journal of Sound and Vibration*, 290:1234–1255, March 2006.

[108] J.C. Simo and T.J.R. Hughes. *Computational Inelasticity*. Springer, New York, NY, USA, 1998.

[109] R. Singh, P. Davies, and A.K. Bajaj. Estimation of the dynamical properties of polyurethane foam through use of Prony series. *Journal of Sound and Vibration*, 264:1005–1043, July 2003.

[110] A. Skovoroda, S. Emelianov, and M. O'Donnell. Tissue elasticity reconstruction based on ultrasonic displacement and strain images. *IEEE Transactions of Ultrasonic Ferroelectrics Frequency Control*, 42:747–765, July 1995.

[111] M. Sridhar, J. Liu, and M.F. Insana. Viscoelasticity imaging using ultrasound: parameters and error analysis. *Physics in Medicine & Biology*, 52:2425–2443, May 2007.

[112] D. D. Steele, T. L. Chenevert, A. R. Skovoroda, and S. Y. Emelianov. Three-dimensional static displacement, stimulated echo NMR elasticity imaging. *Physics in Medicine and Biology*, 45:1633–1648, June 2000.

[113] R.L. Taylor, K.S. Pister, and G.L. Goudreau. Thermomechanical analysis of viscoelastic solids. *International Journal for Numerical Methods in Engineering*, 2:45–59, 1970.

[114] G. H. Templeton and L. R. Nardizzi. Elastic and viscous stiffness of the canine left ventricle. *Journal of Applied Physiology*, January 1974.

[115] F. Viola and W.F. Walker. Radiation force imaging of viscoelastic properties with reduced artifacts. *IEEE Transactions on Ultrasonics, Ferroelectrics, and Frequency Control*, 50:736–742, June 2003.

[116] Curtis R. Vogel. *Computational methods for inverse problems*. Society for Industrial and Applied Mathematics, Philadelphia, PA, USA, 2002.

[117] W.F. Walker, F.J. Fernandez, and L.A. Negrón. A method of imaging viscoelastic parameters with acoustic radiation force. *Physics in Medicine & Biology*, 9:1437–1447, June 2000.

[118] C. W. Washington and M. I. Miga. Modality independent elastography (MIE): A new approach to elasticity imaging. *IEEE Transactions on Medical Imaging*, 23:1117–1128, September 2004.

[119] Y. Zheng, S. Chen, W. Tan, R. Kinnick, and J. F. Greenleaf. Detection of tissue harmonic motion induced by ultrasonic radiation force using pulse-echo ultrasound and kalman filter. *IEEE Transactions on Ultrasonics, Ferroelectrics and Frequency Control*, February 2007.

[120] C. Zhu, R.H. Byrd, and J. Nocedal. L-BFGS-B: Algorithm 778: L-BFGS-B: Fortran subroutines for large-scale bound-constrained optimization. *ACM Transactions on Mathematical Software*, 23:550–560, December 1997.